www.scirp.org/journal/jbise

Scientific Research

JBiSE

ISSN: 1937-6871
Volume 3 Number 7 July 2010

Journal of Biomedical Science and Engineering

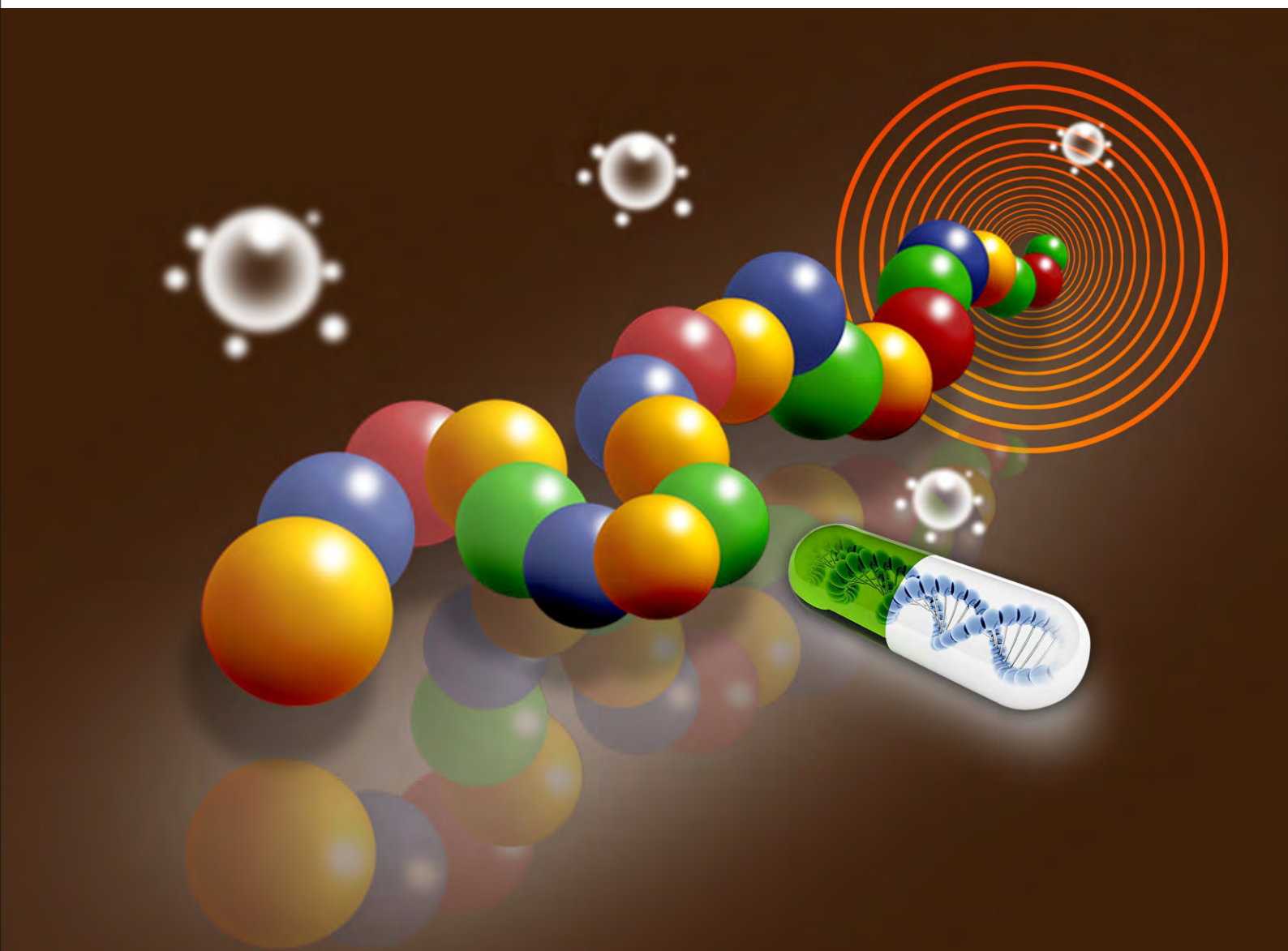

ISSN: 1937-6871

Journal Editorial Board

ISSN 1937-6871 (Print) ISSN 1937-688X (Online)
http://www.scirp.org/journal/jbise

TABLE OF CONTENTS

Volume 3, Number 7, July 2010

Journal of Biomedical Science and Engineering (JBiSE)

Journal Information

SUBSCRIPTIONS

The *Journal of Biomedical Science and Engineering* (Online at Scientific Research Publishing, www.SciRP.org) is published monthly by Scientific Research Publishing, Inc., USA.

Subscription rates:

Print: $50 per issue.
To subscribe, please contact Journals Subscriptions Department, E-mail: sub@scirp.org

SERVICES

Advertisements
Advertisement Sales Department, E-mail: service@scirp.org

Reprints (minimum quantity 100 copies)
Reprints Co-ordinator, Scientific Research Publishing, Inc., USA.
E-mail: sub@scirp.org

COPYRIGHT

PRODUCTION INFORMATION

For manuscripts that have been accepted for publication, please contact:
E-mail: jbise@scirp.org

J. Biomedical Science and Engineering, 2010, 3, 645-652 **JBiSE**
doi:10.4236/jbise.2010.37088 Published Online July 2010 (http://www.SciRP.org/journal/jbise/).

Effect of freezing on the passive mechanical properties of arterial samples

Jorge O. Virues Delgadillo[1], Sebastien Delorme[2], Rouwayda El-Ayoubi[2], Robert DiRaddo[2], Savvas G. Hatzikiriakos[1]

[1]Department of Chemical & Biological Engineering, University of British Columbia, Vancouver, Canada;
[2]Industrial Materials Institute, National Research Council of Canada, Boucherville, Canada.
Email: hatzikir@interchange.ubc.ca; Sebastien.Delorme@imi.cnrc-nrc.gc.ca

Received 19 December 2009; revised 18 January 2010; accepted 27 January 2010.

ABSTRACT

Little mechanical data is available on human arteries because of the difficulty of testing artery samples often obtained from autopsy, while arteries are still considered "fresh". Various solutions mimicking the physiological environment have been used to preserve artery samples from harvesting to testing. Cryopreservation might provide a means to preserve the mechanical properties of arteries for days or weeks after harvesting. The objective of this study is to investigate the effect of several preservation methods, including simplified cryopreservation methods, on the passive mechanical properties of arteries. Eighteen fresh cruciform samples were mechanically tested. Samples were divided in three groups based on preservation medium and freezing method: isotonic saline solution, Krebs-Henseleit buffer solution with dimethyl sulfoxide (DMSO), and dipped in liquid nitrogen. In each group, half of the samples were stored at -20℃ and the other half at -80℃. Two months later, all the tissues were thawed at 4℃ and mechanical tests were repeated. Preservation of arteries for two months in Krebs solution with DMSO (at -20℃ or at -80℃) or in isotonic saline solution at -20℃ were the methods that least changed the mechanical properties of the arteries.

Keywords: Thoracic Aorta; Mechanical Testing; Physiological Solution; Cryopreservation; Cryoprotective Agent

1. INTRODUCTION

The most common method for investigating the mechanical behavior of soft tissues consists of conducting mechanical tests on animal tissue explants, *i.e.*, harvested within a day after the death of the animal [1-3]. There is however few data on *in vitro* mechanical behavior of human arterial tissues, in part because of the logistical difficulty of performing mechanical tests on fresh human tissues. Some studies [4-12] have reported testing human tissues several days after death, assuming that mechaniccal properties of the tissues were preserved by refrigerating and by using chemical solutions mimicking the physiological environment, such as saline, Ringer's, Tyrode's, Hank's, Krebs and variations based on these solutions. Cryopreservation methods [13] developed to preserve artery samples for re-implantation could also provide a means to preserve arteries for days and weeks before mechanical testing.

Artery mechanical properties have been shown to depend on the relative proportion and arrangement of the arterial wall constituents such as collagen, elastin and smooth muscle cells [14,15], as well as on the integrity of the elastin and collagen fibers [16,17]. Smooth muscle cells contribute to structural, mechanical and functional changes in the arterial wall through several processes, including cell growth, elongation and reorganization of cells, and alteration of extracellular matrix composition [18]. The viability of smooth muscle cells, as well as the integrity of elastin and collagen fibers contribute to the arterial wall mechanical behaviour [16,17]. Damage caused to smooth muscle cells by ice formation and fragmentation of extracellular matrix fibers might affect the mechanical properties of the artery. Cryoprotective agents (CPA), such as dimethyl sulfoxide (DMSO), have been used in several studies to protect the cells from cryoinjury [19-21]. These CPAs are typically added to the storing solution in order to reduce ice formation in both intra- and extracellular space by preventing water movement out of the tissue [21]. The effect of cryopreservation has been investigated with respect to cell viability [22,23] and histological changes [24-28], but little is known about the effect of cryopreservation on mechanical properties of the arterial wall.

It has been found [29,30] that major arteries can withstand freezing and thawing without subsequent rupture.

For instance, Pascual *et al.* [30] observed that slow thawing minimizes fissure and crack propagation compared to rapid thawing if the tissue was frozen at -196℃. They also observed that slow and rapid thawing does not significantly change the structure of the vessel frozen at -80℃. Fresh and cryopreserved behaviour of arteries has been investigated using inflation [31] and uniaxial tests [32,33]. Blondel *et al.*, [31] and Venkatasubramanian *et al.*, [33] observed significant stiffening of femoral arteries cryopreserved at -80℃ and -150℃ respectively compared to fresh arteries. Adham *et al.*, [32] observed no difference in high strain modulus of aortas preserved at +4℃ for 1 month compared to cryopreservation with DMSO at -135℃ for 4 months.

The goal of the present study was to evaluate the effect of several conservation methods on the passive biaxial mechanical properties of arteries, regardless of cell viability, for the purpose of delayed mechanical testing. The preservation methods investigated include freezing for two months at either -20℃ or -80℃, in the presence of isotonic saline solution or Krebs-Henseleit solution with DMSO, or without immersing in solutions but dipped in liquid nitrogen. Because some of these methods are simplified adaptations of cryopreservation techniques, cell viability is not expected to be maintained in the samples. This study describes the storing conditions that best preserve the passive mechanical properties of arteries.

2. MATERIALS AND METHODS

2.1. Experimental Setup

Eighteen thoracic aortas were harvested within the day of death of pigs from a local slaughterhouse and cleaned of remaining connective tissue. One cruciform-shaped sample (55-by-55 mm) was cut out from each aorta for equibiaxial testing (**Figure 1(a)**). The average thickness of all tested specimens, measured with a vernier caliper, was 2.3 ± 0.2 mm. During transport and preparation, samples were stored in isotonic saline solution at 4℃ for up to 8 hours prior to testing.

Cruciform samples were mechanically tested on a planar biaxial test bench (ElectroForce® LM1, Bose Corporation, Minnetonka, MN), shown in **Figure 1(b)** and capable of applying a peak force of 200 N over a displacement range of 12 mm per actuator. Samples were mounted in horizontal configuration inside a saline bath heated at body temperature (37℃). Grip clamps were used to attach the four tabs of the cruciform sample to the arms extending from the actuators over the top of the bath, accordingly to a previously described method [34]. As well as being technically less difficult to set-up

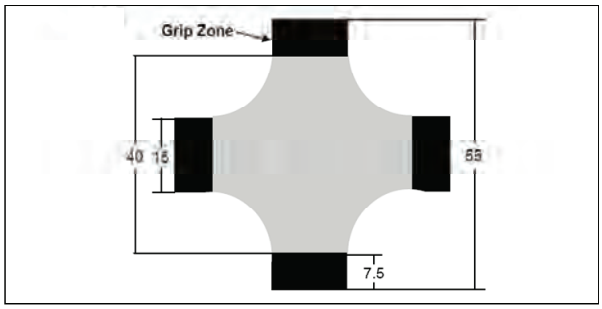

(a)

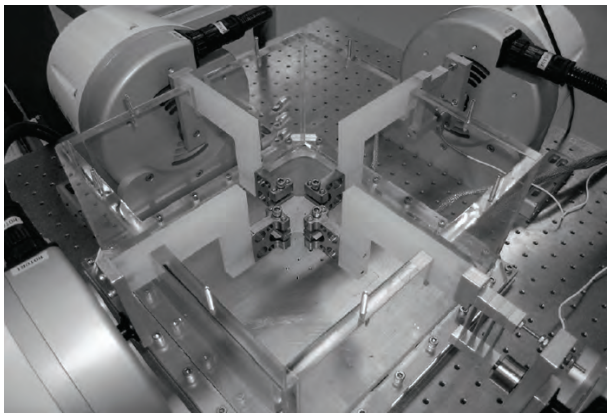

(b)

Figure 1. Sample dimension in millimetres for biaxial testing and (b) biaxial test bench used for cruciform sample clamped with grips.

than using square samples attached with hooks, and eliminating the need for videoextensometry, the cruciform sample method offers the advantage of stretching the samples to higher stretch ratios before failure than square samples with hooks [34]. The experimental data obtained from cruciform samples can be used in further studies (e.g. using inverse modeling) to obtain for example, which material parameters of the constitutive equation selected are most sensitive to freezing effects.

Equibiaxial testing was done by applying a 12 mm displacement (which corresponds to an average nominal stretch ratio of 1.55) on each one of the four grips, creating a non uniform strain distribution in the sample. The nominal stretch ratio was calculated using the distance between facing grips. The 1.55 stretch ratio was selected based on earlier experiments [34] because it allows capturing the nonlinear part of the stress-stretch curve, while avoiding rupture of the samples. Equibiaxial testing created a non uniform strain distribution in the cruciform sample. Triangular displacement wave forms were applied at a deformation rate of 110%/s, which corresponds to a frequency of 1.0 Hz (60 cycles per secod). Displacements were applied for 20 cycles. The first 10

cycles were used for pre-conditioning. The force-stretch data was averaged over the last 10 cycles.

After the 18 fresh samples had been tested biaxially, they were randomized into three groups for storing: Group I, samples were put in a polypropylene tube filled with isotonic saline solution; Group II, samples were put in a polypropylene tube filled with Krebs-Henseleit solution, supplemented by 1.8 M DMSO; and group III, samples were dipped in liquid nitrogen and then put in a polypropylene tube without any solution. For each group, half of the samples were stored at -20℃ and the other half at -80℃. Samples in group II were stored at 4℃ for 20 minutes prior to freezing as proposed by Oliver [35]. Three samples were stored under each of the six different storage conditions, as shown in **Table 1**.

After two months, the samples were thawed at 4℃ for 24 hours and rinsed in isotonic saline solution at body temperature for one minute. The same mechanical testing procedure and conditions were then repeated.

2.2. Statistical Analysis

Medians and ranges (percentile between 75%-25%) were calculated for circumferential and axial force-stretch curves. Thawed/fresh force ratio ($F_{\max}^{Thawed}/F_{\max}^{Fresh}$) at 1.55 stretch ratio were compared between all groups using the ANOVA Krustal-Wallis statistic test for independent variables with a 0.05 level of significance ($p=0.05$). The p value quantifies the probability of concluding that the storing condition used has an effect on the mechanical properties when in reality it did not. Krustal-Wallis test (non-parametric) was selected because the small sample size does not allow verifying the hypothesis of normal distribution, which is required to perform a Student's t-test. A statistical power analysis was also used to know the probability of falsely rejecting the null hypothesis using a threshold of 80%.

3. RESULTS

3.1. Experimental Results

The medians of the force-stretch curves in the circumferential and axial directions for fresh specimens ($n=18$) are plotted in **Figure 2**. The difference in mechanical behavior below a stretch ratio of 1.5 is small.

The medians of the force-stretch curves for the samples in group I, II and III are presented in **Figures 3, 4** and **5** respectively. In groups I, II and III, preserved samples appeared to be stiffer than fresh samples in the circumferential direction, but these differences were not statistically significant. Preserved sample forces in the axial direction appeared to be similar to fresh samples.

Figures 6(a) and **6(b)** shows the Thawed/fresh ratios ($F_{\max}^{Thawed}/F_{\max}^{Fresh}$) of the circumferential forces measured at the maximum stretch ratio ($\lambda=1.55$) for all the samples stored at -20 and -80℃, respectively. The loading forces in the circumferential direction of all thawed samples (Groups, I, II and III) were almost two times higher than the loading forces of fresh samples (median of the ratio $F_{\max}^{Thawed}/F_{\max}^{Fresh}\cong 2.0$). On the other hand, difference in axial forces between fresh and thawed tissue was lower than 40% for all groups (**Figures 6(c)** and **6(d)** shows axial results at -20 and -80 °C, respectively). The medians, percentiles (75%-25%) and the ANOVA Krustal-Wallis test p values are also included in **Figure 6**.

Table 1. Number of samples for each storage condition.

FreshTissue	Thawed Tissue		
	Group	Storage Temperature	
		-20℃	-80℃
18	I	3	3
	II	3	3
	III	3	3

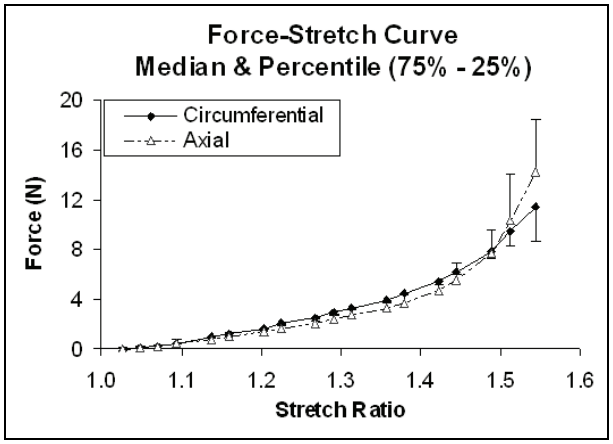

Figure 2. Medians of the force-stretch behavior of fresh cruciform samples tested at 110%/s ($n=18$). Open triangles and closed circles represent axial and circumferential mean forces, respectively. The percentile of the data points is also shown.

4. DISCUSSION

This study investigated the influence of freezing in different solutions on the mechanical properties of arterial wall. Results were reported in terms of force vs. stretch ratio rather than stress vs. stretch ratio. This is due to the fact that stress and strain distributions in a cruciform sample subjected to biaxial extension experiment are not homogeneous, even when an equibiaxial stretch is applied. It was shown in [34] that the highest and lowest stresses can be found near the curved boundaries and near the center of the sample, respectively.

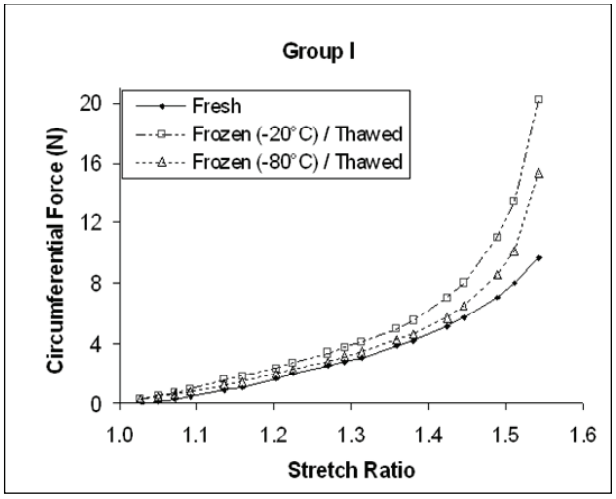

(a)

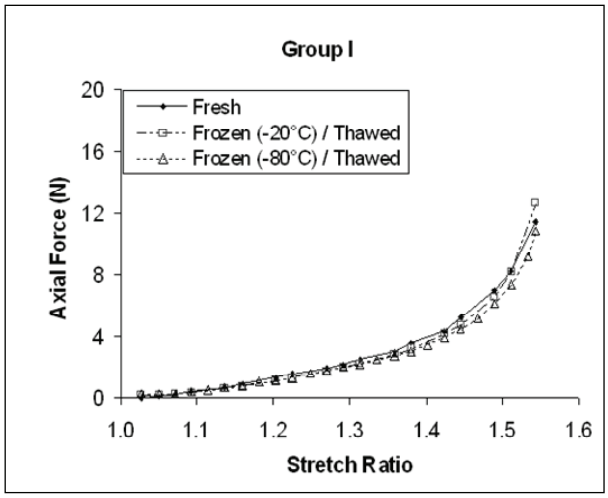

(b)

Figure 3. Medians of cruciform samples tested at a deformation rate of 110%/s, and stored in saline solution ($n = 3$): Arterial wall behavior in (a) circumferential and (b) axial directions.

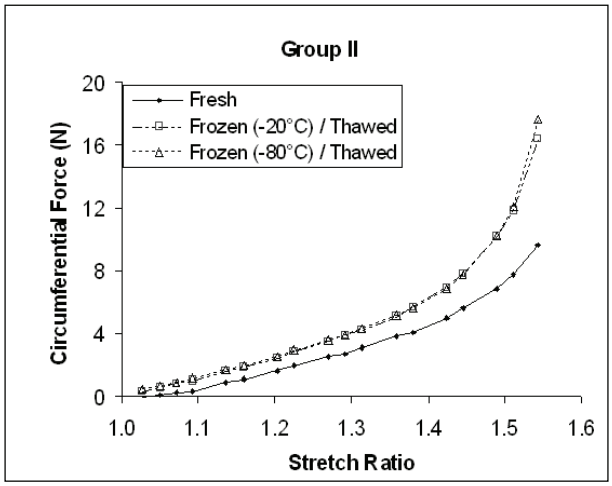

(a)

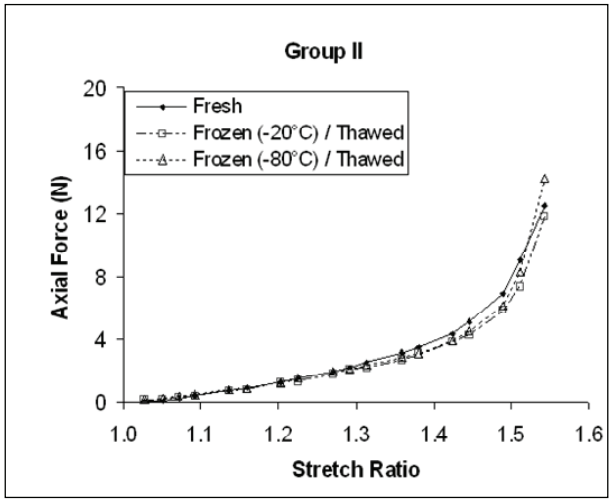

(b)

Figure 4. Medians of cruciform samples tested at a deformation rate of 110 %/s, and stored in Krebs solution with dimethyl sulfoxide, DMSO ($n = 3$): Arterial wall behavior in (a) circumferential and (b) axial directions.

The differences observed in the mechanical behavior (*i.e.* medians of force data points) of thawed samples were not significant ($p = 0.64$) , independently of the storing medium used (saline, Krebs with DMSO and dipping in liquid nitrogen). In order to confirm that indeed there is no differences in fresh and thawed behavior; a statistical power analysis (http://www.dssresearch.com/toolkit) was performed using the force data points obtained at 1.55 stretch ratio for each group between the fresh and the thawed specimens. The probability of rejecting a false null hypothesis (*i.e.* the storing condition used has no effect on the mechanical properties when in reality it might have an effect) and thus minimizing the occurrence of a β error (which occurs if it is concluded that there is no difference in fresh and thawed specimen behavior when in reality there might be a difference) increases as the statistical power increases. Statistical powers between 13% and 93% were obtained in circumferential direction. In axial direction, the power was lower than 47% and higher than 5%. The statistical power obtained for mostly all groups was not high enough to verify how significant the difference was between thawed and fresh tissue. In addition, the software used to obtain the power assumes that the data is parametric. Non-parametric analysis will likely estimate a slightly less power. Future studies with a higher sample size may further support the results obtained in this work. The observed lack of significant differences in this study was

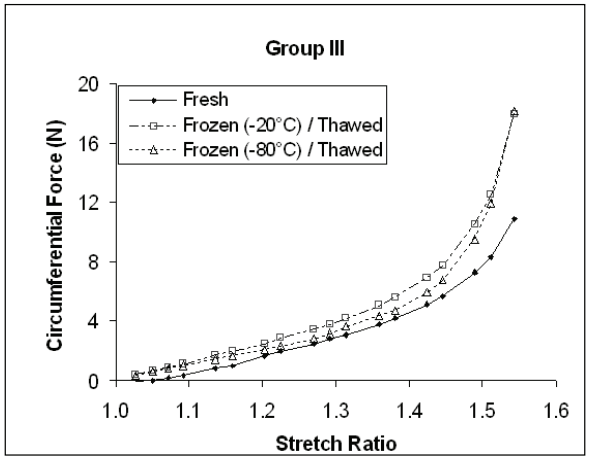

(a)

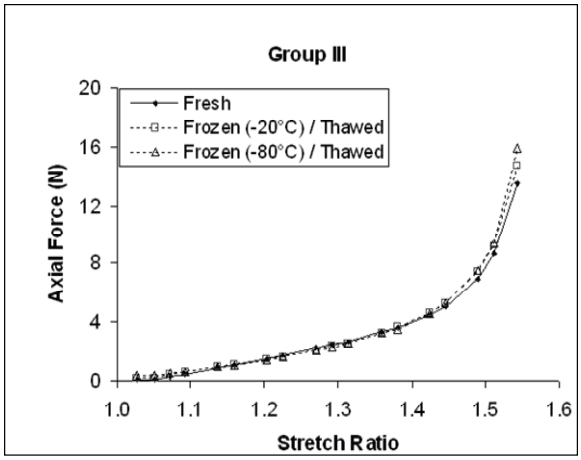

(b)

Figure 5. Medians of cruciform samples tested at a deformation rate of 110 %/s, dipped in liquid nitrogen and stored in air ($n = 3$): Arterial wall behavior in (a) circumferential and (b) axial directions.

likely due to the small number of samples tested per storing group ($n = 3$). However, these results are consistent with findings reported by Adham *et al.* [32] and by Venkatasubramanian *et al.* [33], who reported no significant difference between mechanical behavior of fresh artery samples and of samples cryopreserved with a cryoprotective agent such as DMSO, with up to 13 samples in each group.

The thawed samples appeared to be stiffer than the fresh samples at high stretch ratios. The differences in the load force-stretch curves might be the result of a modification in structure due to crosslinking or a change in fiber alignment. Elder *et al.* [36] stated that the increased tissue stiffness after cryopreservation may be related to the thermal change (*i.e.* drop of temperature) that occurs during preservation, catalyzing the thermal crosslinking of collagen fibers within the extracellular matrix. Collagen fibers are mainly oriented in the circumferential direction [37], thus the collagen matrix would develop stiffer interconnections in the circumferential than in axial direction during freezing. After thawing, the collagen matrix might have been reinforced in the circumferential direction, which is reflected in the stiffer response observed.

In this study the effect of freezing on cell injury and functionality was not investigated. However previous studies [38-40] have shown that contractile function of both endothelial and smooth muscle cells were preserved in arteries of a variety of species following freezing and thawing in DMSO solutions. DMSO reduces the mass transport of water and solutes throughout cell membrane while freezing. When water moves out of the cytoplasm, DMSO dissolves the suspended electrolytes, reducing the harmful effects of high solute concentration. DMSO interacts and partially replaces water molecules in such a way that the freezing point in the solution is lowered during cooling and the intracellular ice is reduced. Ice crystal formation and growth is prevented when the cryoprotectant-water mixture solidifies in a glass-like structure; and thus, preserving cell viability and mechanical properties. Song *et al.* [38] found that the maximum concentration needed to prevent damage in the tissue is 15% (wt/wt). In the present study, the DMSO concentration was 1.8 M, *i.e.* < 12% wt/wt. This concentration is expected to maintain cell viability within the tissue. Evidence has shown that after thawing, both biochemical and functional activities of arterial tissue cryopreserved at low temperatures in Krebs solution containing 1.8 M of DMSO were comparable to fresh tissues [41].

Freezing and storing arteries in saline solution do not conserve the mechanical properties. As described by Lovelock [42], during the freezing process, the volume of liquid water in the cytoplasm decreases due to extracellular ice formation, leading to cellular dehydration. If the dehydration is too severe, the high electrolyte concentration inside the cytoplasm could result in cell death [43]. DMSO reduces the mass transport of water and solutes through the cell membrane while freezing. Ice crystal formation and growth is prevented when the cryoprotectant-water mixture solidifies in a glass-like structure, thus preserving cell viability and mechanical properties. The concentration of DMSO used in this study is expected to maintain cell viability within the tissue, albeit this study was not focused on freezing effects on cell viability. The better results obtained with DMSO suggest that cell death might play a role in changes of tissue stiffness, although this study could not unveil the exact mechanism involved. Also, during thaw-

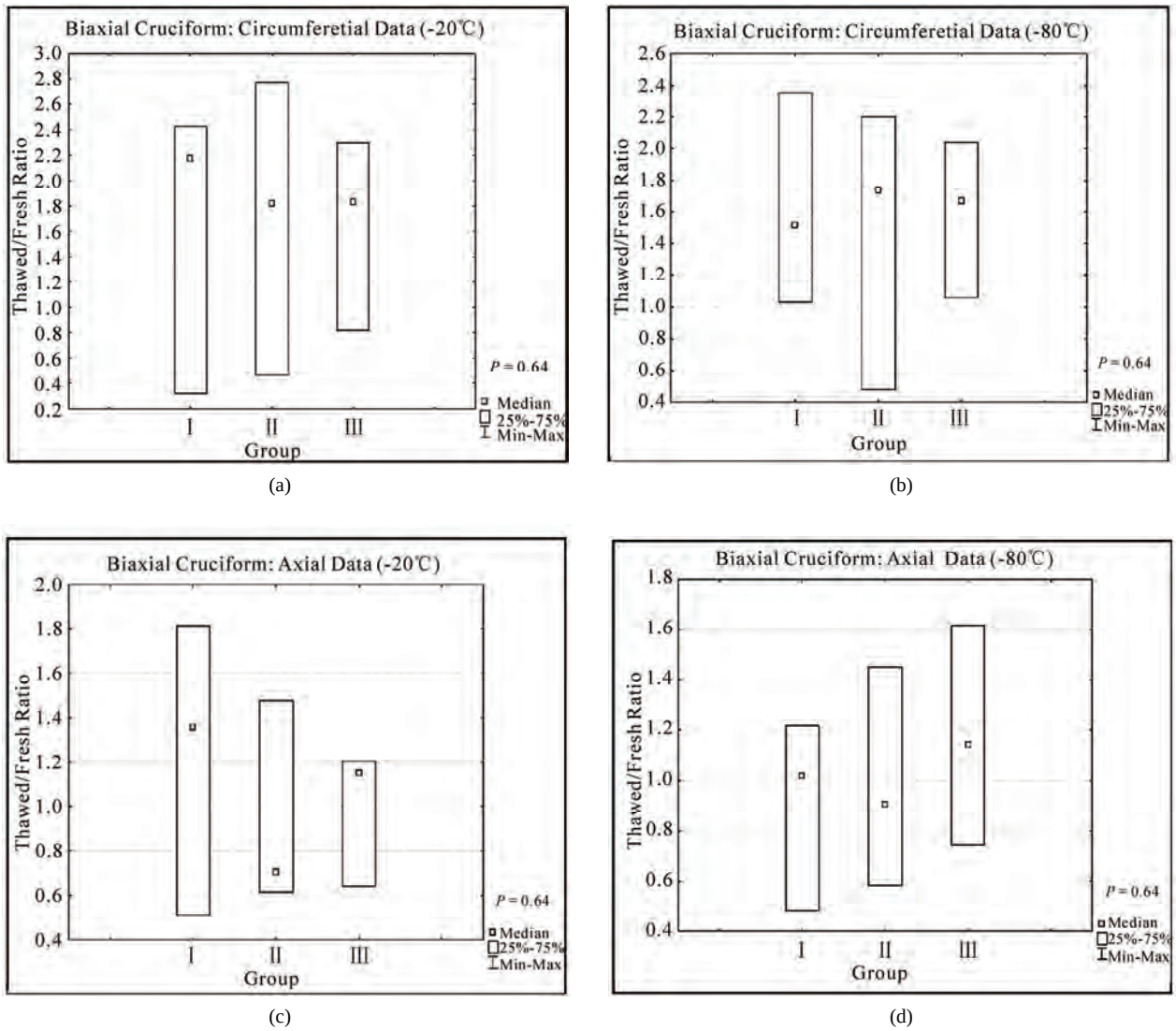

Figure 6. Comparison of Thawed/Fresh force ratios per storage group at the maximum stretch ratio applied ($\lambda = 1.55$): (a, b) circumferential and (c, d) axial direction $F_{\max}^{Thawed} / F_{\max}^{Fresh}$ ratios of samples stored at -20 and -80℃.

ing, the deformation of the cytoplasm due to volume increase could have permanently modified the orientation of the intracellular fibers, and as a result permanently changed the mechanical behaviour of the cells. Therefore our results suggest that, as concluded by Venkatasubramanian *et al.* [33], the changes in mechanical properties could be due to cell loss, to damage to the extracellular matrix or to a combination of both. Stachecki *et al.* [44] suggested that the reduction or removal of sodium from the storing solution is of primary importance to freeze cells efficiently, and proved that it is possible to replace sodium with a bigger molecular size ion, which encounters more obstacles to penetrate the cell membrane.

Dipping the arterial sample in liquid nitrogen could not preserve the mechanical properties of the specimens evaluated in this study. When exposing the specimens to a very rapidly decreasing temperature, ice crystal formation might have occurred faster than cell dehydratation, resulting in intracellular ice formation [45] and cell death. The differences observed between fresh and thawed - samples suggest that the formation of intracellular ice crystals might have and effect on tissue stiffness. Vitrification is an alternative to obtain an amorphous glassy state matrix and thus minimizing ice nucleation and growth. However, it requires high concentrations of cryoprotective agents [46,47]. For example, Song *et al.* [48] were able to avoid crystallization by using a combination of CPAs (DMSO, formamide and 1,2-propanediol) and rapidly cooling the vessel to -196℃. Jiménez Rios and Rabin [49] have improved cell viability by using a specific freezing rate, pressurized liquid nitrogen, and specific type and concentration of CPA. Non-toxic cryopro-

tectants, like glyerol [50] or fetal bovine serum [51] could also be used.

5. CONCLUSIONS

In the present study, we have found that the mechanical properties of arteries were not significantly changed after preserving arteries for two months in Krebs solution with DMSO (at -20℃ or at -80℃) or in isotonic saline solution at -20℃. However, the preservation approach taken here needs to be improved in order to maintain cell viability and as a result determine the best conditions to preserve the mechanical properties of the arterial wall. Selection of the optimal preservation method might be obtained by performing a study where the variables to be adjusted are slow cooling rate and step-wise DMSO loading, and therefore minimize changes to the arterial microstructure by the reduction of thermal stresses within the frozen tissue. Further studies are required to clarify the impact of cryopreservation on extracellular matrix architecture to help tailor an optimized approach in order to preserve the mechanical properties of arteries.

6. ACKNOWLEDGEMENTS

This research was possible thanks to the PhD scholarship given by the Mexican Council of Science and Technology (Consejo Nacional de Ciencia y Tecnología), CONACYT. The authors would also like to thank Marc-Andre Rainville for his guidance and assistance in sample preparation and mechanical testing.

REFERENCES

[1] Waldman, S.D. and Lee, J.M. (2002) Boundary conditions during biaxial testing of planar connective tissues: Part 1: Dynamic behavior. *Journal of Materials Science, Materials in Medicine*, **13(10)**, 933-938.

[2] Prendergast, P.J., Lally, C., Daly, S., Reid, A.J., Lee, T.C., Quinn, D. and Dolan, F. (2003) Analysis of prolapse in cardiovascular stents: A constitutive equation for vascular tissue and finite-element modelling. *Journal of Biomechanical Engineering*, **125(5)**, 692-699.

[3] Lally, C., Reid, A.J. and Prendergast, P.J. (2004) Elastic behavior of porcine coronary artery tissue under uniaxial and equibiaxial tension. *Annals of Biomedical Engineering*, **32(10)**, 1355-1364.

[4] Okamoto, R.J., Wagenseil, J.E., Delong, W.R., Peterson, S.J., Kouchoukos, N.T. and Sundt III, T. M. (2002) Mechanical properties of dilated human ascending aorta. *Annals of Biomedical Engineering*, **30(5)**, 624-635.

[5] Van dE Geest, J.P., Sacks, M.S. and Vorp, D.A. (2004) Age dependency of the biaxial biomechanical behavior of human abdominal aorta. *Journal of Biomechanical Engineering*, **126(6)**, 815-822.

[6] Mohan, D. and Melvin, J.W. (1983) Failure properties of passive human aortic tissue. II Biaxial tension tests. *Journal of Biomechanics*, **16(1)**, 31-44.

[7] Van Andel, C.J., Pistecky, P.V. and Borst, C. (2003) Mechanical properties of porcine and human arteries: Implications for coronary anastomotic connectors. *Annals of Thoracic Surgery*, **76(1)**, 58-65.

[8] Schulze-Bauer, C.H.A.J., Mörth, C.H. and Holzapfel, G. A. (2003) Passive biaxial mechanics response of aged human iliac arteries. *Journal of Biomechanical Engineering*, **125(3)**, 395-406.

[9] Raghavan, M.L., Webster, M.W. and Vorp, D.A. (1996) Ex vivo biomechanical behavior of abdominal aortic aneurysm: assessment using a new mathematical model. *Annals of Biomedical Engineering*, **24(5)**, 573-582.

[10] Carmines, D.V., McElhaney, J.H. and Snack, R. (1991) A piece-wise non-linear elastic stress expression of human and pig coronary arteries tested in vitro. *Journal of Biomechanics*, **24(10)**, 899-906.

[11] Langewouters, G.J., Wesseling, K.H. and Goedhard, W.J. A. (1984) The static elastic properties of 45 human thoracic and 20 abdominal aortas in vitro and the parameters of a new model. *Journal of Biomechanics*, **17(6)**, 425-435.

[12] Hudetz, G., Mark, G., Kovach, A.G.B., Kerenyi, T., Fody, L. and Monos, E. (1981) Biomechanical properties of normal and fibrosclerotic human cerebral arteries. *Atherosclerosis*, **39(3)**, 353-365.

[13] Han, B. and Bischof, J.C. (2004) Engineering challenges in tissue preservation. *Cell Preservation Technology*, **2(2)**, 91-112.

[14] Gamero, L.G., Armentano, R.L., Barra, J.G., Simon, A. and Levenson, J. (2001) Identification of arterial wall dynamics in conscious dogs. *Experimental Physiology*, **86(4)**, 519-528.

[15] Pascual, J.G., Garcia-Honduvilla, N., Gimeno, M.J., Jurado, F., Carrera-San, M.A. and Bellon, J.M. (2000) Rapid thawing increases the fragility of the cryopreserved arterial wall. *European Journal of Vascular and Endovascular Surgery*, **20(1)**, 13-20.

[16] Almassi, G.H., Farahbakhsh, B., Wooldribge, T., Rusch, N.J. and Olinger, G.N. (1996) Endothelium and vascular smooth muscle function in internal mammary artery after cryopreservation. *Journal of Surgical Research*, **60(2)**, 355-360.

[17] Pascual, G., Jurado, F., Rodríguez, M., Corrales, C., Lopez-Hervás, P., Bellón, J.M. and Bujan, J. (2002) The use of ischaemic vessels as prostheses or tissue engineering scaffolds after cryopreservation. *European Journal of Vascular and Endovascular Surgery*, **24(1)**, 23-30.

[18] Intengan, H.D. and Schiffrin, E.L. (2000) Structure and mechanical properties of resistance arteries in hypertension. Role of adhesion molecules and extracellular matrix determinants. *Hypertension*, **36(3)**, 312-318.

[19] Schenke-Layland, K., Madershahian, N., Riemann, I., Starcher, B., Halbhuber, K.J., König, K. and Stock, U.A. (2006) Impact of cryopreservation on extracellular matrix structures of heart valve leaflets. *The Annals of Thoracic Surgery*, **81(3)**, 918-926.

[20] Brockbank, K.G.M. (1989) Basic principles of viable tissue preservation. In: Clarke D.R., Ed., Transplantation techniques and use of cryopreserved allograft cardiac valves and vascular tissue. Adams Publishing Group, Boston, 9-23.

[21] Miles, C.A. (1999) Polymer-in-a-box mechanism for

thermal stabilization of collagen molecules in fibers. *Biophysics Journal*, **76(6)**, 3243-3252.

[22] Devireddy, R.V., Neidert, M.R., Bischof, J.C. and Tranquillo, R.T. (2003) Cryopreservation of collagen-based tissue equivalents. I. Effect of freezing in the absence of cryoprotective agents. *Tissue Engineering*, **9(6)**, 1089-1100.

[23] Neidert, M.R., Devireddy, R.V., Tranquillo, R.T. and Bischof, J.C. (2004) Cryopreservation of collagen-based tissue equivalents. II. Improved freezing in the presence of cryoprotective agents. *Tissue Engineering*, **10(1/2)**, 23-31.

[24] Song, Y.C., Pegg, D.E. and Hunt, C.J. (1995) Cryopreservation of the common carotid artery of the rabbit: Optimization of dimethyl sulfoxide concentration and cooling rate. *Cryobiology*, **32(5)**, 405-421.

[25] Cui, X., Labarrere, C., He, L., Cheng, S., Siderys, H., Kovacs, R. and Gao, D. (2002) Cryopreservation and microsurgical implantation of rabbit carotid arteries. *Cell Preservation Technology*, **1(2)**, 121-128.

[26] Pacholewicz, J.K., Adkins, M.S., Boris, W.J., Gu, J., Xenachis, C., Klabunde, R.E., Jasionowski, T. and McGrath, L.B. (1996) Evaluation of cryopreserved internal thoracic artery as an alternative coronary graft: Evidence for preserved functional, metabolic and structural integrity. *European Journal of Cardio-Thoracic Surgery*, **10(1)**, 20-25.

[27] Hunt, C.J., Song, Y.C., Bateson, E.A.J. and Pegg, D.E. (1994) Fractures in cryopreserved arteries. *Cryobiology*, **31(5)**, 506-515.

[28] Wusteman, M.C. and Pegg, D.E. (2001) Differences in the requirements for cryopreservation of porcine aortic smooth muscle and endothelial cells. *Tissue Engineering*, **7(5)**, 507-518.

[29] Cooper, I.S., Samra, K. and Wisniewska, K. (1971) Effects of freezing on mayor arteries. *Stroke*, **2(5)**, 471-482.

[30] Pascual, G., García-Honduvilla, N., Rodríguez, M., Turégano, F., Bujan, J. and Bellón, M. (2001) Effect of the thawing process on cryopreserved arteries. *Annals of Vascular Surgery*, **15(6)**, 619-627.

[31] Blondel W.C.P.M., Lehalle, B., Maurice, G., Wang, X. and Stoltz, J.F. (2000) Rheological properties of fresh and cryopreserved human arteries tested in vitro. *Rheologica Acta*, **39(5)**, 461-468.

[32] Adham, M., Gournier, J.P., Favre, J.P., De La Roche, E., Ducerf, C., Baulieux, J., Barral, X. and Pouyet, M. (1996) Mechanical characteristics of fresh and frozen human descending thoracic aorta. *Journal of Surgical Research*, **64(1)**, 32-34.

[33] Venkatasubramanian, R.T., Grassl, E.D., Barocas, V.H., Lafontaine, D., Bischof, J.C. (2006) Effects of freezing and cryopreservation on the mechanical properties of arteries. *Annals of Biomedical Engineering*, **34(5)**, 823-832.

[34] Virues-Delgadillo, J. (2008) Mechanical properties of arterial wall. Ph.D. Dissertation, The University of British Columbia, Columbia.

[35] Olivier, S.A. and Ellington, J.E. (2003) Cryopreserving somatic cells with an arabinogalactan containing cryopreservation medium, US Patent, 6593138 B1.

[36] Elder, E., Chen, Z., Ensley, A., Nerem, R., Brockbank, K. and Song, Y. (2005) Enhanced tissue strength in cryopreserved, collagen-based blood vessel constructs. *Transplantation Proceedings*, **37**, 4525-4629.

[37] Humphrey, J.D. (1995) Mechanics of the arterial wall: Review and directions. *Critical Reviews in Biomedical Engineering*, **23(1-2)**, 1-162.

[38] Song, Y.C., Hunt, C.J. and Pegg, D.E. (1994) Cryopreservation of the common carotid artery of the rabbit. *Cryobiology*, **31**, 317-329.

[39] Ku, D.D., Willis, W.L. and Caulfield, J.B. (1990) Retention of endothelium-dependent vasodilatory responses in canine coronary arteries following cryopreservation. *Cryobiology*, **27(5)**, 511-520.

[40] Bateson E.A.J. and Pegg, D.E. (1994) Cryopreservation of arteries: Selection of a model for human small elastic arteries and preliminary results of preservation of ring-segments with dimethyl sulphoxide. *CryoLetters*, **15(6)**, 15-26.

[41] Ellis, P. and Muller-Schweinitzer, E. (1991) Maintenance of functional activity of human pulmonary arteries after cryopreservation. *British Journal of Pharmacology*, **103(2)**, 1377-1380.

[42] Lovelock, J.E. (1953) The haemolysis of human red blood-cells by freezing and thawing. *Biochimica et Biophysica Acta*, **10(3)**, 414-426.

[43] Mazur, P., Rall, W.F. and Rigopoulos, N. (1981) Relative contributions of the fraction of unfrozen water and of salt concentration to the survival of slowly frozen human erythrocytes. *Biophysical Journal*, **36(3)**, 653-675.

[44] Stachecki, J.J., Cohen, J. and Willadsen, S. (1998) Detrimental effects of sodium during mouse oocyte cryopreservation. *Biology of Reproduction*, **59(2)**, pp. 395-400.

[45] Toner, M., Cravalho, E.G. and Karel, M. (1990) Thermodynamics and kinetics of intracellular ice formation during freezing of biological cells. *Journal of Applied Physics*, **67(3)**, 1582-1593.

[46] Fahy, G.M., Macfarlane, D.R., Angell, C.A. and Meryman, H.T. (1984) Vitrification as an approach to cryopreservation. *Cryobiology*, **21(4)**, 407-426.

[47] Thakrar, R.R., Patel, V.P., Hamilton, G., Fuller, B.J. and Seifalian, A.M. (2006) Vitreous cryopreservation maintains the viscoelastic property of human vascular grafts. *The FASEB Journal*, **20(7)**, 874-881.

[48] Song Y.C., Khirabadi, B.S., Lightfoot, F., Brockbank, K. G.M. and Taylor, M.J. (2000) Vitreous cryopreservation maintains the function of vascular grafts. *Nature Biotechnology*, **18(3)**, 296-299.

[49] Jimenez Rios, J.L. and Rabin, Y. (2006) Termal expansion of blood vessels in low cryogenic temperatures Part I: A new experimental device. *Cryobiology*, **52(2)**, 269-283.

[50] Gao, D.Y., Lin, S., Watson, P.F. and Critser, J.K. (1995) Fracture phenomena in an isotonic salt solution during freezing and their elimination using glycerol. *Cryobiology*, **32(3)**, 270-284.

[51] Yiu, W.K., Cheng, S.W.K. and Sumpio, B.E. (2007) Direct comparison of endotelial cell and smooth muscle call response to supercooling and rewarming. *Journal of Vascular Surgery*, **46(3)**, 557-564.

J. Biomedical Science and Engineering, 2010, 3, 653-663 **JBiSE**
doi:10.4236/jbise.2010.37089 Published Online July 2010 (http://www.SciRP.org/journal/jbise/).

Modelling infection spreading control in a hospital isolation room

Carla Balocco, Pietro Liò

[1]Department of Energy Engineering "*Sergio Stecco*", Firenze, Italy;
[2]Computer Laboratory, University of Cambridge, Cambridge, UK.
Email: pl219@cam.ac.uk

Received 9 May 2010; revised 21 May 2010; accepted 27 May 2010.

ABSTRACT

This paper investigates the airflow patterns connected to different cough conditions, the effects of these arrangements on the regions of droplet fallout and dilution time of virus diffusion of coughed gas. We focus on some of the physical processes that occur in a double bed hospital isolation room, investigating the effect of the ventilation system on the spread of particles in air. A cough model was carried out and used for the numerical simulation of virus diffusion inside an existent isolation room. Transient simulations of air pattern diffusion and air velocity field, provided by the existing typical HVAC primary air system designed for infectious patients, were performed using CFD. A multiphysics approach, combined Convection-Conduction, Incompressible Navier-Stokes models on non-isothermal air flow and Convection-Diffusion, was used. Simulations results highlighted that the flow field and velocity distribution induced by the high turbulence air inlet diffuser combined with the air return diffusers produce wide recirculation zones near the wall and partial stagnation areas near the ceiling and between the two beds, but lower particle concentration in the room and their shorter spreading distance. This type of analysis is certainly cost effective to identify all the air recirculation zones which can harbour lingering pathogens.

Keywords: Airborne Diffusion; Hospital Anfection; VAV System; Transient Simulation; CFD

1. INTRODUCTION

The risk of virus particles dispersal in hospitals mainly depends on airflow patterns and on airflow directions changes caused by people's activity, e.g. moving or opening doors. The ventilation system of isolation rooms, operating under closed-door conditions is crucial if the viruses spread and infection must be contained. The quality of the hospital environment is provided by an efficient air-conditioning and ventilating system design, in controlling temperature, humidity, pressure, and indoor air quality. The Heating Ventilation Air Conditioning systems (HVAC) design is fundamental to maintain negative pressure within isolation rooms, to protect health of workers, patients and visitors. This is also necessary to control patient risk from airborne diseases.

In recent years few works have focused on computational models using fluid dynamics approaches to investigated airflow patterns and the related spreading of infection in isolation rooms for different ventilation systems (for example operating under open or closed-door conditions) [1-4]. The main attention of these papers has been the evaluation of the effects of negative pressure in isolation rooms accommodating patients with highly infectious diseases. Recent studies have highlighted that an air velocity above 0.2 m s^{-1} via a doorway effectively prevents the spread of airborne contaminants out of the isolation room in the state of door opening [3,5]. HVAC switch on-off impact on virus and bacteria load has widely investigated recently [6-10].

Techniques such as aerosol particle tracer sampling and computational fluid dynamics can be applied to study the performance of ventilation systems during coughing episodes [4]. HVAC operating for hospitals, must establish optimal airflow pattern inside isolation rooms for infective and in particular for immune-suppressed patients, such that clean air from the air-supply vents may carry the air across infectious sources, and then flow through the exhaust vents completely [2,3]. However, it is not sufficient to provide clean environments, due to the higher cross-infections risk, useful guidelines on public health strategies and management can be obtained studying the risky environments by CFD-FEM simulation. In particular CFD simulations based on multiphysics approach can provide a good predictive efficacy, since the possibility to achieve in hos-

pital stays, accurate experimental measurements is limited and subjected to high costs and difficulties of practical realization. In this paper, referring to obtained results in [11], we developed new transient simulations combining thermo-fluidynamics and diffusion models with heat transfer analysis (convection and conduction). Moreover, we defined a particle tracing and diffusion model taking into account horizontal and vertical components of velocity to carry out a coughing function. Transient simulations were performed to investigate the air flow patterns, distribution and velocity, and the particulate dispersion inside an existing typical hospitalization room equipped with a HVAC primary air system designed for infected patients. We analysed three-dimensional models of the room considering different positions of the patients.

2. PARTICLES TRACING AND DIFFUSION

A dispersion model of droplets carrying viruses due to coughing and sneezing was carried out. We believe that our level of modelling details is an effective trade off between accurate description of the chemistry physics process and computational resource. A theoretical general framework would consider the mixture of viruses/bacteria and water as a two-phase fluid; a complete description would specify virus/bacterial aggregates/colonies in terms of coupled reaction-diffusion equations for the bacterial and water.

These equations are general in the sense that the reaction, diffusion, pressure, stresses and external forcing terms can be chosen differently for different types of micro-organisms. Further details may take into account different shapes of bacteria (round, spirals, ect) and floating behaviour (stroke-averaged swimmer, shakers" (not self-propelled) and "movers" (self-propelled particles), "pushers" (most bacteria) and "pullers" (for example some algae). Coughing and sneezing produce droplets in size range from less than 1 to up to 2000 μm.

Typical diameter of a virus, bacteria and fungal spore is respectively 0.02 ÷ 0.3 μm, 0.3 ÷ 10 μm and 2 ÷ 5 μm. Referring to literature we define large droplets those with diameter larger than 60 μm, and small ones if the diameter is less than 60 μm and nucleus droplets when they are less than 10 μm. Winter season provides optimal conditions for airborne influenza spreading. Coughs and sneezing releases droplets that in cold and low humidity conditions dry out partially the droplets, reducing their size, so to allows the virus to linger longer in the air and the nasal passages making virus transmission more likely. Therefore a multiphysic approach to take into account for temperature variations (in the room) is of key importance. Pathogenic bacteria are generally transported on larger droplets such as skin flakes (13 ÷ 17 μm diameter) or droplets (ejected with peak diameter 20 ÷ 40 μm) coughing/sneezing generates $10^4 \div 10^5$ droplets. The potential for fomites to remain in the air is due to their final fall velocity that varies with the square of their diameter [4]. Finer particles can remain in the air for long period while larger particles usually sediment to surfaces in those regions of slowly moving air. Particles of 10 μm which are responsible of the contagious up to 2 meters distance were taken into account for all the simulations.

A commonly used factor is the Cunningham Slip Correction (C_c) which is a correction to the drag coefficient that is used to predict the drag force between a fluid and a particle moving through this fluid. The drag coefficient on each particle must be divided by the Cunningham correction factor, i.e. molecular slip correction that occurs when the size of the particle is of the same magnitude as the distance between gas and water molecules. The particle no longer moves as a continuum in the gas, but as a particle among discrete gas molecules thereby reducing the drag force. The correction factor is greater than 1 which means that the effective particle drag coefficient goes down: this reduction in particle drag is the "particle slip" [12,13]:

$$C_c = 1 + \frac{\lambda}{D_{pa}}\left[2.34 + 1.05\exp\left(-0.39\frac{D_{pa}}{\lambda}\right)\right] \quad (1)$$

We considered the free mean path λ of a particle, the average distance the particle travels between collisions with other moving particles. The following boundary conditions, that were taken into account, produced a reduction of the Cunningham factor towards its lower boundary of 1: the positive pressure of the isolation room reduces slightly the mean free path with respect to atmospheric pressure; the droplets are initially larger and the evaporation reduces their dimension; the droplets contain glycoproteins, lipidoproteins and lipoglycids constituents of the mucous and also viral particles (and possibly, bacteria); the presence of glycol and lipidproteins could increase the local viscosity of the droplet. The droplet is then subjected to two forces: the force of gravity and the drag force of air resistance [12].

At low velocity v and low Reynolds number the air resistance f for a droplet of mass m, is mainly proportional to the viscosity of the medium and to the linear size of the droplet. This provides the horizontal component of motion. The vertical component of sedimentation velocity is:

$$u_{vertical} = \frac{\rho D_{pa}{}^2 g C_c}{18\eta} \quad (2)$$

The horizontal component of the velocity is provides

by f (u) = (b • u) and then:

$$u_{horizontal} = v_0 \cdot e^{\frac{-b \cdot t}{m}} \quad (3)$$

where (b/m) has the dimension of time (in seconds as unit system used in this study). The horizontal and vertical components of velocity are also important for fomites formation, *i.e.* contaminated environmental surfaces which become secondary sources of infection. For a rain drop (approximated as a sphere) the coefficient b has the form b = (D • β). For a spherical drop in air at atmospheric pressure conditions (101325 Pa) and temperature of 22℃, the value of the coefficient β is $1.6 \cdot 10^{-4}$ Ns m^{-2} [12,13]. The initial concentration is due to the liquid and then density is 1; then velocity which represents the mass transport equation solution is introduced in the software for CFD simulation based on the FEM method [14] as initial condition. The diffusion coefficient of the contaminant is considered to be zero ($1.0 \cdot 10^{-10}$) assuming that the effluent, in the form of aerosol, is immiscible in the air. The progressive dilution of the biological effluent concentration is connected to the mass transport mechanism due to the ventilation plant. An expression that provides the cough velocity function (Co), taking into account both the horizontal and vertical components, was carried out:

$$Co(\tau) = \frac{1}{\left(-0.0781207 + 0.113835 \cdot \exp\left(15.2864 \cdot \tau\right)\right)} \quad (4)$$

At the initial instant is equal to 28 ms^{-1}. For the case of mass transport with diffusion we used the following expression:

$$N_{H_2O} = \frac{\rho_{H_2O} \cdot u_{in}(\tau)}{mm_{H_2O}} \quad (5)$$

assuming for the water molecular mass $18 \cdot 10^{-3}$ kg mol^{-1}.

3. SOLID MODELLING

A full-scale isolation room, present in four hospitals in Tuscany (Italy) was considered. It represents the most typical room for hospitalization in Italian hospitals. Solid model of the room is provided in **Figure 1**. The ventilation plant is a typical HVAC primary air system designed for immune-depressed hospitalization which provides 6 vol h^{-1} of inlet air and 7 vol h^{-1} of extraction air [15-18]. The room is ventilated by a commercial turbulence high induction air diffuser located in the centre of the ceiling and in the middle area between the two beds, indicated with A (**Figure 1**) and the exhaust air is expelled by three return air diffusers located in the ceiling B, in the door of the toilet C and in the door adjacent to the corridor D.

To ensure effective control of virus containment in the

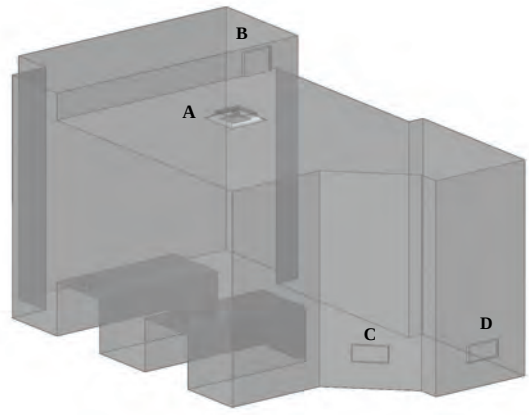

Figure 1. The 3D model of the isolation room.

isolation room, the door must be closed as often as practical so that the air flow can be maintained in a stable state. The scheme of the constant pressures inside the room was calculated referring to this data and to the air diffusers dimensions. For the air inlet, the ceiling return air and the door return air dimensions (transversal section), set constant pressure and air flow rates are respectively the following: 0.36 m^2, pressure 26 Pa and 480 m^3h^{-1}; 0.157 m^2, 7 Pa and 420 m^3h^{-1}; 0.125 m^2, 18 Pa and 130 m^3h^{-1}; 0.125 m^2, 18 Pa and 70 m^3h^{-1}. The exhaust vents of the ventilation system were set at a constant outlet pressure to maintain the negative pressure within the room as imposed for infectious patients [15,16,18].

The inlet turbulence high induction air diffuser was modelled and gradually changed after several attempts testing the simulation results obtained by [14], to control the real diffusion and turbulence effect of the inlet air on the ceiling, at its fixed velocity. The head of the two patients, lying on two parallel beds, was modelled using a solid geometry to take into account their different positions. On the head surface three outflow surfaces were modelled and used for simulate the inlet surface of the organic effluent (mouth) related to the different position of each patient (**Figure 2**).

Typical positions of the patients and their different postural conditions (*i.e.* the first was considered coughing and the second breathing) were modelled: model I for the “supine position”, model II for the “face to face” position as while talking each other, and model III for the “overleaf to overleaf” position. For model simplification we considered sneezing and/or coughing once, in simulation time interval, and its process as pulse. The two bed-headboard lamps, the safety lamps on the ceiling, the external opaque wall and the french-window were also modelled. For all the three 3D models the door was kept closed, such that particles diffusion is influ-

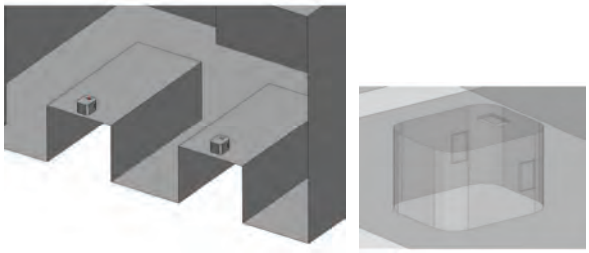

Figure 2. Patients head geometry; head detail (right).

enced by ventilation airflow patterns alone.

4. SIMULATIONS

To investigate the temporal dynamics of the ventilation flow and the particles tracing in the conditions of coughing and breathing of the two patients, time dependent simulations combining Incompressible Navier-Stokes, Convection- Diffusion on non-isothermal air flow and Convection-Conduction models, were performed on the three 3D models. First extensive transient simulations were performed employing coarse and normal mesh, checking its quality to obtain solutions with acceptable accuracy. The mesh density was selected to combine solution accuracy with reduction of computational time needed for convergence: a good quality was obtained by 168000 degrees of freedom with 38000 tetrahedral elements for a no-structured grid. Numerical integration is implicit backward Euler method with BDF multistep which guaranteed the quality and robustness of solution: this method provided by [14] automatically chooses the time step on each iteration with checks and controls on the tolerance imposed to the error and to the stability region. The stop-convergence criterion was chosen $1*10^{-4}$ with independence of the results to the mesh density less than 5% compared to the reference mesh. The direct system solver "UMFPACK" of Unsymmetrical Multi-Frontal was used. The initial conditions for this transient computation were obtained by running the simulation starting from a stationary analysis. These first results provided $10^2 \div 10^3$ for Reynolds number which implies a solution under laminar flow conditions. For the indoor climatic conditions, a uniform internal air temperature of 22℃ and 50% of relative humidity were assumed as provided by the plant system and suggested [15,16]. External climatic data were set at the external design conditions of 0℃ air temperature and 85% relative humidity. Transient simulations were performed considering the coughing events during 10 seconds and then they were also carried out for 60 seconds. Input data, subdomains settings, boundary conditions and basic equations used for transient simulations are provided in the appendix. Due to computational time and complexity, the optimization of system solver was carried out: the final computational time for convergence was about 7 hours for each model, using a Processor Pentium 7 Quad Core with 4 GB Ram.

5. RESULTS

The ventilation and air diffusion pattern inside the room, at different height, with no coughing and breathing events the patients, is provided in **Figure 3**. Noteworthy, the flow field and velocity distribution induced by the high turbulence air inlet diffuser combined with the air return diffusers produce wide recirculation zones near the wall and small partial stagnation areas near the ceiling and between the two beds. Variable directions of the air flow due to the high turbulence air inlet diffuser provide its widespread and homogeneous distribution (*coanda effect*) on the ceiling and then its progressive drop down.

The mean air velocity value of the central diffuser, calculated using simulation results, is 1.36 ms^{-1}, therefore even with reduced surface diffusion, the airflow is laminar the air flow adherence to the ceiling and its fall down. In the zone under the safety light at ceiling, the central inlet air diffuser A and the air return diffuser B, it can be noted the air velocity increasing. Results about temperature distribution inside the room provides values between 22℃ and 26℃ due to the "chimney effect" and heat transfer near the heat sources (radiant panel, lamps and patients head; **Figure 4**). Noteworthy, for small and low temperature variations the effects on air distribution and particle diffusion are not negligible in particular for 60 seconds of simulation time. Thermal buoyancy produces the "chimney effect" even close to the head of patients (vertical component of velocity represented on the surface; **Figure 5**). The central inlet air diffuser provides turbulent air distribution near the ceiling and its low and progressive downfall. The flow in

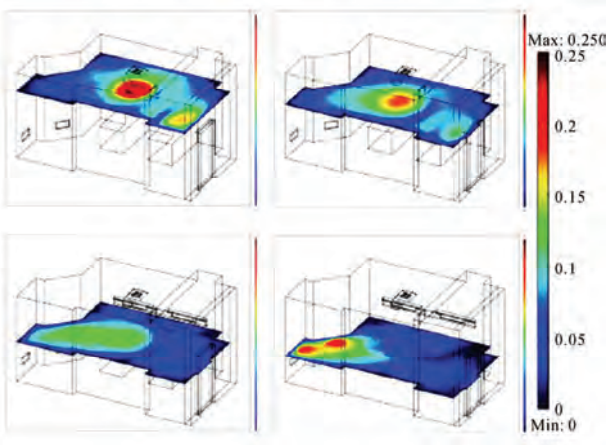

Figure 3. Velocity field at different height; 1 m, 1.5 m, 2.5 m, 2 m from bottom-right side to the upper-right side (clockwise).

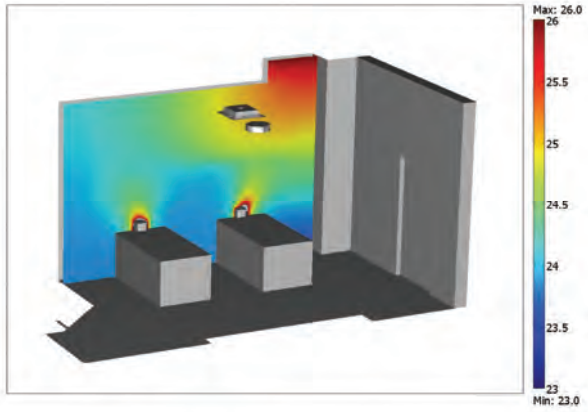

(a)

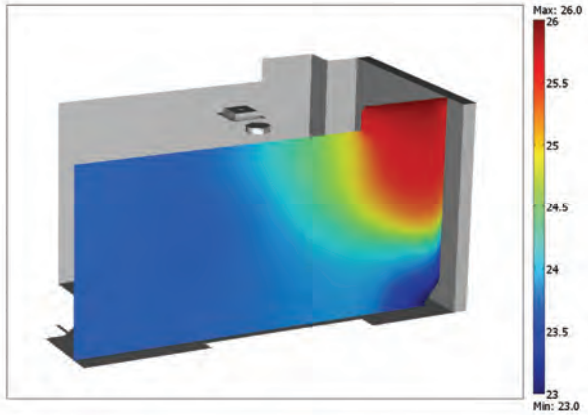

(b)

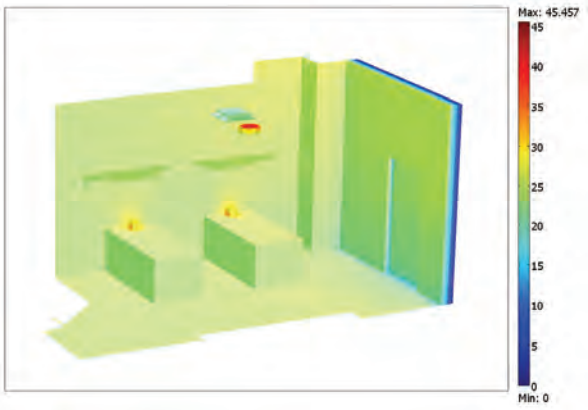

(c)

Figure 4. (a) Temperature field on the wall; (b) slice-detail; (c) entire room.

the region between the three opposite air return diffusers interacts with the local unstable flows, resulting in the generation of an up-flow draft. Particles diffused in the ambient by patient coughing (10 s simulation time) mainly remain in the zone of emission sources. The

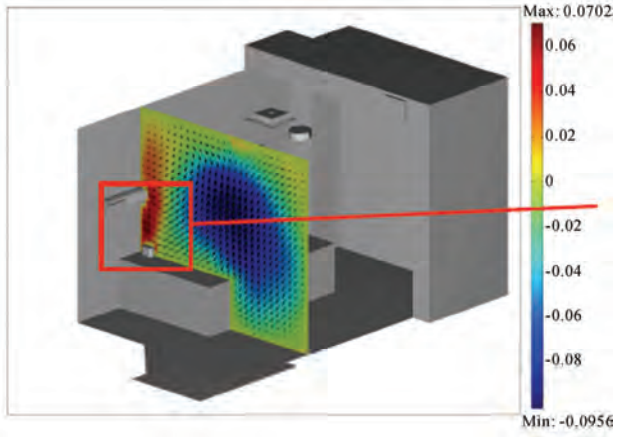

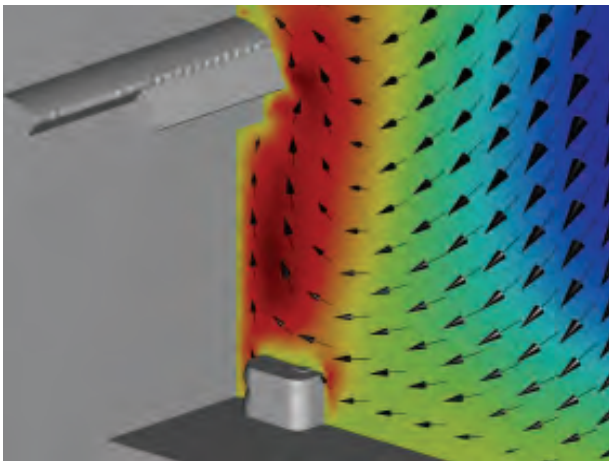

Figure 5. Velocity field – vertical component "z" (left) and detail near the bed (right).

analysis of particle tracing and path distribution connected to their concentration proved the formation of a zone, even though restrained, that should be checked with a *microclimatic* and *contaminant* control between the two beds and around the ceiling surface. In the area near the beds the plant guarantees the maximum admissible indoor value of the air velocity and air flow patterns.

The VAV system provides lower particle concentration and shorter spreading distance of particles (both during 10 s and 60 s of coughing event); this implies that the transport distance of particle-droplets generated by normal respiration and coughing of patients is limited.

Concerning the dynamics of transient air flow: in the all the 3D models near the mouth of the coughing patient the local air velocity reaches the expected value of 28 ms^{-1}; the transient flow due to the impulse has a length of about 0.5 seconds. About the effluent concentration: in model I the effluent concentration in the form of aerosol achieves the higher values in the time interval of 2-4 seconds and then decreases with time because the

continuous dilution provided by the air flow inlet; in the model II the effluent concentration, achieves the higher values in the time interval of 3-5 seconds, but during the transient air flow displacement a local effluent stagnation zone is produced between the two beds and small recirculation flows are generated near the patients (**Figure 6**); in the model III this effluent stagnation reaches the higher values between 4-5 seconds. For the particle path and distance: in the model I, during the first 4 seconds particles collide against the headboard and the head-bed lamp; the trajectories of other particles, in the successive time instants, provide a particle path toward the centre of the room; in the model II, during 10 seconds particles go through 1.6-1.8 meters along the orthogonal direction to the second patient, but due to the buoyancy effect, their path takes up in the area between the two bed; in the model III in about four seconds the particles go through 1.4 meters along the orthogonal direction but they do not collide against the wall directing to the floor at the end of transitory. About particle tracing: the particle tracing obtained from the three transient simulations highlights the position during time of the particles due to cough with a diameter of about $1*10^{-5}$ m; the obtained trajectories (**Figures 7** and **8**) are referred to those particles which position at the initial instant overlap with the surface of the mouth of the first coughing patient and the second breathing. Particles tracing and diffusion obtained by 60 seconds of transitory are different from those obtained by 10 seconds for all the three 3D models.

Particles paths are modified by the inertial/gravitational reduction effect due to thermal buoyancy combined with the air flow displacement in the room. As a matter of fact, the vertical component of particles velocity is prevailing. Comparing results obtained the transient simulations carried out for 60 s:

1) in the model I at the end of 60 s of transient simulation, particles path after crossing the bed-head board is oriented to the ceiling due to the thermal buoyancy and air mixing effects (**Figure 9**);

2) in the model II a higher number of particles collide with the second bed and the lying patient. A small number of particles are driven to the ceiling, up to about 2 m, by the air flow displacement and the local turbulence convective flux. This last effect results comparable to that obtained in model I (**Figure 10**);

3) in the model III the all particles during 60 s of transient simulation collide with the opposite wall. Particles tracing highlights and follows the descending air flow due to the combined thermal and convective effects (air mixing and shorting effect). At the end of transitory the all particles are deposited on the wall (**Figure 11**).

4. CONCLUSIONS

Results indicate the best conditions for the high induction air inlet diffuser and the scheme of pressures imposed in the room to provide the effective means of controlling flows of virus-loaded droplets. Our findings stress that the position of the air-supply inlets in the ceiling and the exhaust vents at the opposite side of the

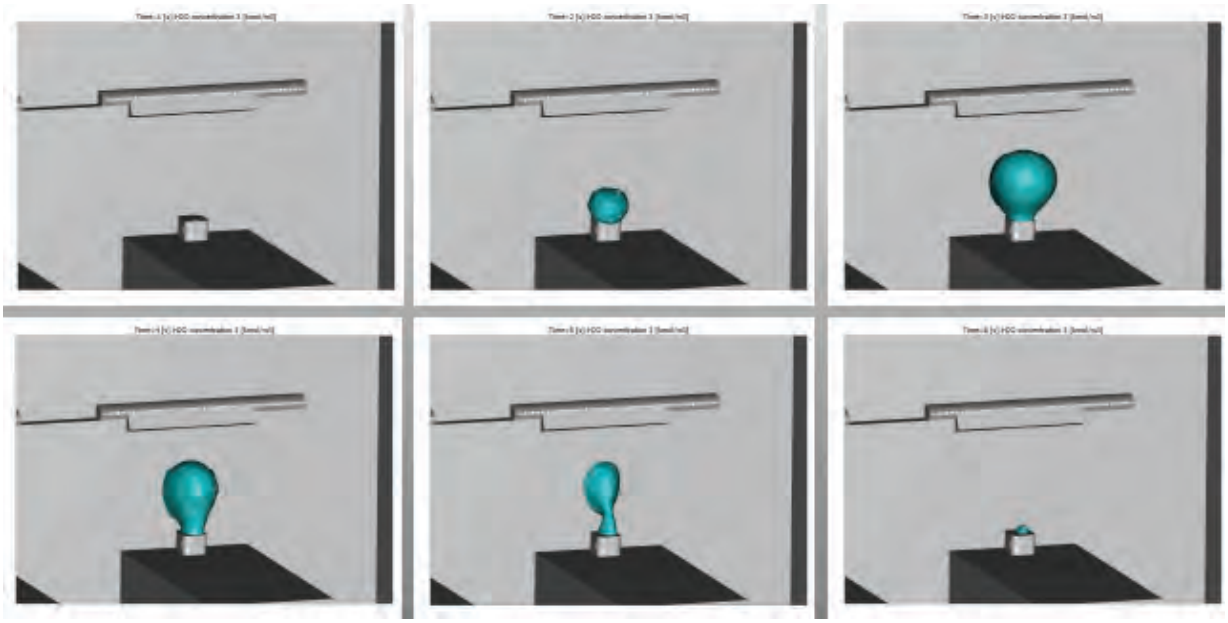

Figure 6. Particle concentration (mol m^{-3}) during the coughing and breathing of the patients (time from 3 to 6 seconds) - results obtained by the Model II transient simulation.

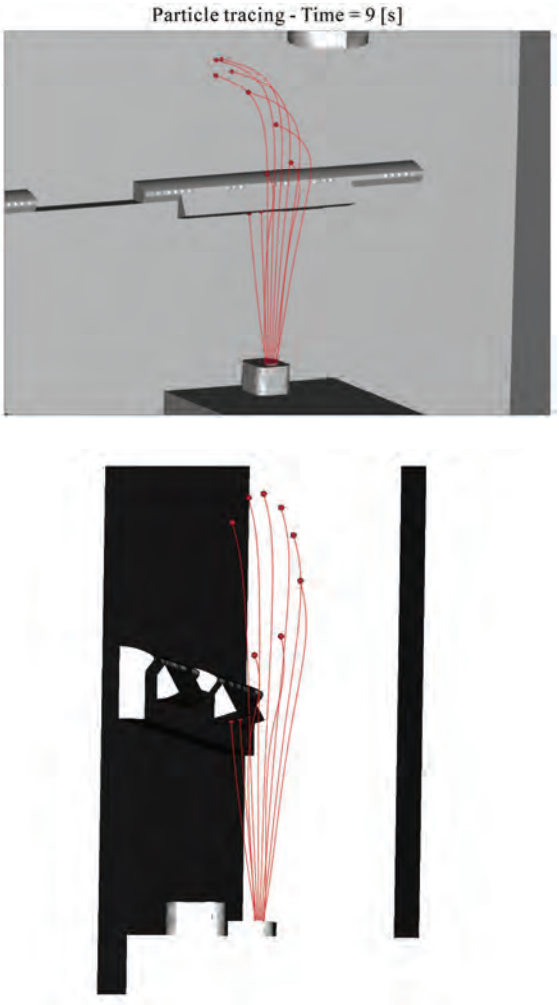

Figure 7. Model I, particle tracing carried out for 10 seconds; detail near the bed-headboard lamp (right).

room and in the ceiling, provide an up-draft effect and infection control efficiency. When the air-supply inlet is located in the middle of the ceiling of the room, and the exhaust vents are positioned in the wall behind the patient beds, the coughed particles and gas are contained at the side of the patient in the region of the exhaust vents. This can minimize the region of coughed gas diffusion and droplet fallout. The high induction air inlet diffuser and the scheme of pressures imposed in the room provide the effective means of controlling droplet flows containing viruses. This type of analysis allows to predict air recirculation zones which can host pathogens. Indeed our analysis of the particle tracing and path distribution combined with their concentration, was effective in identifying examples of such zones between the two beds, around the ceiling surface and on the surface of the bed lamps. Current simulation results yield mean-

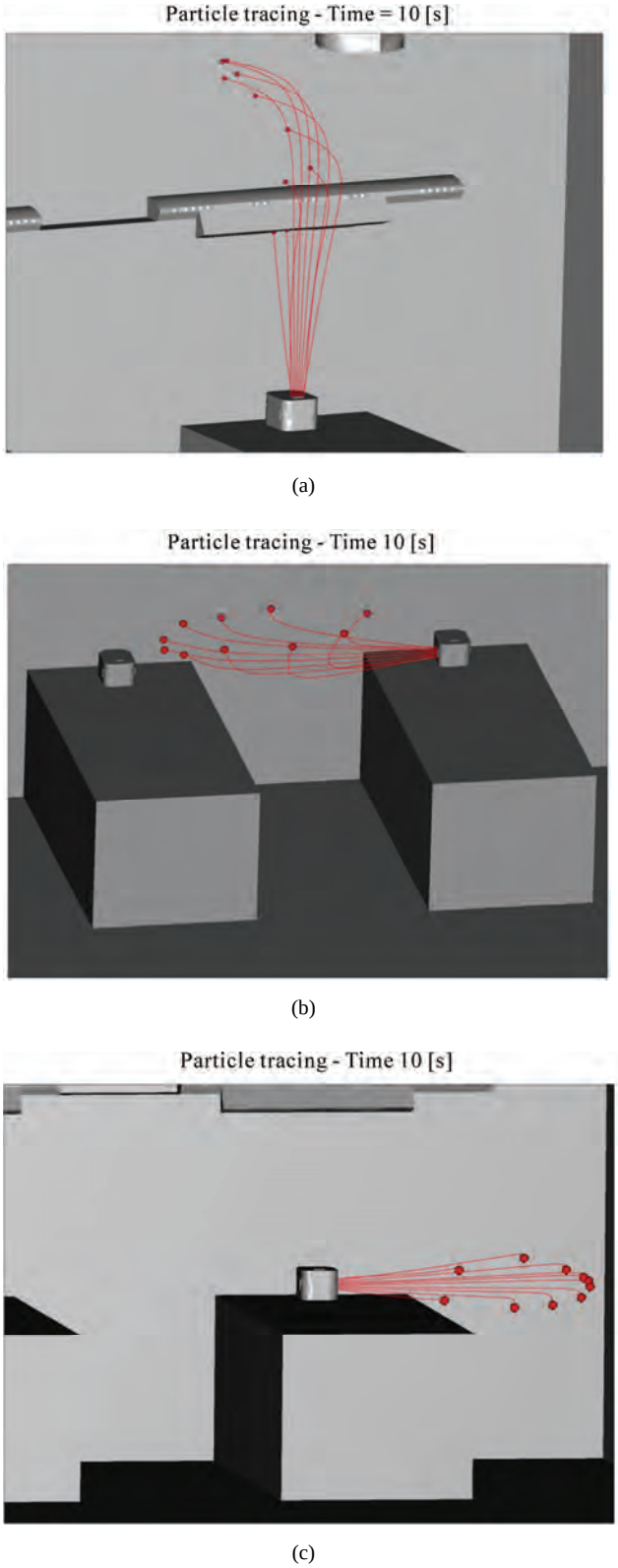

Figure 8. Particle tracing carried out for 10 seconds. (a) model I; (b) model II and (c) model III.

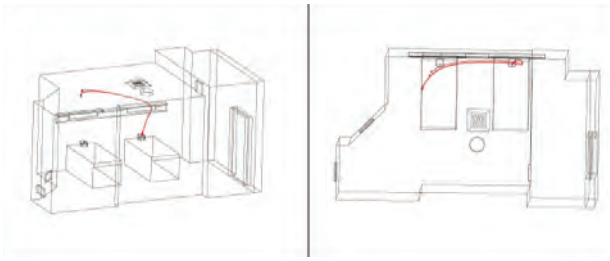

Figure 9. Model I – particle tracing carried out for 60 seconds.

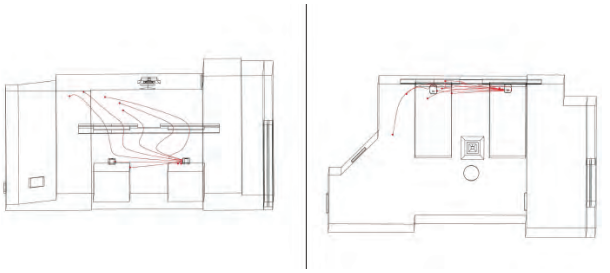

Figure 10. Model II; particle tracing carried out for 60 seconds.

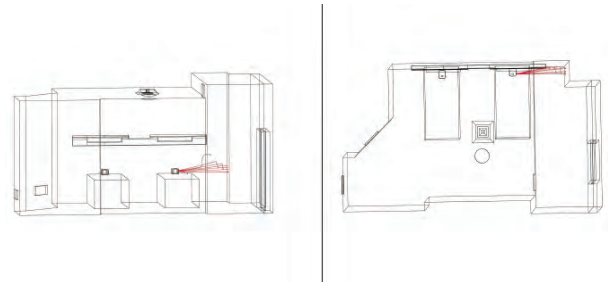

Figure 11. Model III; particle tracing carried out for 60 seconds.

ingful findings and recommendations for disease control and careful design and optimization of ventilation in hospitals for also preventing cross infection processes. Our work provides the key insights and developments for hospital management who would like to control the architecture room (e.g. dimensions, form, arrangement of the furniture) the position and dimensions of openings (doors and windows; windows orientation), in particular, type and location of supply and return air diffusers connected to the design of the HVAC system (variable or constant air volume) and the better length and shape of the air-inlet jet.

5. ACKNOWLEDGEMENTS

This work is supported by the EC IST SOCIALNETS project, grant agreement number 217141, and the International Technology Alliance, sponsored by the U.S. Army Research Laboratory and the U.K. Ministry of Defense. The authors thank *Sani Engineering Consulting Office* (Florence, Italy) for provided data on the hospitalization room and plant system.

REFERENCES

[1] Tang, J., Li, Y., Eames, I., Chan, P. and Ridgway, G. (2006) Factors involved in the aerosol transmission of infection and control of ventilation in healthcare premises. *Journal of Hospital Infection*, **64(2)**, 100-114.

[2] Zhao, B., Yang, C.Q., Chen, C., Chao F., Xu D.Y., Sun, L.C., Wei, G. and Li Y. (2009) How many airborne particles emitted from a nurse will reach the breathing zone/body surface of the patient in ISO Class-5 single-bed hospital protective environments? A numerical analysis. *Aerosol Science and Technology*, **43(10)**, 990-1005.

[3] Stanley, N.J., Kuehn, T.H., Kim, S.W., Raynor, P.C., Anantharaman, S., Ramakrishnan, M.A. and Goyal, S.M. (2008) Background culturable bacteria aerosol in two large public buildings using HVAC filters as long term, passive, high-volume air samplers. *Journal of Environmental Monitor*, **10(4)**, 474-481.

[4] Eames, I., Shoabi, D., Klettner, C.A. and Taban, V. (2010) "Movement of airborne contaminants in a hospital isolation room," *Journal of the Royal Society Interface*, 6757-6766.

[5] Tunga, Y.-C., Hu, S.-C., Tsaia, T.-I. and Changa, I.-L. (2009) An experimental study on ventilation efficiency of isolation room. *Building and Environment*, **44(2)**, 271-279.

[6] Walker, J., Hoffman, P., Bennett, A., Vos, M., Thomas, M. and Tomlinson, N. (2007) Hospital and community acquired infection and the built environment – design and testing of infection control rooms. *Journal of Hospital Infection*, **65(Suppl 2)**, 43-49.

[7] Soper, M. (2008) Pandemic ready, HVAC systems for worst-case scenarios. *Health Facilities Management*, **21(10)**, 49-52.

[8] Bonetta, S., Bonetta, S., Mosso, S., Sampò, S. and Carraro, E. (2009) Assessment of microbiological indoor air quality in an Italian office building equipped with an HVAC system. *Environmental Monitoring and Assessment*, **161(1-4)**, 18-28.

[9] Rygielski, L. and Uden, D. (2007) Creating comfort. Nine considerations for selecting the right hospital HVAC system. *Health Facilities Management*, **20(1)**, 19-23.

[10] Grinshpun, S.A., Adhikari, A., Honda, T., Kim, K.Y., Toivola, M., Rao, K.S. and Reponen, T. (2007) Control of aerosol contaminants in indoor air: combining the particle concentration reduction with microbial inactivation. *Environmental Science Technology*, **15(41)**, 606-612.

[11] Balocco, C., Liò, P. and Sani, L. (2010) Simulazione di un sistema di ventilazione per il controllo degli agenti eziologici nei reparti infettivi. Un caso reale. Condizionamento dell' Aria Riscaldamento Refrigerazione, CdA n.1 febbraio.

[12] Zhao, B., Zhang, Z. and Li, X.T. (2005) Numerical study of the transport of droplets or particles generated by respiratory systems indoors. *Building and Environment*, **40(8)**, 1032-1039.

[13] Cunningham, E. (1910) On the velocity of steady fall of spherical particles through fluid medium. *Proceedings of the Royal Society A*, **83(561)**, 94-96.
[14] www.comsol.com
[15] (1995) UNI 10339, Air-conditioning systems for thermal comfort in buildings. General, classification and requirements. Offer, order and supply specifications. *Italian Standard*.
[16] (2005) UNI EN 13779, Ventilation for non-residential buildings - Performance requirements for ventilation and room conditioning systems. *Italian Standard*.
[17] ASHARE-Handbook, HVAC-applications, SI, 1995.
[18] (1991) ASHRAE. Health facilities. *ASHRAE Handbook of Applications*. S.I. Edition, Atlanta.

APPENDIX

The sub-domains settings and boundary conditions, used for all the time dependent simulations, combining the incompressible Navier-Stokes, Convection-Conduction and Convection-Diffusion models on the non-isothermal air flow, are provided in this appendix.

The equations used by CFD FEM transient simulation are the following: Sub-domain settings equation used for Convection-Conduction model:

$$\delta_{ts}\frac{\rho\cdot C_p\cdot\partial T}{\partial\tau}+\nabla\cdot\left(-k\nabla T\right)=Q-\rho\cdot C_p\cdot u\cdot\nabla T \qquad (6)$$

Sub-domain settings equation used for Convection-Diffusion model:

Air (fluid)

$$\delta_{ts}\frac{\delta H_2O}{\partial\tau}+\nabla\cdot\left(-D\nabla H_2O\right)=R-u\cdot\nabla H_2O \qquad (7)$$

with H_20 = concentration

Sub-domain settings equation used for the Incompressible Navier-Stokes model:

$$\rho\frac{\delta u}{\delta\tau}+\rho\left(u\nabla\right)u=\nabla\left[-p\cdot I+\eta\left(\nabla u+\left(\nabla u\right)^T\right)\right]+F \qquad (8)$$

with $\nabla u=0$

The boundary settings used are provided for the Convection-Conduction model (1-5), Convection-Diffusion model (6-8) and then for the Incompressible Navier-Stokes model (9-14):

1) "insulation" for all the internal walls and doors, the two beds, ceiling, floor, the two bed-headboard lamps and the lamps on the ceiling;

2) "heat flux" for the external wall and the french-window taking into account for the convective coefficient and the external air temperature a constant value respectively 25 W m^{-2} ℃$^{-1}$ and 0℃;

3) "temperature" for the radiant panel on the ceiling, at the fixed value of 26℃ as suggested [15];

4) "convective flux" for all the return air diffusers;

5) "temperature" for the inlet air diffuser, assuming the constant value of the air inlet of 22℃;

6) "insulation symmetry" linked to all the walls and doors, the two beds, the ceiling, floor and all the lamps;

7) "convective flux" for all the air return diffuser and also for the air inlet diffuser;

8) for the "supine position" of the patients (Model I), for the "face to face" position (Model II) and then for the "overleaf to overleaf" position (Model III): the boundary condition associated to the mouth of the patient near the toilet was "convective flux"; the boundary condition associated to the mouth of the patient near the wall, was "Inward flux" linked to the "cough function" evaluated by the **Eq.4**;

9) "no-slip" for the all walls and doors, the two beds, the ceiling and floor;

10) "pressure-no viscous stress" with a boundary type "outlet" for the air return diffuser B, located in the ceiling (**Figure 1**);

11) "pressure-no viscous stress" with a boundary type "outlet" for the air return diffuser C, located in the door of the toilet (**Figure 1**);

12) "pressure-no viscous stress" with a boundary type "outlet" for the air return diffuser D, located in the door adjacent to the corridor (**Figure 1**);

13) "pressure-no viscous stress" with a boundary type "inlet" for the air inlet diffuser A, located in the centre of the ceiling (**Figure 1**);

14) For model I, model II and model III: the boundary type and boundary condition associated to the mouth of the patient near the toilet were respectively "outlet" and "velocity" with the fixed velocity (normal outflow) of 0.9 ms^{-1}; the boundary type and boundary condition associated to the mouth of the patient near the wall, were respectively "inlet" to take into account his breathe and "velocity" with a velocity value associated to the cough function.

Input data used were the following:

1) thermal conductivity, density, viscosity conductivity and specific heat of the air were considered constant;

2) the density, molecular mass ($18*10^{-3}$ kg mol^{-1}) and diffusion coefficient of the water ($1*10^{-10}$ m^2 s^{-1}) were considered constant;

3) inlet velocity at the initial instant due to the cough was considered constant (28 ms^{-1});

4) the inlet/outlet breathe velocity was considered constant (0.9 ms^{-1});

5) inlet air temperature form the central air diffuser was taken at 22°C as provided by the engineering consulting office;

6) mean ambient temperature and relative humidity were fixed to the values provided by the plant at 22°C and 50%;

7) sensible and latent loads due to "rest and sat" activity, taking into account the clothes and the ambient air temperature of 22°C, are respectively 76W and 26W for the standard body area of 1.8 m^2 from DuBois formula. Then taking into account the mean body conductivity and the head volume, the specific dissipation heat and total power of the head were evaluated;

8) the pressure scheme inside the room was calculated referring to the HVAC-VAV primary air system and to the air diffusers dimensions. The exhaust vents of the ventilation system were set at a constant outlet pressure to maintain the negative pressure within the room as imposed for infectious patients;

9) taking into account the thermo-physical properties

of the different constituent layers, the equivalent thermal transmittance of the external wall and french-window were evaluated and considered constant, (external wall 0.287 W $m^{-2}K^{-1}$; french-window 1.048 W $m^{-2}K^{-1}$);

10) specific dissipating heat and power for the two bed-headboard lamps were calculated taking into account their lighting parameters (compact fluorescent, 4000 K colour temperature, 58 W absorbed power, 1350 lm lighting flux);

11) safety lamps on the ceiling were considered barrier to the air displacement.

NOMENCLATURE

Latin

B coefficient
C Cunningham factor
Co coughing function
C_p heat capacity at constant pressure (J kg^{-1} K^{-1})
D diameter (m)
F air resistance
G acceleration of gravity (m s^{-2})
M mass (kg)
Mm molecular mass
N mass transport with diffusion (kgs^{-1})
Q heat source (W m^{-3})
R thermal resistance (m^2 K W^{-1})
Re Reynolds number
T temperature (℃)
U velocity (m)

Greek

B coefficient
λ mean free path (m)
η dynamic viscosity (Pa s)
μ air viscosity (Pa s)
P density (kg m^{-3})
τ time

Footer

C correction
H_2O water
In inlet
P pressure
Pa particle

J. Biomedical Science and Engineering, 2010, 3, 664-671 **JBiSE**
doi:10.4236/jbise.2010.37090 Published Online July 2010 (http://www.SciRP.org/journal/jbise/).

Analysis of spine loads in dentistry—impact of an altered sitting position of the dentist

Max Wunderlich[1], Thomas Eger[2], Thomas Rüther[1], Andreas Meyer-Falcke[3], Dieter Leyk[1,4]

[1]German Sport University Cologne, Department of Physiology and Anatomy, Cologne, Germany;
[2]Department of Periodontology, German Armed Forces Central Hospital, Koblenz, Germany;
[3]Health Care Campus North Rhine-Westphalia, Universitätsstraße 136, Bochum, Germany;
[4]Department IV - Military Ergonomics and Exercise Physiology, German Armed Forces, Koblenz, Germany.
Email: M.Wunderlich@dshs-koeln.de; Ruether@dshs-kolen.de; Leyk@dshs-koeln.de; ThomasEger@bundeswehr.org; andreas.meyer-falcke@gc.nrw.de; DieterLeyk@bundeswehr.org

Received 25 March 2010; revised 6 April 2010; accepted 8 April 2010.

ABSTRACT

Neck and low back pain causes highest disability rates in industrialized countries. Apart from blue-collar occupations dentists and dental care personnel are also strongly affected by work related back pain. However, due to missing analysing systems spine exposure could not be adequately estimated for sitting and non load bearing tasks. Therefore, a new biomechanical measurement system was developed to analyze spine and trunk kinematics. To explore the potential kinematics impact on the spine two days of periodontology care have been examined. Moreover, to asses the influence of an altered sitting position data was collected in 9 (day 1) and 12 (day 2) o'clock position. Data were collected and analyzed by the new 3D-SpineMoveGuard. The systems analyze postures and movements of spine and trunk by ultrasound and inclinometer. Two days of routine non-surgical periodontal treatment were recorded by a frequency of 10 Hz. Moderate awkward postures could be assessed for 90% of the treatment. Up to 85% of the working days were spent in isometric position. Movements were rare and of small amplitude. There were no relevant differences between 9 and 12 o'clock position. The frequently reported back pain in dentists is not only related to severe body postures rather than to the high amount of isometric spine loads. Moreover, an altered sitting position did not reduce this physiological stress. Therefore, dentist specific interventions concepts should pay more attention to physical training during and off work. Ergonomic investments should be carefully evaluated before implemented.

Keywords: Occupational Medicine; Periodontal Treatment; Back Pain, Ergonomics; 3D-SpineMoveGuard

1. INTRODUCTION

About 80% of the adult population of industrialized countries are affected by at least some episode of back pain [1,2]. The highest prevalence rates can be estimated for employees in the "mid-ages". Moreover, the major economic burden results from the high disability rates and the persistent recurrence of the preliminary cervical or lumbar pain [3,4]. As a large part of these disabilities are caused by specific job demands preventive strategies have to focus on the reduction of occupational stressors to avoid chronic episodes of back pain.

The most common causes for occupation related back pain are biomechanics impacts. Beside the negative effects of load bearing tasks, there is evidence from epidemiological studies that awkward trunk postures (bending, twisting, isometrics, repetitive movements) are the most reasonable cause for work related back pain [5,6]. Furthermore, numerous of psycho-social co-factors could be estimated to intensify the pain episode or to be involved in the recurrence of the unspecific pain.

Back pain in dentistry

Regarding the existing tools to assess spine loads at the workplace it appears that the tasks which dental workers routinely perform are at low risk for ergonomically related disorders [7]. This rating is founded because of the probably good environmental conditions (no cold or wet climate), excellent individual job motivation and social background, no load bearing tasks, no extreme body posture etc. However, low back and neck pain is a severe and common occupation related injury in dentistry. Survey data revealed a one year prevalence of back and neck pain of about 70%-90% [8-10]. Moreover, Wunderlich *et al.* [10] could estimate that about 80% of

the affected German military dentist population occupy medical help to deal with the pain. These data indicate that back pain is a major health problem for dental practitioners and methods are needed objectifying the causes and to identify appropriate intervention strategies [11]. With regard to ergonomic improvements studies indicated that a specific treatment position ("9 o'clock" vs. "12 o'clock") or a specific dentist's stool directly affects the impact on the spine and the dentist's health [8,12]. However, up to date potential risk factors for musculoskeletal disorders (MSD) in dentistry were only assessed due to questionnaires and qualitative reports of observation studies [13]. As long as only a rough and almost invalid analysis could be done it seems unlikely to objectify the real biomechanics impact on the spine and to justify useful preventive or ergonomic interventions.

The aim of the present explorative study was to assess information in detail on trunk posture and movements by a newly developed ultrasound based mobile device: 3D-SpineMoveGuard (3-D SMG). Beside the objective information on the working posture and spine kinematics two different treatment positions ("9 o'clock" vs. "12 o'clock") where compared to give insight in a potentially less stressful working posture.

2. MATERIALS AND METHODS

The present study was proven and positively evaluated by the ethics committee of the German Sport University Cologne. Every subject voluntarily participated in the study and gave their written informed consent.

2.1. The 3-Dimensional SpineMoveGuard (3D-SMG)

Movements and postures of the trunk and spine were captured with the 3D-SMG system. The 3D-SMG is a further developed ultrasound based mobile measurement device to assess three dimensional posture and movement profiles of spine and trunk in real-time. Moreover, to standardise data analysis and to reveal new kinematic parameters the analysing software "JSpinal" was developed.

The basic component of the 3D-SMG is the ultrasound device "sonoSens® Monitor" (Friendly Sensors AG, Jena, Germany). Details of the device are described elsewhere [14,15]. In brief: Four pairs of ultrasound transmitters and receivers (diameter 20 mm, height 4 mm) were fixated on the skin (**Figure 1**) with adhesive tape. For each channel the skin distance between transmitter and receiver is determined at a sampling rate of 10 Hz. The transmitters and receivers are cable connected to a small data logger. Variations in inter transmitter skin distance (shorter or longer running times of the ultra

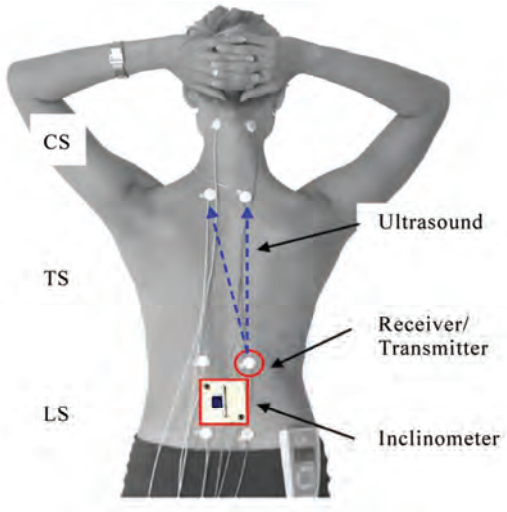

Figure 1. Hardware application of the 3D-SpineMoveGuard. Ultrasound transmitters/receivers and the sagittal inclinometer have their defined positions at the cervical (CS), thoracic (TS) and lumbar spine (LS).

sound signal) represent a change in spine posture within the associated segment of the spine (**Figure 1**). The data points of the 12 channel system represent a 3D model (sagittal-, frontal- and horizontal plane) of the external spine curvature and can be stored for up to 10 hours.

In addition to the changes in spine curvature knowledge of the independent occurrence of trunk inclination is important. Therefore, a one dimensional capacitive, dielectric liquid-based inclinometer (NA4-70, Seika Mikrosystemtechnik GmbH, Kempten, Germany) was taped to the skin with the top edge at the middle of the spinous process of the 2nd lumbar vertebra (**Figure 1**). The inclinometer is cable-connected to a data logger. The range of measurement was adjusted between +110° and -30° (frontal/dorsal). Data was captured at a sampling rate of 10 Hz.

2.2. The Analyzing Software "JSpinal"

The newly developed analyzing software JSpinal enables the valid data management and the detection of movements and postures. JSpinal analyses the segmental data to

1) adjust the row data with the occupation specific reference position (segmental spine length in upright sitting position).

2) calculate relative (%) length indices to separately detect sagittal (SLI), frontal (FLI) and horizontal (HLI) movements or postures. The relative (%) spine curvature enables the comparison of individuals with different spine proportion.

3) automatically detect the direction of deviations from the reference position (neutral zero): SLI forward (flexion)/backward (extension), FLI lateral flexion right/left and HLI torsion right/left

4) analyze the frequency distribution of spine and trunk posture.

5) analyze the frequency and the amount of combined spine postures: detecting the deviation from neutral zero in at least two body planes independent of the direction (e.g. flexion + torsion or torsion + lateral flexion etc.).

6) analyze the kinematic characteristic of the data: duration, frequency and magnitude of movements as well as duration, frequency and spine/trunk position of isometric postures. Both, dynamic and isometric parameters were analysed within every single spine segment and body plane

7) rate the variability of the occupational demands data can be chronologically analysed. Therefore the time of the analysis will be divided in to 10 segments (percentiles of the time) though the intensity/frequency of spinal stressors can be compared between the segments.

2.3. Subject and Examination Procedure

The explorative assessment of spine loads in dentistry was conducted by a single case study. Data collection was done on the same days of two consecutive weeks. At the first day data were assessed in the 9 o'clock position; at the second date in the 12 o'clock position. To keep the medical treatments comparable only 20 patients for periodontol maintenance were recruited for the two examination days. All patientes were treated with two different hand scalers, curettes, ultrasonic devices, rotating and polishing instruments. Each treatment session lasted 45 minutes.

After the instrumentation of the measurement devices maximal voluntary range of movements were assessed within the three body planes in standardised positions [14]. Furthermore, to identify the reference working position (neutral zero) the dentist set down on his working stool with his hands relaxed on his thighs and an upright trunk position with the head held according to the Frankfurt horizontal. Each of the positions was kept for about 30 seconds. Shortly thereafter the routinely treatment of the patients began in the usual and necessary duration and velocity.

2.4. Statistics

Data analyses were reduced to the time of treatment procedure. Periods between the treatments and breaks were excluded to reduce the bias due to individual behaviouristic. Because of the explorative character of the study only descriptive data analyses were done by SPSS© 17.0. Data is shown as frequency and percentile (5^{th}, 25^{th}, median, 75^{th}, and 95^{th}) distributions.

3. RESULTS

The maximal voluntary range of motion is shown in **Table 1**. The magnitudes can be used to compare the deviations from neutral zero (upright sitting) during the non surgical periodontal treatment.

Figure 2 indicates the percentile values of spine and trunk positions throughout the whole working day. The different profiles of the 9 and 12 o'clock working position indicate the necessary adoption of the posture by the dentist. In detail:

Cervical spine (CS): sagittal deviations from neutral zero are very small. The spectrum of lateral flexion and torsion is about 3 times broader in both 9 and 12 o'clock positions. In 9 o'clock position FLI and HLI values are almost normal distributed around zero. During the 12 o' clock manoeuvre the CS is in 75% of the treatment time in a lateral left position and turned to the right.

Thoracic spine (TS): the range of movement is very small. The TS were held in the almost identical position in both 9 and 12 o'clock position. During the 12 o'clock treatment FLI and HLI data ranges in a contra lateral relation to the values of CS.

Lumbar spine (LS): the range of motion is moderate and between the spectrum of CS and TS. In 9 o'clock SLI and FLI indicate an almost upright sitting position. HLI values show a continuous left rotation toward the patient. During 12 o'clock treatment SLI is in a flexed position during 75% of the treatments (the head of the patient was in front of the abdomen of the dentist). Moreover, LS is laterally flexed to the right (FLI) and rotated to the left during the whole working day.

Trunk inclination (TI): the range of trunk motion in 9 o'clock indicating a broader spectrum of trunk positions and is almost normal distributed. In 12 o' clock TI is negative in 75% of the treatments, indicating the tilt of the pelvis.

Table 1. Maximum voluntary range of motion for each part of the spine and within the three body planes.

Body planes	Maximum voluntary range of motion upright sitting = 0%		
	CS	TS	LS
Sagittal plane (Extension/Flexion)	-25%/24%	-8%/20%	-10%/22%
Frontal plane (left/right)	-18%/21%	-16%/17%	-15%/16%
Horizontal plane (left/right)	-20%/21%	-8%/10%	-8%/12%

CS = cervical spine; TS = thoracic spine; LS = lumbar spine

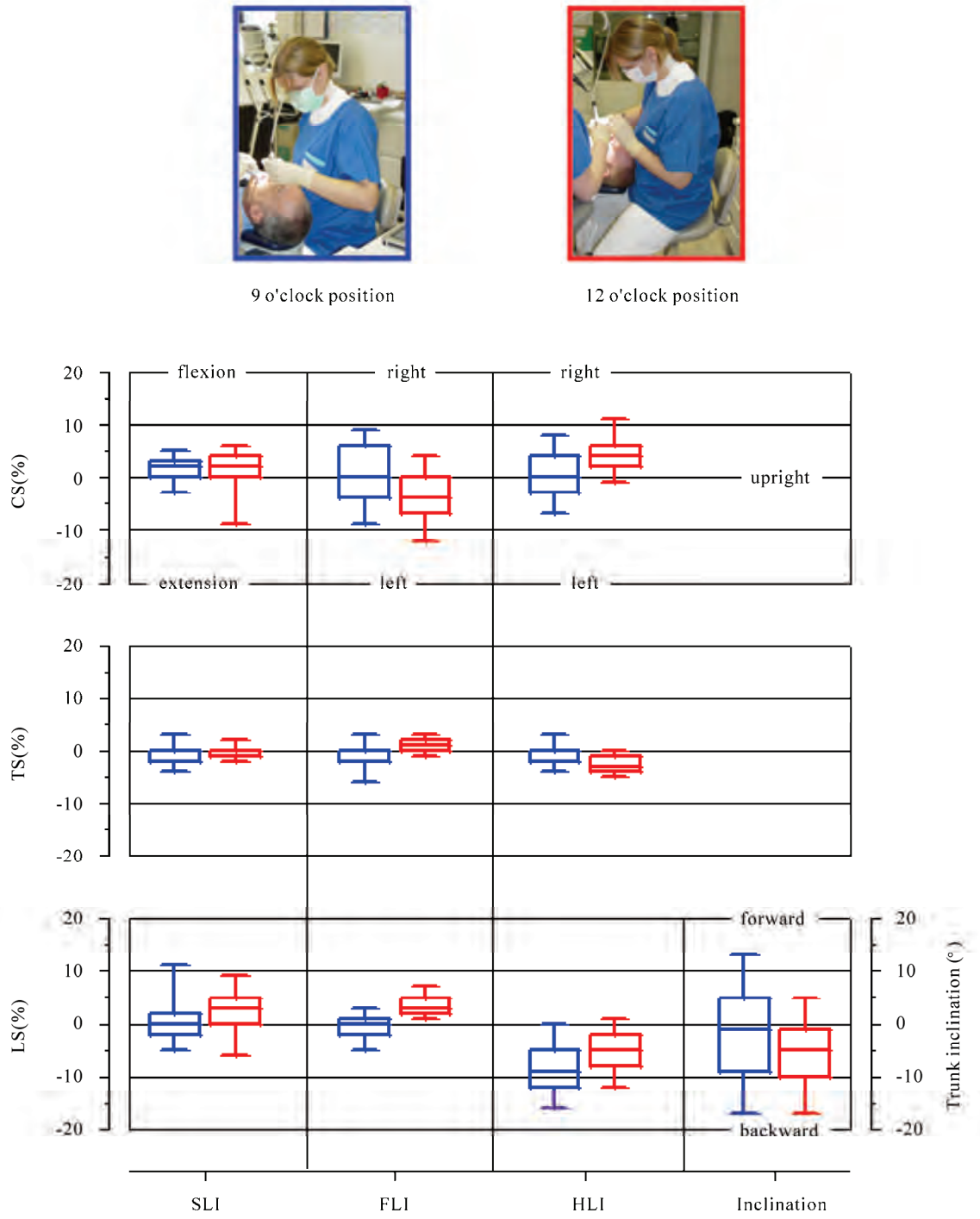

Figure 2. Distributions of segmental spine positions of the dentist in 9 o'clock (blue/left symbol) and 12 o'clock treatment positions. Deviations from upright sitting "0" can be determined for sagittal (SLI), frontal (FLI) and horizontal (HLI) spine and trunk (sagittal inclination) postures. Box-Plots are showing 5th, 25th, 50th, 75th, and 95th percentile for cervical (CS), thoracic (TS) and lumbar (LS) spine.

Apart from the postures within one body plane the analyses further revealed the amount of "combined postures". **Figure 3** shows the frequency of combined spine postures during periodontology care in 9 and 12 o'clock position. The postures are grouped from "small" (0-2%), "medium" (> 2-6%), "large" (> 6-10%) to "extreme" (>

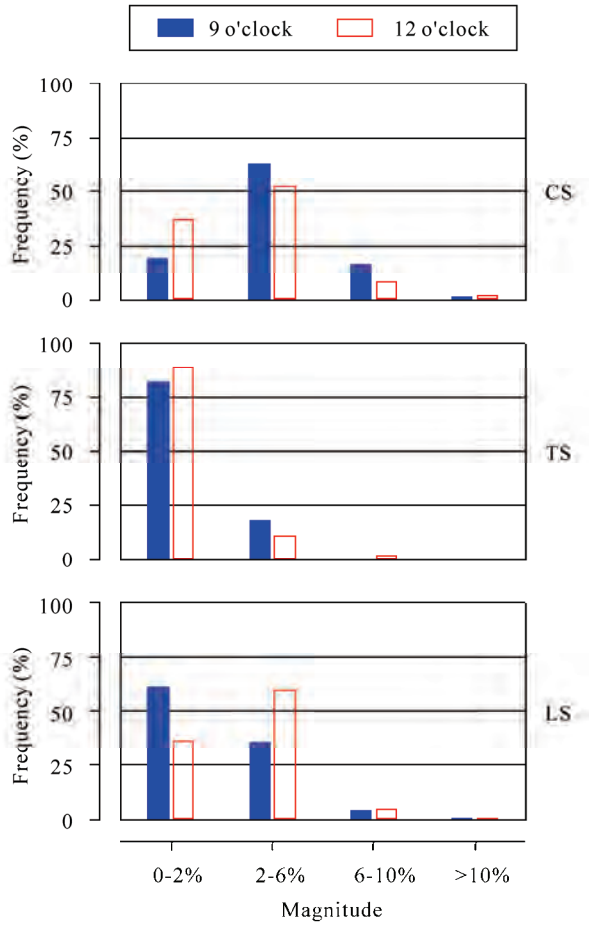

Figure 3. Frequency of multi-directional combined postures of the spine. Values are shown depending on magnitude (deviation from upright sitting) of the combined postures for cervical (CS), thoracic (TS) and lumbar (LS) spine.

10%). During 90% of the treatment time the combined postures ranged between "small" and "medium" with clear differences between the segments of the spine. Position related (9 vs. 12 o'clock) varieties could only be estimated for the LS, where about 2/3 of the treatment time in 12 o'clock position where spend in a "medium" combined posture.

The further analysis of the kinematic work demand revealed that in more than 75% of the treatment time no spine movements occur. Small or medium movements of the trunk could be estimated in about 25% of the work time (**Table 2**). In addition, during 75% to 85% of the periodontology care the dentist worked in an isometric posture (**Figure 4**). As could be drawn from **Figure 3** there exit some differences in static work posture between the segments of the spine but none between treatment positions of the dentist (9 vs. 12 o'clock). Moreover, **Figure 5** shows the durations (s) of isometric

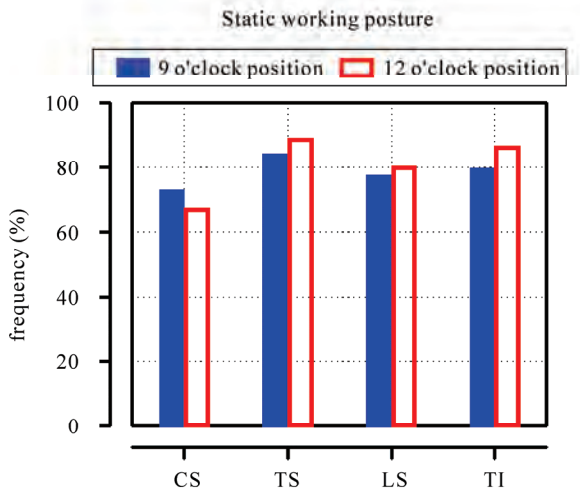

Figure 4. Frequency of static work posture during periodontologic care. Values are shown for cervical (CS), thoracic (TS) and lumbar (LS) spine as well as trunk inclination (TI).

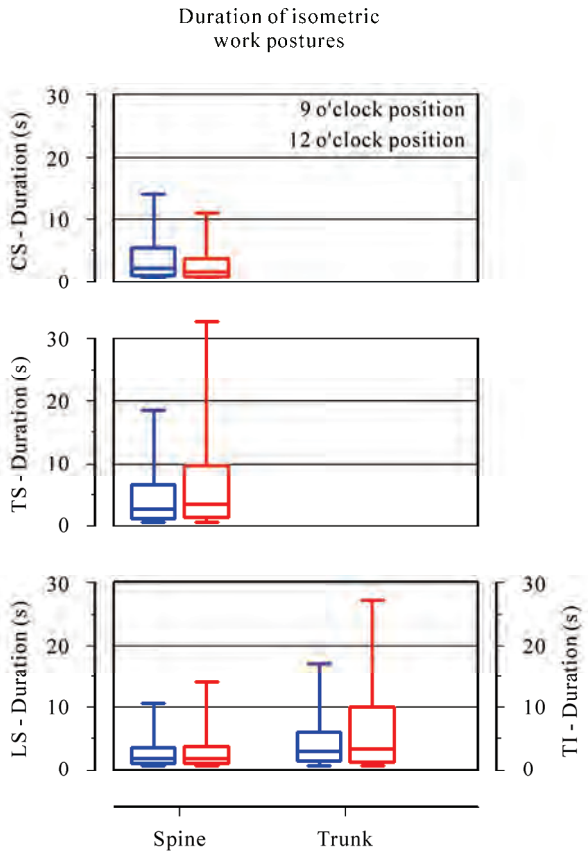

Figure 5. Duration of isometric work postures within the cervical (CS), thoracic (TS) and lumbar (LS) spine as well as for trunk inclination (TI). Box-Plots are showing 5th, 25th, 50th, 75th, and 95th percentile.

Table 2. Distribution of movement amplitudes of the cervical (CS), thoracic (TS) and lumbar (LS) spine. The amplitudes represent relative (%) differences in segmental spine length per movement. Amplitudes of the trunk are expressed as degree (°) changes per movement.

Percentile	Distribution of movement amplitudes							
	Amplitude (%) CS		Amplitude (%) TS		Amplitude (%) LS		Amplitude (°) Inclination	
	9 o'clock	12 o'clock	9 o'clock	12 o'clock	9 o'clock	12 o'clock	9 o'clock	12 o'clock
5.	,00	,00	,00	,00	,00	,00	,00	,00
25.	,00	,00	,07	,07	,02	,03	,00	,00
50.	,22	,20	,16	,16	,14	,15	3,00	3,00
75.	,44	,44	,54	,48	,40	,34	5,00	5,00
95.	3,07	3,54	2,28	1,74	2,51	2,51	14,00	11,00

Rating of spine movements

0-<2 % = "no movement"

2-6 % = small to medium amplitude

> 6 % = large amplitude

Rating of trunk inclination movements

0°-< 3° = "no movement"

3-20° = small to medium amplitude

>20° = large amplitude

work postures. The median values could be estimated by 3 to 4 seconds for both spine and trunk. However, interruptions where even shorter (median duration of movements ≈ 1 s) and as shown in **Table 2** of small amplitudes.

4. DISCUSSION

During periodontology care spine and trunk of the dentist where held within a small range of movement. The deviation from neutral zero was very small in TS and higher in CS and LS. The frequently postulated assumption that dentists work in a sewer bended and twisted posture [8,11] could not be confirmed. During 90% of the non-surgical treatments the combined postures ranged between "small" and "medium" deviation from neutral zero. It turned out that the preliminary posture specific risk factor could be the continuous phases of isometric spine and trunk position. Moreover, the changes of work postures were done very slowly and by small movements. The revealed kinematics and postures of spine and trunk differed only slightly between the most popular treatment positions (9 o'clock vs. 12 o'clock) of the dentist.

As it has been frequently reported more than 90% of the back pain is unspecific: No structural damage or injury can be detected to explain the cause of the aches [16]. Hence, the pain seems to be triggered by the active and/or passive structures of the back and spine. In this context it seems important to remember that the muscles are much more than a contractile organ. The muscles are rather a large sensory part of the body which registers a broad spectrum of chemical and mechanical changes [17,18].

With regard to the new quantitative findings of the task analysis the static none neutral work postures can lead to reduced muscle circulation. As a result metabolites accumulate within the extracellular space. Beside these perfusion and metabolic related volumes and concentration shifts mechanical pressure to the tissue could also lead to acute or delayed exposure induced pain [17,19]. Chemical or mechanical changes will be registered by free interstitial nerve endings (chemo and mechano receptors) of slow afferent nerve fibres (group III and IV). This will not only lead to an increase in heart circulation and breathing but can also reveal reflectively pain phenomena and changes in muscle tension [17,19]. In addition to these acute reactions prolonged static none neutral posture can also cause structural damage of the spine. Additionally, none neutral work posture of the dentist leads to a continuous eccentric exposure of the intervertebral disc. Static and eccentric pressures to the disc can lead to deficits in locale nutrition, metabolic imbalance and can cause cumulative trauma within the structure of the disc and the vertebral end plates [20].

Former studies concluded that changes in treatment positions of the dentist and/or ergonomic sitting stools and/or arrangements of the medical practice will lead to significant reductions in spine exposure [8,12]. However, the detailed data of the explorative study did not reveal substantial differences of exposure relevant body postures due to an altered treatment position of the dentist.

Moreover, the data suggests that dental care is per se strongly associated with a certain, uncomfortable work posture and spinal loads. Intervention concepts should consider both ergonomics and individual alterations. To be more precisely, specific physical intervention concepts have to be adapted for dental care personnel to cope with the physical stress of work postures. The activity programs have also to be adapted to the daily routine of the personnel to interrupt and reduce the cumulative isometric load to the spine [21,22].

The results of the present explorative study are of course not representative for body postures during dental care. Moreover, due to limited methodical capabilities of former studies the parameters are not directly comparable with the literature. But to the best of our knowledge there is no comparable detailed data of kinematics parameter of trunk and spine during dental care. However, the data documents exemplarily the task specific work load characteristic, enables the objective evaluation of interventions (sitting position) and leads to occupation relevant intervention concepts.

5. CONCLUSIONS

The frequently reported back pain in dentist is not only related to severe body postures rather than to the high amount of isometric spine loads. Moreover, with regard to an altered sitting position of the dentist only slightly exposure relevant differences could be estimated. Therefore, intervention concepts for dental care personnel should pay more attention to individual physical training during and off work.

6. ACKNOWLEDGEMENTS

The analysis was funded by the Medical Service of German Armed Forces (M/SAB1/4/A009) and supported by the Department of Periodontology of the German Armed Forces Central Hospital Koblenz.

7. CONFLICT OF INTEREST

The authors declare that they have no conflict of interest.

REFERENCES

[1] Schneider, S., Schmitt, H., Zoller, S. and Schiltenwolf, M. (2005) Workplace stress, lifestyle and social factors as correlates of back pain: A representative study of the German working population. *International Archives of Occupational and Environmental Health*, **78(4)**, 253-269.

[2] Schneider, S. and Schiltenwolf, M. (2006) Occupations associated with a high risk of self-reported back pain: Representative outcomes of a back pain prevalence study in the Federal Republic of Germany. *European Spine Journal*, **15(6)**, 821-833.

[3] Kumar, S. (2001) Theories of musculoskeletal injury causation. *Ergonomics*, **44(1)**, 17-47.

[4] Juniper, M., Le, T.K. and Mladsi, D. (2009) The epidemiology, economic burden, and pharmacological treatment of chronic low back pain in France, Germany, Italy, Spain and the UK: A literature-based review. *Expert Opinion on Pharmacotherapy*, **10(16)**, 2581-2592.

[5] Harkness, E.F., Macfarlane, G.J., Nahit, E.S., Silman, A.J. and McBeth, J. (2003) Risk factors for new onset low back pain amongst cohorts of newly employed workers. *Rheumatology*, **42(8)**, 959-968.

[6] Hoogendoorn, W.E., Bongers, P.M., Vet, H.C.W., de Douwes, M., Koes, B.W., Miedema, M.C. Ariëns, G.A. and Bouter, L.M. (2000) Flexion and rotation of the trunk and lifting at work are risk factors for low back pain: Results of a prospective cohort study. *Spine*, **25(23)**, 3087-3092.

[7] Guay, A.H. (1998) Commentry: Ergonomically related disorders in dental practice. *Journal of the American Dental Association*, **129(2)**, 184-186.

[8] Thornton, L.J., Barr, A.E., Stuart-Buttle, C., Gaughan, J.P., Wilson, E.R., Jackson, A.D., Wyszynski, C.T. and Smarkola, C. (2008) Perceived musculoskeletal symptoms among dental students in the clinic work environment. *Ergonomics*, **51(4)**, 573-586.

[9] Wassan, A.L., Almas, K.A. and Shethri, S.E. (2001) Rückenund Nackenbeschwerden bei Zahnärzten und zahnmedizinischem Personal. *Journal of Contemporary Dental Practice*, **2(3)**, 17-30.

[10] Wunderlich, M., Rüther, T., Eßfeld, D., Rohde, U., Eger, T., Leyk, D. (2009) Rückenschmerzen und Wirbelsäulenbelastungen – Befragung des zahnmedizinischen Personals in der Bundeswehr. *Wehrmed Mschr*, **53(1)**, 230-234.

[11] Leggat, P.A., Kedjarune, U. and Smith, D.R. (2007) Occupational health problems in modern dentistry: A review. *Industrial Health*, **45(5)**, 611-621.

[12] Morita Europe GmbH, J. (2008) Dr. Beach ergonomic concept. Warum sich intuitive Arbeitswege lohnen und Rückenschmerzen nicht sein müssen. *DDZ*, **117(4)**, 188-189.

[13] Marklin, R.W. and Cherney, K. (2005) Working postures of dentists and dental hygienists. *CDA Journal*, **33(2)**, 133-136.

[14] Baum, K., Hoy, S. and Essfeld, D. (1997) Continuous monitoring of spine geometry: A new approach to study back pain in space. *International Journal of Sports Medicine*, **18(Suppl 4)**, 331-333.

[15] Friedrich M (2002) Measuring lumbar sagittal posture in sewgae workers using an ultrasonic device. *Journal of Musculoskelet Research*, **6(3-4)**, 135-145.

[16] Waddell, G. and Burton, A.K. (2001) Occupational health guidelines for the management of low back pain at work: evidence review. *Occupational Medicine*, **51(2)**, 124-135.

[17] Sjøgaard, G., Lundberg, U. and Kadefors, R. (2000) The role of muscle activity and mental load in the development of pain and degenerative processes at the muscle cell level during computer work. *European Journal of Applied Physiology*, **83(2-3)**, 99-105.

[18] Leyk, D. (2009) The preventive and therapeutic roles of regular physical activity. *Deutsches Aerzteblatt international*, **106(44)**, 713-714.

[19] Baum, K., Selle, K., Leyk, D. and Essfeld, D. (1995)

Comparison of blood pressure and heart rate responses to isometric exercise and passive muscle stretch in humans. *European Journal of Applied Physiology*, **70(3)**, 240-245.

[20] Davis, K.G. and Marras, W.S. (2000) The effects of motion on trunk biomechanics. *Clinical Biomechanics*, **15(10)**, 703-717.

[21] Finsen, L., Christensen, H. and Bakke, M. (1998) Musculoskeletal disorders among dentists and variation in dental work. *Applied Ergonomics*, **29(2)**, 119-125.

[22] Ratzon, N.Z., Yaros, T., Mizlik, A. and Kanner, T. (2000) Musculoskeletal symptoms among dentists in relation to work posture. *Work*, **15(4)**, 153-158.

J. Biomedical Science and Engineering, 2010, 3, 672-676 **JBiSE**
doi:10.4236/jbise.2010.37091 Published Online July 2010 (http://www.SciRP.org/journal/jbise/).

Predicting DNA methylation status using word composition

Lingyi Lu[1,2], Kao Lin[2,3]*, Ziliang Qian [1,2], Haipeng Li[3], Yudong Cai[4], Yixue Li[1,5,6]

[1]Key Lab of Molecular Systems Biology, Shanghai Institutes for Biological Sciences, Chinese Academy of Sciences, Shanghai, China;
[2]Graduate School of the Chinese Academy of Sciences, Beijing, China;
[3]CAS-MPG Partner Institute for Computational Biology, Shanghai Institutes for Biological Sciences, Chinese Academy of Sciences, China;
[4]Department of Chemistry, College of Sciences, Shanghai University, Shanghai, China;
[5]Shanghai Center for Bioinformation Technology, Shanghai, China;
[6]College of Life Science & Biotechnology, Shanghai Jiao Tong University, Shanghai, China.
Email: lylu@sibs.ac.cn; cyd@picb.ac.cn

Received 1 April 2010; revised 20 April 2010; accepted 21 April 2010.

ABSTRACT

Background: DNA methylation will influence the gene expression pattern and cause the changes of the genetic functions. Computational analysis of the methylation status for nucleotides can help to explore the underlying reasons for developing methylations. Results: We present a DNA sequence based method to analyze the methylation status of CpG dinucleotides using 5bp (5-mer) DNA fragments – named as the word composition encoding method. The prediction accuracy is 75.16% when all 5bp word compositions are used (totally 4^5 = 1024). Furthermore, 5-bp DNA fragments/words having the most impact on the methylation status are identified by mRMR (Maximum-Relevant-Minimum-Redundancy) feature selection method. As a result, 58 words are selected, and they are used to build a compact predictor, which achieves 77.45% prediction accuracy. When the word composition encoding method and the feature selection strategy are coupled together, the meaning of these words can be analyzed through their contribution towards the prediction. The biological evidence in the literature supports that the surrounding DNA sequence of the CpG dinucleotides will affect the methylation of the CpG dinucleotides. Conclusions: The main contribution of this paper is to find out and analyze the key DNA words taken from the neighborhood of the CpG dinucleotides that are inducing the DNA methylation.

Keywords: Feature Selection; MRMR; 5bp Nucleotide Fragment; Nearest Neighbor Algorithm

The last three authors contributed equally to this work.

1. BACKGROUND

DNA methylation is an epigenetic modification that typically occurs on cytosine of CpG dinucleotide, during which the cytosine is transferred to 5-methylcytosine by DNA methyltransferase. In human genome, unmethylated CpG dinucleotides are normally clustered together in a region called CpG island which is highly associated with gene promoters [1]. Methylation of CpG inhibits the expression of the downstream gene by firstly preventing some DNA-binding factors from recognizing their binding sites [2,3], and secondly by captivating some proteins that recognizing the methyl-CpG [4,5] to elicit the DNA's repressive capacity. When CpG dinucleotides are methylated, it may affect the transcription and cause diseases [6]. DNA methylation patterns are altered in many cancer cells [7-9] since the tumor suppression genes are silenced by the DNA methylation. A study in [10] shows that CpG methylation may veil the presence of virus from cytotoxic T-cell immune surveillance and cause viral tumorigenesis. Berretta esophagus, Helicobacter pylori gastritis, inflammatory bowl disease and viral hepatitis are also thought to be associated with CpG methylation [11]. It is not possible to predict the DNA methylation status purely from the DNA sequence because the DNA methylation status is affected by many outer factors, *i.e.*, the same sequence may have different methylation status due to these factors. A computational approach will be very hard to be devised to analyze the DNA methylation status affected by the outer factors, e.g. DNA methylation caused by heat stress [12], by overproduction of DNA cytosine methyltransferases [13] and hepatitis B virus [14]. However, using computational tools, we are able to analyze what DNA sequence environment is more feasible for inducing methylation caused by those factors.

Machine learning method is used to predict DNA methylation status in our study. The DNA sequence, containing the CpG dinucleotides, is truncated into a 1000bp DNA sequence with the CpG dinucleotides being the center of the sequence. Instead of raw binary encoding approach [15], a 5bp (5-mer) word composition method, which slices the 1000bp sequence into 996 5bp-words, is used as the input data for the predictor. Nearest neighbor classification algorithm [16] is adopted as the predictor, which achieves an accuracy rate of 75.16%, evaluated by 10-fold cross validation. These 5bp DNA fragments (words) are analyzed by a feature analysis method – the mRMR algorithm [17], and 58 most important words are identified. The literature evidence shows that these 5bp words have other significant roles in their biological functions, e.g. some of them are modifying sites and binding sites of enzymes and some are binding motifs of some transcription factors. Since these 5bp words are important for DNA methylation, they are probably associated with the binding of DNA methyltransferase. Using these 58 words instead of all the words, the prediction accuracy increases from 75.16% to 77.45%. This indicates that the predictor suffers from over-fit problem when all words are used for the prediction.

An online web server for the predictor used in this study is freely available at http://pcal.biosino.org/.

2. RESULTS

Firstly, all 1024 features were used to distinguish the methylated CpG dinucleotides from unmethylated ones. Based on the 10-fold cross-validation test, we got 75.16% prediction accuracy rate. The accuracy rate is shown in **Figure 1** as the red dashed line. The top features, generated by the MaxRel (Max-Relevance) algorithm, are input into the predictor. The prediction accuracy curve, in increasing number of features, is shown in **Figure 1** as the grey curve. Compared with the prediction accuracy using the total 1024 features, no significant improvement is achieved from the mRMR features. Thus a backward sequential feature selection is applied to extract a compact feature subset to improve the prediction accuracy. The black curve in **Figure 1** shows prediction accuracy curve obtained from the backward feature searching algorithm. The prediction curve is smooth indicating that the prediction performance is stable using backward feature searching method. The highest prediction accuracy occurs when 58 features are included, achieving an accuracy rate of 77.45% (see **Table 1**).

The result of mRMR feature selection program contains two lists of features (see supplemental material l). The first part lists 500 MaxRel features in a descending order, and the second part lists the mRMR features in the feature selection order. Since the MaxRel features indicate how well each 5bp word contributes to the prediction, these words may have other significant biological functions besides the DNA methylation prediction. By manually searching over the internet, we found that more than half of the top MaxRel features have other significant roles in biological function. This may indicate that these 5bp words are important in binding with many enzymes including the methyltransferase. For example, it is reported that both methylases (LlaDII and Bsp6I R/M) have two recognition sites (5'-GCGGC-3' and 5'-GCCGC-3') [18]. DNA methyltransferase (methylase) FauIA (of the restriction-modification system FauI from Flavobacterium aquatile)'s recognization site is 5'-CCCGC-3' [19]. Our study offers a perspective to find a connection between the DNA sequence fragments and the methylation mechanism.

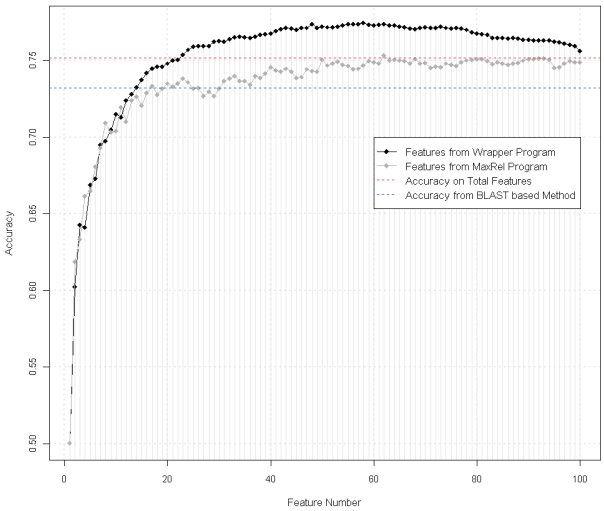

The highest accuracy 77.40% is achieved using backward feature selection when 58 features are included. The red dashed line indicates the 75.16% prediction accuracy obtained by using all 1024 features, and the blue dashed line indicates the 73.23% prediction accuracy obtained by the BLAST method.

Figure 1. Prediction accuracy curves.

3. CONCLUSIONS

We introduce a DNA word encoding method for the analysis of the DNA methylation status. The most important words inducing the methylation are found using mRMR and backward feature selection methods. Some of these words are the recognition sites for methylases, while most words' biological role in methylation still remains unknown. These words should be paid with more attention when the biologists investigate the mechanism of methylation. The length of the words is set to be 5 as the length is a bit longer than the 3-length DNA words for the translation of the proteins, and the number of the variation of the words can be coped easily with by the feature selection methods. A future research could be

Table 1. The final 58 features selected.

Feature Index	Accuracy	Annotation
411	0.500419111	CGCGG
667	0.602402906	GGCGG
471	0.642917016	CTCCG
927	0.64124057	TGCTG
358	0.668901928	CCGCC
591	0.673093043	GCATG
275	0.695166248	CACAG
475	0.697401509	CTCGG
287	0.704666108	CACTG
427	0.715004191	CGGGG
933	0.713048338	TGGCA
79	0.723945236	ACATG
335	0.728136351	CCATG
360	0.732606873	CCGCT
425	0.737636211	CGGGA
872	0.742106734	TCGCT
148	0.74490081	AGCAT
363	0.746018441	CCGGG
663	0.748253702	GGCCG
347	0.750488963	CCCGG
346	0.753841855	CCCGC
313	0.757194747	CATGA
303	0.759150601	CAGTG
419	0.759709416	CGGAG
167	0.759709416	AGGCG
935	0.762224085	TGGCG
155	0.7627829	AGCGG
405	0.762503493	CGCCA
361	0.764179939	CCGGA
345	0.765297569	CCCGA
316	0.765576977	CATGT
325	0.765297569	CCACA
406	0.764738754	CGCCC
619	0.765576977	GCGGG
858	0.766974015	TCCGC
343	0.767253423	CCCCG
414	0.767812238	CGCTC
551	0.769209276	GAGCG
423	0.770606315	CGGCG
428	0.771444538	CGGGT
603	0.770885722	GCCGG
26	0.770326907	AACGC
665	0.77116513	GGCGA
613	0.771444538	GCGCA
39	0.773959206	AAGCG
874	0.771444538	TCGGC
401	0.772282761	CGCAA
875	0.771723945	TCGGG
439	0.771723945	CGTCG
422	0.772282761	CGGCC
90	0.772841576	ACCGC
983	0.773679799	TTCCG
23	0.773959206	AACCG
923	0.773679799	TGCGG
602	0.774518022	GCCGC

committed to link multi-methylation with DNA words, e.g. investigating the number of methylations occurs in 2000bp DNA sequence. It is also applicable to use mixed-length DNA words for the analysis of the methylation status and other biological subjects.

4. METHODS

4.1. Dataset

The DNA methylation status data, used in this study, were originated from the Human Epigenome Project (HEP) website (http://www.sanger.ac.uk/PostGenomics/epigenome/,Release26thJun2006) [20]. These data were determined through experiments [6,20]. Current data release (26th Jun 2006) contains about 1.9 million CpG methylation values, assigned by analyzing the 2,524 amplicons from 4 chromosomes and 12 different tissues. According to [20], in more than 80% cases the methylation status of the same locus is consistent among the 12 different tissues. Especially in cell types like $CD4^+$ and $CD8^+$ lymphocytes, the difference level of methylation status is as low as 5%. Therefore we investigate methylation data derived from $CD4^+$ lymphocytes in this contribution and ignore the minor variances across the tissues and cell types. The methylation scores of CpG sites reported by HEP range from 0 to 100, indicating the degree of methylation from null to full scale. CpG sites with the high scores (between 90 and 100) and low socres (between 0 and 10) were assigned to be the methylated and unmethylated ones respectively. As a result, 26397 $CD4^+$ lymphocytes specific CpG methylation records were collected, including 11345 methylated CpG sites and 15052 unmethylated ones.

Why does DNA methylation occur on some CpG sites whereas not take place on other ones? From the perspective of DNA sequence, flanking sequences of various CpG sites are thought to encode hints of this problem.

An early study [21] showed that a flanking sequence size of 800bp is optimal for methylation status determination. We focus on flanking sequences around CpG sites with total length 1000bp, exactly 499bp nucleotides upstream and 499bp nucleotides downstream of the CpG site. Comethylation occurs over short distance (≤ 1000bp) [20], which may cause the flanking sequences of the neighboring methylation sites overlapped. To avoid this, similar sequences were filtered using the homologous sequence alignment program CD-HIT [22]. Finally, a sequence set with no more than 80% sequence similarity between any pair of them is obtained. The dataset comprises 1994 flanking sequences of methylated CpG sites and 1585 unmethylated sequences. The human genome data of chromosome 6, 20 and 22 were downloaded from Ensembl ftp site (ftp://ftp.ensembl.org/pub/release-25/human-25.34e/data/fasta/dna).

4.2. Word Composition Based Encoding Approach

Given a piece of DNA sequence without other transcendent knowledge such as the genome location and the gene context, how can the DNA sequence provide information to infer the CpG methylation status? An intuitive thought would be to use the difference between the DNA sequences to determine the methylation status. However, though the differences can be located relatively easy, the analysis afterwards will be a rather complex task. In this study, we encode the long sequence into short pieces so as to easily analyze the DNA pieces using feature analysis method. We fix the length of each piece to be 5 bp, thus combining the 4 different nucleotides into a length of 5 will give 1024 (= 4^5) variations/compositions. Notice that a 1000-length sequence will result in 996 words by sliding the sequence from the first nucleotide to the 996th. The prediction data is built by counting the occurrence of each composition among the 996 words. Thus, each DNA sequence will result in a 1024-dimensional vector. The encoding approach can be summarized as follows: 1) each 1000bp DNA sequence is sliced into 5bp nucleotide fragments by the shift-by-one cut; 2) a 1024 dimensional vector is built by counting the occurrence of each composition of the 5-length words appearing in the sliced 5bp fragments. For example, if "AAGTT" is the i^{th} component of the 1024D vector and the 996 fragments contain n "AAGTT" fragments, the i^{th} component of the corresponding vector is set to be n (n can be null).

The next step is to apply the mRMR (Maximum-Relevant-Minimum-Redundancy) [17] and backward feature selection methods for the searching of the prominent words.

4.3. The mRMR and Backward Feature Selection Wrapper

The mRMR (minimum-redundancy-maximum-relevance) framework aims at maximizing the relevance between the to-be-selected feature set S and the target class c and at the same time minimizing the redundancy between the to-be-selected features [23]. The maximum relevance criterion (Max-Relevance) drives to search for features that are maximizing the mutual information between S and c:

$$\max D(S,c), D = 1/|S| \cdot \sum_{x_i \in S} I(x_i;c) \qquad i = 1,2,...,m \quad (1)$$

where $I(x_i;c)$ is the mutual information between feature x_i and c, and $m = 1024$ is the total number of features.

The minimum redundancy criterion (Min-Redundancy) is formulated as:

$$\min(R), R = 1/|S|^2 \cdot \sum_{x_i, x_j \in S} I(x_i, x_j) \quad (2)$$

which is used to minimize the mutual information of all couples of the features.

The mRMR method combines the Max-Relevance and Min-Redundancy as:

$$\max \Phi(D,R), \Phi = D - R \quad (3)$$

to optimize D and R simultaneously.

An incremental search procedure is adopted to implement the mRMR algorithm. Suppose we already have a feature set S_{k-1} with $k-1 (2 \le k \le m)$ features, the k^{th} feature can be selected from the rest of the feature set $\{X - S_{k-1}\}$ as:

$$\max_{x_j \in \{X - S_{k-1}\}} \left[I(x_i,c) - 1/(k-1) \cdot \sum_{x_j \in S_{k-1}} I(x_j, x_i) \right] \quad (4)$$
$$2 \le k \le m$$

The first feature is selected through the Max-Relevance criterion using Formula 1. The rest features are gained using Formula 4.

Since mRMR method only performs pre-selection role in the feature selection, these pre-selected features need to be refined using a more accurate yet more time-consuming feature selection method. Backward sequential selection scheme is adopted here to do the refinement. It works by excluding one feature each time from the current feature set S_k. Initially, S_k is the pre-selected feature set resulted from the mRMR method. Each feature is in turn excluded from S_k and the prediction accuracy is obtained using the rest $k-1$ features by the KNN predictor, *i.e.*, there are k different

configurations in obtaining the $k-1$ features. The configuration that achieves the highest prediction rate is chosen as the next selected feature set S_{k-1}. If multiple configurations lead to the same accuracy, one of them is chosen randomly. This decremental selection procedure is repeated until one feature is left. The optimal feature subset can be chosen by selecting the feature subset that performs the best prediction.

5. COMPETING INTERESTS

No competing of interests.

6. AUTHORS' CONTRIBUTIONS

LL, KL, HL, YC and YL proposed the research topics, developed the methods, designed the experiments, analyzed the data, and wrote the paper. LL and KL implemented the experiments.

7. ACKNOWLEDGEMENTS

This work was supported by National Technology Research and Development Program (Grant No. 2006AA02Z320, part of a general science and technology plan, known as the Jiu-Liu-San plan, started in 1986) and National Natural Science Foundation of China (Grant No. 30700154).

REFERENCES

[1] Tost, J., Schatz, P., Schuster, M., Berlin, K. and Gut, I.G. (2003) Analysis and accurate quantification of CpG methylation by MALDI mass spectrometry. *Nucleic Acids Research*, **31(9)**, e50.

[2] Klose, R.J. and Bird, A.P. (2006) Genomic DNA methylation: the mark and its mediators. *Trends in Biochemical Sciences*, **31(2)**, 89-97.

[3] Watt, F. and Molloy, P.L. (1988) Cytosine methylation prevents binding to DNA of a HeLa cell transcription factor required for optimal expression of the adenovirus major late promoter. *Genes & Development*, **2(9)**, 1136-1143.

[4] Boyes, J. and Bird, A. (1991) DNA methylation inhibits transcription indirectly via a methyl-CpG binding protein. *Cell*, **64(6)**, 1123-1134.

[5] Hendrich, B. and Bird, A. (1998) Identification and characterization of a family of mammalian methyl-CpG binding proteins. *Molecular and Cellular Biology*, **18(11)**, 6538-6547.

[6] Rakyan, V.K., Hildmann, T., Novik, K.L., Lewin, J., Tost, J., Cox, A.V., Andrews, T.D., Howe, K.L., Otto, T., Olek, A., *et al.* (2004) DNA methylation profiling of the human major histocompatibility complex: a pilot study for the human epigenome project. *PLoS Biology*, **2(12)**, e405.

[7] Schulz, W.A. (1998) DNA methylation in urological malignancies (review). *International Journal of Oncology*, **13(1)**, 151-167.

[8] Ushijima, T. (2005) Detection and interpretation of altered methylation patterns in cancer cells. *Nature Reviews*, **5(2)**, 223-231.

[9] Agrawal, A., Murphy, R.F. and Agrawal, D.K. (2007) DNA methylation in breast and colorectal cancers. *Modern Pathology*, **20(7)**, 711-721.

[10] Robertson, K.D., Manns, A., Swinnen, L.J., Zong, J.C., Gulley, M.L. and Ambinder, R.F. (1996) CpG methylation of the major Epstein-Barr virus latency promoter in Burkitt's lymphoma and Hodgkin's disease. *Blood*, **88(8)**, 3129-3136.

[11] Chan, A.O. and Rashid, A. (2006) CpG island methylation in precursors of gastrointestinal malignancies. *Current Molecular Medicine*, **6(4)**, 401-408.

[12] Zhu, J.Q., Liu, J.H., Liang, X.W., Xu, B.Z., Hou, Y., Zhao, X.X. and Sun, Q.Y. (2008) Heat stress causes aberrant DNA methylation of h19 and igf-2r in mouse blastocysts. *Molecules and Cells*, **25(2)**, 211-215.

[13] Bandaru, B., Gopal, J. and Bhagwat, A.S. (1996) Overproduction of DNA cytosine methyltransferases causes methylation and C --> T mutations at non-canonical sites. *The Journal of Biological Chemistry*, **271**, 7851-7859.

[14] Zhang, J.C., Lu, J., Li, H.P., Wu, J.M. and Hu, L.H. (2006) High Rate of P16 Methylation Associated with Hepatitis B Virus Infection in Hepatocellular Carcinoma. *The Chinese-German Journal of Clinical Oncology*, **5**, 84-89.

[15] Bhasin, M., Zhang, H., Reinherz, E.L. and Reche, P.A. (2005) Prediction of methylated CpGs in DNA sequences using a support vector machine. *FEBS Letters*, **579(20)**, 4302-4308.

[16] Chou, K.C. and Cai, Y.D. (2006) Predicting protein-protein interactions from sequences in a hybridization space. *Journal of Proteome Research*, **5(2)**, 316-322.

[17] Peng, H., Long, F. and Ding, C. (2005) Feature selection based on mutual information: criteria of max-dependency, max-relevance, and min-redundancy. *IEEE Transactions on Pattern Analysis and Machine Intelligence*, **27(3)**, 1226-1238.

[18] Madsen, A. and Josephsen, J. (1998) Cloning and characterization of the lactococcal plasmid-encoded type II restriction/modification system, LlaDII. *Applied and Environmental Microbiology*, **64(7)**, 2424-2431.

[19] Chernukhin, V.A., Kashirina, Y.G., Sukhanova, K.S., Abdurashitov, M.A., Gonchar, D.A. and Degtyarev, S. (2005) Isolation and characterization of biochemical properties of DNA methyltransferase FauIA modifying the second cytosine in the nonpalindromic sequence 5'-CCCGC-3'. *Biochemistry*, **70(6)**, 685-691.

[20] Eckhardt, F., Lewin, J., Cortese, R., Rakyan, V.K., Attwood, J., Burger, M., Burton, J., Cox, T.V., Davies, R., Down, T.A., *et al*. (2006) DNA methylation profiling of human chromosomes 6, 20 and 22. *Nature Genetics*, **38(12)**, 1378-1385.

[21] Das, R., Dimitrova, N., Xuan, Z., Rollins, R.A., Haghighi, F., Edwards, J.R., Ju, J., Bestor, T.H. and Zhang, M.Q. (2006) Computational prediction of methylation status in human genomic sequences. *Proceedings of the National Academy of Sciences of the United States of America*, **103(28)**, 10713-10716.

[22] Li, W. and Godzik, A. (2006) Cd-hit: A fast program for clustering and comparing large sets of protein or nucleotide sequences. *Bioinformatics* (*Oxford, England*), **22(13)**, 1658-1659.

[23] Ding, C. and Peng, H. (2005) Minimum redundancy feature selection from micro array gene expression data. *Journal of Bioinformatics and Computational Biology*, **3(2)**, 185-205.

J. Biomedical Science and Engineering, 2010, 3, 677-683 **JBiSE**
doi:10.4236/jbise.2010.37092 Published Online July 2010 (http://www.SciRP.org/journal/jbise/).

A pilot study of a novel pulsatile flow generator using large collapsible bladder

Ponangi Udaya Prashant[1], Nagaraj Balasubramanya[2]

[1]Institute G-5, Sneha Sindhu Apartments, Kavalabyrasandra, Bangalore;
[2]Department of Civil Engineering, M.S. Ramaiah Engineering College, Bangalore, India.
Email: udayaprashant_p@yahoo.co.in; jhrumbaa@gmail.com

Received 30 April 2010; revised 21 May 2010; accepted 22 May 2010.

ABSTRACT

Background: There are different experimental models avialable for generating pulsatile flow in laboratory and study their heamodynamic effects on blood vessels. We aim to produce a novel pulsatile flow generator utilizing a large collapsible rubber bladder and the phenomenon of fluid structure interactions occurring in a specially designed flexible tube arrangement. Mehtods: Water enters from a reservoir above into a large collapsible bladder made of rubber which opens into 'U' shaped tube made of flexible material and held by non rigid structures. As liquid starts flowing the distal end of collapsible bladder collapses under the negative atmospheric pressure generated inside closing the mouth of 'U' shaped tube and produces pulsatile flow. Resuts: The frequency of pulsations, pressure fluctuations and velocity profile resemble that of in vivo blood flow. As the flow entering into collapsible bladder increases the frequency of pulsatile flow decreases and also when height of the collapsible bladder from the ground was changed. The whole cycle of alternate collapse/expansion of collapsible bladder with generation of pulsatile flow continue indefinitely as long as there is enough water in reservoir and vertical gradient to sustain the flow. Conclusions: The pulsatile flow so produced has many of the characteristics of physiological blood flow and can be used to study mechanisms of various cardiovascular diseases in laboratory.

Keywords: Collapsible Tubes; Buckling; Pulsatile Flow Generator; Unsteady Flow; Fluid Structure Interactions

1. INTRODUCTION

Cardiovascular diseases are major causes of death throughout the world, yet the mechanisms of these diseases, especially atherosclerosis is poorly understood. The most important aspect of the development and progression of cardiovascular diseases is the role of pulsatile flow in hemodynamics of cardiovascular diseases like atherosclerosis [1,2]. Pulsatile flow induces complex shear stress on walls of vessels and is basis for many atherosclerotic diseases like aneurysms and stenotic lesions [3]. A number of attempts have previously been made to simulate pulsatile human arterial flow [4-7].

Hopmann and Liu described a pump that uses an elastic chamber squeezed by a cam, with pressure-actuated check valves [4]. The use of a gear pump controlled by a closed-loop servosystem was reported by Issartier *et al.* [4,7]. Kiyose *et al.* have described a mechanical piston pump system for simulating peripheral arterial flow [4]. Petersen described a system using two gear pumps, one to generate forward flow and the other to generate reverse flow [5]. A microcomputer regulated a pneumatic control valve so that the total flow at any instant could be controlled. Errikson *et al.* used a microcomputer controls a motor which in turn drives a piston pump to generate the flow [6]. However, the system appears to lack the flexibility to generate different waveforms.

Many of the existing pulsatile flow generators are complicated, consume significant power and require computers to function [4-7]. They are also expensive and none of them are based on principle of flow limitation occurring in collapsible tubes. Many interesting phenomena are observed like flow limitation and the propensity to develop large amplitude self-excited oscillations during study of flows in collapsible tubes [8].

Flow induce collapse is very common in many physiological situations like regulation of blood vessel caliber, generation of murmurs, snoring sounds, wheezing in airways, micturation etc [9]. The collapsible tubes buckles and collapses at the distal most point of tube as the internal pressure is least between entry and exit end due to viscous pressure drop [10]. Buckled vessels are very flexible and even small changes in fluid pressure can induce large changes of their cross-sectional area [11].

Many of the physiologically observed phenomena described above can be reproduced in laboratory experiments using the 'Starling Resistor', shown below [9] (**Figure 1**). Inside a pressure chamber, a thin-walled elastic tube (typically made of latex rubber) is mounted on two rigid tubes. Fluid (typically air or water) is driven through the tube, either by applying a controlled pressure drop *p-entry* and *p-exit*, between the ends of the rigid tubes or by controlling the flow rate *Q*. At sufficiently large Reynolds numbers, the system buckles axisymmetrically and readily produces self-excited oscillations [9,11].

The present experiment may be considered as extreme modification of this basic "Starling Resistor". There are certain practical applications described for pulsatile flow produced by rapid flutter of collapsed tube. Microfiltration performance of Bentonite suspension was greatly enhanced when a pulsatile flow generated from rapid flutter of collapsible tube was used [20]. But the pulsatile flow produced by Waxing *et al*. was different from the present experimental setup both in mechanism and the pulsatile waveform generated [20].

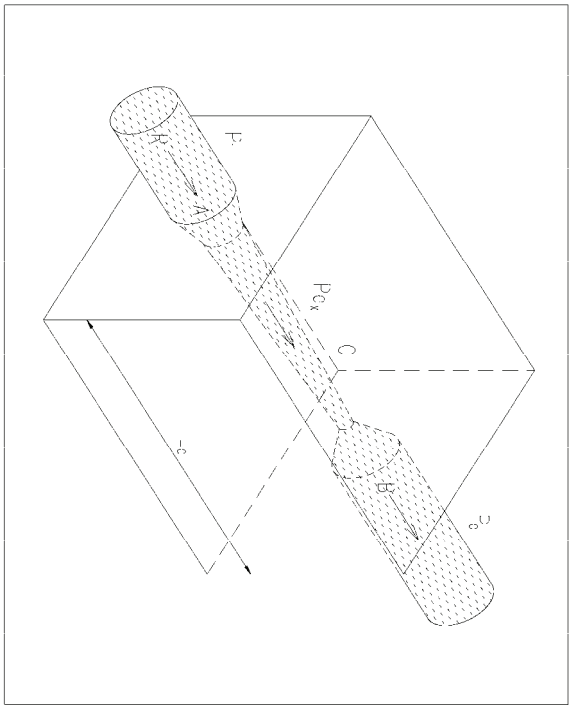

Figure 1. The classic "Starling Resistor". The figure shows how classical Starling Resistor works. The liquid enters the collapsible tube at A with velocity *V* which is enclosed in a pressurized chamber (p_{ext}) and travels distance L and starts buckling at B. The diameters of entry and exit pipes are same as that of collapsible tube diameter R_0 and all the pipes are aligned in one straight line.

The cyclical opening and collapse of a large rubber bladder used here produces large amplitude low frequency pulsatile flow from continuously flowing liquid unlike previous experiments by a very unique arrangement. The flow very much resembles that occurring inside cardiovascular system of living organisms having characteristics of sinusoidal rise and fall with sharp spike in between during collapse of bladder.

2. METHODS

The experimental model can be demonstrated by constructing a simple device using commonly available materials (**Figures 2** and **3**). To a source water that has very negligible head is connected to collapsing rubber bladder. This rubber bladder is highly elastic and the lower end is connected to flexible thin garden hosepipe made of synthetic rubber or PVC. This flexible rubber tube hangs freely after taking initial 'U' shaped curve. The distal end is open to atmosphere and all the connections are airtight. If the vertical height from the tap to balloon is less than from ground to the balloon ($h_1 > h_o$) and during certain range of flow rates it exhibits an interesting phe-

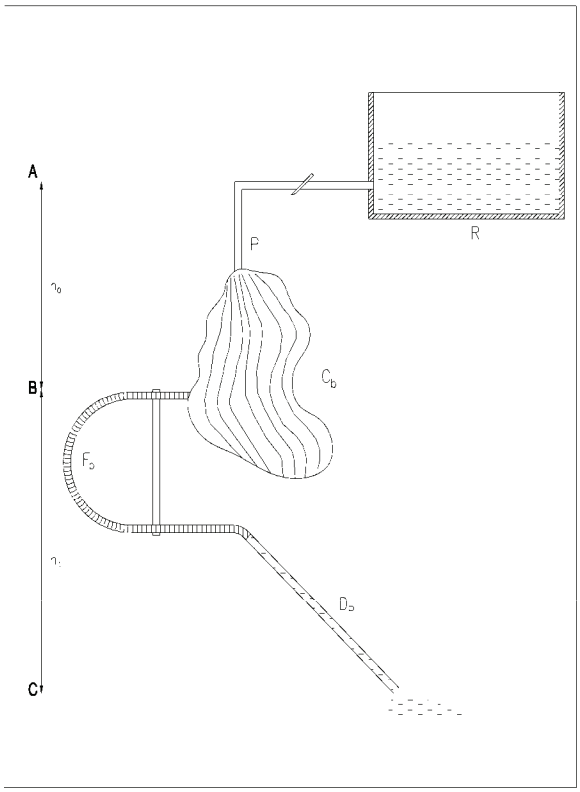

Figure 2. Simple sketch of the novel pulsatile flow generator. R is reservoir; P are connecting pipes from reservoir to collapsing bladder C_b. The collapsible bladder is connected to 'U' shaped flexible tube F_p which is in turn connected to long rigid distal pipe D_p.

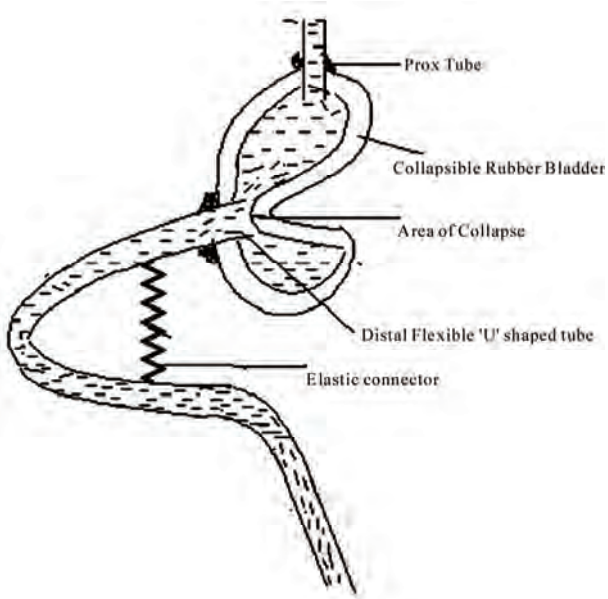

Figure 3. Schematic diagram showing distal flexible 'U' shaped tube and its attachements.

nomenon of alternate collapse (buckling) and opening, along with generation of pulsatile flow of water. The flow of water or any liquid entering into the collapsible bladder is regulated by a valve and the flow rate can be measured by flow meter attached to it. Pressures are recorded at two points, one at the entry at the collapsible bladder and other at the end of 'U' tube with help of Phlips portable MP20 monitor and electronic pressure transducer system. Average velocity of flow was calculated by dividing flow rate with area of connecting pipe to collapsible bladder.

Simultaneous pressure was recorded at the proximal and distal end of balloon. The pressure at the entry of the collapsing bladder remains fairly constant at a –ve pressure of -6 to -12 cm of water with slight fluctuations during the entire cycle.

The distal end of collapsible bladder exhibits rapid and wide range of fluctuations which can be explained by very strong fluid structure interactions happening due to sudden stoppage of flow. This is because the 'U' shaped tube is made of flexible plastic pipe and also the supporting structures are non rigid. An attempt has been made to graphically record the fluid velocity flow with help of doppler at the distal end of collapsible bladder but the flow in this region is very turbulent whereas other regions it is smooth.

3. RESULTS

Below are experiments conducted using above model which study the relationship rate of fluid flowing and the frequency of oscillations produced.

3.1. About Collapsible Bladder

The dimensions of the balloon in fully expanded state, which assumes a geometric shape of ellipsoid are: - Horizontal diameter is = 11.5 cm

Vertical diameter =19 cm

Volume of fully expanded Balloon is = 1600 cc

The thickness of the rubber used in the rubber is = 0.75 mm

3.2. About Distal 'U' Shaped Tube

The distal 'U' shaped tube is made of relatively flexible PVC pipe with following characteristics

The length of 'U' tube is = 60 cm

Height of U tube is from collapsible balloon to distal rigid tube is = 30 cm

Vertical height of distal rigid tube from flexible U shaped tube is = 140 cm

Inner Diameter of U shaped flexible tube is = 12 mm

Thickness of U shaped tube is = 2 mm

Inner Diameter of distal rigid tube is = 11 m

Thickness of distal rigid tube is = 1.8 mm

The angle of 'U' tube which makes to vertical is between 80°- 70

Similar experiments were conducted in much small scale using small sized balloons and tubes which worked very well, though data was not recorded, due to low volume flows and small sized equipment used.

The dimensions of the pipes and bladder are so chosen to resemble those of small sized human beings cardiovascular system. The flows used are comparable to normal physiological range of blood flow. The oscillations produced by this experiment also are in range of normal heart beating frequency. The basic experiments illustrate how simple parameter of flow rate can be varied to alter the frequency of collapsing bladder (**Tables 1** and **2**). Also at constant flow conditions and when all other parameters are kept constant of varying height of the bladder from ground affects the frequency of collapsing bladder (**Tables 3** and **4**). Thus by altering these two simple parameters any desired flow condition can be simulated in laboratory. The effects of pipe's stiffness and diameters of tubing can be studied and their flow patterns analyzed when all other parameters are held constant. Also side branches can be attached to distal 'U' tube or rigid pipe which represent the branches of main vessels and their flow characteristics during pulsatile flow can be studied.

Here fall of pressures is sharp unlike the rise which is observed during pressure recordings inside large arteries and the pressures recorded here are in negative range which is reverse of that seen normally inside blood vessels. But the pressure fluctuations resemble closely to those recorded inside vascular compartment invasively.

Table 1. Relationship of change in frequency of oscillations with change in flow rate when height of bladder from ground is constant.

Flow rate in ml/sec	Freq of collapse per min	Pressure at inlet in mm Hg	Max pressure at outlet in mm Hg	Min pressure at outlet in mm Hg	Range of pressure fluctuations in mm Hg	Average velocity of flow in m/sec
146	108	-7	-116	-154	37	1.2
200	100	-9	-122	-158	37	1.8
250	74	-10	-146	-196	50	2.2
278	80	-7	-94	-150	56	2.5
303	62	-9	-112	-150	38	2.5
332	52	-7	-100.	-127	26	2.6
435	30	-9	-146	-176	30	2.9

Table 2. Similar experiment as above when the vertical height of 'U' tube from Ground is changed (h = 90 cm)

Flow rate in ml/sec	Freq of collapse per min	Pressure at inlet in mm Hg	Max outlet pressure in mm Hg	Min outlet pressure in mm Hg	Range of pressure fluctuations in mm Hg	Average velocity of flow in m/sec
85	128	-5	-50	-70	20	0.75
108	122.	-5.5	-65	-75	10	0.95
187	86	-6	-59	-70	11	1.6
188	82	-7	-54	-67	13	1.6
218	75	-5.5	-60	-67	7	1.9
228	72	-7	-34	-56	22	2.0
250	70.	-7	-33	-59	26	2.2
286	72	-4.5	-63	-79	6	2.5
298	62	2.5	-67	-72	5	2.6
342	45	-5.5	-60	-75	15	3.0
362	48	-6	-52	-67	15	3.2

Table 3. Variation of frequency with varying vertical height at constant flow rate of = 278 ml/sec average velocity of flow is 2.45 m/sec.

Vertcial height from ground in cm	Freq of collapse per min	Pressure at inlet in cm of ater	Outlet Max pressure in mm Hg	OutletMin pressure in mm Hg	Range of pressure fluctuations in mm Hg
36	76	-7	-63	-100	37
96	66	-8	-68	-108	40
130	58	-7	-116	-154	38
142	70	-7	-94	-130	37
162	57	-6	-2	-4	2

4. DISCUSSION

In our study instead of classical models of 'starling resistor [9,11] we use large balloon such that its diameter is greater than 3 times the inlet rigid tube diameter. Also the exit is not along the straight rigid tube but through the lower side of balloon such that when the balloon collapses the opposite wall impinges on the exit end completely occluding it and the flow stops (The path of fluid in the balloon is not straight as in 'starling resistor' but affectively changed to 90').

Table 4. Variation of frequency with change in height at constant flow rate of 240 ml/sec & average velocity of flow is 2.14 m/sec.

Vertical height from ground in cm	Frequency of collapse per min	Pressure at inlet in mm Hg	Max Pressure at outlet in mm Hg	Min pressure at outlet in mm Hg	Range of pressure fluctuations in mm Hg
30	96	-2	-3	-4	1
50	92.	-4	-1	-21	20
96	91	-4	-41	-47	27
130	86.	-5	-60	-70	30
150	98	-5	-82	-96	20
165	58	-4	-80	-90	14

There is another major deviation from classical approach the distal end is not exactly 'rigid straight tube' but a 'U' shaped flexible tube with mobile supports. The purpose of it was to make the distal end flexible, so that during the collapse, it executes rotational motion and also swings forward. The axial and radial motion of distal 'U' shaped pipe due fluid solid coupling can be described by series of differential equations [13]. As the supports holding the distal 'U' tube are elastic and the 'U' tube are itself flexible, due to strong fluid structure interactions occurring inside the system, the 'U' tube gets displaced [14] and the collapsed rubber bladder opens up and fills with liquid flowing continuously from reservoir above. Also some doubts about the flow resembling certain kinds of slug flow have to be dismissed totally as it is purely a monophasic flow and experimental observations revealed that the presence of air or any gas inside the tubes does not produce pulsatile flow. All the connections have to be airtight and very little air is sucked inside the tubes at the lower end of distal rigid tube (7 of **Figure 2**).

The basic mechanism is that once flow of water starts the positive hydrostatic pressure acting inside collapsible bladder proportional to height ho (ho*d*g) becomes negative lateral pressure when flow is fully established flow and this negative pressure ($-h_1$*d*g) is proportional to height h_1 [17]. Also this negative pressure is the compressing transmural pressure acting on the collapsible bladder which causes it to buckle axisymmetrically at its distal end [12]. This sudden collapse occludes the mouth of 'U' shaped tube and stops the flow instantly creating a large –Ve waterhammer wave distally with strong junction coupling [15,18].

The pressure wave form so produced can be analyzed by combined effects of pressure surges and pipe motion with help of method of characteristics and finite element methods respectively [16,18]. This strong junction coupling occurring at U shaped tube has sufficient force to overcome the collapsing force of the bladder at the mouth of 'U' tube $\{(h_1 - h_0)$*d*g*A$\}$ and causes the bladder to open up with re-establishment of flow, thus producing pulsatile flow [18]. The total strain energy which has developed due to the fluid structure interactions can be calculated knowing bulk modulus of flowing liquid and elastic modulus of pipe as well as its mass density per unit length [17].

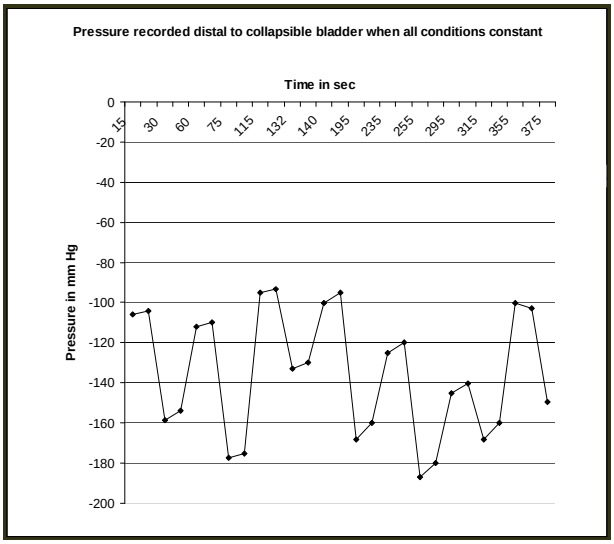

Typical pressure fluctuations recorded at the mouth of 'U' tube when all the flow conditions are held constant. Here flow rate was = 280 ml/sec, vertical height of 'U' tube from ground is 140 cm and frequency of collapse is = 84/min

Figure 4. Graph showing pressure readings with time.

From these basic experiments it can be concluded that as the flow rate increases the frequency of oscillations progressively reduce and the average velocity of flow increases. The pressure at the inlet of balloon remains relatively constant with minor fluctuations per collapse of bladder. The outlet pressure fluctuates widely and the range is 30 – 40 mm Hg which can be comparable to pulse pressure of human cardiovascular system.

Definite relationship between pressure and flow rate could not be established one reason being relatively insensitive instruments used to record a very dynamic and

unstable pressure tracing. The minimum flow where it functions is where the flow inside the pipe work becomes closed channel laminar flow [17].

That means the whole of pipe area is in contact with flowing water. At flow rates below this it is open channel flow. Also the velocity of flow is 0.5 -2 m/sec which is very low. At flow velocity > 3 m/sec or at higher Reynolds numbers the efficiency markedly falls and little higher flow velocity it doesn't behave as pulsatile balloon but it simply expands and remains in that position and water starts flowing passively. When diameter of U and distal pipe is increased the lower and upper flow rate limit where these pulsations are observed both are increased and also simultaneously the range at which operates efficiently are increased correspondingly.

Yannick *et al.* performed in a specially designed mockup simulating the heart's behavior (the Dual Activation Simulator) to understand pulsatile flow inside heart like chambers in terms of mechanical behavior to understand cardiovascular diseases in laboratory without resorting to animal models or patients [19].

The gear pumps used by Issartier *et al.*, Petersen *et al.*, etc produce cavitation and damage to suspended particles [4-5] whereas the present model the occurrence of cavitation is very less and can be easily prevented by altering flow conditions. There is also no damage to blood particles as it does not involve rotating metal gears.

Peristaltic pumps which were developed later to prevent particle damage of gear pumps suffer the drawback of production of only limited subset of waveforms even if they are computer controlled and the systems lack flexibility to operate under wide flow conditions [4,6,7]. Also generating continuous flow from peristaltic pumps is difficult. The present model operates under wide range of flow conditions which can be produced by simply opening the inflow valve or raising the height of collapsible bladder from ground. Besides pulsatile flow, continuous can be easily produced simply by halting the oscillations of 'U' shaped tube and no further additional arrangement is required.

Microcomputer controlled piston pumps are very complicated, difficult to set up and cumbersome to operate [4-7]. The present apparatus offers an easier solution of producing pulsatile flow in laboratory by using readily available cost effective materials and can save lot of expenses and power.

The collapse of collapsible bladder resembles somewhat superficially of "beating heart" and waveforms produced are very close to invivo flow including sudden surges of pressures seen during valve closure. The pulsatile flow so produced can be studied for progression of diseases like atherosclerosis, effects of vessel wall stiffness and other properties for development of vascular diseases like hypertension and atherosclerosis.

Initial preliminary studies the apparatus works even when glycerol water having viscosity similar to blood are used as flowing liquid instead of water. However this is a pilot study and needs to be validated by further research and all the variables which affect the flow have to be studied more exhaustively with better instrumentation and advanced mathematical approach, before real useful conclusions drawn.

5. CONCLUSIONS

A novel and cost-effective pulsatile flow generator can be constructed using a large collapsible bladder connected to a flexible 'U' shaped tubing system and the pulsatile flow so produced can be used as simulation model for studying in vivo blood flow.

6. AUTHOR'S CONTRIBUTIONS

PUP developed the experimental setup from beginning, conducted the experiments and drafted the manuscript. NBS provided technical support for conducting experiments in MSRIT lab and suggested the utility of using it as simulation model for cardiovascular system.

7. ACKNOWLEDGEMENTS

I thank MSRIT institute for providing me laboratory support for my research especially Dept of Civil engineering and the Principal of MSRIT.

REFERENCES

[1] Afshin, A.-B., Mohammad, T.-S., Nasser, F., *et al.* (2008) A new system to analyze pulsatile flow characteristics in elastic tubes for hemodynamic applications. *American Journal of Applied Sciences*, **5(12)**, 1730-1736.

[2] Chatzizisis, Y.S. and Giannoglou, G.D. (2006) Pulsatile flow: A critical modulator of the natural history of atherosclerosis. *Electronic Publication*, **67(2)**, 338-340.

[3] Finol, E.A. and Amon, C.H. (2001) Blood flow in abdominal aortic aneurysms: Pulsatile flow hemodynamics. *Journal of Biomechanical Engineering*, **123(5)**, 474-484.

[4] Law, Y.F., Cobbold, R.S.C., *et al.* (1987) Computer-controlled pulsatile pump system for physiological flow simulation. *Medical & Biological Engineering & Computing*, **25(5)**, 590-595.

[5] Petersen, J.N. (1984) Digitally controlled system for reproducing blood flow waveforms *in vitro*. *Medical and Biological Engineering and Computing*, **22(3)**, 277-280.

[6] Eriksson, A., Persson, H.W. and Lindstrom, K. (2000) A computer-controlled arbitrary flow wave form generator for physiological studies. *Review of Scientific Instruments*, **71(1)**, 235-242.

[7] Holdswoth, D.W., Rickey, D.W., *et al.* (1991) "Computer-controlled positive pump for physiological flow

simulation," *Medical & Biological Engineering & Computing*, **29(4)**, 565-570.

[8] Kamm, R.D. and Shapiro, A.H. (1979) Unsteady flow in a collapsible tube subjected to external pressure or body forces, *Journal of Fluid Mechanics*, **95(1)**, 1-78.

[9] Heil, M. and Jensen, O.E. (2003) Flows in deformable tubes and channels -- Theoretical models and biological applications. Chapter 2 of: flow in collapsible tubes and past other highly compliant boundaries. Pedley, T.J. and Carpenter, P.W., Eds., Kluwer, Dordrecht, Netherlands Heil, 15-50.

[10] Heil, M. (1996) The stability of cylindrical shells conveying viscous flow. *Journal of Fluids and Structures*, **10(2)**, 173-196.

[11] Heil, M. and Pedley, T.J. (1996) Large post-buckling deformations of cylindrical shells conveying viscous flow. *Journal of Fluids and Structures*, **10(6)**, 565-599.

[12] Heil, M. (1998) Stokes flow in an elastic tube -- A large-displacement fluid-structure interaction problem. *The International Journal for Numerical Methods in Fluids*, **28(2)**, 243-265.

[13] Tijsseling, A. (2007) Water hammer with fluid-structure interaction in thick-walled pipes. *Computers and Structures*, **85(11-14)**, 844-851.

[14] Heinsbroek, A.G.T.J. and Tijsseling, A.S. (1994) The influence of support rigidity on waterhammer pressures and pipe stresses. *Proceedings of the Second International Conference on Water Pipeline System and BHR Group*, Edinburgh, 17-30.

[15] Wiggert, D.C. and Tijsseling, A. S. (2001) Fluid transients and fluid-structure interaction in flexible liquid filled piping. *ASME*, 455-481.

[16] Tijsseling, A.S. and Heinsbroek. A.G.T.J. (1999) The influence of bend motion on waterhammer pressures and pipe stresses. *Proceedings of the* 3*rd ASME & JSME Joint Fluids Engineering Conference, Symposium S*-290 *Water Hammer* (*Editor JCP Liou*), *San Francisco, July* 1999, *ASME-FED*, **248**, *Paper FEDSM*99-6907.

[17] Kumar, D.S. (2010) Fluid mechanics and fluid power engineering. S. K. Kataria & Sons Publishers and Distributors, New Delhi, Chapter 9.

[18] Ahmad A. and Ali R.K. (2008) Investigation of the junction coupling due to various types of the discrete points in a piping system. *The* 12*th International Conference of International Association for Computer Methods and Advances in Geomechanics* (*IACMAG*), Goa, India.

[19] Knapp, Y., Bertrand, E. and Mouret, F. **(**2003) 2D-PIV measurements of the pulsatile flow in a left heart simulator. *Proceedings of PSFVIP*-4, Chamonix, F4082**.**

[20] Wang, W.X. and Christopher D.B. (2007) Effects of collapsible-tube-induced pulsation vigour on membrane filtration performance. *Journal of Membrane Science*, **288 (1-2)**, 298-306.

J. Biomedical Science and Engineering, 2010, 3, 684-699 **JBiSE**
doi:10.4236/jbise.2010.37093 Published Online July 2010 (http://www.SciRP.org/journal/jbise/).

Nucleotide host markers in the influenza A viruses

Wei Hu

Department of Computer Science, Houghton College, Houghton, USA.
Email: wei.hu@houghton.edu

Received 7 May 2010; revised 23 May 2010; accepted 25 May 2010.

ABSTRACT

In the efforts to understand the molecular characteristics responsible for the ability of influenza viruses to cross species, various amino acid host markers in influenza viruses were uncovered. Our previous study identified a collection of novel amino acid host markers in ten proteins of 2009 pandemic H1N1. As an extension of our prior work, the objective of the current study was to employ Random Forests, a robust pattern recognition technique, to discover nucleotide host makers in the ten corresponding genes of 2009 pandemic H1N1, along with those in the genes of avian and swine viruses. Although different, there was an association between the amino acid markers in proteins and the nucleotide markers in the related genes due to codon translations. Moreover, nucleotide host markers have the capability to indicate important positions within a codon for host switches as well as the significance of synonymous mutations on host shifts, all of which amino acid markers could not provide. Our findings highlighted that two or even three nucleotide markers could coexist within a single codon, and the different importance values of these markers could further discriminate the multiple markers within a codon. The nucleotide markers found in this study rendered a comprehensive genomic view of the complex and systemic nature of host adaptation. They verified and enriched the known amino acid markers and offered a larger set of finer host markers for further experimental confirmation.

Keywords: 2009 Pandemic H1N1; Host Switch Marker; Influenza; Mutation; Random Forests

1. INTRODUCTION

The swine-origin 2009 pandemic H1N1 was a clear reminder that understanding the biological mechanisms of cross-species transmission of influenza viruses remained an urgent and crucial research topic. Extensive search of host-shift markers in the influenza viruses resulted in a rich set of avian-human or swine-human markers [1-7]. However, sequence analysis of the recently emerged 2009 pandemic H1N1 virus suggested the absence of these well-known host switch markers [8]. Although the symptoms of 2009 pandemic H1N1 were mild, the fear was that the new virus might mutate to a more virulent virus. A recent experiment [9] indicated that the introduction of traditional virulence markers (mutations) in PB2 of 2009 pandemic H1N1 did not confer increased virulence or transmission, implying that these markers had minimum impact on this new virus.

To tackle the question of where to find the host markers in 2009 pandemic H1N1, it was hypothesized in [8] that they might exist outside of the space of the previously discovered markers. A new procedure using Random Forests was designed to identify a collection of novel amino acid host markers in ten proteins of 2009 pandemic H1N1, which included, in addition to the SR polymorphism found in [10], a set of markers in PB2 that might play compensatory roles in efficient replication and transmission of this novel virus. The purpose of this study was to uncover nucleotide host markers in the ten corresponding genes of 2009 pandemic H1N1 to provide finer and complement information about the host adaptation of this new virus. Furthermore, the nucleotide host markers in the ten corresponding genes of avian and swine viruses were also included in this report.

Using nucleotide sequences, it was found in [11,12] that mononucleotide composition, rather than the higher-order compositions, was sufficient to distinguish the human and avian viruses with high accuracy. The viruses that replicated in mammals including 2009 pandemic H1N1 were more likely to change G to A in the mRNA than vice versa. The patterns of nucleotide frequency according to host species demonstrated that the 2009 pandemic H1N1 virus had been evolving in swine prior to its emergence. Another separate report [13] confirmed that the pattern of nucleotide composition of HA and NA genes of 2009 pandemic H1N1 was closest to that of swine H1N1 compared with the viruses of other

origins and this novel virus originated from swine H1N1 based on the codon usage bias. To study the selective pressure acting on each gene segment of 2009 pandemic H1N1 [14], the ratio between the rate of non synonymous substitutions per non synonymous site and the rate of synonymous substitutions per synonymous sites was computed, exhibiting an active purifying selection on all segments. Specially, purifying selection was extreme on NP, MP, PA and PB1, moderate on NS and HA. PB1-F2 protein is a virulence factor in influenza viruses. However, genomic annotations of 2009 pandemic H1N1 [15] discovered a nucleotide mutation (C → A) to render a stop codon at position 12, which resulted in a truncated PB1-F2 protein for this new virus.

Many host markers are amino acid markers including the ones in [8]. However, amino acids and nucleotides are related because of codon translations. Some codon substitutions are more likely than others due to the genetic code structure and selective pressures favor some codons for enhanced translation speed and fidelity. Therefore, it is not realistic to assume that each amino acid is equally likely to be encoded by any of its codons. In general codon-based host shift information is more accurate than the amino acid-based. Based on this observation, the current study aimed to identify nucleotide host markers through a large-scale comparative analysis of ten genes of influenza viruses. These markers could demonstrate which positions within a codon were important and uncover the synonymous mutations that might be crucial for host switches. To facilitate the discovery of these markers, this report proposed to employ Random Forests, a robust pattern recognition technique that was previously applied successfully as a cost effective approach to the study of ten proteins of influenza viruses in [8].

2. MATERIALS AND METHODS

2.1. Sequence Data

All influenza virus nucleotide sequences corresponding to the protein sequences used in [8] were retrieved from the Influenza Virus Resource (http://www.ncbi/nlm.nih.giv/genomes/FLU/FLU.html) of the National Center for Biotechnology Information (NCBI). All the sequences used in the study were aligned with MAFFT [16].

2.2. Random Forests

Random Forest, proposed by Leo Breiman in 1999 [17], is an ensemble classifier based on many decision trees. Each tree is built on a bootstrap sample from the original training set and is unpruned to obtain low-bias trees. The variables used for splitting the tree nodes are a random subset of the whole variable set. The classification decision of a new instance is made by majority voting over all trees. About one-third of the instances are left of the bootstrap sample and not used in the construction of the tree. These instances in the training set are called "out-of-bag" instances and are used to evaluate the performance of the classifier, which can achieve both low bias and low variance with bagging and randomization.

2.3. Feature Selection Using Random Forests

Random Forest calculates several measures of variable importance. The mean decrease in accuracy measure was employed in [18] to rank the importance of the features in prediction. This measure is based on the decrease of classification accuracy when values of a variable in a node of a tree are permuted randomly. In this study, two packages of R, randomForest and varSelRF [18], were utilized to compute the importance of the nucleotides in a given gene sequence dataset. The effectiveness and robustness of this technique as a feature selection method has been demonstrated in various studies [19-24].

Random Forests produce non-deterministic outcomes. To compensate this bias, the Random Forests algorithm was run multiple times and then the average of the results was taken. The importance of each position in the nucleotide sequences was based on the averaged calculations by using the function randomVarImpsRF in varSelRF repeated 5 times.

3. RESULTS

3.1. Comparison of Ten Genes of Influenza Viruses Based on their Consensus Nucleotide Sequences

To explore the relationship among the genes of influenza viruses, the Hamming distance, defined as the number of positions at which the corresponding nucleotides of two sequences are different, of any two consensus nucleotide sequences of avian, human, 2009 pandemic H1N1, and swine viruses was calculated. The distance information in **Table 1** provided insight into the sequence similarity between the genes of different viruses. In particular, the distances between 2009 pandemic H1N1 and avian, human, and swine viruses reflected the origin of 2009 pandemic H1N1 with its genes derived from avian (PB2 and PA), human H3N2 (PB1), classical swine (HA, NP, and NS), and Eurasian avian-like swine H1N1 (NA and M) lineages [25].

3.2. Important Nucleotide Host Markers in Ten Genes of Influenza Viruses

In [8], important amino acid host markers in ten proteins of influenza viruses were uncovered, based on which the novel host markers in 2009 pandemic H1N1 were identified. The main task here was to find the nucleotide host markers in the ten corresponding genes of 2009 pan-

Table 1. This table contains the Hamming distances of ten genes of avian, human, 2009 pandemic H1N1, and swine viruses based on their consensus nucleotide sequences.

Genes	HA	NA	NP	M1	M2	NS1	NS2	PA	PB1	PB2
Dist (Avian, 2009_pandemic)	389	249	242	51	15	108	40	160	256	231
Dist (Human, 2009_pandemic)	389	298	250	98	35	115	55	352	118	354
Dist (Swine, 2009_pandemic)	135	263	78	83	15	47	19	192	184	211
Dist (Avian, Human)	390	339	254	79	28	61	40	332	215	329
Dist (Avian, Swine)	337	316	212	64	12	77	28	161	158	177
Dist (Human, Swine)	342	244	222	64	30	89	42	269	152	286

demic H1N1, avian, and swine viruses, thus offering further information about the adaptation of these viruses to humans. In the following sections, each of the ten genes of human viruses was compared to that of 2009 pandemic H1N1, avian, and swine viruses. Random Forests were employed to locate the top 20 important codons, served as host markers, in the genes of influenza that could separate human from 2009 pandemic H1N1, avian, and swine viruses. In different genes there were several codons that contained two or even three important nucleotide markers selected by Random Forests, a remarkable feature that amino acid markers lack.

The top important codons in each gene for differentiating human from 2009 pandemic H1N1, avian, and swine viruses were displayed in single figure (**Figures 1-10**). The comparison of amino acid markers in [8] and nucleotide markers found in this study revealed several shared sites in each protein/gene, illustrating their significance as host markers. The consensus nucleotides (codons) comprising these sites in each gene were presented in **Tables 2-11**, which could also serve as a confirmation and refinement of the results in [8].

Due to high genetic variation of the HA and NA genes, only the HA nucleotide sequences of H1 subtype and the NA nucleotide sequences of N1 subtype of 2009 pandemic H1N1, avian, human, and swine viruses were utilized in the current analysis. Therefore, the important codons in HA and NA found in this study were subtype-specific. Because all the PB1-F2 proteins of 2009 pandemic H1N1 were truncated and nonfunctional, the genes encoding these proteins were excluded in this study.

3.2.1. HA Gene

One of the advantages of the nucleotide markers over amino acid markers is their ability to represent the synonymous mutations that might be significant for host shifts. In comparison of human with avian, 2009 pandemic H1N1, and swine viruses, there were several synonymous mutation positions in HA with high importance. They were 197(3) (cac(H), cat(H)) and 230(3) (gag(E), gaa(E)) in avian and 197(3) (cac(H), cat(H)) and 254(3) (gga(G), ggg(G)) in 2009 pandemic H1N1. Codon 197(3) had a very high importance in both avian and 2009 pandemic H1N1, although it contained a synonymous mutation in both cases. The codons in 2009 pandemic H1N1 (**Figure 1**) including 184, 258, and 314 had significant effects on the receptor binding specificity of HA of 2009 pandemic H1N1 [26]. The HA active site located in a cleft is composed of the codons 91, 150, 152, 180, 187, 191, and 192, and the active site cleft of HA is formed by its right edge (131_GVTAA) and left edge (221_RGQAGR) [27]. Three codons 127(2), 128(1), and 129(2) in **Table 2** were near the right edge and codon 225(3) in avian (**Figure 1**) was on the left edge of the active site.

The importance values of top codons in avian were more homogenous than those in the 2009 pandemic H1N1 and swine. As in case of the amino acid markers [8], the HA1 domain of HA contained more significant codons than the HA2 domain (**Figure 1**).

3.2.2. NA Gene

In comparison of human with avian, 2009 pandemic H1N1, and swine viruses, there were several synonymous mutation positions in NA with high importance. They were 263(3) (gtg(V), gtt(V)) and 410(3) (cca(P), cct(P)) in avian, 156(1) (aga(R), agg(R)), 339(3) (act(T), tcg(S)), and 440(3) (agt(S), agc(S)) in 2009 pandemic H1N1, and 89(3) (tcc(S), tca(S)) and 267(3) (gtt(V), ata(I)) in swine. Furthermore, sequence alignment revealed a deletion at codon 435 in the NA nucleotide sequences of 2009 pandemic H1N1, avian, and swine viruses, causing a very high importance at that codon in avian and swine (**Figure 2**).

The NA active site is a shallow pocket constructed from conserved residues, some of which contact the substrate directly and participate in catalysis, while others

Table 2. This table contains the consensus nucleotides (codons) at positions in HA that have high importance in separating 2009 pandemic H1N1, avian H1, and swine H1 from human H1 viruses. The single digit in parenthesis is the position within the codon that was selected by Random Forests. The single letter 'a' (for avian) or 'p' (for pandemic 2009) or 's' (for swine) in parenthesis after a position number indicates whether the position is important for avian or 2009 pandemic H1N1 or swine viruses.

Position	45(3) (a)	71(2)(p)	72(1)(s)	74(1)(s)	94(1)(s)	127(2)(s)	128(1)(p)	129(2)(s)	139(1)(a)	141(2)(s)	152(2)(s)	157(2)(s)	168(1)(p)
Avian	aat(N)	ctc(L)	act(T)	aac(N)	gaa(E)	gag(E)	aca(T)	act(T)	tct(S)	gcc(A)	aca(T)	tca(S)	aat(N)
Human	aaa(K)	att(I)	tcc(S)	gaa(E)	tat(Y)	acc(T)	gta(V)	acc(T)	aat(N)	aaa(K)	acg(T)	ttg(L)	aac(N)
2009 H1N1	aga(R)	tcc(S)	aca(T)	agc(S)	gat(D)	gac(D)	tcg(S)	aac(N)	gct(A)	gca(A)	gtt(V)	tca(S)	gat(D)
Swine	agg(R)	ttc(F)	aca(T)	agc(S)	gat(D)	gaa(E)	aca(T)	aac(N)	gct(A)	gca(A)	gta(V)	tca(S)	aat(N)
Position	205(3)(s)	216(2)(p)	235(3)(a)	236(2)(a)	259(2)(a)	275(3)(p)	298(1)(p)	302(1)(p)	314(1)(p)	365(2)(p)	374(2)(p)	404(3)(a)	472(1)(s)
Avian	aag(K)	gct(A)	gac(D)	caa(Q)	aag(K)	tgc(C)	atc(I)	gaa(E)	atg(M)	cag(Q)	gga(G)	att(I)	gat(D)
Human	cat(H)	aaa(K)	gaa(E)	ccc(P)	aga(R)	tgt(C)	gtc(V)	gag(E)	atg(M)	caa(Q)	ggg(G)	atg(M)	aac(N)
2009 H1N1	aga(R)	ata(I)	gag(E)	ccg(P)	aga(R)	tgc(C)	atc(I)	aaa(K)	ctg(L)	ctg(L)	gag(E)	ata(I)	gat(D)
Swine	aaa(K)	gca(A)	gag(E)	cct(P)	aga(R)	tgt(C)	gtc(V)	gaa(E)	atg(M)	caa(Q)	ggg(G)	ata(I)	gat(D)

Table 3. This table contains the consensus nucleotides (codons) at positions in NA that have high importance in separating 2009 pandemic H1N1, avian N1, and swine N1 from human N1 viruses. The single digit in parenthesis is the position within the codon that was selected by Random Forests. The single letter 'a' (for avian) or 'p' (for pandemic 2009) or 's' (for swine) in parenthesis after a position number indicates whether the position is important for avian or 2009 pandemic H1N1 or swine viruses.

Position	126(2)(p)	157(1)(s)	163(3)(s)	166(2)(p)	189(2)(p)	214(3)(a,s)	221(3)(a)	222(3)(a)	257(2)(p)	269(1)(p)	285(1)(p)	329(3)(a,s)	331(2)(p)
Avian	cac(H)	aca(T)	gtg(V)	gct(A)	agt(S)	gac(D)	aac(N)	aac(N)	aaa(K)	ttg(L)	gcc(A)	aat(N)	gga(G)
Human	cac(H)	gcc(A)	cta(L)	gct(A)	ggc(G)	gaa(E)	aag(K)	caa(Q)	aag(K)	ttg(L)	act(T)	aaa(K)	gga(G)
2009 H1N1	ccc(P)	acc(T)	att(I)	gtt(V)	aat(N)	gac(D)	aac(N)	aat(N)	aga(R)	atg(M)	tct(S)	aat(N)	aag(K)
Swine	cac(H)	acc(T)	att(I)	gct(A)	gga(G)	gat(D)	aac(N)	aaa(K)	aaa(K)	ctg(L)	aca(T)	aat(N)	ggg(G)
Position	336(1)(s)	340(1)(a,s)	344(1)(a)	351(2)(a)	365(2)(p,s)	369(2)(a)	395(2)(p)	397(2)(p)	398(3)(p)	435(1)(a,s)	435(2)(a,s)	435(3)(a,s)	
Avian	ggt(G)	cct(P)	tat(Y)	ttt(F)	act(T)	agc(S)	gca(A)	act(T)	gat(D)	---	---	---	
Human	aat(N)	gtt(V)	aac(N)	tac(Y)	aac(N)	aag(K)	gca(A)	act(T)	gat(D)	aca(T)	aca(T)	aca(T)	
2009 H1N1	ggt(G)	tct(S)	aat(N)	ttc(F)	att(I)	aac(N)	gga(G)	aat(N)	gag(E)	---	---	---	
Swine	ggc(G)	tct(S)	aat(N)	ttt(F)	atc(I)	agt(S)	gca(A)	act(T)	gat(D)	---	---	---	

provide a structural framework [28]. According to the numbering in [29], these residues of N1 are 118, 119, 151, 152, 156, 179, 180, 223, 225, 228, 247, 277, 278, 293, 295, 368, and 402. The important codons in **Figure 2** including 157(1), 221(3), 222(3), and 369(2) were near these residue positions, and codon 156(1) carrying a synonymous mutation in 2009 pandemic H1N1 is at one of these positions.

3.2.3. M1 Gene

Residue positions 115, 121, and 137 were avian-human host shift markers in [5]. Codons 103(3), 115(1), 121(1), 137(1), 218(1), 218(3), and 239(1) were identified as avian-human markers in this study and in [8], with codon 218 being selected twice, 218(1) and 218(3). Remarkably, codons 149 and 180 carrying a synonymous mutation had a very higher importance than residue positions 115, 121, and 137.

Residue position 137 was a swine-human marker in [2]. There were codons 115(1), 115(3), 137(1), 218(1), and 218(3) selected as swine-human markers in this study and in [8], and two codons 115 and 218 were chosen

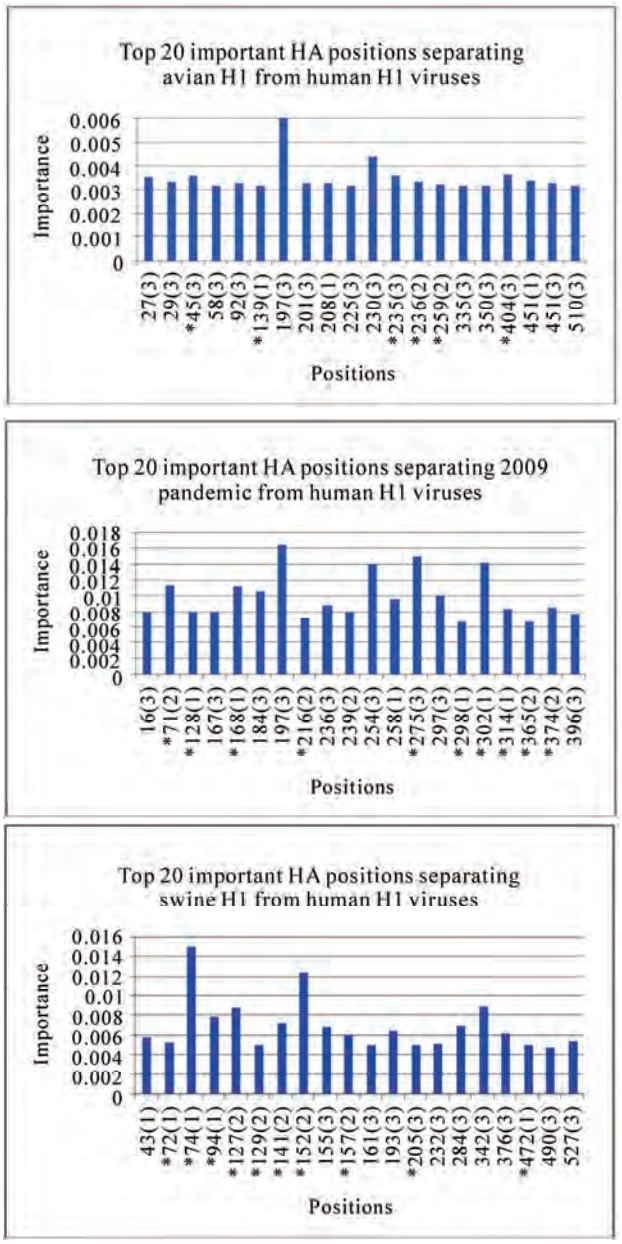

Figure 1. Top important HA codon positions in distinguishing avian H1, human H1, 2009 pandemic H1N1, and swine H1 viruses. The single digit in parenthesis is the position within the codon that was selected by Random Forests. The positions with an asterisk are the important residue positions identified in [8].

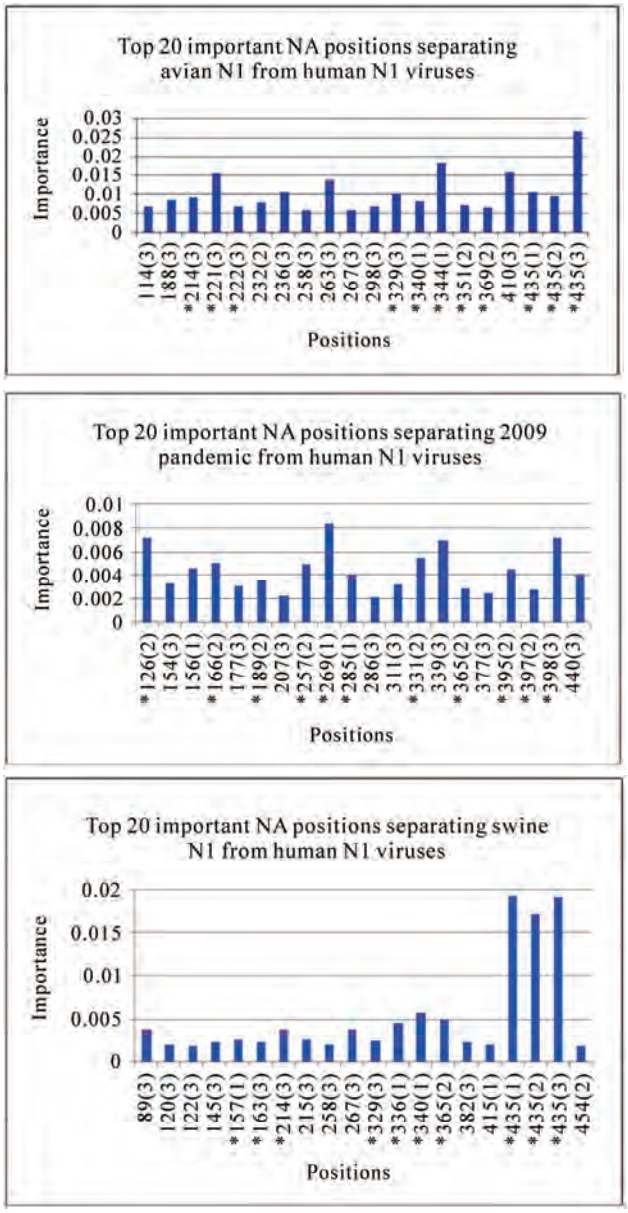

Figure 2. Top important NA codon positions in distinguishing avian N1, human N1, 2009 pandemic H1N1, and swine N1 viruses. The single digit in parenthesis is the position within the codon that was selected by Random Forests. The positions with an asterisk are the important residue positions identified in [8].

twice, *i.e.*, 115(1), 115(3), and 218(1), 218(3). Even though the previously discovered residue position 137 received the highest importance, the two newly found codons 173 and 180 had a very high importance as well. It was noteworthy that codon 180 was significant in both avian and swine and was located in the C-terminal part of M1 (codons 165-252) that bind to vRNP (viral ribonucleoproteins) [30] (**Figure 3**). This study and [8] found that codons 30(1), 30(2), 115(3), 142(3), 166(3), 209(1), 214(3), and 218(3) were important host markers in 2009 pandemic H1N1 with codon 30 being chosen twice.

In comparison of human with avian, 2009 pandemic H1N1, and swine viruses, there were several synonymous mutation positions in M1 with high importance. They were 149(3) (gcc(A), gca(A)) and 180(3) (gtg(V),

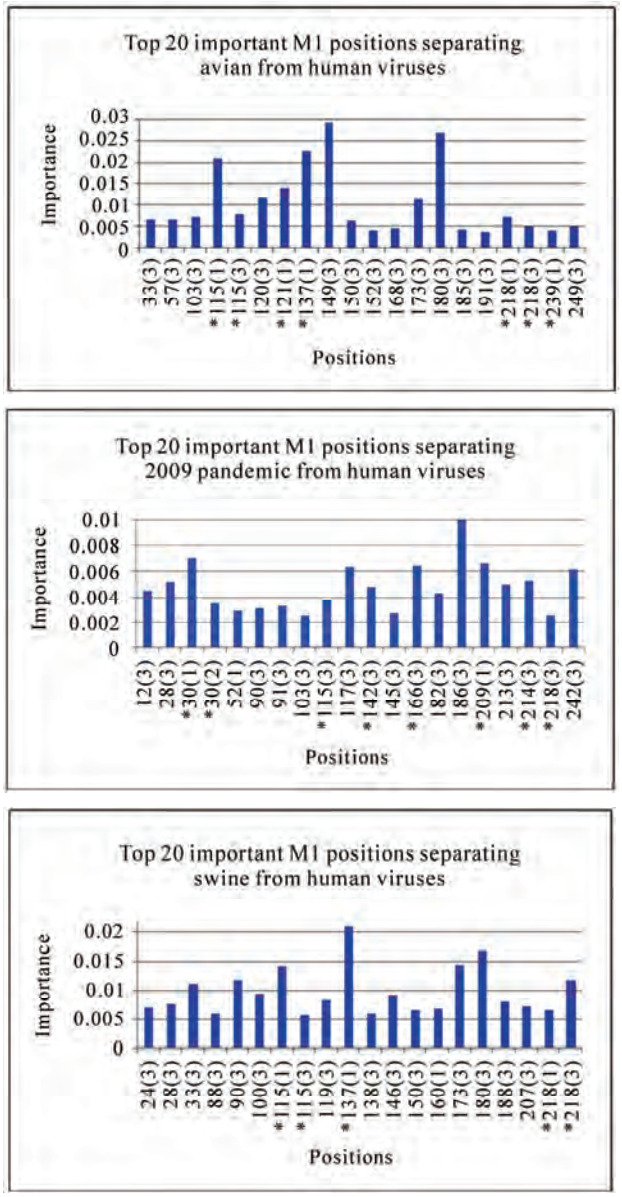

Figure 3. Top important M1 codon positions in distinguishing avian, human, 2009 pandemic H1N1, and swine viruses. The single digit in parenthesis is the position within the codon that was selected by Random Forests. The positions with an asterisk are the important residue positions identified in [8].

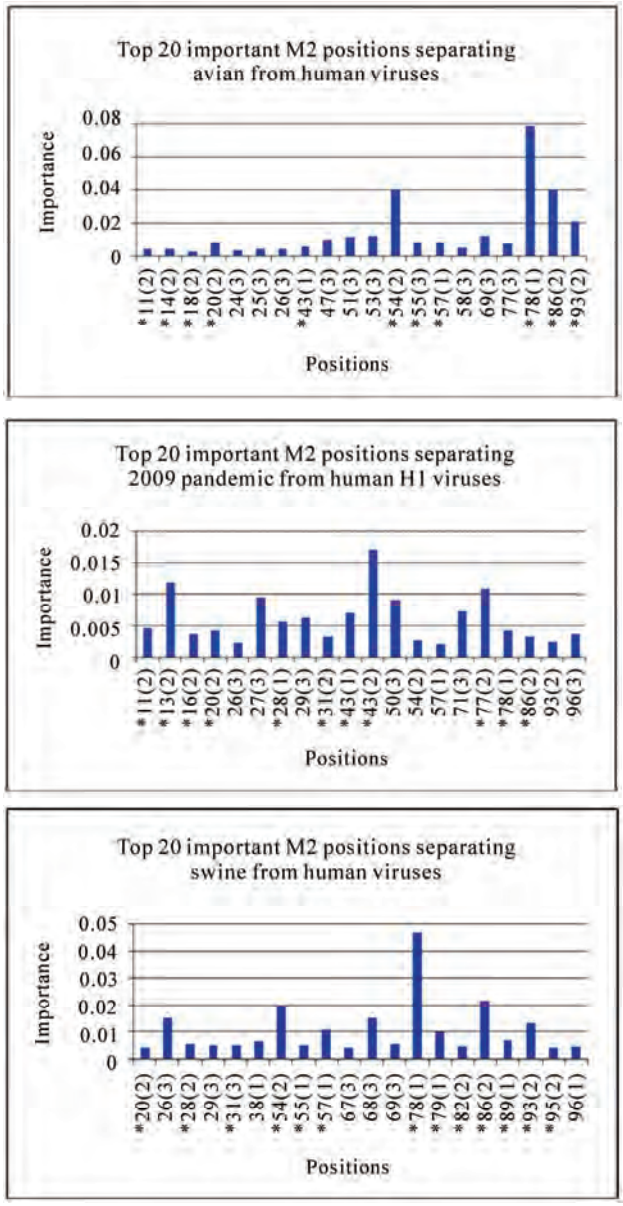

Figure 4. Top important M2 codon positions in distinguishing avian, human, 2009 pandemic H1N1, and swine viruses. The single digit in parenthesis is the position within the codon that was selected by Random Forests. The positions with an asterisk are the important residue positions identified in [8].

gtt(V)) in avian, 117(3) (cta(L), ctc(L)), 186(3) (gct(A), gca(A)), and 242(3) (aaa(K), aag(K)) in 2009 pandemic H1N1, and 90(3) (ccg(P), cca(P)), 173(3) (atc(I), ata(I)) and 180(3) (gta(V), gtt(V)) in swine (**Figure 3**).

3.2.4. M2 Gene

This gene has three domains, one N-terminal extracellular domain (24 codons) recognized by host immune system, one transmembrane domain (19 codons) responsible for ion channel activity, and one cytoplasmic tail (54 codons) interacting with M1 and required for genome packing and formation of virus particles [31].

Residue positions 11, 14, 20, 28, 54, 55, 57, 78, and 86 were avian-human host shift sites found in [5]. Codons 11(2), 14(2), 18(2), 20(2), 43(1), 54(2), 55(3), 57(1), 78(1), 86(2), and 93(2) were important avian-human markers in this study and in [8], plus codons 18(2), 43(1), and 93(2) were new markers, with codon 93(2) carrying a high importance.

Table 4. This table contains the consensus nucleotides (codons) at positions in M1 that have high importance in separating 2009 pandemic H1N1, avian, and swine from human viruses. The single digit in parenthesis is the position within the codon that was selected by Random Forests. The single letter 'a' (for avian) or 'p' (for pandemic 2009) or 's' (for swine) in parenthesis after a position number indicates whether the position is important for avian or 2009 pandemic H1N1 or swine viruses.

Position	30(1)(p)	30(2)(p)	115(1)(a,s)	115(3)(a)	115(3)(p,s)	121(1)(a)	137(1)(a,s)
Avian	gat(D)	gat(D)	gtt(V)	gtt(V)	gtt(V)	act(T)	acg(T)
Human	gat(D)	gat(D)	ata(I)	ata(I)	ata(I)	gct(A)	gct(A)
2009 H1N1	agt(S)	agt(S)	gtg(V)	gtg(V)	gtg(V)	act(T)	aca(T)
Swine	gat(D)	gat(D)	gta(V)	gta(V)	gta(V)	gct(A)	act(T)
Position	142(3)(p)	166(3)(p)	209(1)(p)	214(3)(p)	218(1)(a,s)	218(3)(a,p,s)	239(1)(a)
Avian	gtg(V)	gtg(V)	gct(A)	cag(Q)	aca(T)	aca(T)	gcc(A)
Human	gtg(V)	gtg(V)	gcc(A)	cag(Q)	gcc(A)	gcc(A)	acc(T)
2009 H1N1	gct(A)	gct(A)	act(T)	cat(H)	act(T)	act(T)	gcc(A)
Swine	gtg(V)	gtg(V)	gct(A)	cag(Q)	aca(T)	aca(T)	gcc(A)

Table 5. This table contains the consensus nucleotides (codons) at positions in M2 that have high importance in separating 2009 pandemic H1N1, avian, and swine from human viruses. The single digit in parenthesis is the position within the codon that was selected by Random Forests. The single letter 'a' (for avian) or 'p' (for pandemic 2009) or 's' (for swine) in parenthesis after a position number indicates whether the position is important for avian or 2009 pandemic H1N1 or swine viruses.

Position	11(2)(a,p)	13(2)(p)	14(2)(a)	16(2)(p)	18(2)(a)	20(2)(a,p,s)	28(1)(p)	28(2)(s)	31(2)(p)	31(3)(s)	43(1)(a,p)	43(2)(p)
Avian	acc(T)	aac(N)	gga(G)	gag(E)	aga(R)	agc(S)	att(I)	att(I)	agt(S)	agt(S)	ctt(L)	ctt(L)
Human	atc(I)	aac(N)	gaa(E)	ggg(G)	aga(R)	aac(N)	gtt(V)	gtt(V)	agt(S)	agt(S)	ctt(L)	ctt(L)
2009 H1N1	acc(T)	agc(S)	gaa(E)	gag(E)	aga(R)	agc(S)	att(I)	att(I)	aat(N)	aat(N)	act(T)	act(T)
Swine	acc(T)	aac(N)	gga(G)	gag(E)	aga(R)	aac(N)	gtt(V)	gtt(V)	agc(S)	agc(S)	ctt(L)	ctt(L)
Position	54(2)(a,s)	55(1)(s)	55(3)(a)	57(1)(a,s)	77(2)(p)	78(1)(a,p,s)	79(1)(s)	82(2)(s)	86(2)(a,p,s)	89(1)(s)	93(2)(a,s)	95(2)(s)
Avian	cgc(R)	ctt(L)	ctt(L)	tac(Y)	cgg(R)	cag(Q)	gaa(E)	agt(S)	gtt(V)	ggt(G)	aac(N)	gag(E)
Human	ctc(L)	ttc(F)	ttc(F)	cac(H)	cga(R)	aag(K)	gaa(E)	aat(N)	gct(A)	agt(S)	agc(S)	gag(E)
2009 H1N1	cgc(R)	ttt(F)	ttt(F)	tac(Y)	caa(Q)	cag(Q)	gaa(E)	agt(S)	gtt(V)	ggt(G)	aac(N)	gag(E)
Swine	cgc(R)	ttt(F)	ttt(F)	tac(Y)	cga(R)	cag(Q)	aaa(K)	agt(S)	gtt(V)	ggt(G)	aac(N)	gag(E)

Residue positions 57, 86, and 93 were swine-human shift markers in [32]. Codons 20(2), 28(2), 31(3), 54(2), 55(1), 57(1), 78(1), 79(1), 82(2), 86(2), 89(1), 93(2), and 95(2) were primary swine-human markers in this study and in [8], and in particular codon 78(1) was new and had a much higher importance than the residue positions 57, 86, and 93 discovered in [32]. Similarly, codons 11(2), 13(2), 16(2), 20(2), 28(1), 31(2), 43(1), 43(2), 77(2), 78(1), and 86(2) were major host markers in 2009 pandemic H1N1 in this study and in [8].

In comparison of human with avian, 2009 pandemic H1N1, and swine viruses, there were several synonymous mutation positions in M2 with high importance. They were 53(3) (cgt(R), cga(R)) in avian, 27(3) (gtc(V), gtt(V)) and 50(3) (tgt(C), tgc(C)) in 2009 pandemic H1N1, and 26(3) (ctc(L), ctt(L)) and 68(3) (gtg(V), gta(V)) in swine (**Figure 4**).

Figure 4 indicated that codons 20(2), 78(1), 86(2) were significant in all three categories: 2009 pandemic H1N1, avian, and swine, also codon 20(2) was in the N- terminal

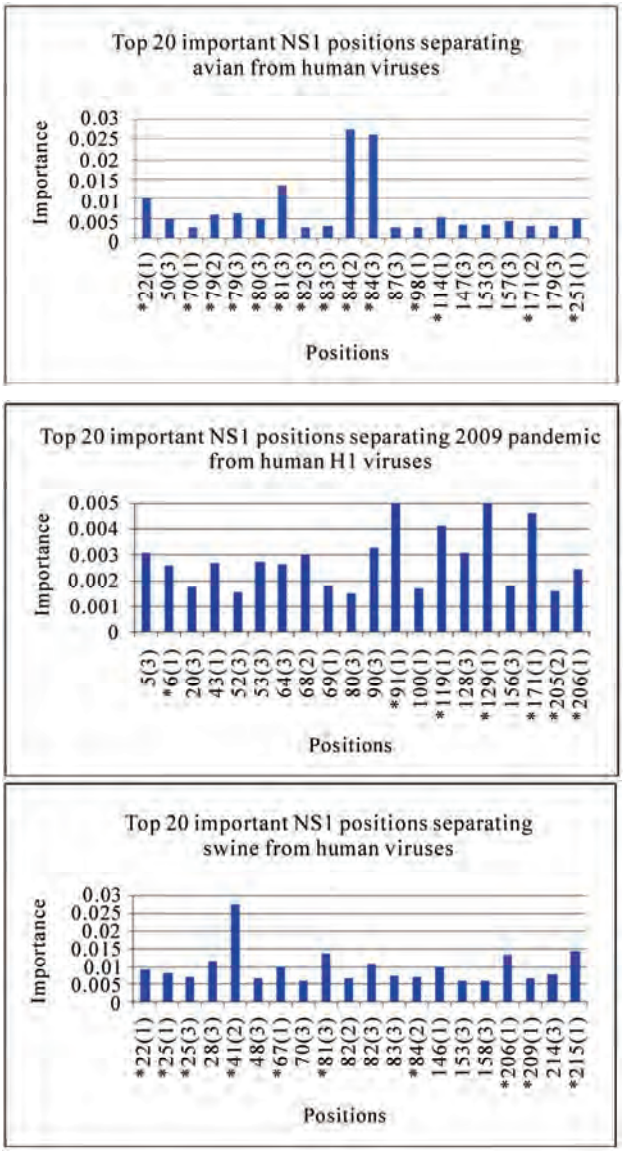

Figure 5. Top important NS1 codon positions in distinguishing avian, human, 2009 pandemic H1N1, and swine viruses. The single digit in parenthesis is the position within the codon that was selected by Random Forests. The positions with an asterisk are the important residue positions identified in [8].

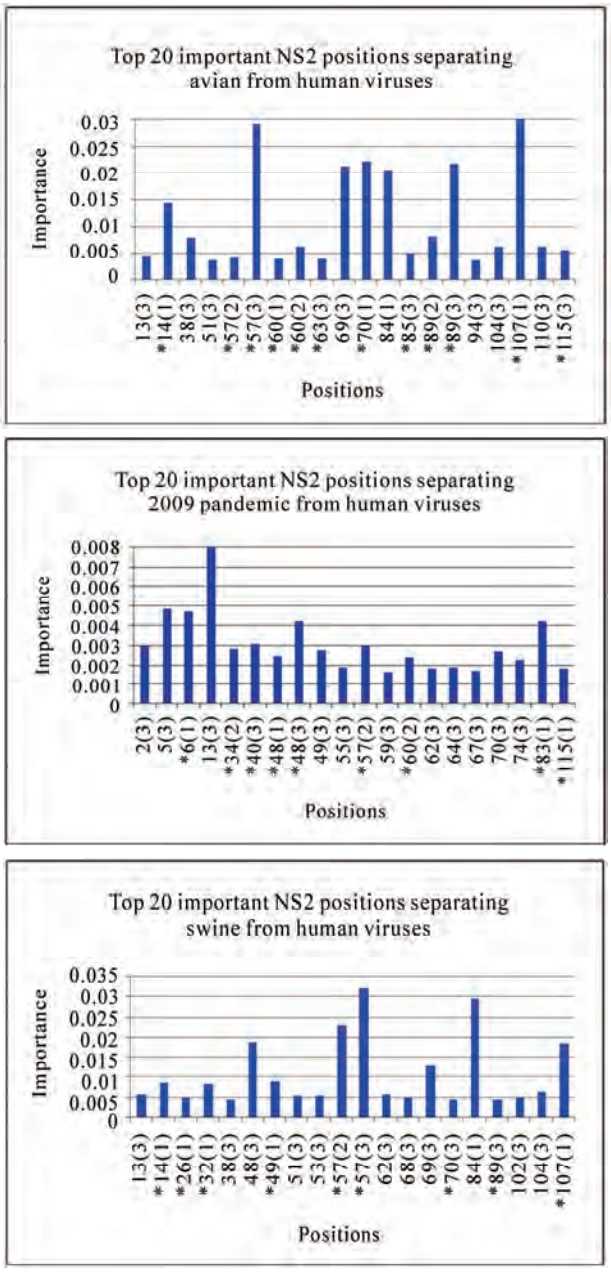

Figure 6. Top important NS2 codon positions in distinguishing avian, human, 2009 pandemic H1N1, and swine viruses. The single digit in parenthesis is the position within the codon that was selected by Random Forests. The positions with an asterisk are the important residue positions identified in [8].

extracellular domain and codons 78(1) and 86(2) in the cytoplasmic tail.

3.2.5. NS1 Gene

NS1 is a multifunctional gene [33]. Its N-terminal region has an RNA-binding domain (codons 1-73) and its C-terminal region (codons 74-237) contains the effector domain that inhibits the maturation and exportation of the host cellular antiviral mRNAs [34].

Residue positions 22, 60, 81, 84, 215, and 227 were avian-human host shift markers in [4]. Codons 22(1), 70(1), 79(2), 79(3), 80(3), 81(3), 84(2), 84(3), 98(1), 114(1), 171(2), and 215(1) were significant avian-human markers in this study and in [8] (**Figure 5**). Furthermore, our analysis selected two positions 2 and 3 within codon 84 with a much higher importance than the previous residue positions 22, 60, 81, 215, and 227 discovered in [4]. Another codon had two positions selected at 79(2)

Table 6. This table contains the consensus nucleotides (codons) at positions in NS1 that have high importance in separating 2009 pandemic H1N1, avian, and swine from human viruses. The single digit in parenthesis is the position within the codon that was selected by Random Forests. The single letter 'a' (for avian) or 'p' (for pandemic 2009) or 's' (for swine) in parenthesis after a position number indicates whether the position is important for avian or 2009 pandemic H1N1 or swine viruses.

Position	6(1)(p)	22(1)(a,s)	25(1)(s)	25(3)(s)	41(2)(s)	67(1)(s)	70(1)(a)	79(2)(a)	79(3)(a)	80(3)(a)	81(3)(a,s)	82(3)(a)
Avian	gtg(V)	ttt(F)	caa(Q)	caa(Q)	aag(K)	cgg(R)	gag(E)	atg(M)	atg(M)	act(T)	att(I)	gct(A)
Human	gtg(V)	gtt(V)	caa(Q)	caa(Q)	aag(K)	agg(R)	aag(K)	atg(M)	atg(M)	acc(T)	atg(M)	gcc(A)
2009 H1N1	atg(M)	ttt(F)	aat(N)	aat(N)	aag(K)	tgg(W)	aaa(K)	atg(M)	atg(M)	aca(T)	att(I)	gca(A)
Swine	gtg(V)	ttt(F)	aat(N)	aat(N)	aag(K)	tgg(W)	aaa(K)	atg(M)	atg(M)	acc(T)	att(I)	gca(A)
Position	84(2)(a,s)	84(3)(a)	91(1)(p)	98(1)(a)	114(1)(a)	119(1)(p)	129(1)(p)	171(1)(p)	171(2)(a)	205(2)(p)	206(1)(p,s)	209(1)(s)
Avian	gtg(V)	gtg(V)	act(T)	atg(M)	tcc(S)	atg(M)	ata(I)	gat(D)	gat(D)	agc(S)	agt(S)	gat(D)
Human	aca(T)	aca(T)	act(T)	ttg(L)	cct(P)	atg(M)	atg(M)	att(I)	att(I)	agc(S)	agt(S)	aat(N)
2009 H1N1	gta(V)	gta(V)	tct(S)	atg(M)	cct(P)	ttg(L)	gta(V)	tat(Y)	tat(Y)	aac(N)	tgt(C)	aat(N)
Swine	gta(V)	gta(V)	gct(A)	atg(M)	tct(S)	atg(M)	ata(I)	gat(D)	gat(D)	agc(S)	cgt(R)	gat(D)

Table 7. This table contains the consensus nucleotides (codons) at positions in NS2 that have high importance in separating 2009 pandemic H1N1, avian, and swine from human viruses. The single digit in parenthesis is the position within the codon that was selected by Random Forests. The single letter 'a' (for avian) or 'p' (for pandemic 2009) or 's' (for swine) in parenthesis after a position number indicates whether the position is important for avian or 2009 pandemic H1N1 or swine viruses.

Position	6(1)(p)	14(1)(a,s)	26(1)(s)	32(1)(s)	34(2)(p)	40(3)(p)	48(1)(p)	48(3)(p)	49(1)(s)	57(2)(a,p,s)	57(3)(a,s)	60(1)(a)
Avian	gtg(V)	atg(M)	gag(E)	ata(I)	cag(Q)	ctc(L)	gca(A)	gca(A)	gtg(V)	tcc(S)	tcc(S)	agc(S)
Human	gtg(V)	ttg(L)	gag(E)	ata(I)	cag(Q)	atc(I)	gca(A)	gca(A)	gta(V)	tta(L)	tta(L)	aac(N)
2009 H1N1	atg(M)	atg(M)	gag(E)	gta(V)	cgg(R)	ata(I)	act(T)	act(T)	gtg(V)	tac(Y)	tac(Y)	agc(S)
Swine	gtg(V)	atg(M)	gag(E)	gta(V)	cag(Q)	atc(I)	gcc(A)	gcc(A)	gta(V)	tac(Y)	tac(Y)	aac(N)
Position	60(2)(a,p)	63(3)(a)	70(1)(a)	70(3)(s)	83(1)(p)	85(3)(a)	89(2)(a)	89(3)(a,s)	107(1)(a,s)	115(1)(p)	115(3)(a)	
Avian	agc(S)	gga(G)	agt(S)	agt(S)	gtg(V)	cat(H)	att(I)	att(I)	ctt(L)	act(T)	act(T)	
Human	aac(N)	gga(G)	ggt(G)	ggt(G)	gtg(V)	cac(H)	aca(T)	aca(T)	ttt(F)	act(T)	act(T)	
2009 H1N1	agc(S)	gaa(E)	gga(G)	gga(G)	atg(M)	cac(H)	gcg(A)	gcg(A)	ctt(L)	gct(A)	gct(A)	
Swine	aac(N)	gaa(E)	ggt(G)	ggt(G)	gtg(V)	cac(H)	atg(M)	atg(M)	ctt(L)	act(T)	act(T)	

and 79(3) as well. Both of these double selected codons were located in the C-terminal region.

The results of this study and [8] suggested that codons 22(1), 25(1), 25(3), 41(2), 67(1), 81(3), 84(2), 206(1), 209(1), and 215(1) were key swine-human markers and codons 6(1), 91(1), 100(1), 119(1), 128(3), 129(1), 171(1), 205(2), and 206(1) were essential host markers in 2009 pandemic (**Figure 5**).

In comparison of human with avian, 2009 pandemic H1N1, and swine viruses, there were several synonymous mutation positions in NS1 with high importance. They were 157(3) (gtg(V)), (gtt(V)) in avian, 5(3) (acc(T)), (act(T)), 68(3) (atc(I)), (att(I)), 90(3) (ctt(L)), cta(L)), and 128(3) (ata(I)), (atc(I)) in 2009 pandemic H1N1, and 146(1) (cta(L)), (tta(L)) in swine (**Figure 5**).

3.2.6. NS2 Gene

Residue positions 60, 70, and 107 were avian-human host shift markers in [4]. Codons 14(1), 57(2), 57(3), 60(1), 60(2), 63(3), 70(1), 85(3), 89(2), 89(3), 107(1), and 115(3) were avian-human markers in this study and

in [8] with codons 57, 60, and 89 being selected twice. Codons 57(3) and 89(3) were not only new markers but also had a very high importance, comparable to that of positions 70 and 107 in [4] (**Figure 6**).

Codons 14(1), 26(1), 32(1), 49(1), 57(2), 57(3), 70(3), 89(3), and 107(1) were important swine-human markers in this study and in [8] with codon 57 being selected twice. The same analysis also identified codons 16(1), 34(2), 40(3), 48(1), 48(3), 57(2), 60(2), 83(1), and 115(1) as important host markers in 2009 pandemic H1N1, with codon 48 being selected twice.

Notably, there was one codon position 57(2) that was important in all three categories: avian, 2009 pandemic H1N1, and swine, and it was in the M1 binding domain (codons 59-116) [5].

In comparison of human with avian, 2009 pandemic H1N1, and swine viruses, there were several synonymous mutation positions in NS2 with high importance. They were 69(3) (ttg(L), cta(L)) and 84(1) (cga(R), aga(R)) in avian, 5(3) (acc(T), act(T)) and 13(3) (ctt(L), cta(L)) in 2009 pandemic H1N1, and 48(3) (gcc(A), gca(A)) and 84(1) (cgg(R), aga(R)) in swine (**Figure 6**). Furthermore, codons 84(1) and 13(3) received a very high importance in both avian and swine and in 2009 pandemic H1N1, respectively. Codon 84(1) was in the M1 binding domain.

3.2.7. NP Gene

Residue positions 16, 33, 61, 100, 136, 214, 283, 305, 313, 357, 375, and 423 were avian-human host shift markers in [4]. Codons 16(2), 61(1), 100(1), 100(2), 283(2), 305(1), 305(3), 313(2), 357(1), and 455(3) were significant for discriminating avian and human viruses in this study and in [8] with codons 100 and 305 being chosen twice (**Figure 7**).

In this study and in [8], codons 16(2), 61(1), 214(2), 283(2), 289(1), 313(2), 372(3), 442(1), and 455(3) were main swine-human markers, and similarly codons 53(3), 289(1), 313(1), 316(3), 430(2), and 444(1) were vital host markers in 2009 pandemic H1N1.

In comparison of human with avian, 2009 pandemic H1N1, and swine viruses, there were several synonymous mutation positions in NP with high importance. They were 108(3) (ctg(L), ctc(L)) and 155(3) (gtg(V), gtt(V)) in avian, 177(3) (ggt(G), gga(G)), 182(3) (gcg(A), gca(A)), and 363(3) (gtc(V), gta(V)) in 2009 pandemic H1N1, and 3(3) (tct(S), tcc(S)), 94(3) (gga(G), ggg(G)), and 376(3) (tcc(S), tca(S)) in swine (**Figure 7**).

NP has three regions (codons 1-160, 256-340 and 340–498) that bind to PB1 and PB2 [35], and codons 108(3) and 155(3) in avian and codons 3(3), 94(3), and 376(3) in swine were in two of these three regions. One region, codons 360-374, in NP of 2009 pandemic H1N1 was deemed extremely important for host range restriction and is a common feature of pandemic viruses [36], and codon 363(3) carrying a synonymous mutation in 2009 pandemic H1N1 was in this region.

3.2.8. PA Gene

Residue positions 28, 55, 57, 65, 66, 100, 225, 268, 321, 337, 356, 382, 400, 404, 409, 421, and 552 were avian-human host shift markers in [4], whereas this study and [8] indicated that codons 55(1), 56(1), 225(1), 337(1), 337(3), 421(2), and 552(2) were important avian-human markers, with codon 337 being chosen twice (**Figure 8**).

Residue positions 268 and 552 were swine-human markers uncovered in [32]. Codons 225(1), 268(1), 272(1), 337(1), 421(2), and 552(2) were key swine-human markers in our analysis and in [8] with codon 337(1) having a similar importance as position 268. Also codons 85(2), 186(1), 275(2), 277(1), and 388(3) were crucial for classifying 2009 pandemic H1N1 and human viruses in this study and in [8].

The N-terminal domain of PA (codons 1-256) harbors several functional domains, including an endonuclease active site with a putative active site motif, two putative nuclear transport motifs (codons 124-139 (NLS1) and codons 186-247 (NLS2)), and a proteolytic domain that can induce generalized proteolysis of both viral and host proteins. The C-terminal domain of PA (codons 257-716) binds to PB1 for complex formation and nuclear transport [37].

In comparison of human with avian, 2009 pandemic H1N1, and swine viruses, there were several synonymous mutation positions in PA with high importance. They were 106(3) (ctc(L), cta(L)), 138(3) (ata(I), att(I)), and 270(3) (tta(L), ctt(L)) in avian, 44(3) (gtt(V) , gta(V)), 173(3) (act(T), acc(T)), and 526(3) (tca(S), tct(S)) in 2009 pandemic H1N1, and 106(3) (ctt(L), cta(L)), 290(3) (tta(L), ttg(L)), and 345(3) (cta(L), ttg(L)) in swine (**Figure 8**). Codon 138(3) was in the first putative nuclear localization signal (NLS1) region, and codons 270(3) and 526(3) were in the C-terminal domain of PA.

3.2.9. PB1 Gene

Residue position 336 was the only avian-human host shift markers in [4]. Codons 327(2), 336(1), 361(3), 401(3), and 576(3) were important host markers in avian in this study and in [8] with codons 361(1), 401(3), and 576(3) having a much higher importance than position 336 (**Figure 9**).

The analysis of this study and [8] suggested that codons 327(2), 339(3), and 638(3) were important swine-human markers, and codons 12(1), 175(1), 212(1), 339(3), 364(1), 435(2), 618(3), 638(3), 728(1), and 728(3) were vital for classifying 2009 pandemic H1N1 and human viruses with codon 728 being selected twice.

Table 8. This table contains the consensus nucleotides (codons) at positions in NP that have high importance in separating 2009 pandemic H1N1, avian, and swine from human viruses. The single digit in parenthesis is the position within the codon that was selected by Random Forests. The single letter 'a' (for avian) or 'p' (for pandemic 2009) or 's' (for swine) in parenthesis after a position number indicates whether the position is important for avian or 2009 pandemic H1N1 or swine viruses.

Position	16(2)(a,s)	53(3)(p)	61(1)(a,s)	100(1)(a)	100(2)(a)	214(2)(s)	283(2)(a,s)	289(1)(p,s)	305(1)(a)	305(3)(a)
Avian	ggt(G)	gaa(E)	ata(I)	aga(R)	aga(R)	aga(R)	ctt(L)	tat(Y)	cgt(R)	cgt(R)
Human	gat(D)	gaa(E)	ttg(L)	gta(V)	gta(V)	aaa(K)	cct(P)	tac(Y)	aaa(K)	aaa(K)
2009 H1N1	ggt(G)	gat(D)	ata(I)	ata(I)	ata(I)	agg(R)	ctt(L)	cat(H)	aaa(K)	aaa(K)
Swine	ggt(G)	gag(E)	ata(I)	gta(V)	gta(V)	agg(R)	ctt(L)	cat(H)	aaa(K)	aaa(K)
Position	313(1)(p)	313(2)(a,s)	316(3)(p)	355(3)(a)	357(1)(a)	372(3)(s)	430(2)(p)	442(1)(s)	444(1)(p)	455(3)(s)
Avian	ttc(F)	ttc(F)	att(I)	aga(R)	caa(Q)	gaa(E)	aca(T)	act(T)	atc(I)	gat(D)
Human	tac(Y)	tac(Y)	atc(I)	cgg(R)	aaa(K)	gat(D)	act(T)	gca(A)	atc(I)	gaa(E)
2009 H1N1	gtc(V)	gtc(V)	atg(M)	aga(R)	aag(K)	gaa(E)	agc(S)	aca(T)	gtt(V)	gat(D)
Swine	ttc(F)	ttc(F)	atc(I)	aga(R)	aag(K)	gaa(E)	act(T)	act(T)	att(I)	gat(D)

Table 9. This table contains the consensus nucleotides (codons) at positions in PA that have high importance in separating 2009 pandemic H1N1, avian, and swine from human viruses. The single digit in parenthesis is the position within the codon that was selected by Random Forests. The single letter 'a' (for avian) or 'p' (for pandemic 2009) or 's' (for swine) in parenthesis after a position number indicates whether the position is important for avian or 2009 pandemic H1N1 or swine viruses.

Position	55(1)(a)	65(1)(a)	85(2)(p)	186(1)(p)	225(1)(a,s)	268(1)(s)	272(1)(s)
Avian	gat(D)	tct(S)	aca(T)	ggt(G)	agc(S)	ctc(L)	gat(D)
Human	aat(N)	ctt(L)	aca(T)	ggc(G)	tgc(C)	atc(I)	aat(N)
2009 H1N1	gac(D)	tct(S)	atc(I)	agt(S)	agc(S)	ctc(L)	gat(D)
Swine	gat(D)	tct(S)	aca(T)	ggt(G)	agc(S)	ctc(L)	gat(D)
Position	275(2)(p)	277(1)(p)	337(1)(a,s)	337(3)(a)	388(3)(p)	421(2)(a,s)	552(2)(a,s)
Avian	cct(P)	tct(S)	gct(A)	gct(A)	agc(S)	agt(S)	act(T)
Human	cct(P)	tat(Y)	tca(S)	tca(S)	agc(S)	atc(I)	agt(S)
2009 H1N1	ctt(L)	cat(H)	gct(A)	gct(A)	gga(G)	agc(S)	act(T)
Swine	ccc(P)	tct(S)	gct(A)	gct(A)	agt(S)	agc(S)	act(T)

PB1 contains several functional domains, including cRNA binding domain (codons 1-139 and 267-493), vRNA binding domain (codons 1-83 and 233-249 and 494-758), NLS region (codons 180-195 and 202-252), PA binding domain (codons 1-25), and PB2 binding domain (codons 600-757) [5].

In comparison of human with avian, 2009 pandemic H1N1, and swine viruses, there were several synonymous mutation positions in PB1 with high importance. They were 148(3) (gag(E), gaa(E)), 322(3) (ata(I), att(I)), and 454(3) (ccg(P), cca(P)) in avian, 62(3) (ggt(G) , ggg(G)), 167(1) (tta(L), ctc(L)), 543(3) (acg(T), aca(T)), and 601(3) (ata(I), atc(I)) in 2009 pandemic H1N1, 60(3) (gag(E), gaa(E)) and 726(3) (gca(A), gcc(A)) in swine (**Figure 9**). It was striking that codons 322(3), 167(1), and 60(3), each carrying a synonymous mutation, had the highest importance in 2009 pandemic H1N1, avian, and swine, respectively. Many of these significant codons carrying synonymous mutations were located in the functional domains of PB1.

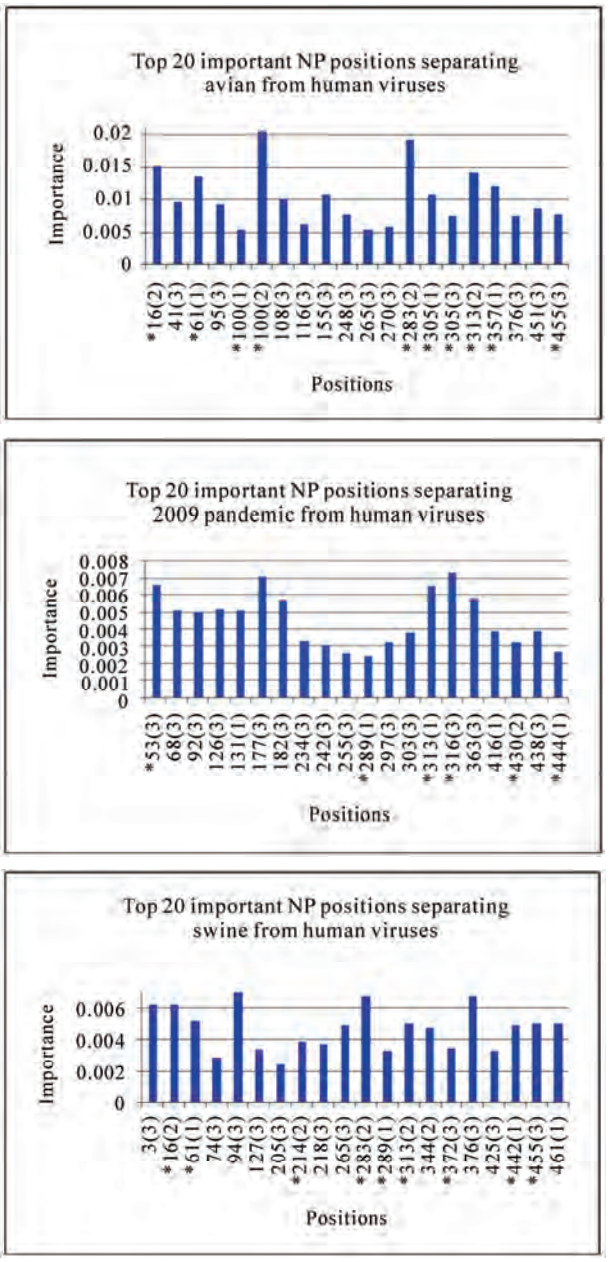

Figure 7. Top important NP codon positions in distinguishing avian, human, 2009 pandemic H1N1, and swine viruses. The single digit in parenthesis is the position within the codon that was selected by Random Forests. The positions with an asterisk are the important residue positions identified in [8].

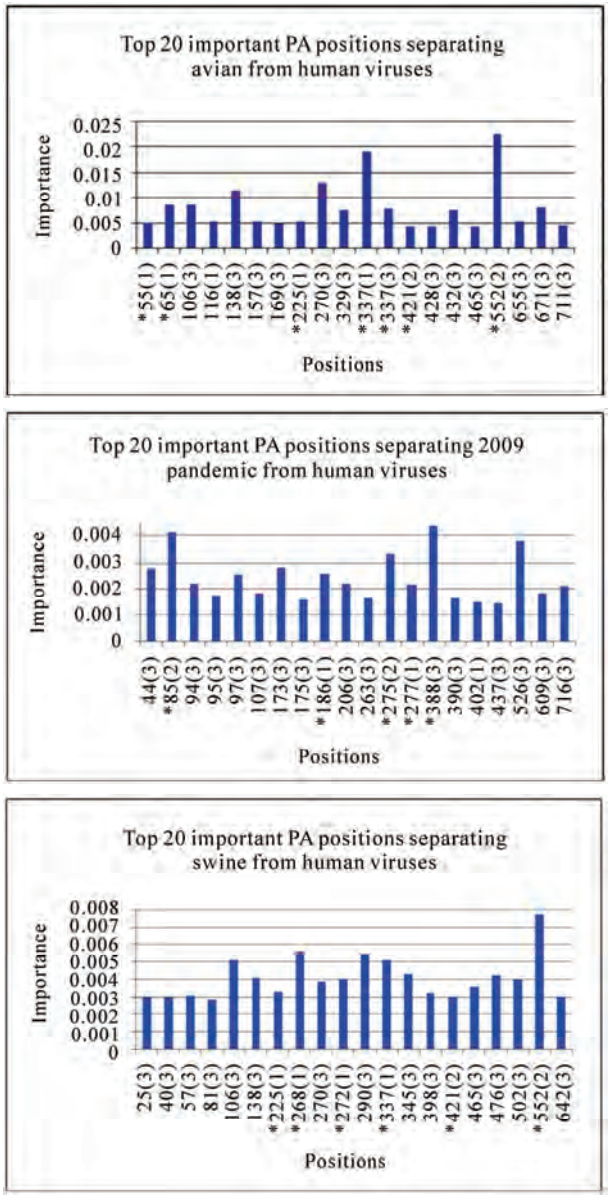

Figure 8. Top important PA codon positions in distinguishing avian, human, 2009 pandemic H1N1, and swine viruses. The single digit in parenthesis is the position within the codon that was selected by Random Forests. The positions with an asterisk are the important residue positions identified in [8].

3.2.10. PB2 Gene

Amino acid positions 9, 44, 64, 81, 105, 199, 271, 292, 368, 475, 567, 588, 613, 627, 661, 674, and 702 were avian-human host shift markers in [4]. Codons 81(2), 105(2), 199(1), 271(1), 475(1), 588(2), 627(1), 674(1), and 674(3) were significant avian-human markers in this study and in [8]. In particular, our analysis revealed codon 199(1) as equally essential as codon 627(1), a well-known host marker (**Figure 10**).

Residue position 44 was a swine-human marker in [32]. Our analysis and [8] implied codons 81(2), 199(1), 567(1), 613(1), and 674(1) were as equally significant as position 44. In fact, codon 674(1) received the highest importance in swine. Moreover, codons 54(2), 225(1), 315(3), 559(2), 591(2), and 645(1) were key host markers in 2009 pandemic H1N1.

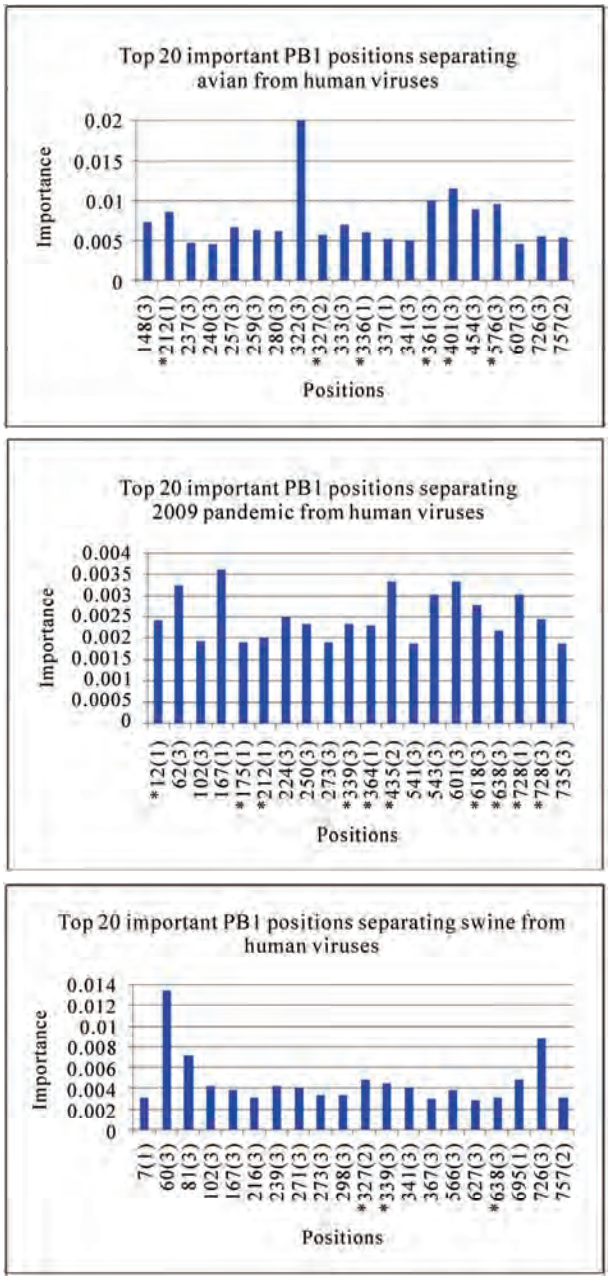

Figure 9. Top important PB1 codon positions in distinguishing avian, human, 2009 pandemic H1N1, and swine viruses. The single digit in parenthesis is the position within the codon that was selected by Random Forests. The positions with an asterisk are the important residue positions identified in [8].

In comparison of human with avian, 2009 pandemic H1N1, and swine viruses, there were several synonymous mutation positions in PB2 with high importance. They were 373(3) (att(I), ata(I)), 598(3) (aca(T), act(T)), and 604(3) (cgt(R), aga(R)) in avian, 142(1) (agg(R), cgc(R)), 142(3) (agg(R), cgc(R)), 221(3) (gcc(A), gct(A)), 553(3) (ata(I),atc(I)), and 664(1) (cga(R), aga(R)) in 2009 pandemic H1N1, and 169(3) (cca(P), ccc(P)) and 527(1) (ttg(L), ctg(L)) in swine (**Figure 10**). There was one codon 142 carrying two synonymous mutation positions, both were selected as important host markers in 2009 pandemic H1N1. Codons 221(3), 553(3), and 664(1) were the top three important ones in 2009 pandemic H1N1. The PB2-NP binding domain contains codons 1-269 and 580-683, and the PB2-PB1 binding domain contains codons 51-259 and 580-759 [5]. Codons 142(1), 142(3), 169(3), 221(3), 598(3), 604(3), and 664(1) were in the PB2-PB1 and PB2-NP binding domains.

In addition to codon 142 in 2009 pandemic H1N1, there was one codon 674 in avian (**Figure 10**) that included two significant positions. The likelihood to affect the host shifts by any potential mutations at these multiple selected codons might be higher than any other codons.

4. DISCUSSION

In the current study, a comprehensive analysis of the nucleotide sequences of ten genes of influenza viruses was performed to discover a catalogue of host markers, illustrating the complex and systematic nature of host adaptation. One of the benefits of using nucleotide sequences was their capability to detect synonymous mutations that were essential for host switches. These synonymous mutations could not be found at the amino acid level. Moreover, the nucleotide markers could pinpoint exactly where the important positions were within a codon.

Our investigation also revealed several codons in ten genes of 2009 pandemic H1N1, avian, and swine viruses that contained two or even three important positions selected by Random Forests for host shifts, thus providing extra and finer information about the host adaptation. These codons might have a higher probability to affect the host switch than those codons containing only a single important position.

Amino acid mutation E627K in PB2 is a well-known determinant for adaptation from avian to human hosts. The nucleotide marker information uncovered in this study suggested that generally it was codon gaa to encode E in avian viruses and codon aag to encode K in human viruses. Furthermore, it was the first position within codon 627 that was essential for the discrimination of avian and human viruses, although there was another possibility in the third position within codon 627. The SR polymorphism found in [10] contained two positions 590 and 591. Our analysis demonstrated that it was the second position within codon 591 that was really vital for the separation of 2009 pandemic H1N1 and human viruses (**Table 11**).

Table 10. This table contains the consensus nucleotides (codons) at positions in PB1 that have high importance in separating 2009 pandemic H1N1, avian, and swine from human viruses. The single digit in parenthesis is the position within the codon that was selected by Random Forests. The single letter 'a' (for avian) or 'p' (for pandemic 2009) or 's' (for swine) in parenthesis after a position number indicates whether the position is important for avian or 2009 pandemic H1N1 or swine viruses.

Position	12(1)(p)	175(1)(p)	212(1)(a,p)	327(2)(a,s)	336(1)(a)	339(3)(p,s)	361(3)(a)	364(1)(p)
Avian	gtt(V)	gat(D)	ctg(L)	aga(R)	gtc(V)	att(I)	agc(S)	ctt(L)
Human	gtt(V)	gat(D)	gtg(V)	aaa(K)	atc(I)	atc(I)	aga(R)	ctc(L)
2009 H1N1	att(I)	aac(N)	ctg(L)	aga(R)	atc(I)	atg(M)	aga(R)	att(I)
Swine	gtg(V)	gat(D)	ttg(L)	aga(R)	gtt(V)	att(I)	agc(S)	ctc(L)
Position	401(3)(a)	435(2)(p)	576(3)(a)	618(3)(p)	638(3)(p,s)	728(1)(p)	728(3)(p)	
Avian	gcc(A)	aca(T)	ctg(L)	gaa(E)	gag(E)	att(I)	att(I)	
Human	gca(A)	aca(T)	cta(L)	gag(E)	gag(E)	att(I)	att(I)	
2009 H1N1	gca(A)	ata(I)	tta(L)	gat(D)	gat(D)	gtc(V)	gtc(V)	
Swine	gca(A)	aca(T)	cta(L)	gaa(E)	gaa(E)	att(I)	att(I)	

Table 11. This table contains the consensus nucleotides (codons) at positions in M1 that have high importance in separating 2009 pandemic H1N1, avian, and swine from human viruses. The single digit in parenthesis is the position within the codon that was selected by Random Forests. The single letter 'a' (for avian) or 'p' (for pandemic 2009) or 's' (for swine) in parenthesis after a position number indicates whether the position is important for avian or 2009 pandemic H1N1 or swine viruses.

Position	44(1)(s)	54(2)(p)	81(2)(a,s)	105(2)(a)	199(1)(a,s)	225(1)(p)	271(1)(a)	315(3)(p)	475(1)(a)
Avian	gca(A)	aaa(K)	aca(T)	aca(T)	gct(A)	agc(S)	aca(T)	atg(M)	ctg(L)
Human	tca(S)	aaa(K)	atg(M)	gtg(V)	tct(S)	agc(S)	gca(A)	atg(M)	atg(M)
2009 H1N1	gca(A)	aga(R)	aca(T)	aca(T)	gct(A)	ggc(G)	gca(A)	ata(I)	ctg(L)
Swine	gca(A)	aaa(K)	aca(T)	aca(T)	gct(A)	agc(S)	aca(T)	atg(M)	ctg(L)
Position	559(2)(p)	567(1)(s)	588(2)(a)	591(2)(p)	613(1)(s)	627(1)(a)	645(1)(p)	674(1)(a,s)	674(3)(a)
Avian	act(T)	gac(D)	gcc(A)	caa(Q)	gtt(V)	gaa(E)	atg(M)	gca(A)	gca(A)
Human	gct(A)	aat(N)	att(I)	caa(Q)	acc(T)	aag(K)	atg(M)	act(T)	act(T)
2009 H1N1	att(I)	gat(D)	acc(T)	cgg(R)	gtc(V)	gaa(E)	ttg(L)	gca(A)	gca(A)
Swine	act(T)	gac(D)	gcc(A)	caa(Q)	gtc(V)	gaa(E)	atg(M)	gca(A)	gca(A)

In [8], a set of residue positions in the PB2 protein including the SR polymorphism found in [10] were identified as host markers in 2009 pandemic H1N1. Codons 54(2), 225(1), 315(3), 559(2), 591(2), and 645(1) in PB2 of 2009 pandemic H1N1 were concluded as essential host markers both in this study and in [8]. Furthermore, the current study found three new codons 221(3), 553(3), and 664(1) that were the top three significant codons in 2009 pandemic H1N1. They could augment the repertoire of existing host markers in PB2 that might play compensatory roles, as the SR polymorphism, in the viral replication and transmission of 2009 pandemic H1N1. Additionally, the new nucleotide markers carrying synonymous mutations found in NP, PA, and PB1, along with those in PB2 would provide further information for the life cycle of 2009 pandemic H1N1. Also, codons 728(1), 728(3) in PB1, carrying a non-synonymous mutation, and codons 142(1), 142(3) in PB2, carrying a synonymous mutation, were of special interest in this regard as multiple selected markers within the same codon.

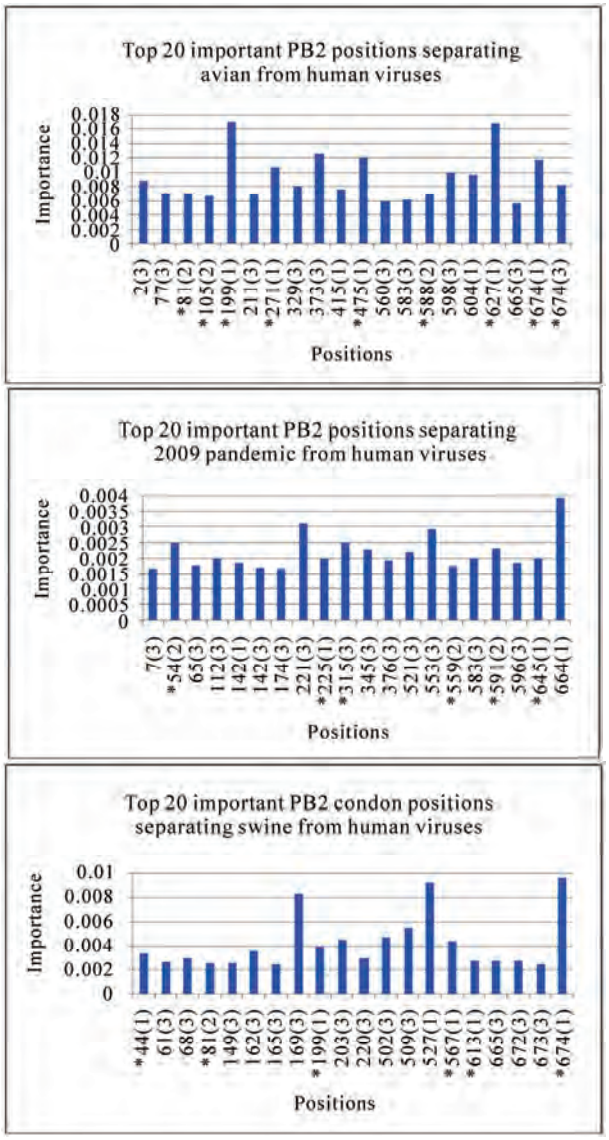

Figure 10. Top important PB2 codon positions in distinguishing avian, human, 2009 pandemic H1N1, and swine viruses. The single digit in parenthesis is the position within the codon that was selected by Random Forests. The positions with an asterisk are the important residue positions identified in [8].

5. CONCLUSION

As an extension of our earlier work in [8], Random Forests were employed to discover a collection of nucleotide positions, served as host markers, in ten genes of influenza that could separate 2009 pandemic H1N1, avian, and swine viruses from human viruses with high confidence. Our results indicated that two or even three important positions could coexist within a single codon, i.e., multiple nucleotide markers might be present within one codon, and the different importance values of these positions could further differentiate these multiple markers within a codon. The nucleotide markers uncovered in the current study provided a complete genomic view of host adaptation of influenza viruses. They verified and enriched the known amino acid host markers and generated new information about the adaptation of zoonotic viruses to humans, thus offering a larger set of finer potential sites for further experimental verification to elucidate their biological functions in cellular processes.

6. ACKNOWLEDGEMENTS

We thank Houghton College for its financial support.

REFERENCES

[1] Chen, G.W., Chang, S.C., Mok, C.K., Lo, Y.L., Kung, Y.N., *et al.* (2006) Genomic signatures of human versus avian influenza A viruses. *Emerging Infectious Diseases*, **12(9)**, 1353-1360.

[2] Chen, G.W. and Shih, S.R. (2009) Genomic signatures of influenza A pandemic (H1N1) 2009. *Emerging Infectious Diseases*, **15(12)**, 1897-1903.

[3] Pan, C., Cheung, B., Tan, S., Li, C., Li, L., *et al.* (2010) Genomic signature and mutation trend analysis of pandemic (H1N1) 2009. *Influenza A Virusus PLoS One*, **5(3)**, e9549.

[4] Miotto, O., Heiny, A., Tan, T.W., August, J.T. and Brusic, V. (2008) Identification of human-to-human transmissibility factors in PB2 proteins of influenza A by large-scale mutual information analysis. *BMC Bioinformatics.*, **9(Suppl 1)**, S18.

[5] Miotto, O., Heiny, A.T., Albrecht, R., García-Sastre, A., Tan, T.W., August, J.T. and Brusic, V. (2010) Complete-proteome mapping of human influenza A adaptive mutations: Implications for human transmissibility of zoonotic strains. *PLoS One*, **5(2)**, e9025.

[6] Finkelstein, D.B., Mukatira, S., Mehta, P.K., Obenauer, J.C., Su, X., Webster, R.G. and Naeve, C.W. (2007) Persistent host markers in pandemic and H5N1 influenza viruses. *Journal of Virology*, **81(19)**, 10292-10299.

[7] Allen, J.E., Gardner, S.N., Vitalis, E.A. and Slezak, T.R. (2009) Conserved amino acid markers from past influenza pandemic strains. *BMC Microbiology*, **9(1)**, 77.

[8] Hu, W. (2010) Novel host markers in the 2009 pandemic H1N1 influenza A virus. *Journal of Biomedical Science and Engineering*, **3(6)**, 584-601.

[9] Herfst, S., Chutinimitkul, S., Ye, J., de Wit, E., Munster, V.J., Schrauwen, E.J., Bestebroer, T.M., Jonges, M., Meijer, A., Koopmans, M., Rimmelzwaan, G.F., Osterhaus, A.D., Perez, D.R. and Fouchier, R.A. (2010) Introduction of virulence markers in PB2 of pandemic swine-origin influenza virus does not result in enhanced virulence or transmission, *Journal of Virology*, **84(8)**, 3752-3758.

[10] Mehle, A. and Doudna, J.A. (2009) Adaptive strategies of the influenza virus polymerase for replication in humans. Proceedings of National Academic Science in USA., **106(50)**, 21312-21316.

[11] Alexande,r S., Benjamin, G., Gustavo, P., Ian Lipkin, W. and Raul R. (2010) Host dependent evolutionary patterns

and the origin of 2009 H1N1 pandemic influenza. *PLoS Current Influenza*, RRN1147.

[12] Rabadan, R., Levine, A.J. and Robins, H. (2006) Comparison of avian and human influenza A viruses reveals a mutational bias on the viral genomes. *Journal of Virology*, **80(23)**, 11887-11891.

[13] Microbiol Biotechnol, J. (2010) Comparative study of the nucleotide bias between the novel H1N1 and H5N1 subtypes of influenza A viruses using bioinformatics techniques. *Ahn I, Son HS. Bioinformatics Team*, **20(1)**, 63-70.

[14] Valli, M.B., Meschi, S., Selleri, M., Zaccaro, P., Ippolito, G., Capobianchi, M.R. and Menzo, S. (2010) Evolutionary pattern of pandemic influenza (H1N1) 2009 virus in the late phases of the 2009 pandemic. *PLoS Current Influenza*, RRN1149.

[15] Ramakrishnan, M.A., Gramer, M.R., Goyal, S.M. and Sreevatsan, S. (2009) A Serine12Stop mutation in PB1-F2 of the 2009 pandemic (H1N1) influenza A: a possible reason for its enhanced transmission and pathogenicity to humans. *Journal of Veterinary Science*, **10(4)**, 349-351.

[16] Katoh, K., Kuma, K., Toh, H. and Miyata, T. (2005) MAFFT version 5: improvement in accuracy of multiple sequence alignment. *Nucleic Acid Research*, 33, 511-518.

[17] Breiman, L. (2001) Random Forests, Machine Learning, **45(1)**, 5-32.

[18] Díaz-Uriarte, R. and Alvarez de Andrés, S. (2006) Gene selection and classification of microarray data using random forest. *BMC Bioinformatics*, **7(3)**, 3-16.

[19] Archer, K.J. and Kimes, R.V. (2008) Empirical characterization of random forest variable importance measures. *Computational Statistics and Data Analysis*, **52(4)**, 2249-2260.

[20] Reif, D.M., Motsinger, A.A., McKinney, B.A., Crowe, J.E. and Moore, J.H. (2006) Feature selection using a random forests classifier for the integrated analysis of multiple data types. *Proceedings of 2006 IEEE Symposium on Computational Intelligence and Bioinformatics and Computational Biology*, CIBCB '06.

[21] Granittoa, P.M., Furlanellob, C., Biasiolia, F. and Gasperia, F. (2006) Recursive feature elimination with random forest for PTR-MS analysis of agroindustrial products. *Chemometrics and Intelligent Laboratory Systems*, **83(2)**, 83-90.

[22] Menze1, B.H., Kelm, B.M., Masuch, R., Himmelreich, U., Bachert, P., Petrich, W. and Hamprecht, F.A. (2009) A comparison of random forest and its Gini importance with standard chemometric methods for the feature selection and classification of spectral data. *BMC Bioinformatics*, **10**, 213.

[23] Gao, D., Zhang, Y.-X. and Zhao, Y.-H. (2009) Random forest algorithm for classification of multi-wavelength data. *Research in Astronomy and Astrophysics*, **9(2)**, 220-226.

[24] Hu, W. (2009) Identifying predictive markers of chemosensitivity of breast cancer with random forests. *Journal of Biomedical Science and Engineering*, **3(1)**, 59-64.

[25] Gavin, J.D., Smith, D.V., Justin, B., Samantha, J.L., *et al.* (2009) Origins and evolutionary genomics of the 2009 swine-origin H1N1 influenza A epidemic. *Nature*, **459(7250)**, 1122-1125.

[26] Hu, W. (2010) Quantifying the effects of mutations on receptor binding specificity of influenza viruses. *Journal of Biomedical Science and Engineering*, **3(3)**, 227-240.

[27] KováccaronOVá, A., Ruttkay-Nedecký, G., HaverlíK1, I.K. and Janecccaronek, S. (2002) Sequence similarities and evolutionary relationships of influenza virus A hemagglutinins. *Virus Genes*, **24(1)**, 57-63.

[28] Colman, P.M., Hoyne, P.A. and Lawrence, M.C. (1993) Sequence and structure alignment of paramyxovirus hemagglutinin-neuraminidase with influenza virus neuraminidase. *Journal of Virology*, **67(6)**, 2972-2980.

[29] Maurer-Stroh, S., Ma, J.M., Lee, R.T.C., Sirota, F.L. and Eisenhaber, F. (2009) Mapping the sequence mutations of the 2009 H1N1 influenza A virus neuraminidase relative to drug and antibody binding sites. *Biology Direct*, **4**, 18.

[30] Baudin, F., Petit, I., Weissenhorn, W. and Ruigrok, R.W.H. (2001) In vitro dissection of the membrane binding and RNP binding activities of influenza virus M1 protein. *Virology*, **281(1)**, 102-108.

[31] Furuse, Y., Suzuki, A., Kamigaki, T. and Oshitani, H. (2009) Evolution of the M gene of the influenza A virus in different host species: Large-scale sequence analysis. *Journal of Virology*, **6(1)**, 67.

[32] Yang, H., Carney, P. and Stevens, J. (2010) Structure and Receptor binding properties of a pandemic H1N1 virus hemagglutinin. PLoS Current Influenza, RRN1152.

[33] Dundon, W.G. and Capua, I. (2009) A closer look at the NS1 of influenza virus. *Viruses*, **1(3)**, 1057-1072.

[34] Lin, D., Lan, J. and Zhang, Z. (2007) Structure and function of the NS1 protein of influenza A virus. *Acta Biochim Biophys Sin* (Shanghai), **39(3)**, 155-162.

[35] Ye, Q., Krug, R.M. and Tao, Y.J. (2006) The mechanism by which influenza A virus nucleoprotein forms oligomers and binds RNA. *Nature*, **444(7122)**, 1078-1082.

[36] Liu, X. and Zhao, Y.P. (2010) Switch region for pathogenic structural change in conformational disease and its prediction. *PLoS One*, **5(1)**, e8441.

[37] Yuan, P.W., Bartlam, M., Lou, Z.Y., Chen, S.D., Zhou, J., He, X.J., Lv, Z.Y., Ge, R.W., Li, X.M., Deng, T., Fodor, E., Rao, Z.H. and Liu, Y.F. (2009) Crystal structure of an avian influenza polymerase PAN reveals an endonuclease active site. *Nature*, **458(7240)**, 909-913.

J. Biomedical Science and Engineering, 2010, 3, 700-710 **JBiSE**
doi:10.4236/jbise.2010.37094 Published Online July 2010 (http://www.SciRP.org/journal/jbise/).

Modelling social determinants of self-evaluated health of poor older people in a middle-income developing nation

Paul A. Bourne

Department of Community Health and Psychiatry Faculty of Medical Science University of the West Indies, Mona.
Email: paulbourne1@yahoo.com

Received 15 March 2010; revised 6 April 2010; accepted 8 April 2010.

ABSTRACT

Over the last 2 decades (1988-2007), poverty in Jamaica has fallen by 67.5%, and this is within the context of a 194.7% increase in inflation for 2007 over 2006. It does not abate there, as Jamaicans are reporting more health conditions in a 4-week period (15.5% in 2007) and at the same time this corresponds to a decline in the percentage of people seeking medical care. Older people's health status is of increasing concern, given the high rates of prostate cancer, genitourinary disorders, hypertension, diabetes mellitus and the presence of risk factors such as smoking. Yet, there is a dearth of studies on the health status of older people in the two poor quintiles. This study examined 1) the health status of those elderly Jamaicans who were in the two poor quintiles and 2) factors that are associated with their health status. A sample of 1,149 elderly respondents, with an average age of 72.6 years (SD = 8.7 years) were extracted from a total survey of 25,018 Jamaicans. The initial survey sample was selected from a stratified probability sampling frame of Jamaicans. An administered questionnaire was used to collect the data. Descriptive statistics were used to examine background information on the sample, and stepwise logistic regression was used to ascertain the factors which are associated with health status. The health status of older poor people was influenced by 6 factors, and those factors accounted for 26.6% of the variability in health status: Health insurance coverage (OR = 13.90; 95% CI: 7.98-24.19), age of respondents (OR = 7.98; 95% CI: 1.02-1.06), and secondary level education (OR=1.82; 95% CI: 1.35-2.45). Males are less likely to report good health status than females (OR = 0.56; 95% CI: 0.42-0.75). Older people in Jamaica do not purchase health insurance coverage as a preventative measure but as a curative measure. Health insurance coverage in this study does not indicate good health but is a proxy of poor health status. The demand of the health services in Jamaica in the future must be geared towards a particular age cohort and certain health conditions, and not only to the general population, as the social determinants which give rise to inequities are not the same, even among the same age cohort.

Keywords: Health Status; Self-Evaluated Health; Older Poor; Socioeconomic Factors; Jamaica

1. INTRODUCTION

Factors determining the poor health status of the elderly in Jamaica can be viewed from the perspective of a socio-medical dichotomy. Such factors include poverty (resulting in one's inability to access loans, quality education and health care), lifestyle (e.g. smoking, sedentary habits, sexual and dietary practices and physical inactiveity), resulting in prostate cancer, genitourinary disorders, hypertension, diabetes mellitus and premature death. In 2005, the World Health Organization began a thrust in examining the social determinants of health, and despite that reality there is a lack of literature in this regard on the elderly poor people in Jamaica. These parameters were explored in the current research by using a sample of 1,149 elderly poor Jamaicans.

The findings of this paper reveal that the cost of medical care is positively correlated with health conditions, and that economic constraints account for the decline in the elderly seeking medical care. Older people in Jamaica do not purchase health insurance coverage as a preventative measure but as a curative measure. Health insurance coverage in this study does not indicate good health, but on the contrary, it is a proxy of poor health status. It is also noted that income is positively correlated with a higher standard of living and life expectancy. In support of this claim, studies have shown that life expectancy in many developing countries [1], in particular the Caribbean (Barbados, Guadeloupe, Jamaica, Martinique, Trinidad and Tobago) has exceeded 70 years,

and they are now experiencing between 8-10% of their population living to 60+ years old. Life expectancy, which is a good indicator of the health status of a populace, is higher in countries with high GDP per capita. This means that income is able to purchase better quality products [2], and indirectly affects the length of years lived by people. GDP per capita is used as an objective valuation of standard of living [3-12]. While a country's GDP per capita may be low, life expectancy is high because health care is free for the population. Despite this fact, material living standards undoubtedly affect the health status and wellbeing of people, as well as the level of females' educational attainment [6] and the nutrition intake of the poor. On the other hand, when there is economic growth, the society has more to spend on nutrition, health care, better physical milieu, better quality food, safer sanitation and education.

Good health is, therefore, linked to economic growth, something which is established in a plethora of studies by economists. Developing countries (a term synonymous with poverty) do not only constitute low levels of democracy, civil unrest, corruption [13], high mortality and crude birth rates, but one must also include nutriational deficiency [14]. The WHO in 1998 put forward the position that 20% of the population in developing countries do not have access to enough food to meet their basic needs and provide vital nutrients for survival.

In the Caribbean, and in particular Jamaica, poverty is typical, and many of the ills that affect other developing nations outside of this region are the same. The poor in this society are facing insurmountable challenges in buying the necessary health care. In 2007, between 51 and 53% of those in the poor quintiles in Jamaica sought medical care, compared to 61-68% of those in the middle-to-wealthiest quintiles. When those who had reported that they were ill were asked why they had not sought medical care, 51% of those in the poorest quintile indicated that they 'could not afford it', with 36.7% of those in the poor quintile giving the same response, and the percentage declines as the wealth of the person increases to the wealthiest quintile (7.7% of those in the wealthiest quintile).

Over the last 2 decades (1988-2007), poverty in Jamaica has fallen by 67.5% and this is in the context of a 194.7% increase in inflation for 2007 over 2006. Jamaicans are reporting more health status in a 4-week period (15.5% in 2007) and at the same time this is associated with a decline in the percentage of people seeking medical care. Older people's health status is of increasing concern, given the high rates of prostate cancer, genitourinary disorders, hypertension, diabetes mellitus and the presence of risk factors such as smoking in earlier life. Yet, there is a dearth of studies on the health status of older people in the two poor quintiles.

Works which have examined the social determinants of health have used data for the population [2,3], but none emerged from a literature research using data for poor old people. This study examined 1) the health status of those elderly Jamaicans who were in the two poor quintiles, and 2) factors that are associated with their health status.

2. MATERIALS AND METHODS

2.1. Sample

A sample of 1,149 elderly respondents was extracted from a larger survey of 25,018 Jamaicans. The sample was based on being 60 + years old, and being classified in the two poorest income categorizations. The initial survey sample (n = 25, 018) was across the 14 parishes, and was conducted between June and October 2002. The sample (n = 25,018 or 6,976 households out of a planned 9,656 households) was drawn using a stratified random sampling technique. This design was a two-stage stratified random sampling design, where there was a Primary Sampling Unit (PSU) and a selection of dwellings from the primary units. The PSU is an Enumeration District (ED), which constitutes of a minimum of 100 dwellings in rural areas and 150 in urban zones. An ED is an independent geographic unit that shares a common boundary. This means that the country was grouped into strata of equal size based on dwellings (EDs). Based on the PSUs, a listing of all the dwellings was made, and this became the sampling frame from which a Master Sample of dwellings was compiled, and which provided the frame for the labour force. The survey adopted was the same design as that of the labour force, and it was weighted to represent the population of the country.

The survey was a joint collaboration between the Planning Institute of Jamaica and the Statistical Institute of Jamaica. The data were collected by a comprehensive administered questionnaire, which was primarily completed by heads of households for all household members. The questionnaire was adapted from the World Bank's Living Standards Measurement Study (LSMS) household surveys, and was modified by the Statistical Institute of Jamaica with a narrower focus, to reflect policy impacts as well. The instrument assessed: 1) the general health of all household members; 2) social welfare; 3) housing quality; 4) household expenditure and consumption; 5) poverty and coping strategies, 6) crime and victimization, 7) education, 8) physical environment, 9) anthropometrics measurement and immunization data for all children 0-59 months old, 10) stock of durable goods, and 11) demographic questions.

Data were stored and retrieved in SPSS for Windows, version 16.0 (SPSS Inc; Chicago, IL, USA). The current study is explanatory in nature. Descriptive statistics were presented to provide background information on the sampled population. Following the provision of the aforementioned demographic characteristics of the sub-sample, chi-square analyses were used to test the statistical association between some variables, t-test statistics and analysis of variance (*i.e.* ANOVA) were also used to examine the association between a metric dependent variable and either a dichotomous variable or non-dichotomous variable respectively. Logistic regression was used to examine the statistical association between a single dichotomous dependent variable and a number of metric or other variables (Empirical Model). The logistic regression was used because in order to test the association between a single dichotomous dependent variable and a number of explanatory factors simultaneously, it was the best available technique. A p-value < 0.05 (two-tailed) was selected to indicate statistical significance in this study. Where collinearity existed ($r > 0.7$), variables were entered independently into the model to determine those that should be retained during the final model construction. To derive accurate tests of statistical significance, SUDDAN statistical software was used (Research Triangle Institute, Research Triangle Park, NC), and this was adjusted for the survey's complex sampling design.

2.2. Measure

Social determinants. These denote the conditions under which people are born, grow, live, work and age, including the health system.

Crowding: This is the total number of persons living in a room with a particular household.

Crowding = $\sum_{i=1}^{n} \frac{h_i}{r}$, where h_i is each person in the household and r is the number of rooms excluding kitchen, bathroom and verandah.

Age: This is a continuous variable in years, ranging from 15 to 99 years.

Old/Aged/Elderly: An individual who has celebrated his/her 60th birthday or beyond.

Negative Affective Psychological Condition: Number of responses from a person on having lost a breadwinner and/or family member, loss of property, having been made redundant, failure to meet household and other obligations.

Private Health Insurance Coverage (or Health Insurance Coverage) proxy Health-Seeking Behaviour, is a dummy variable which speaks to 1 for self-reported ownership of private health insurance coverage, and 0 for not reporting ownership of private health insurance coverage.

Gender: Gender is a social construct which speaks to the roles that male and female perform in a society. This variable is a dummy variable, 1 if male and 0 if otherwise.

Health conditions: The report of having had an ailment, injury or illness in the last four weeks, which was the survey period. This variable is a binary measure, where 1 = self-reported health status or illnesses, and 0 = otherwise (not reporting an illness, injured or dysfunctions).

Poverty: In this study, the definition of poverty is the same as that used to estimate poverty in Jamaica. It is established from the basis of a poverty line. In order to compute the per capita poverty line in each geographical area (Kingston Metropolitan Area, Other Towns and Rural Areas), the cost of living for a basket of goods is divided by an average family of five. The basket of goods is established by the Ministry of Health based on the normal nutrients of the average family. Based on a per capita approach, there are five per capita income quintiles, with the poorest being below the poverty line (quintile 1) and the wealthiest being in quintile 5.

Elderly, aged or old persons: Using the same definition offered by the United Nations in the Report of the World Assembly on Ageing, July 26-August 6, 1982 in Vienna, that the elderly are persons who are 60+ years old.

Older-poor (elderly-poor, aged-poor): All aged persons below and just above the poverty line (quintiles 1 & 2) in Jamaica.

3. RESULTS

3.1. Demographic Characteristics of Sample

Consistent with the demographic characteristics of the ageing population, the sample was 1,149 of which there were 45% males (N = 517) compared to 55% females (N = 632). The mean age of the sample was 72.6 years (SD = 8.7 years). Most of the sample were married (40%, N = 452), 50.5% (N=580) of the sample were in the poorest 20% of per capita income quintile, 95% (N = 1,087) were not receiving retirement income; those who were heads of households (98.3%, N = 1,129), those who had at most primary education (65.2%, N = 700) and those who did not have health insurance coverage (86.0%, N = 973) (**Table 1**).

Thirty-seven percent (37.2%) of the sample indicated having had an illness in the last 4-week period. Approximately 64% of the respondents indicated that they sought health care for their health conditions. When the respondents were asked if they had visited a health practitioner for any other reason during the last 12 months, 57.1% reported yes and 30.3% reported going for 'regular checkups'. Of those who indicated yes, 37.2% visited

Table 1. Socio-demographic characteristics of sample.

Description	N	Percent
Gender		
Male	517	45.0
Female	632	55.0
Marital status		
Married	452	40.0
Never married	357	31.6
Divorced	10	0.9
Separated	22	1.9
Widowed	290	25.6
Per capita Income quintile		
Poorest	580	50.5
Poor	569	49.5
Retirement Income		
No	1087	95.0
Yes	57	5.0
Household head		
No	20	1.7
Yes	1129	98.3
Health Insurance coverage		
No	973	86.0
Yes	158	14.0
Educational Level		
Primary and below	700	65.2
Secondary	363	33.8
Tertiary	10	0.9
Age	72.63 years (SD = 8.7 years)	
Total Medical Care Expenditure	$1,067.64 (SD = $2,000.00)	
Per capita consumption	$30,998.07 (SD = $9,833.00)	

US $1.00 = JA$50.9

public health care institutions, and 18.7% went to private clinics, compared to 5.7% who claimed that they attended both health care facilities. The typologies of illness included colds (1.4%), diabetes mellitus (5.7%), hypertension (42.9%) and arthritis (31.4%), while 18.6% did not specify their health condition(s). Only 2% of the respondents had health insurance coverage; 61% purchased the prescribed medication; and 81.8% of those who indicated having not bought their medication reported that they could not afford it.

The median number of days for how long an illness lasted was 7 days, with a median medical expenditure of US $7.85 (US $1.00 = Ja. $50.97).

3.2. Bivariate Correlation of Health Status and Age Cohort

Of the 1,149 sample respondents for this study, 98.8% (N = 1,135) were used for the statistical correlation between health status and gender. Of the 1,135 respondents, there were 688 young-old, 327 old-old and 120 oldest-old poor Jamaicans. There was a correlation between the two above-mentioned variables – $\chi 2$ (df = 2) = 22.863, p-value < 0.001. On an average, 46% of the aged-poor (N = 523) reported that they had at least one illness/injury in the survey period. The most health status was reported by the oldest-old poor (59.2%, N = 71), 52.9% (N = 173) and the least by the young-old (40.6%, N = 279). Embedded in these findings is that for every 1 young-old poor who indicated that he/she had an illness/injury, there are 1.5 oldest-old and 1.3 old-old poor.

3.3. Multivariate Analysis

The results of the multiple logistic regression model (in **Table 2**), were statistically significant [Model $\chi 2$ (df = 18) = 229.47; –2Log likelihood = 1130.37; p-value < 0.001]. **Table 2** showed that 26.6% of the variances in the health status of older people in Jamaica were accounted for by the independent variables used in the multiple logistic regressions. The mold revealed that there were 6 statistically significant factors that determined health conditions. These predictors are age (OR = 1.04, 95% CI = 1.02-1.06), health insurance coverage (OR = 13.90, 95% CI = 7.98-24.19), physical environment (OR = 1.42, 95% CI = 1.06-1.89), cost of medical care (OR = 1.00, 95% CI = 1.00-1.00), secondary level education (OR = 1.82, 95% CI = 1.35-2.45) with reference to primary and below education, and gender of respondents (OR = 0.56, 95% CI = 0.42-0.75). Controlling for the effect of other variables, the average likelihood of reporting illness/injury in a 4-week reference period declined by 17 times for those who had dysfunctions.

The model had statistically significant predictor power (Model $\chi 2$ (df = 18) = 229.47; -Homer and Lemeshow goodness of fit $\chi 2$ = 3.739, P = 0.880), and correctly classified 70% of the sample (correctly classified 55.4% of those with dysfunctions and 82.3% of those without dysfunctions) (**Table 2**). The logistic regression model can be written as: *Log* (*probability of dysfunctions/ probability of not reporting dysfunctions*) = –4.185 + 0.039 (*Age*) + 2.632 (*Health Insurance coverage*, 1 = *yes*, 0 = *no)* + 0.348 (*Physical Environment*, 1 = *yes*, 0 = *no)* + 0.000 (*Cost of Medical Care*) + 0.598 (*Secondary level education* = 1, 0 = *primary and below*) – 0.581 (*Sex*).

4. DISCUSSION

People are living longer [15], which means that on average the elderly are living 15-20 years after retirement. Demographic ageing at the micro and macro levels implies a demand for certain services such as geriatric care. In addition to preventative care, there will be a need for particular equipment and products (*i.e.* wheelchairs, walkers etc.). Then there are future preparations for pension and labour force changes, along with the social and economic costs associated with ageing, as well as the policy based research to better plan for the reality of these age groups. The World Health Organization (WHO), in explaining the 'problems' that are likely to occur because of population ageing, argues that the 21st Century will not be easy for policy makers as it is pivotal in the preparation process to postpone ailments and disabilities, and the challenge of providing a particular standard of health for the populace [16]. What constitutes population ageing? Some demographers have put forward the benchmark of 8-10% as an indicator of population ageing [17]. Within the construct of Gavrilov and Heuveline's perspective, the Jamaican population began experiencing this significant population ageing as of 1975 (using 60+ years for ageing) or 2001 (if ageing is 65+ years). The issue of population ageing will double come 2050, irrespective of the chronological definition of ageing, but what about the elderly poor health conditions?

Let us examine the disparity between long life and quality of lived years. Ali, Christian & Chung [18] who is medical doctors, cite the case of a 74 year-old man who had epilepsy, and presented the findings in the West Indian Medical Journal. They write that "Elderly patients are frequently afflicted with paroxysmal impairments of consciousness, because they frequently have chronic medical disorders such as diabetes mellitus and hypertension, and can also be on many medications….Many elderly patients may have more than one cause for this symptom" [18].

The case presented by the medical doctors emphasizes the point we have been arguing that long life does not

Table 2. Logistic Regression: Socio-demographic correlates of health status of poor older people in Jamaica, N = 1,033.

Variable	OR	95.0% C.I.
Age	1.04	1.02-1.06***
Retirement income	0.75	0.38-1.49
Per capita consumption	1.00	1.00-1.00
Separated, divorced or widowed	1.07	0.74-1.55
Married	1.11	0.77-1.58
Never married (reference group)	1.00	
Health insurance	13.90	7.98-24.19***
Environment	1.42	1.06-1.89*
Household head	3.34	0.37-30.01
Cost of medical care	1.00	1.00-1.00**
Secondary	1.82	1.35-2.45***
Tertiary	0.43	0.07-2.63
Primary and below (reference group)	1.00	
Semi-urban	0.78	0.51-1.19
Urban areas	0.86	0.50-1.49
Rural areas (reference group)	1.00	
Sex	0.56	0.42-.75***
Living arrangement	1.20	0.77-1.88
Crowding	0.89	0.78-1.02
Crime index	1.00	0.98-1.03
Positive affective	0.96	0.90-1.01

Model Chi-square (df =18) = 229.47, p-value < 0.0001; -2Log likelihood = 1130.37; Nagelkerke R-square = 0.266; Hosmer and Lemeshow test P = 0.880; *P < 0.05, **P < 0.01, ***P < 0.001

imply quality of lived years. Although the case study cited here does not constitute a general perspective on all the elderly, other quantitative studies have concurred with Ali, Christian and Chung's general findings. Scientists agree that biological ageing means degeneration of the human body, and such a reality means that longer life will not mean quality years. Population ageing is going to be a socioeconomic, psychological and political challenge today, tomorrow and in the future of developing countries and nations like Jamaica. This reinforces the position postulated by the WHO that healthy life expectancy [19] is where we ought to be going, as the new thrust is not living longer but how many of those years are lived without dysfunctions. Within the context of healthy life expectancy, studies that will be used to guide policy are those that incorporate many determinants, and not only biological conditions [20-25]. But none of those studies examined poor old people. Hambleton [20] and Bourne [23-25] are Caribbean scholars who have researched social determinants using the population of the poor, and this gap to date in the literature needs to be addressed, as the elderly constitute a vulnerable group, and the poor elderly group is even more vulnerable. Any policy which seeks to reduce poverty must take into account the poor elderly.

'Ageing in poverty' implies that persons remain in their local environments with the ability to live in their own home - wherever that might be - for as long as confidently

and comfortably possible. It inherently includes not having to move from one's current residence in order to secure the necessary support services in response to changing needs. The ageing of Caribbean populations has been accompanied by a shift to chronic non-communicable diseases as major causes of morbidity. While overall national trends have been reported, examination of local patterns of morbidity are increasingly important, as they have implications for the services to be provided, the mix of human resources, and the maintenance of health and functional status that facilitate ageing in place.

Research has shown that crowding is strongly correlated with the wellbeing of the elderly (ages 60+ years) [23]; however this phenomenon, which is synonymous with poverty, does not influence the health status of poor elderly Jamaicans. Embedded in this finding is the fact that older people, in particular those in poor quintiles, interpret people around not as a negative force but as good social networking and interaction. What, then, influences their health conditions?

Poverty speaks to a particular environment; Pacione [26] showed that one's physical environment affects one's quality of life, and other scholars have agreed with this finding. The current study concurs with Pacione and others, in that the physical milieu is positively correlated with health conditions. Although Michael Pacione's work was on the general population, Bourne's works [23, 24] examined the elderly population (ages 60+ years) and found a negative association between physical environment and wellbeing, and this study concurred with that of the aforementioned researcher on the correlation between physical environment and health conditions. In this study, an important finding is to refine the correlation.

Health insurance coverage is among the many indicators of the health-seeking behaviour of a populace. For the poor elderly, it is the most significant predictor of health conditions. The correlation is a strong positive one, indicating that health insurance coverage is a good proxy for more ill-health than good health. The current research found that those elderly poor who owned health insurance were 14 times more likely to report dysfunctions (or injuries) than those who did not. Health insurance is, therefore, a cost reducer for those who are aware that they are ill, and it is not in demand as a preventative measure. Arising from this fact is the role played by the costs of medical and curative care. Health is influenced by more than disease-causing pathogens. [27]

The cost of medical care is positively correlated with health conditions, suggesting that the more dysfunctions (or injuries) that the elderly poor report, the more they are likely to spend on medical care. The elderly poor are prevented from seeking preventative care as against curative care. The latest data published by the Planning Institute of Jamaica and the Statistical Institute of Jamaica [28] showed that 37.3% of elderly people are at least poor, with 20.6% falling in the poorest quintile. This further explains the rationale for the reduction in the demand for medical care within the context of a precipitous increase in inflation in 2007 over 2006 (194%). With the steady rise in the cost of health care, as well as the increase in general food and non-alcoholic beverage prices in Jamaica, coupled with the fact that illness in older age requires care, the elderly poor are facing increasingly difficult times. The severity of the economic situation has seen a dramatic increase in the number of Jamaicans not seeking medical care for illness/injury. Although there is a decline in the general population seeking medical care (66%), more of the elderly do seek health care (72.3%) and this is owing to recurrent chronic illness which was shown to affect 74.2% of them [28]. Illnesses/injuries are precipitously affecting the elderly, and the data showed that self-reported illness for the elderly was 2.3 times more (36.6%) than in the general population (15.5%) [28]. In 2007, the elderly poor who constitute 38% of the poor-to-poorest in the population are mostly household heads (67.3%) and often unemployed, and within this context they must provide for their own health needs and those of their family, despite the harsh economic challenges and increased cost of health care.

In 2002, 12.9% of Jamaicans were unable to afford medical care, and approximately 4 years later, the figure had risen by 162.8% to 33.9% in 2007. This is within the context of a 26.3% decline in poverty for the same period. Generally poverty has been falling over the last 2 decades in Jamaica, and inflation has fluctuated, justifying the increased amount spent on food and beverages [28], and the corresponding reduction in health care expenditure. In Jamaica remittances, which subsidize income for many households, have fallen by 7.7% and the reduction is 33% for those in the poor-to-the-poorest income quintiles. If the cost of medical care is positively correlated with the health status of the elderly poor, then can it be said that the poor elderly have more ill-health within the context of biological ageing and lowered access to employment income? Marmot [2] opined that there is a direct association between income and poor health, and this further helps us to understand the embedded health challenge of the elderly poor, as they must meet the increasing costs of medical care, cost of living, lower income, illnesses and severity of health conditions. On examining the health statistics for 2007 [28], the indication was that 50.8% of those in the poorest income quintile were unable to afford to seek medical care, and

the figure was 36.7% of those in the poor quintile. In order to understand the severity of the situation regarding the aged-poor people in Jamaica, let us analyze the aforementioned within the context of the aged-poor. The official statistical publication for Jamaica for 2007 [28] showed that 20.6% percent of the elderly people are in the poorest quintile and 17.7% in the poor quintile which means that a little over half of the aged-poorest in Jamaica (10.4%) were unable to afford medical care, and 6.5% of the aged-poor had financial difficulty affording medical care expenditure. One of the choices that must be made by the aged-poor in Jamaica is a switch from the formal medical care service to utilizing home remedies and over-the-counter medications, instead of visiting their personal physicians or health care facilities.

Since 1988 when the Jamaican authorities began collecting data on self-reported health conditions, men have been reporting less health status than women [28]. The reporting of less illness does not mean that men are healthier than women, as the same statistical report [28] shows that women seek more medical care than men. Morbidity data for the sexes in Jamaica is typical, as in Mexico City, Havana and Santiago-Chile at least 60% of females compared to 50% of males aged 60+ years old reported fair-to-poor health [29]. Continuing, Buenos Aires, Montevideo and Bridgetown-Barbados had twice the figures of the aforementioned geo-political zones [29]. This is in keeping with women's protective role of self, and their willingness to have a regard for their future health status accounts for a higher health status and not a lower one, although they report more dysfunctions than men. If life expectancy were to be used to proxy good health status, females are healthier than men given that they outlive them by 6 years in Jamaica and 8 years in the world. Furthermore, in 2000-2005, life expectancy for men was 69.5 years and 74.7 years for women, and come 2045-2050 they both would have gained an additional 2 and one-quarter years more to their life span. The equal and constant rate of change in the life expectancy of both sexes in Jamaica highlights the fact that men do not enjoy better overall health status than their female counterparts. More years of life for both sexes means that the life course opens itself to coronary heart disease, stroke and diabetes mellitus, and so morbidity must be examined in this discourse.

Studies done by the Ministry of Health reveal that of the five leading causes of mortality in Jamaica, which are malignant neoplasm, heart disease, diabetes mellitus, homicide and cerebrovascular diseases [30], more men die from more of the aforementioned conditions than women. Malignant neoplasms are 39% greater for men than women; cerebrovascular diseases are 14% higher for females than males; heart disease was 71.2 per 100,000 for men and 66.1 per 100,000 for women; and diabetes mellitus was 64% more for females than males [30]. The greater vulnerability of men to particular mortality than women is typical across Latin America and the Caribbean [29], pointing to gender bias (that is feminization) in visits to health care facilities, which are embedded in the life expectancy rates and visits to health care institutions. The matter of reporting less health status, once again, does not imply a healthier person, as health is not on a continuum, with ill-health on one extreme and good health on the other. Health is more in keeping with cyclical flow, and changes over the life course with time, experiences and socio-physical environmental conditions. Hence, asking about ill-health is not a good proxy for health status, as in 2007 a group of Caribbean scholars conducted a national representative prevalence survey of some 1,338 Jamaicans, and found that those who indicated themselves to be of the lower class had the least self-reported health status [13].

The discipline of gerontology – scientific inquiry into the biological, psychological, and social aspects of ageing - has shown that ageing is not necessarily without increased health conditions; it is natural for aged people to complain and die more of dysfunctions than other age cohorts [31,32] and that is directly related to their basal metabolic rate [33] and the nature of the life course of the aged [34]. Here functional ageing is an explanation for the image of ageing, and it can be measured by normal physical changes, diminished short-term memory, reduced skin elasticity and a decline in aerobic capacity. It is well established in the research literature that age is directly correlated with health status for the elderly, and in this study the finding concurs with the literature. The current research shows that age is the second most significant predictor of health status for the elderly poor, and explains why the disparity in poor health in Latin and America and the Caribbean is higher for older persons than younger people [29]. Population ageing is synonymous with more disability and more non-communicable diseases such as malignant neoplasms, hypertension, diabetes, and heart diseases than younger ages. Donald Bogue [35] noted that health problems increase with ageing, and that one's health issues intensify with ageing. Therefore, an unhealthy lifestyle – tobacco consumption, physical inactivity, unprotected sex, and unhealthy diet - over the life course will affect the elderly in latter life, and the declining health of the elderly poor is the same within the sub-categories of the elderly – young-old, old-old and oldest old.

Issues of the elderly cannot be discussed without an examination of area of residence. This study found no correlation between the aged-poor's health status and area of residence. Using data since 1989 (from various

issues of the Jamaica Survey of Living Conditions), population ageing is biased by gender as well as by specific area of residence. Over the last decade (1997-2007), the number of elderly Jamaicans living in rural areas has declined from 54.3% to 46.6% (a rate of 14.1%). For the same period, the rate of increase of the aged populace in the Kingston Metropolitan Area (100% cities) was 19.5%, down from 27.2% (in 1997) while the increase in the aged population over the same period in Other Towns was 12.9% over 18.5% in 1997. Regarding the prevalence of poverty for the region (2007), rural poverty was 3.8 times more than that in Other Towns, and 2.5 times more than that in the Kingston Metropolitan Area. Despite the compounding economic challenges of poverty coupled with ageing, the poor-elderly in Jamaica do not experience a difference in their health status owing to area of residence. Here the health issues of the aged poor are independent of their area of residence, suggesting that in the population the poor are age-residence insensitive. This contradicts research literature on the health status of the elderly which has shown a correlation between the aged and their areas of residence [23,24,48], indicating that the physical characteristics of the aged poor are the same in different areas of residence, and therefore do not account for any poor health, disability, functional inability or psychological conditions.

Like the WHO [35,36], the researcher believes that although ageing is a biological phenomenon, it cannot be due only to biological conditions, as ageing relates to bio-psycho-social [20,25,37-49] and environmental conditions [23-26], since people – biological organisms – must operate in a socio-physical milieu throughout their life span, and this demands an expansion of biological conditions in the ageing discourse. The very nature of gerontology must coalesce biopsychosocial and environmental conditions in assessing ageing and the health of the aged, which are in keeping with the WHO's Constitution of 1948, and this has also been established in many Caribbean scholarships [20,23-25,42-49]. Within the context of the above-mentioned challenges for elderly people, when this is coupled with poverty which affects 10.2% of elderly Jamaicans (N = 29,794) in 2007, it intensifies the challenges experienced by elderly people. With the increased cost of food and non-alcoholic beverages, fuel and household supplies, housing and household operational expenses, the health status of the older-poor will continue to deteriorate, as they will not be able to afford health care services. The decline in medical care-seeking behaviour of Jamaicans speaks to the challenges of older people and the rise in instances of switching to alternative medicine. This is further intensified by poverty; and rural poverty, which is more severe than that found in urban areas, [50] will further compound the challenges of the health status of the aged populace. Older people who are poor must operate within the same biopsychosocial and physical environment during their lifetimes as other persons.

Even among the WHO commissioned studies [51-53], as well as other studies on the social determinants of health [2,3,20-25], the population of the poor elderly were not examined. Likewise in the Caribbean, scholars have examined the social determinants of the population or the elderly population, with poverty being an independent variable [20,23-25]. Any policy that seeks to address the health status of the elderly poor must take into consideration, or concentrate and/or rely on, not only the population in general, but the cohort of the elderly in particular. The experiences and demands of the elderly are not the same as the general population, and the current study shows that social determinants of health are somewhat different for the general elderly population and the poor elderly cohort. The WHO [51] opined that the social determinants of health for the most part account for the health inequities between and within nations, which substantiates the differences that emerged between the elderly in other studies [20,23-24] and the current study of the poor elderly. These findings are far-reaching, and can be used to guide policy and research. The elderly-poor in Jamaica are experiencing 'health poverty' which cannot be alleviated by unresearched policies or research policies on the general population, but by the elderly cohorts in particular.

5. CONCLUSION

In summary, the number of elderly persons who reported health conditions in Jamaica is 3 times more than that for the nation (*i.e.* 12.6%), suggesting that health care expenditure for Jamaicans is substantially used to address health care needs for the aged population. With the number of elderly come 2025 estimated to be 14.5% over 10.9% for 2007, health care expenditure will be primarily absorbed in caring for this age cohort. Public health practitioners must begin programmes to deal with this pending reality. Ageing is a process which denotes that the high number of health conditions affecting the elderly would have started earlier, based on some of the decisions that they undertook (or did not) leading up to their current age. Hence, there is a need to have a public health campaign geared towards the promotion of healthy lifestyle practices for ages close to sixty years, in conjunction with one for children and for the working-age population. The programme should target check-ups, preventative care, signs of the onset of particular health conditions, and the distinction between ill health and good health care practices. The demand of the health services in Jamaica in the future must be geared towards

a particular age cohort and certain health conditions, and not only to the general population, as the social determinants which give rise to inequities are not the same even among the same age cohort.

6. DISCLOSURE

The author reports no conflict of interest for this study.

7. DISCLAIMER

The researcher would like to note that while this study used secondary data from the Jamaica Survey of Living Conditions, none of the errors in this paper should be ascribed to the Planning Institute of Jamaica or the Statistical Institute of Jamaica, but to the researcher.

8. ACKNOWLEDGEMENTS

The dataset for this study was made available from the databank of SALISES (Sir Arthur Lewis Economic Institute), Faculty of Social Sciences, the University of the West Indies, Mona, Jamaica and for this the researcher is indebted and greater appreciate this gesture.

REFERENCES

[1] WHO, (1998) The world health report 1998. Life in the 21st century. A vision for all. WHO, Geneva.

[2] Marmot, M. (2002) The influence of income on health: Views of an epidemiologist. Does money really matter? Or is it a marker for something else? *Health Affairs*, **21**(**2**), 31-46.

[3] Graham, H. (2004) Social determinants and their unequal distribution: Clarifying policy understanding. *The Milbank Quarterly*, **82(1)**, 101-124.

[4] Marmot, M. and Wilkinson, R.G., Eds. (2003) Social determinants of health. 2nd Edition, Oxford University Press.

[5] Kawachi, I. (2000) Income inequality and health. In *Social Epidemiology*, Ed., Berkman, L.K. and Kawachi, I., Oxford Univeristy Press, New York.

[6] Kawachi, I., Kennedy, B.P., Lochner, K. and Prothrow-Stitch, D. (1997) Social capital, income inequality, and mortality. *American Journal of Public Health*, **87(9)**, 1491-1498.

[7] Rojas, M. (2005) Heterogeneity in the relationship between income and happiness: A conceptual-referent-theory explanation. *Journal of Economic Psychology*, **28**(**1**), 1-14.

[8] United Nations Development Programmed, (2006) Human development report 2006. United Nations Development Programme, New York:

[9] Sen, A. (1998) Mortality as an indicator of economic success and failure. *Economic Journal*, **108(446)**, 1-25.

[10] Roos, L., Magoon, J., Gupta, S., Chateau, D. and Veugelers, P.J. (2004) Socioeconomic determinants of mortality in two Canadian provinces: Multilevel modeling and neighborhood context. *Social Sciences and Medicine*, **59(11)**, 1435-1447.

[11] Murray, S. (2006) Poverty and health. *Canadian Medical Association Journal*, **174(7)**, 923-923.

[12] Benzeval, M., Judge, K. and Shouls, S. (2001) Understanding the relationship between income and health: How much can be gleamed from cross-sectional data? Social Policy and Administration Quoted in Benzeval, M. and Judge, K., Income and health: The time dimension. *Social Science and Medicine*, **52(4)**, 1371-1390.

[13] Powell, L.A., Bourne, P. and Waller, L. (2007) Probing Jamaica's political culture, Vol. 1: Main trends in the July-August 2006 leadership and governance survey. Centre of Leadership and Governance, Kingston, Department of Government, University of the West Indies, Mona.

[14] WHO, (1998) The world health report, 1998. Life in the 21st century. A vision for all. WHO, Geneva.

[15] Rowland DT, (2003). Demographic methods and concepts. Oxford University Press, Oxford.

[16] WHO, (1998) Health promotion glossary. WHO, Geneva.

[17] Gavrilov, L.A. and Heuveline, P. (2003) Aging of population. Quoted in the Encyclopedia of Population Demeny, P. and McNicol, G., Eds., Macmillan, New York.

[18] Ali, A., Christian, D. and Chung, E. (2007) Funny turns in an elderly man. *West Indian Medical Journal*, **56(4)**, 376-379.

[19] WHO, (2000) WHO issues new healthy life expectancy rankings: Japan number one in new 'healthy life' system. WHO, Washington D.C. & Geneva.

[20] Hambleton, I.R., Clarke, K., Broome, H.L., Fraser, H.S., Brathwaite, F. and Hennis, A.J. (2005) Historical and current predictors of self-reported health status among elderly persons in Barbados. *Revista Panamericana de Salud Pública*, **17(5-6)**, 342-352.

[21] Smith, J.P. and Kington, R. (1997) Demographic and economic correlates of health in old age. *Demography*, **34**(**1**), 159-170.

[22] Grossman, M. (1972) The demand for health - A theoretical and empirical investigation. National Bureau of Economic Research, New York.

[23] Bourne, P. (2007) Determinants of well-being of the Jamaican Elderly. Unpublished thesis, The University of the West Indies, Mona.

[24] Bourne, P. (2007) Using the biopsychosocial model to evaluate the wellbeing of the Jamaican elderly. *West Indian Medical Journal*, **56(suppl 3)**, 39-40.

[25] Bourne, P.A. (2008) Health determinants: Using secondary data to model predictors of well-being of Jamaicans. *West Indian Medical Journal*, **57(5)**, 476-481.

[26] Pacione, M. (2003) Urban environmental quality and human wellbeing – A social geographical perspective. *Landscape and Urban Planning*, **65(1-2)**, 19-30.

[27] Abel-Smith, B. (1994) An introduction to health: Policy, planning and financing. Pearson Education, Harlow.

[28] Planning Institute of Jamaica, (PIOJ), Statistical Institute of Jamaica (STATIN), (1989-2008) Jamaica survey of living conditions, 1988-2007. PIOJ, STATIN, Kingston.

[29] United Nations, ECLAC, (2003) Older Person in Latin America and the Caribbean: Situation and policies. *Regional Intergovernmental Conference on Ageing: Towards a Regional Strategy for the Implementation in Latin America and the Caribbean of the Madrid International Plan of Action on Ageing*, UN Economic Commission for Latin America and the Caribbean, Santiago,

Chile.
[30] The Health Promotion and Protection Division, Jamaican Ministry of Health (MOH), (2005) Epidemiology profile of selected health status and services in Jamaica, 1990-2002, MOH, Kingston.
[31] Wu, D., Cypser, R., Yashin, A.I. and Jonson, T.E. (2008) The U-shaped response of initial mortality in caenorhabditis elegans to mild heat shock: Does it explain recent trends it human mortality. *The Journal of gerontology: Biological Sciences*, **63(7)**, 660-668.
[32] Raynaud-Simon, A., Kuhn, M. and Moulis, J. (2008) Tolerance and efficacy of a new enteral formula specifically designed for elderly persons: An experimental study in the aged rat. *The Journal of Gerontology*: *Biological Sciences*, **63(7)**, 669-677.
[33] Ruggiero, C., Metter, E.J., Melenovsky, V., Cherubini, A., Najjar, S.S., Ble, A., Senin, U., Longo, D.L. and Ferrucci, L. (2008) High basal metabolic rate is a risk factor for mortality: The Baltimore longitudinal study of aging. *The Journal of gerontology: Biological Sciences*, **63**(**7**), 668-706.
[34] WHO, (2001) Life course perspectives on coronary heart disease, stroke and diabetes: Key issues and implications for policy and research. *Summary Report of a Meeting of Experts*, WHO, Geneva.
[35] Bogue, D.J. (1999) The ecological impact of population aging. *Essays in Human Ecology*, **4**, Social Development Center, Chicago.
[36] WHO, (2002) Active ageing: A policy framework. WHO, Geneva.
[37] Engel, G. (1960) A unified concept of health and disease. *Perspectives in Biology and Medicine*, **3(4)**, 459-485.
[38] Engel, G. (1977) The care of the patient: art or science? *Johns Hopkins Medical Journal*, **140(5)**, 222-232.
[39] Engel, G. (1977) The need for a new medical model: A challenge for biomedicine. *Science*, **196(4286)**, 129-136.
[40] Engel, G. (1978) The biopsychosocial model and the education of health professionals. *Annals of the New York Academy of Sciences*, **310(1)**, 169-181.
[41] Engel, G. (1980) The clinical application of the biopsychosocial model. *American Journal of Psychiatry*, **137(5)**, 535-544.
[42] Eldemire, D. (1995) A situational analysis of the Jamaican elderly, 1992. The Planning Institute of Jamaica, Kingston.
[43] Eldemire, D. (1997) The Jamaican elderly: A socioeconomic perspective & policy implications. *Social and Economic Studies*, **46(1)**, 175-193.
[44] Eldemire-Shearer, D. (2003) Organization of long-term care services for seniors. *Workshop Proceedings, Ageing Well: A Life Course Perspective*, the University of the West Indies, Mona and WHO/PAHO Collaborating Centre on Ageing and Health.
[45] Eldemire, D. (1996) Older women: A situational analysis, Jamaica 1996. United Nations Division for the Advancement of Women, New York.
[46] Eldemire, D. (1994) The elderly and the family: The Jamaican experience. *Bulletin of Eastern Caribbean Affairs*, **19**, 31-46.
[47] Eldemire, D. (1987) The elderly – A Jamaican perspective. In: Grell, Gerald, A.C., Ed., *The Elderly in the Caribbean: Proceedings of Continuing Medical Education Symposium*, University Printery, Kingston, Jamaica.
[48] Eldemire, D. (2008) Ageing - The response: Yesterday, today and tomorrow. *Inaugural Professorial Lecture*, UWI, Mona, Jamaica.
[49] Kalache, A. (2003) Active ageing: WHO perspective. *Workshop Proceedings, Ageing Well*: *A Life Course Perspective*, The University of the West Indies, Mona and WHO/PAHO Collaborating Centre on Ageing and Health.
[50] Henry-Lee, A. (2001) The dynamics of poverty in Jamaica, 1989-1999. *Social and Economic Studies*, **51(1)**, 199-228.
[51] WHO, (2008) The Social Determinants of Health. http://www.who.int/social_determinants/en/
[52] Kelly, M.P., Morgan, A., Bonnefoy, J., Butt, J. and Bergman, V. (2007) The social determinants of health: Developing an evidence base for political action. Final Report to World Health Organization Commission on the Social Determinants of Health from Measurement and Evidence Knowledge Network. http://www.who.int/social_determinants/resources/mekn_final_report_102007.pdf
[53] Solar, O. and Irwin, A. (2005) Towards a conceptual framework for analysis and action on the social determinants of health. Commission on Social Determinants of Health, Geneva.

J. Biomedical Science and Engineering, 2010, 3, 711-718 **JBiSE**
doi:10.4236/jbise.2010.37095 Published Online July 2010 (http://www.SciRP.org/journal/jbise/).

Bayesian and hierarchical Bayesian analysis of response - time data with concomitant variables

Dinesh Kumar

Department of Community Medicine, Government Medical College, Chandigarh, India.
Email: dinesh_walia@rediffmai.com

Received 9 January 2010; 19 January 2010; 30 January 2010.

ABSTRACT

This paper considers the Bayes and hierarchical Bayes approaches for analyzing clinical data on response times with available values for one or more concomitant variables. Response times are assumed to follow simple exponential distributions, with a different parameter for each patient. The analyses are carried out in case of progressive censoring assuming squared error loss function and gamma distribution as priors and hyperpriors. The possibilities of using the methodology in more general situations like dose-response modeling have also been explored. Bayesian estimators derived in this paper are applied to lung cancer data set with concomitant variables.

Keywords: Bayes Estimator; Bayesian Posterior Density; Gamma Prior Density (GPD); Hierarchical Bayes Estimator; Hyperprior; Noninformative Prior Quasi-Density (NPQD); Progressive Censoring; Squared Error Loss Function (SELF); Whittaker Function W s1, s2 (.).

1. INTRODUCTION

In biomedical studies, a considerable interest is laid upon developing statistical techniques for analyzing survival data which utilize information available on concomitant variables. In classical analysis of survival data, several models [1-7] are used for such situations. The usual proportional hazards (PH) regression model proposed by Cox [8] has been extensively discussed in the literature. Byar *et al.* [9] and Greenberg *et al.* [10] presented analysis of survival data assuming linear hazard model in classical set-up.

Bhattacharya *et al.* [11] discussed for the first time the problem on estimation of survival probabilities adjusting the effect of a single concomitant variable in the Bayesian framework. The present paper presents the Bayesian and hierarchical Bayesian analysis of response-time data in more general situations of more than one concomitant variables available for their effects to be adjusted. The exponential survival model

$$f\left(y \mid \lambda\right) = \lambda e^{-\lambda y}\left(0 \le \infty;\ \lambda > 0\right), \tag{1}$$

representing the death density function (DDF) corresponding to the survival time Y is assumed. We also assume that the hazard λ for a patient under clinical investigation is linearly related to measurements on 'p' concomitant variables $x_1, x_2, \ldots, x_p$ as follows

$$\lambda = \lambda\left(t; \underset{\sim}{x}\right) = \beta_0 + \sum_{r=1}^{p}\beta_r x_r = \sum_{r=1}^{p}\beta_r x_r \left(0 < \beta_0, \beta_1, \ldots, \beta_p < \infty\right) \tag{2}$$

where $\beta_0, \beta_1, \ldots, \beta_p$ are $(p + 1)$ unknown parameters and $x_0 = 1$ is a dummy variable which is set equal to 1 for all individuals for notational symmetry. In (2) β_0 can be interpreted as the underlying hazard rate or the intercept. Of course, it is necessary that the right hand side of (2) be positive. The above hazard model can also be written as

$$\lambda\left(t; \underset{\sim}{x}\right) = \underset{\sim}{x}\ \underset{\sim}{\beta} \tag{3}$$

where $\underset{\sim}{x} = (x_0, x_1, \ldots, x_p)$ is a $1 \times (p + 1)$ vector of concomitant variables measured on the individual under clinical investigation and $\underset{\sim}{\beta} = (\beta_0, \beta_1, \ldots, \beta_p)'$ is a $(p + 1) \times 1$ vector of unknown parameters.

A natural extension of the model (2) is a dose-response model with hazard as a polynomial function of concomitant variables covering the situations wherein some concomitant variables are functions of others. In dose-response studies, Y represents the time to occurrence of a toxic response and x represents the dose metameter, the hazard can be expressed in the form (2) with $\underset{\sim}{x} = (x^0, x^1, \ldots, x^q)$ and $\underset{\sim}{\beta} = (\beta_0, \beta_1, \beta_2 \ldots, \beta_q)'$, where q is the number of stages in the dose-response phenomena.

Prentice *et al.* [12] gave specific applications of the Cox model to the analysis of dose-response experiments. The detailed account of dose-response models is available in an expository paper by Kalbfleisch *et al.* [13].

Bayesian and hierarchical Bayesian estimation of the parameters $\beta_0, \beta_1, \ldots, \beta_p$, the hazard rate, and the survival function are presented here under the assumptions of the squared error loss function (SELF) and suitable joint prior density of $(\beta_0, \beta_1, \ldots, \beta_p)$. A numerical illustration based on the model (2) is presented for survival data set on advanced lung cancer patients.

2. TOOLS AND TECHNIQUES

2.1. Model Parameters

Under the model assumptions (1) and (2), the hazard rate (HR) and the survival function (SF) are respectively given by

$$h\left(t;\underset{\sim}{x}\right)=\sum_{r=0}^{p}\beta_r x_r \tag{4}$$

$$S\equiv S\left(t;\underset{\sim}{x}\right)=\exp\left[-\left(\sum_{r=0}^{p}\beta_r x_r\right)t\right]\qquad (t>0) \tag{5}$$

The SF (5) gives the probability of survival of an individual with a given vector $\underset{\sim}{x}$ of concomitant variables, up to time t measured from the chosen origin, which may be the start of the clinical study or the point at diagnosis.

2.2. Data Set

It is assumed that 'n' individuals enter the clinical study at different points of time and the clinical study lasts a predetermined follow-up period $t = T_0$. Let 'd' be the number of individuals responding prior to the follow-up period T_0, then the rest of individuals, say $s = (n - d)$ consist of those who are lost to follow-up at different time points during the study and those who did not respond till the end of the clinical study. This type of censoring is also known as "progressive censoring" in the literature. It is also assumed that measurements on $(p + 1)$ concomitant variables for all the patients are also available. For this situation the sample data will consist of the observation vectors $(t_j, x_{j0}, x_{j1}, \ldots, x_{jp})$, $j = 1, 2, \ldots, d$ and $(t'_k, x'_{k0}, x'_{k1}, \ldots x'_{kp})$, $k = 1, 2, \ldots, s$, where t_j denotes the time-to-response of the j^{th} individual measured from his entry point, t'_k denotes the censored response-time of the k^{th} individual and x_{jr} and x'_{kr}, $r = 0, 1, 2, \ldots, p$ denote r^{th} concomitant variable on the said j^{th} and k^{th} individuals respectively.

2.3. Likelihood Function

For the hazard model (2) and the Type III censored sample data set described earlier LF works out as

$$\ell\left(\underset{\sim}{\beta}\right)=\left[\prod_{j=1}^{d}\left(\beta_0 x_{j0}+\beta_1 x_{j1}+\ldots+\beta_p x_{jp}\right)\right]e^{-\sum_{r=0}^{p}\beta_r Q_r} \tag{6}$$
$$\left(0<\beta_0,\beta_1,\ldots,\beta_p<\infty\right)$$

where

$$Q_r=\left[\sum_{j=1}^{d}t_j x_{jr}\right]+\left[\sum_{k=1}^{s}t'^{k}x'^{kr}\right],\qquad r=0,1,2,\ldots,p \tag{7}$$

The product term in (6) can be written as a sum as

$$\prod_{j=1}^{d}\left(\beta_0 x_{j0}+\beta_1 x_{j1}+\ldots+\beta_p x_{jp}\right)=\sum{}^{*}S_{\underset{\sim}{m},d}\,\beta_0^{m_0}\beta_1^{m_1}\ldots\beta_p^{m_p} \tag{8}$$

where $\sum^*$ is the sum over all possible combinations of $m_0, m_1, \ldots, m_p$, such that

$$\sum_{r=0}^{p}m_r=d\qquad m_r\in(0,1,2,\ldots,d) \tag{9}$$

and for given $(m_0, m_1, \ldots, m_p)$, $S_{\underset{\sim}{m}}$, d has been defined in the appendix. Hence, the LF can be written as

$$\ell\left(\underset{\sim}{\beta}\right)=\sum{}^{*}S_{\underset{\sim}{m},d}\left\{\prod_{r=0}^{p}\beta_r^{m_r}e^{-\beta_r Q_r}\right\}\qquad \left(0<\beta_0,\beta_1,\ldots,\beta_p<\infty\right) \tag{10}$$

Throughout this paper, g and g* will be used as the generic notations for the prior and the posterior densities respectively and the loss structure will be characterized by the usual squared error loss function (SELF). We shall also use the generic notation K for the normalization constant.

3. BAYESIAN ESTIMATION OF THE MODEL PARAMETERS

Here it is assumed that prior densities of $\beta_0, \beta_1, \ldots, \beta_p$ mentioned earlier are *a priori* independent and that β_r, $r = 0, 1, 2, \ldots, p$, follows the gamma prior density with known scale and shape hyperparameters b_r and a_r respectively. For this situation, the joint prior density of $(\beta_0, \beta_1, \ldots, \beta_p)$ is given by

$$g\left(\beta_0,\beta_1,\ldots,\beta_p\right)\propto\prod_{r=0}^{p}\beta_r^{a_r-1}e^{-b_r\beta_r}\qquad \left(0<\beta_0,\beta_1,\ldots,\beta_p<\infty\right) \tag{11}$$

The Bayesian results for the non-informative prior quasi-density (NPQD) specified by

$$g\left(\beta_0,\beta_1,\ldots,\beta_p\right)=1\qquad \left(0<\beta_0,\beta_1,\ldots,\beta_p<\infty\right) \tag{12}$$

are also obtained. The role of NPQD in Bayesian analysis is elucidated in a basic paper of Bhattacharya [14]. The raison d'être for priors mentioned above and details

of their use are available in Raiffa and Schlaifer [15].

On the basis of sample data set described earlier, the Bayesian posterior density of ($\beta_0, \beta_1, \ldots, \beta_p < \infty$) is obtained by combining the LF (10) and joint prior density (11) with the help of the Bayes theorem. This works out to be

$$g^*(\beta_0,\beta_1,...,\beta_p) = K^{-1}\sum{}^*S_{\underset{\sim}{m,d}}\left\{\prod_{r=0}^{p}\beta_r^{a_r+m_r-1}e^{-\beta_r(b_r+Q_r)}\right\}$$
$$(0<\beta_0,\beta_1,...,\beta_p<\infty) \quad (13)$$

where

$$K = \sum{}^*S_{\underset{\sim}{m,d}}\left\{\prod_{r=0}^{p}\frac{\Gamma(a_r+m_r)}{(b_r+Q_r)^{a_r+m_r}}\right\} \quad (14)$$

From (13), the marginal posterior density of β_r (r = 0, 1, . . , p) is given by

$$g^*(\beta_r) = K^{-1}\sum{}^*S_{\underset{\sim}{m,d}}\beta_r^{a_r+m_r-1}e^{-\beta_r(b_r+Q_r)}\left\{\prod_{r\neq u=0}^{p}\frac{\Gamma(a_u+m_u)}{(b_u+Q_u)^{a_u+m_u}}\right\} \quad (15)$$
$$(0<\beta_r<\infty;\ r=0, 1, 2, ..., p)$$

Under the assumption of the SELF, the Bayes estimator of β_r (r = 0, 1, 2, . . ., p) and its posterior variance respectively are obtainable from the following expressions

$$\hat{\beta}_r = K^{-1}\sum{}^*S_{\underset{\sim}{m,d}}\frac{(a_r+m_r)}{(b_r+Q_r)}\left\{\prod_{u=0}^{p}\frac{\Gamma(a_u+m_u)}{(b_u+Q_u)^{a_u+m_u}}\right\} \quad (16)$$

$$V(\beta_r) = K^{-1}\sum{}^*S_{\underset{\sim}{m,d}}\frac{(a_r+m_r)(a_r+m_r+1)}{(b_r+Q_r)^2}\left\{\prod_{u=0}^{p}\frac{\Gamma(a_u+m_u)}{(b_u+Q_u)^{a_u+m_u}}\right\}-\left(\hat{\beta}_r\right)^2 \quad (17)$$

The Bayes estimator of the SF is given by the expression:

$$\hat{S}(t;\underset{\sim}{x}) = \int_0^\infty\int_0^\infty..\int_0^\infty \exp\left[-(\beta_0 x_0+\beta_1 x_1+...+\beta_p x_p)t\right] g^*(\beta_0,\beta_1,...,\beta_p)\,d\beta_0 d\beta_1..d\beta_p \quad (18)$$

Evaluating the above multiple integral we obtain

$$\hat{S}(t;\underset{\sim}{x}) = K^{-1}\sum{}^*S_{\underset{\sim}{m,d}}\left\{\prod_{u=0}^{p}\frac{\Gamma(a_r+m_r)}{(b_r+Q_r+x_r t)^{a_r+m_r}}\right\} \quad (19)$$

Similarly, the posterior variance of $\hat{S}(t; x)$ is obtained as

$$V\hat{S}(t;\underset{\sim}{x}) = K^{-1}\sum{}^*S_{\underset{\sim}{m,d}}\left\{\prod_{u=0}^{p}\frac{\Gamma(a_r+m_r)}{(b_r+Q_r+2x_r t)^{a_r+m_r}}\right\}-\left(\hat{S}(t;\underset{\sim}{x})\right)^2 \quad (20)$$

The Bayes estimator of the HR of the patient having concomitant variable vector x = ($x_0, x_1, \ldots, x_p$) is obtained as

$$\hat{h} = \sum_{r=0}^{p}x_r\hat{\beta}_r \quad (21)$$

where $\hat{\beta}_r$ (r = 0, 1, 2, . . . , p) is to be substituted from (16). The Bayesian results for the NPQD (12) can be obtained from those corresponding to the prior density (11) given above, by replacing $b_r = 0$, and $a_r = 1$, r = 0, 1, 2, . . . p.

4. HIERARCHICAL BAYESIAN ESTIMATION OF THE MODEL PARAMETERS

In hierachical Bayes approach [16-20] a second stage prior is assumed for the unknown hyperparameter of the prior distribution assumed at the first stage. Here the hirachical Bayes (HB) estimators of the parameters: β_r (r = 0, 1, 2, . . . , p) , the HR and the SF have been derived under the assumptions of the SELF and the gamma distributions as prior and hyperprior densities. At the first stage β_r (r = 0, 1, 2, . . . , p) is assumed to follow the gamma prior density.

$$g(\beta_r) = g(\beta_r \mid b_r) = \frac{b_r^{a_r}}{\Gamma a_r}\beta_r^{a_r-1}e^{-b_r\beta_r}$$
$$(0<\beta_r<\infty;\ b_r, a_r>0;\ a_r \text{ known}) \quad (22)$$

For the unknown scale hyperparameter b_r in (22) the following GPD as hyperprior is assumed at the second stage

$$g(b_r) = g(b_r \mid p_r,\ v_r) = \frac{\rho_r^{v_r}}{\Gamma v_r}b_r^{v_r-1}e^{-\rho_r b_r}$$
$$(0<b_r<\infty;\ \rho_r, v_r>0;\ \rho_r, v_r \text{ known}) \quad (23)$$

From (22) and (23) the prior pdf of β_r is obtained as

$$g(\beta_r) = \int_0^\infty g(\beta_r,\ b_r)db_r = \int_0^\infty g(\beta_r \mid b_r)g(b_r)\,db_r \quad (24)$$

Assuming *a priori* independence, the joint prior density of ($\beta_0, \beta_1, \ldots, \beta_p$) in this case comes out to be

$$g(\beta_0, \beta_1, ..., \beta_p) \propto \left\{\prod_{r=0}^{p}\frac{\beta_r^{a_r-1}}{(\rho_r+\beta_r)^{\rho_r}}\right\} \quad (25)$$

On the basis of sample data set described earlier obtained by combining the LF (10) joint prior density (25)

with the help of the Bayes theorem. This works out to be

$$g^*(\beta_0, \beta_1, ..., \beta_p) = K^{-1} \sum^* S_{\underset{\sim}{m},d} \left\{ \prod_{r=0}^{p} \frac{\beta_r^{\,m_r+a_r-1} e^{-\beta_r Q_r}}{(\rho_r+\beta_r)^{v_r}} \right\} \quad (26)$$

where K can be computed by using the result (A.2) of the appendix as

$$K = \sum^* S_{\underset{\sim}{m},d} \left\{ \prod_{r=0}^{p} \frac{\Gamma(m_r+a_r) e^{\rho_r Q_r/2} \rho_r^{(\delta_1-1)/2}}{Q_r^{(\delta_1+1)/2}} \quad \frac{\delta_2^W}{2}, \frac{-\delta_1^{(\rho_r Q_r)}}{2} \right\} \quad (27)$$

where

$$\delta_1 = m_r + a_r - v_r \quad (28)$$

and

$$\delta_2 = 1 - v_r - m_r - a_r \quad (29)$$

From (26) the marginal posterior density of β_r (r = 0, 1, . . , p) is obtained as

$$g^*(\beta_r) = K^{-1} \sum^* S_{\underset{\sim}{m},d} A(\underset{\sim}{m}) \left\{ \frac{\beta_r^{mr+ar-1} e^{-\beta_r Q_r}}{(\rho_r+\beta_r)^{v_r}} \right\} \quad (30)$$

where

$$A(\underset{\sim}{m}) = \prod_{r\neq u=0}^{d} \frac{\Gamma(m_u+a_u) e^{\rho_u Q_u/2} \rho_u^{(\delta^*_1-1)/2}}{Q_u^{(\delta_1+1)/2}} \quad \frac{W_{\delta^*_2}}{2}, \frac{-\delta^{*(\rho_u Q_u)}_1}{2} \quad (31)$$

where

$$\delta^*_1 = m_u + a_u - v_u \quad (32)$$

and

$$\delta^*_2 = 1 - v_u - m_u - a_u \quad (33)$$

Using the BPD (30) and the result (A.3) of the appendix, the HB estimator of β_r(r = 0, 1, 2, . . . , p) is given by

$$\tilde{\beta}_r = K^{-1} \sum^* S_{\underset{\sim}{m},d} B(\underset{\sim}{m})(m_r+a_r) \left[\frac{\rho_r}{Q_r}\right]^{1/2} \frac{W_{\delta_{2-1}}}{2}, \frac{-(\delta_1+1)^{(\rho_r Q_r)}}{2} \quad (34)$$

where

$$B(\underset{\sim}{m}) = \frac{\Gamma(m_r+a_r) e^{\rho_r Q_r/2} \rho_r^{(\delta_1-1)/2}}{Q_r^{(\delta_1+1)/2}} A(\underset{\sim}{m}) \quad (35)$$

Similarly, the posterior variance of $\tilde{\beta}_r$ (r = 0, 1, 2, . . . , p) is computed as

$$V(\tilde{\beta}_r) = K^{-1} \sum^* S_{\underset{\sim}{m},d} B(\underset{\sim}{m})(m_r+a_r)(m_r+a_r+1) \left\{\frac{\rho_r}{Q_r}\right\}^{1/2} \frac{W_{(\delta_2-2)}}{2}, \frac{-(\delta_1+2)^{(\rho_r Q_r)}}{2} \quad (36)$$

The HB estimator of S and its posterior variance respectively are evaluated as

$$\tilde{S}(t; \underset{\sim}{x}) = \sum^* S_{\underset{\sim}{m},d} \left\{ \prod_{r=0}^{p} \frac{\Gamma(m_r+a_r) e^{\rho_r (Q_r+x_r t)} \rho_r^{(\delta_1-1)/2}}{(Q_r+x_r t)^{(\delta_1+1)/2}} \quad \frac{W_{\delta_2}}{2}, \frac{-\delta_1^{(\rho_r [Q_r+x_r t])}}{2} \right\} \quad (37)$$

and

$$V(\tilde{S}t; \underset{\sim}{x}) = \sum^* S_{\underset{\sim}{m},d} \left\{ \prod_{r=0}^{p} \frac{\Gamma(m_r+a_r) e^{\rho_r (Q_r+2x_r t)} \rho_r^{(\delta_1-1)/2}}{(Q_r+2x_r t)^{(\delta_1+1)/2}} \quad \frac{W_{\delta_2}}{2}, \frac{-\delta_1^{(\rho_r [Q_r+2x_r t])}}{2} \right\} - \left(\tilde{S}(t; \underset{\sim}{x})\right)^2 \quad (38)$$

The HB estimator of the HR for the patient having concomitant variable vector x = (x_0, x_1, . . . , x_p) is given by

$$\tilde{h} = \sum_{r=0}^{p} x_r \tilde{\beta}_r \quad (39)$$

where $\tilde{\beta}_r$ (r=0, 1, 2, . . . , p) is to be substituted from (34).

5. NUMERICAL ILLUSTRATION ON LUNG CANCER PATIENTS

To illustrate the use of the model characterized by the **Eq.4**, the survival data set on 137 advanced lung cancer patients previously studied by Prentice [21] is used. Patients were randomized according to one of two chemotherapeutic agents: standard and test. To study the possible differential effects of therapy on tumor cell type, tumors were classified into four broad groups termed as squamous, small, adeno and large. The author used four covariates: performance status, time from diagnosis to study, age, and previous therapy to be denoted by x_1, x_2, x_3 and x_4 respectively. Assuming the intercept to be zero and taking noninformative prior quasi-density (NPQD) at (12) for (β_1, β_2, β_3, β_4) the Bayes estimates of the model parameters are obtained for different tumor types and the results for the standard and the test therapies are compared.

The Bayes estimates of β_1, β_2, β_3, and β_4 for different

Table 1. Estimates of model parameters for different tumor types.

Type of therapy	i	Estimates of β_i			
		Type of Tumor			
		Squamous	Small	Adeno	Large
Standard	1	2.331×10^{-5}	1.841×10^{-5}	3.707×10^{-5}	1.027×10^{-5}
	2	4.274×10^{-5}	6.649×10^{-5}	6.690×10^{-5}	1.010×10^{-4}
	3	2.206×10^{-5}	1.484×10^{-5}	6.316×10^{-5}	1.520×10^{-5}
	4	2.091×10^{-4}	2.364×10^{-4}	8.790×10^{-3}	1.802×10^{-4}
Test	1	5.753×10^{-6}	3.352×10^{-5}	3.539×10^{-5}	1.739×10^{-5}
	2	5.041×10^{-5}	1.445×10^{-4}	2.934×10^{-4}	1.561×10^{-4}
	3	7.354×10^{-6}	6.449×10^{-5}	3.584×10^{-5}	2.116×10^{-5}
	4	6.563×10^{-5}	8.231×10^{-4}	7.890×10^{-4}	2.201×10^{-4}

Table 2. Estimates of the survival function for different tumor types.

Therapy	Survival time in days	Estimates of the SF			
		Type of Tumor			
		Squamous	Small	Adeno	Large
Standard	10	0.9488	0.9515	0.4405	0.9583
	20	0.9007	0.9057	0.2426	0.9186
	30	0.8554	0.8627	0.1506	0.8810
	40	0.8128	0.8221	0.1008	0.8451
	50	0.7726	0.7837	0.0709	0.8109
	60	0.7347	0.7475	0.0518	0.7784
	70	0.6990	0.7133	0.0389	0.7475
	80	0.6653	0.6810	0.0298	0.7179
	90	0.6335	0.6504	0.0234	0.6898
	100	0.6034	0.6215	0.0185	0.6630
Test	10	0.9810	0.8580	0.8637	0.9422
	20	0.9625	0.7402	0.7497	0.8881
	30	0.9443	0.6417	0.6536	0.8376
	40	0.9265	0.5589	0.5722	0.7904
	50	0.9091	0.4887	0.5028	0.7462
	60	0.8921	0.4290	0.4434	0.7048
	70	0.8755	0.3779	0.3923	0.6660
	80	0.8592	0.3339	0.3482	0.6297
	90	0.8432	0.2960	0.3099	0.5956
	100	0.8276	0.2631	0.2765	0.5636

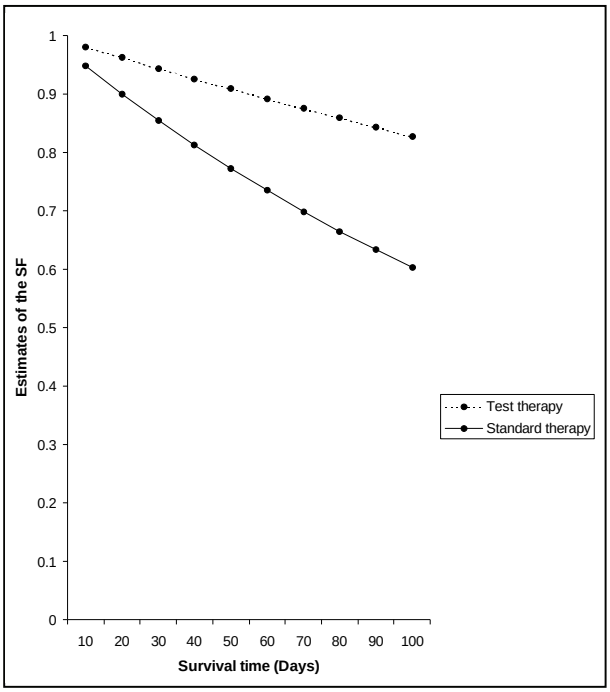

Figure 1. Estimates of the survival functions of standard and test therapies for 'squamous' tumor cell.

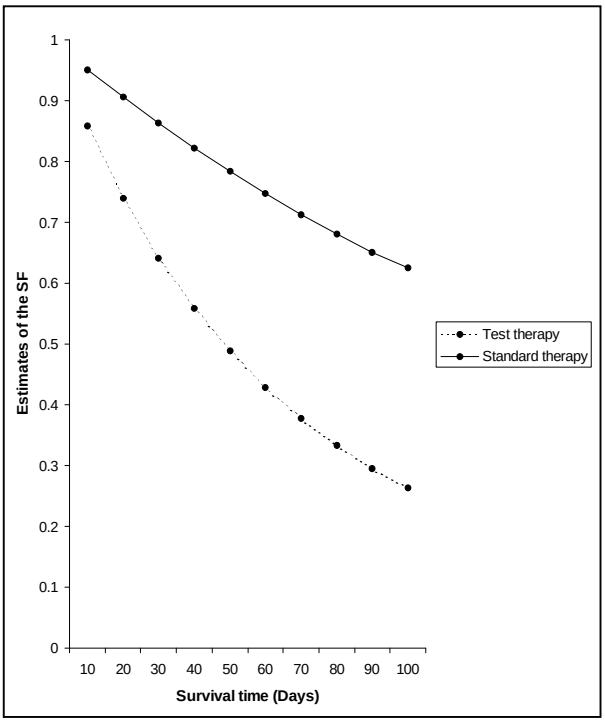

Figure 2. Estimates of the survival functions of standard and test therapies for 'small' tumor cell type.

tumor types for the standard and test therapies are shown in **Table 1**. The estimates of the survival function S = S (t; x) for given vector $\underset{\sim}{x}$ = (60, 9, 63, 10) (say) of con-

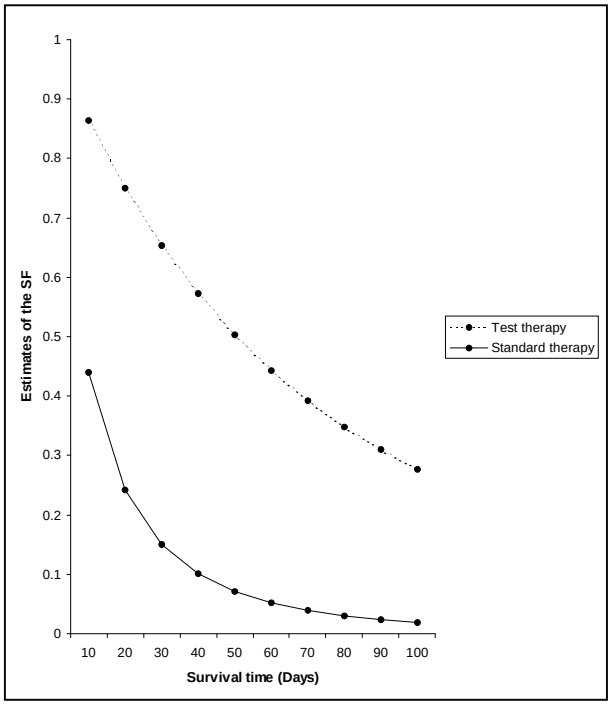

Figure 3. Estimates of the survival functions of standard and test therapies for 'adeno' tumor cell type.

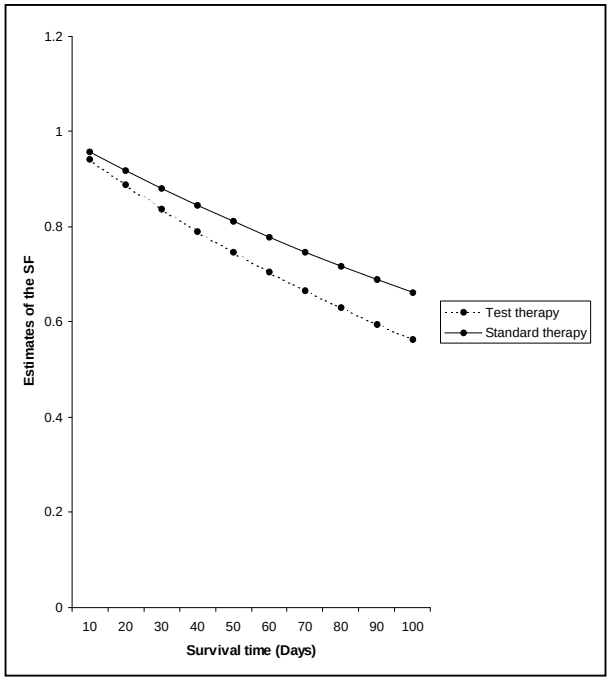

Figure 4. Estimates of the survival functions of standard and test therapies for 'large' tumor cell type.

comitant variables are presented in **Table 2**. **Figures 1** to **4** provide the plots of estimates of the survival function of standard and test therapies for different tumor cell types.

From the comparison of estimates for the two therapies, for given arbitrary concomitant vector $\underset{\sim}{x}$ for squamous and adeno tumor cell types, the test therapy prolong the survival of patients. The test therapy comes out to be the most effective for adeno tumor cell type for this particular case.

6. ACKNOWLEDGEMENTS

The present work is respectful homage to my respected teacher Late Professor Sameer K Bhattacharya, Head, Department of Mathematics and Statistics, University of Allahabad India. The paper was written when author was working asAssistant Professor, Department of Social and Preventive Medicine, MLN Medical College, Allahabad. The help rendered by Dr. Nand Kishore Singh, Department of Mathematics and Statistics, University of Allahabad, at each stage of the present work is greatly acknowledged. The work in the present form was also not possible without critical evaluation and computer programming by Dr. AK Lal, Indian Institute of Technology, Kanpur India. The author is also thankful to Mr. Parminder Kumar, Data Entry Operator, GMCH-32, Chandigarh for his help in typing the manuscript.

REFERENCES

[1] Cox, D.R. (1964) Some applications of exponential ordered scores. *JRSS, Series B*, **26**, 103-110.

[2] Feigl, P. and Zelen, M. (1965) Estimation of exponential survival probabilities with concomitant information. *Biometrics*, **21(4)**, 826-838.

[3] Zippin, C. and Armitage, P. (1966) Use of concomitant variables and incomplete survival information in the estimation of an exponential survival parameter. *Biometrics*, **22**, 665-672.

[4] Glasser, M. (1967) Exponential survival with covariance. *Journal of American Statistical Association*, **62**, 561-568.

[5] Cox, D.R. and Snell, E.J. (1968) A general definition of residuals, (with Discussion). *Journal of the Royal Statistical Society B*, **30**, 248-275.

[6] Crowley, J. and Hu, M. (1977) Covariance analysis of heart transplants survival data. *Journal of American Statistical Association*, **72(357)**, 27-36.

[7] Mantel, N. and Myers, M. (1971) Problems of convergence of maximum likelihood iterative procedures in multiparameter situation. *Journal of American Statistical Association*, **66(335)**, 484-491.

[8] Cox, D.R. (1972) Regression models and life tables, (with discussion), *Journal of the Royal Statistical Society B*, **34(2)**, 187-220.

[9] Byar, D.P., Huse, R., Bailar, J.C. and The Veterans Administration Cooperative Urological Research Group (1974) An exponential model relating censored survival data and concomitant information for prostatic cancer patients. *Journal of National Cancer Institute*, **52(2)**, 321-326.

[10] Greenberg, R.A. and Bayard, S. (1974) Selecting concomitant variables using a likelihood ratio step-down procedure and a method of testing goodness of fit in an exponential survival model. *Biometrics*, **30(4)**, 601-608.

[11] Bhattacharya, S.K., Singh, N.K. and Kumar, D. (1995) Bayesian survival analysis of clinical data using a covariate. *Revista Brasileira de Probabilidade e Estadistica*, **9**, 141-156.

[12] Prentice, R.L., Peterson, A.V. and Marek, P. (1982) Dose mortality relationships in RFM mice following 137 gamma ray irradiation. *Radiation Research*, **90(1)**, 57-76.

[13] Kalbfleisch, J.D., Krewski, D.R. and Van Ryzin, J. (1983) Dose-response models for time to response toxicity data. *The Canadian Journal of Statistics*, **11(1)**, 25-49.

[14] Bhattacharya, S.K. (1967) Bayesian approach to life testing and reliability estimation. *Journal of American Statistical Association*, **62**, 48-62.

[15] Raiffa, H. and Schlaifer, R. (1961) Applied statistical decision theory. Harward University Press, Boston.

[16] Berger, J. (1986) Multivariate estimation: Bayes, empirical bayes and stein approaches. *Society for Industrial and Applied Mathematics*, Philadelphia.

[17] Bhattacharya, S.K. and Tiwari, R.C. (1992) Hierarchical Bayesian reliability analysis using Erlang families of priors and hyperpriours. *Microelectronics Reliability*, **32(1-2)**, 241-247.

[18] Bhattacharya, S.K., Singh, N.K. and Tiwari, R.C. (1992) Hierarchical Bayesian survival Bayesian survival analysis based on generalized exponential model. *Metron*, **50(3)**, 161-183.

[19] Good, I.J. (1980) Some history of the hierarchical bayesian methodology in bayesian statistics. Bernardo, J.M., De Groot, M.H., Lindley, D.V. and Smith, A.F.M., Eds., University Press, Valencia.

[20] Stangl, D.K. and Greenhouse, J.B. (1998) Assessing placebo response using Bayesian hierarchical survival models. *Lifetime Data Analysis*, **4(1)**, 5-28.

[21] Prentice, R.L. (1973) Exponential survival with censoring and explanatory variables. *Biometrika*, **60(2)**, 279-288.

[22] Gradshteyn, I.S. and Ryzhik, I.M. (1980) Tables of Integrals, Series and Products. Academic Press, New York.

APPENDIX

The definition of $S_{\underset{\sim}{m,d}}$ notation and a mathematical result on a special function used in the present work are presented here.

1) The $S_{\underset{\sim}{m,d}}$ Notation

Let X denotes a d x (p + 1) matrix of concomitant variables given below

$$X = \begin{pmatrix} x_{10} & x_{11} & \cdots & x_{1p} \\ x_{20} & x_{21} & \cdots & x_{2p} \\ & & & \\ x_{d0} & x_{d1} & \cdots & x_{dp} \end{pmatrix} \qquad (A.1)$$

and $\underset{\sim}{m} = (m_0, m_1, \ldots, m_p)$. For given combinations of $m_0, m_1, \ldots, m_p$, satisfying the condition:

$$m_0 + m_1 + \ldots + m_p = d \qquad (A.2)$$

$S_{\underset{\sim}{m,d}}$ is given by the sum of all products of m_r elements from r^{th} column (r = 0, 1, 2, . . . , p) of the matrix X, such that no two elements in the product term lie in same row of the matrix.

2) Integral for the Whittaker Function

The following variant of the integral representation ([22] p.319, Sec. 3. 383, Formula 4) has been used in the present work:

$$\int_0^\infty \frac{w^{A-1}e^{-Bw}}{(v+w)^q}\,dw = \Gamma A\, e^{Bv/2} B^{(q-A-1)/2} v^{(A-q-1)/2} W_{\frac{(1-q-A)}{2}, \frac{(q-A)}{2}}(Bv) \qquad (A.3)$$

This results holds good provided that ReA > 0, ReBν > 0, where $W_{s_1, s_2}(\,.\,)$ is the well known Whittaker function.

J. Biomedical Science and Engineering, 2010, 3, 719-726 **JBiSE**
doi:10.4236/jbise.2010.37096 Published Online July 2010 (http://www.SciRP.org/journal/jbise/).

A novel voting system for the identification of eukaryotic genome promoters

Lin Lei[3], Kaiyan Feng[4], Zhisong He[5], Yudong Cai[1,2]*

[1]Institute of System Biology, Shanghai University, Shanghai, China;
[2]Centre for Computational Systems Biology, Fudan University, Shanghai, China;
[3]School of Computer Engineering, Nanyang Technological University, Singapore;
[4]Division of Imaging Science & Biomedical Engineering, The University of Manchester, Manchester, UK;
[5]Department of Bioinformatics, College of Life Sciences, Zhejiang University, Hangzhou, China.
Email: cai_yud@yahoo.com.cn

Received 5 April 2010; revised 6 May 2010; accepted 9 May 2010.

ABSTRACT

Motivation: Accurate identification and delineation of promoters/TSSs (transcription start sites) is important for improving genome annotation and devising experiments to study and understand transcriptional regulation. Many promoter identifiers are developed for promoter identification. However, each promoter identifier has its own focuses and limitations, and we introduce an integration scheme to combine some identifiers together to gain a better prediction performance. Result: In this contribution, 8 promoter identifiers (Proscan, TSSG, TSSW, FirstEF, eponine, ProSOM, EP3, FPROM) are chosen for the investigation of integration. A feature selection method, called mRMR (Minimum Redundancy Maximum Relevance), is novelly transferred to promoter identifier selection by choosing a group of robust and complementing promoter identifiers. For comparison, four integration methods (SMV, WMV, SMV_IS, WMV_IS), from simple to complex, are developed to process a training dataset with 1400 sequences and a testing dataset with 378 sequences. As a result, 5 identifiers (FPROM, FirstEF, TSSG, eponine, TSSW) are chosen by mRMR, and the integration of them achieves 70.08% and 67.83% correct prediction rates for a training dataset and a testing dataset respectively, which is better than any single identifier in which the best single one only achieves 59.32% and 61.78% for the training dataset and testing dataset respectively.

Keywords: MRMR (Minimum Redundancy Maximum Relevance); Transcription Start Sites (TSS); Promoter Identification; Promoter Identifier Integration

1. INTRODUCTION

Promoter, a short DNA sequence, is the binding site of RNA polymerases. It determines the transcription start site (TSS). After RNA polymerase binding to a promoter, the promoter initiates the transcription and indicates where the transcription should start. In order to be recognized by the RNA polymerases, the structure of promoters is rather stable, e.g. in eukaryotic genome, many promoters contain TATA box, which can help locate promoters by searching TATA sequences. Besides TATA box, functional motifs, oligonucleotide composition and compositional features are also used for promoter identification [1-8]. However, each promoter identifier has its own focuses. Even when the same identification strategy is applied by some different identifiers, they differ in detail. Since some promoter identifiers maybe complement with each other because their principles are different, their integration will be able to enhance the promoter identification performance [9,10]. This paper investigates a novel way to combine some promoter identifiers together to improve the identification rate.

Voting has long been recognized as a useful integration tool to improve the robustness of a decision system. Nearly all investigations find that if a decision gains the majority votes, that decision is more likely to be the right decision. These investigations are found in all kinds of research areas, including pattern recognitions [11-13], character and hand-writing recognitions [14-17], image analysis [18,19], credit card slip processing [20] and speaker identification [21]. Voting has also been applied to identify promoters/TSSs [9,22]. In [10], 6 promoter identifiers were investigated, and 5 of them were integrated to enhance the recognition rate by excluding a non user-friendly and poor-performed on-line promoter identifier. In a recent work [22], Won *et al.*

investigated 8 promoter/TSS (transcription start site) identifiers and tried to find out what combinations were best for the identification. They introduced a cut-off value to exclude any promoter identifiers whose identification rate was lower than the cut-off value. However, the work in [22] did not take consideration of the order of adding the promoters into the integration, whereas, the order will also affect the identification performance, as will be explained later in the paragraph. In this study, 8 promoter identifiers (Proscan, TSSG, TSSW, FirstEF, eponine, ProSOM, EP3, FPROM) are investigated. For the eight promoter identifiers, two criteria should be considered for the integration: firstly, the better the identifiers perform, the more preferable the identifiers should be chosen, and secondly, dissimilar/less-correlated identifiers complement each other better and are also more preferable to be chosen. The first criterion is straightforward. The second criterion is applied because similar identifiers may strengthen each other and dominate the decisions, e.g. if one identifier is used twice, the decision will be biased towards this identifier. Similarly, if too many identifiers are similar to each other, the decision will be biased towards that type of identifiers. Since the two criteria could be incompatible with each other, optimization is needed to balance both criteria. In this paper, identifiers are selected one by another. The order of the identifiers for the selection is important, illustrated by the following example. Suppose 4 identifiers i_1, i_2, i_3 and i_4 are under examination and the combination of i_1 and i_2 produces best results, if identifiers are added according to the list $[i_1, i_4, i_3, i_2]$, the optimized combination can never be found. Thus following the two criteria to make a list is important. mRMR (minimum Redundancy Maximum Relevance) method [23] is originally developed for feature selection, and is transferred into the selection of promoter identifiers to satisfy the two criteria. mRMR tries to maximize the relevance between variables and the targets, which is in accordance with criterion 1, and at the same time, minimize the redundancy between variables, which is in accordance with criterion 2. mRMR is introduced in detail in section 2.3. However, voting cannot solve the intrinsic problems of individual identifiers and the right decision of one identifier will be ignored if most of identifiers vote for the wrong decision. Therefore, future researches are still needed.

For comparison, four integration methods SMV (simple majority voting), WMV (weighted majority voting), SMV_IS (simple majority voting plus identifier selection) and WMV_IS (weighted majority voting plus identifier selection), from simple to complex, are developed to process a training dataset with 1400 sequences and a testing dataset with 378 sequences. As a result, WMV_IS achieves the best TSS-based recognition rates with 70.08% and 67.83% correct recognition rates for the training dataset and testing dataset respectively.

2. MATERIAL AND METHODS

2.1. Datasets

The EPD (The Eukaryotic Promoter Database Current Release 95, http://www.epd.isb-sib.ch/) [24], a promoter database of the EMBL Data Library, is an annotated non-redundant collection of experimentally determined eukaryotic polymerase II promoters. Since promoters are defined and confirmed by experimentally determined TSSs, the underlying promoter definition is given by the position of TSS in EPD database.

First, 1871 human gene sequences were downloaded from the EPD website, and 1778 DNA sequences were chosen by excluding any sequence containing missing base pairs. The sequence length is 1.5 kb while the true TSS is located at a random position on the sequence. These 1778 sequences are then divided into a training dataset with 1400 sequences and a testing dataset with 378 sequences randomly. The training dataset is evaluated by 5-fold cross-validation to obtain the recognition rates for each promoter identifier. These recognition rates are later fed back to weight the identifiers in voting for both training and testing dataset. Since the recognition rates are gained from the training dataset and then fed back to the training dataset for weighting, the recognition might be biased. However, since the identification accuracy is rather stable especially with a large dataset, the bias is neglectable. For scrutiny, a testing dataset is independently used for testing by taking the promoter recognition rates from the training dataset. Please refer to *supplemental material 1* and *supplemental material* 2 for the training datasets and the testing datasets respectively.

2.2. Promoter Identifiers

Many TSS predictors are available on the internet. Eight identifiers are chosen as they have been actively maintained and widely used. These identifiers are Proscan, TSSG, TSSW, FirstEF, eponine, ProSOM, EP3, FPROM. Detail of these identifiers can be found in *Supplemental Material* 3. Their different recognition mechanisms and mathematical architectures may enable them to complement each other during voting.

2.3. MRMR (Minimum Redundancy Maximum Relevance)

Minimum Redundancy Maximum Relevance (mRMR) [23] is first developed by Peng. In mRMR analysis, a good feature is characterized by its relevance with the target variable and its correlation with other features – it will be more likely to be chosen if it is more relevant to

the target class and less correlated with other features. Both relevance and correlation can be estimated by mutual information (MI), indicating how much one vector is related to another. MI is defined as follows:

$$I(x,y)=\iint p(x,y)\log\frac{p(x,y)}{p(x)p(y)}dxdy \quad (1)$$

where x and y are two vectors; $p(x,y)$ is the joint probabilistic density; $p(x)$ and $p(y)$ are the marginal probabilistic densities.

Let Ω denote the whole vector set. The already-selected vector set with m vectors is denoted by Ω_s, and the to-be-selected vector set with n vectors is denoted by Ω_t. Relevance D of a feature f in Ω_t with a target variable c can be computed by **Eq.2**.

$$D=I(f,c) \quad (2)$$

Redundancy R of a feature f in Ω_t with all the features in Ω_s can be computed by **Eq.3**

$$R=\frac{1}{m}\sum_{f_i\in\Omega_s} I(f,f_i) \quad (3)$$

To maximize relevance and minimize redundancy, mRMR function is obtained by integrating **Eq.2** and **Eq. 3**:

$$\max_{f_j\in\Omega_t}\left[I(f_j,c)-\frac{1}{m}\sum_{f_i\in\Omega_s} I(f_j,f_i)\right](j=1,2,...,n) \quad (4)$$

Let the initial $\Omega_s=\{f_i\}$ where f_i is the vector produced by the best performed promoter identifier, and $\Omega_t=\{f_1,f_2,...,f_{i-1},f_{i+1},...,f_n\}$ by excluding only f_i. **Eq.4** is used to obtain one vector by another in totally $n-1$ rounds, resulting a vector list with the selection order $S=\left[f_0^{'},f_1^{'},...,f_h^{'},...,f_{N-1}^{'}\right]$ where h denotes at which round the feature is selected.

In this research, mRMR method is used to rank the 8 promoter identifiers. The predicted/identified results are coded by integer numbers as is described in Subsection 2.6. The real coded promoters are the target vector, and the predicted ones are treated as the input features for the mRMR method.

2.4. Voting Systems

Four voting systems are developed for the promoter recognition. They are Simple Majority Voting (SMV), Weighted Majority Voting (WMV), Simple Majority Voting plus Identifier Selection (SMV_IS), Weighted Majority Voting plus Identifier Selection (WMV_IS).

2.4.1. Simple Majority Voting (SMV)

Each promoter identifier will give a decision. The majority decisions over a TSS are taken as the predicted TSS. This is the simplest voting system that does not require any additional complex computation.

2.4.2. Weighted Majority Voting (WMV)

In SMV, all identifiers are treated equally regardless of their identification capability, while, in WMV, the vote of an identifier is weighted by its recognition rate. For example, when integrating 4 predictors, assume the detected rates for the eight promoter identifiers are 0.4, 0.45, 0.5 and 0.55. The to-be-predicted sample is judged to be a positive one with the first two identifiers, while the other two give out negative results. With SMV, the score of this sample obtained is 2 because two identifiers agree that this sample is in promoter region. But with WMV, the score become (0.4 + 0.45)/(0.4 + 0.45 + 0.5 + 0.55) = 0.447. Here, if the score is no more than 0.5, the sample would be predicted as a negative sample, i.e. not located in promoter. So the output for this sample would be negative. Because the performance of some identifiers is much better than others, these better performed identifiers should be weighted more heavily. The recognition rate is obtained by evaluating the training dataset using cross-validation.

2.4.3. Simple Majority Voting Plus Identifier Selection (SMV_IS)

The 8 investigated algorithms are first ranked by the mRMR method. Identifiers in the topper ranks are regarded to be less redundant between each other and more relevant to the SST recognition. Next, we need to find out how many identifiers should be chosen from the mRMR ranking list $S=\left[f_0^{'},f_1^{'},...,f_7^{'}\right]$ by adding one identifier by other from the list as the candidate identifiers, starting from the first identifier $f_0^{'}$. Each time when an identifier is added, SMV is applied among the selected identifiers. The integrated identifier through SMV, with the highest correct recognition rate evaluated by cross-validation test, is regarded as the optimized identifier/predictor of SMV_IS.

2.4.4. Weighted Majority Voting Plus Identifier Selection (WMV_IS)

The only difference between SMV_IS and WMV_IS is that, towards the integration of the candidate identifiers, WMV is applied instead of SMV.

2.5 Detection and Prediction Rate

If an identifier outputs a predicted promoter instead of an explicit TSS, the prediction is regarded to be correct if the predicted promoter is within the range from 200bp upstream to 100bp downstream of the experimentally determined TSS. The Detected TSS Rate is defined as the number of recognized TSSs divided by the total number of experimentally determined TSSs, and Non-

detected TSS Rate is calculated as 1 minus the detected rate. The Correct Prediction Rate is defined as the number of correctly recognized TSSs divided by the total number of the predicted TSSs, and the False Prediction Rate is calculated as 1 minus the correct prediction rate.

The prediction rates we use are defined as follows:

$$\text{Detected TSS Rate} = \frac{\text{the number of recognized TSSs}}{\text{the total number of experimentally determined TSSs}}$$

Non - detected TSS Rate = 1 - Detected TSS Rate

$$\text{Correct Prediction Rate} = \frac{\text{the number of correctly recognized TSSs}}{\text{the total number of the predicted TSSs}}$$

False Prediction Rate = 1 - Correct Prediction Rate

2.6. Generate Input Matrix for MRMR Algorithm

First the prediction results need to be organized in a way that can be input into mRMR. Each residue is predicted by N predictors (N is the number of predictors used), and its true identity is determined by experiment. Thus each residue can be coded by N + 1 digits. The experimentally determined TSSs are regarded as the target variable of mRMR while the N predicted TSSs are regarded as the features of mRMR.

The final matrix is a 1-0 matrix of 2100000 × (N + 1) (2100000 = 1400 × 1500), including the true TSS region and N prediction results. Each sequence consists of 1500 nucleotides, and the matrix contains all the 1400 sequences. The input matrix is shown in **Figure 1**. The first column: The sites from 200bp upstream to 100bp downstream of the TSS are set to be 1, and others are set to be 2. The other N columns: The predicted TSSs are set to be 1, and others are set to be 0.

Then mRMR is applied to filter the features and get the rank.

All supplemental materials mentioned above are available upon request.

3. RESULTS

3.1. Training Sets

3.1.1. The Prediction Results of the Eight Predictors

The training dataset (1400 sequences) were input into the 8 promoter predictors (refer to Subsection 2.2) and the prediction results were produced. The prediction rates (defined in Subsection 2.5) were calculated to rate the performance of the predictors, which are shown in **Table 1**. Correct prediction rate is the best standard to evaluate the prediction performance. If two predictors have similar correct prediction rates, the one achieving significantly better detection rate is regarded to perform better. The predictor FPROM is considered to have best prediction performance since it achieves the best correct prediction accuracy, 59.32%, among all the 8 predictors, and at the same time has a reasonable detected rate (64.57%). Correct prediction rates, obtained by the train- ing dataset, are used to weight the corresponding predictors when they are integrated by WMV and WMV_IS.

3.1.2. Voting Method (SMV and WMV)

The sequence of 1500 bps is divided into 15 regions, each of which contains 100 bps. Votes are counted on each region, *i.e.*, if a predicted TSS falls on a region, the region gets a vote. The prediction rates of Simple Majority Voting are shown in **Table 2**. For the SMV, though its correct prediction rate is a little lower (1.52%) than that of the best predictor FPROM, the detected rate is much higher (8.14%) than FPROM. For WMV, both its detected rate and correct prediction rate are higher than FPROM, indicating that WMV performs better than any individual predictor and also the SMV.

3.1.3. Output of MRMR Program

The mRMR program used in this contribution is downloaded from website http://research.janelia.org/peng/proj/mRMR/. As all of the input vectors are integer vectors, we specify the parameter $t = 0$ in the mRMR program to satisfy the integral calculation. Submit the matrix, resulted from the promoter identifiers to the mRMR program, (resulted from Subsection 2.6) to get the ranks of the identifiers. The list, provided by mRMR, is shown in **Figure 2**.

Table 1. The performance of 8 promoter predictors.

Software	*Detected Rate*	*Correct Prediction Rate*
Proscan	35.79%	47.35%
TSSG	59.36%	47.35%
TSSW	66.21%	49.47%
FirstEF	31.29%	55.17%
eponine	42.86%	50.81%
ProSOM	50.43%	44.17%
EP3	29.50%	49.17%
FPROM	64.57%	59.32%

Table 2. The performance of SMV and WMV.

Software-Integration	*Detected*	*Correct*
SMV(8 identifiers together)	73.36%	63.01%
WMV(8 identifiers together)	68.57%	69.03%

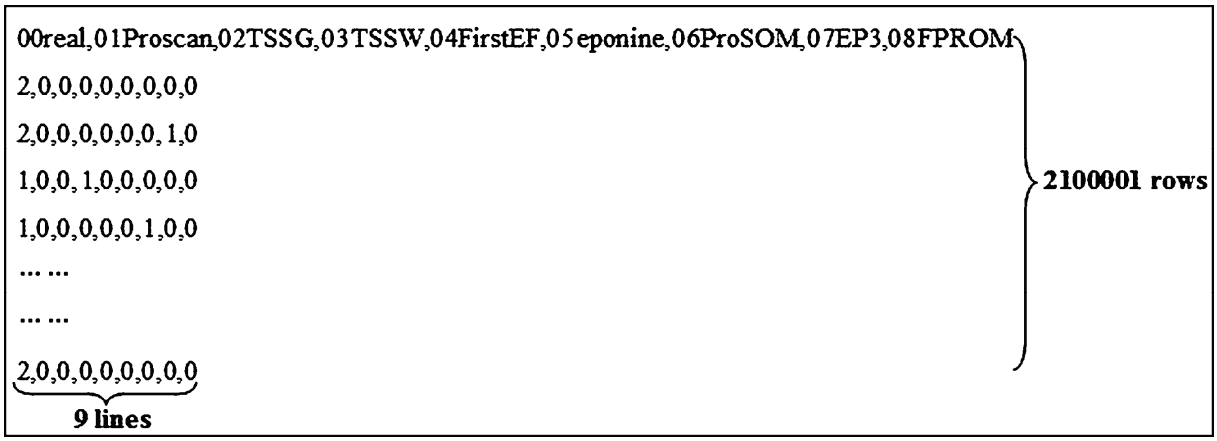

Figure 1. The input matrix of mRMR, suppose N = 8. The first row shows the titles of columns. The first column shows the category of each sample, representing positive ones with 1 while negative ones with 2. The other eight columns show the outputs of the eight individual predictors. If the sample is predicted as in promoter region, the corresponding value of the sample will be assigned to 1, otherwise, 0.

You have specified parameters: no discretization, #fea=8, selection method=MID, #maxVar=8, #maxSample=316.
Target classification variable (#1 column in the input data) has name=00real entropy score=0.982
*** mRMR features ***

Order	Fea	Name	Score
1	8	10FPROM	0.017
2	4	05FirstEF	0.001
3	2	03TSSG	0.000
4	5	06eponine	-0.001
5	3	04TSSW	-0.001
6	1	02Proscan	-0.002
7	6	08ProSOM	-0.003
8	7	09EP3	-0.004

Figure 2. The output rank of mRMR. The first two rows show the parameters of mRMR program, while entropy score was calculated based on the probabilities of each feature obtained from the training dataset. The order of features was calculated based on **Eq.4** in methods.

3.1.4 Software-Integration (SMV_IS and WMV_IS)

According to the rank of mRMR result, we add the identifiers to be integrated through voting one by one. The integration results of SMV_IS and WMV_IS are shown in **Table 3** and **Table 4**. The best correct prediction rate is achieved by integrating 5 identifiers, FPROM, FirstEF, TSSG, eponine and TSSW using WMV_IS, shown in **Table 4**. The correct prediction rate of the integration is 70.08, a slight improvement to the WMV. At the same time, the correct detected rate has also been improved, confirming that WMV_IS performs better than WMV. The integration of 7 identifiers of SMV_IS is also slightly better than including all the 8 identifiers, as is shown in **Table 3**.

The best results obtained from different prediction methods are shown in **Table 5**. When sorted by the correct prediction rates, the order of these prediction methods is WMV_IS>WMV>SMV_IS>SMV>FPROM.

3.2. Testing Sets

3.2.1. Results of the Eight Individual Identifiers

The testing dataset with 378 sequences was input into the eight promoter predictors (refer to Subsection 2.2, two predictors are deleted). The prediction rates (defined in Subsection 2.5) were calculated to rate the performance of the identifiers. These values are shown in **Table 6**.

3.2.2. Identifier-Integration

We use the same voting methods, SMV and WMV, as in Subsection 3.1.2, and methods WMV_IS and SMV_IS, as in Subsection 3.1.4. Because testing dataset is only used for testing, the list and the number of the identifiers are adopted from the training dataset. The purpose of the testing dataset is to validate the results from the training dataset, as it is regarded to be unbiased in the voting. The prediction results of the testing dataset are shown in **Table 7**. By comparing the results in **Table 5** with those

Table 3. The SMV_IS results.

Software-Integration	*Detected*	*Correct prediction*
FPROM	64.57%	59.32%
FPROM&FirstEF	73.00%	57.31%
FPROM&FirstEF&TSSG	77.07%	56.04%
FPROM&FirstEF&TSSG&eponine	76.07%	60.99%
FPROM&FirstEF&TSSG&eponine&TSSW	73.57%	63.35%
FPROM&FirstEF&TSSG&eponine&TSSW&Proscan	72.71%	62.71%
FPROM&FirstEF&TSSG&eponine&TSSW&Proscan&ProSOM	73.57%	64.12%
FPROM&FirstEF&TSSG&eponine&TSSW&Proscan&ProSOM&EP3	73.36%	64.01%

Table 4. The WMV_IS results.

Software-Integration	*Detected*	*Correct Prediction*
FPROM	64.57%	59.32%
FPROM&FirstEF	67.57%	60.37%
FPROM&FirstEF&TSSG	69.29%	64.58%
FPROM&FirstEF&TSSG&eponine	69.43%	68.62%
FPROM&FirstEF&TSSG&eponine&TSSW	69.01%	70.08%
FPROM&FirstEF&TSSG&eponine&TSSW&Proscan	68.79%	68.87%
FPROM&FirstEF&TSSG&eponine&TSSW&Proscan&ProSOM	68.64%	69.01%
FPROM&FirstEF&TSSG&eponine&TSSW&Proscan&ProSOM&EP3	68.57%	69.03%

Table 5. The prediction results of the training dataset.

Predicction Methods	*Detected*	*Correct Prediction*
The best single software(FPROM)	64.57%	59.32%
SMV(8 softwares together)	73.36%	63.01%
WMV(8 softwares together)	68.57%	69.03%
SMV_IS(FPROM&FirstEF&TSSG&eponine&TSSW&Proscan&ProSOM)	73.57%	64.12%
WMV_IS(FPROM&FirstEF&TSSG&eponine&TSSW)	69.01%	70.08%

Table 6. The performance of 8 promoter identifiers using testing sets.

Identifiers	*Detected Rate*	*Correct Prediction Rate*
ProSOM	48.15%	40.63%
EP3	28.04%	45.30%
Proscan	34.92%	45.52%
TSSG	59.52%	47.77%
TSSW	62.96%	49.64%
eponine	46.56%	49.93%
FirstEF	32.80%	60.08%
FPROM	67.99%	61.78%

in **Table 7**, we can tell that WMV_IS performs the best in both training dataset and testing dataset. However, we cannot tell whether SMV or SMV_IS performs better than the best single software FPROM in the testing, since they produces lower prediction accuracy than the FPROM. As a conclusion, several observations can be made: 1) The prediction rate of integrating several identifiers is not necessarily better than the best single identifier, e.g. the SMV and SMV_IS have lower correct prediction rates than the best single identifier; 2) In all cases, the prediction rate is greater with the identifier selection than those without; 3) The prediction rate of WMV is greater than that of SMV.

Table 7. The prediction resluts of the testing dataset.

Software-Integration	*Detected*	*Correct*
The best single software(FPROM)	67.99%	61.78%
SMV(8 softwares together)	71.16%	59.33%
WMV(8 softwares together)	65.87%	67.30%
SMV_IS(FPROM&FirstEF&TSSG&eponine&TSSW &Proscan&ProSOM)	70.10%	62.82%
WMV_IS(FPROM&FirstEF&TSSG&eponine&TSSW)	66.67%	67.83%

4. CONCLUSIONS

We introduce a voting system to integrate several eukaryotic promoter identifiers to predict promoters in the human genome. We find that the integration of several identifiers through a simple voting does not necessarily improve the prediction performance. However, after the identifiers are weighted using their prediction accuracies, the prediction performance is improved. Moreover, filtering the identifiers is able to improve the prediction accuracy than using all identifiers without a filtering. The order of the identifiers to be added, provided by the mRMR, may not be truly optimized since mRMR makes the list without an attempt to integrate the identifiers, which could potentially be a topic for a future research.

5. ACKNOWLEDGEMENTS

This work is supported by National Basic Research Program of China (2004CB518603), grant from Shanghai Commission for Science and Technology (KSCX2-YW-R-112), and the grant supported by Shanghai Leading Academic Discipline Project (J50101).

REFERENCES

[1] Abeel, T., Saeys, Y., Bonnet, E., Rouze, P. and Van de Peer, Y. (2008) Generic eukaryotic core promoter prediction using structural features of DNA. *Genome Research*, **18(2)**, 310-323.

[2] Abeel, T., Saeys, Y., Rouze, P. and Van de Peer, Y. (2008) ProSOM: Core promoter prediction based on unsupervised clustering of DNA physical profiles. *Bioinformatics*, **24(13)**, i24-31.

[3] Davuluri, R.V., Grosse, I. and Zhang, M.Q. (2001) Computational identification of promoters and first exons in the human genome. *Nature Genetics*, **29(4)**, 412-417.

[4] Down, T.A. and Hubbard, T.J. (2002) Computational detection and location of transcription start sites in mammalian genomic DNA. *Genome Research*, **12(3)**, 458-461.

[5] Prestridge, D.S. (1995) Predicting Pol II promoter sequences using transcription factor binding sites. *Journal of Molecular Biology*, **249(5)**, 923-932.

[6] Solovyev, V.V. and Shahmuradov, I.A. **(**2003) PromH: Promoters identification using orthologous genomic sequences. *Nucleic Acid Research*, **31(13)**, 3540-3545.

[7] Solovyev, V.V. and Salamov, A. (1997) The Gene-Finder computer tools for analysis of human and model organism genome sequences. *The Fifth International Conference on Intelligent Systems for Molecular Biology*, 294-302.

[8] Werner, T. (1999) Models for prediction and recognition of eukaryotic promoters. *Mamm Genome*, **10(2)**, 168-175.

[9] Altincay, H. and Demirekler, M. (2000) An information theoretic framework for weight estimation in the combination of probabilistic classifiers for speaker identification. *Speech Communication*, **30(4)**, 255-272.

[10] Liu, R. and States, D.J. (2002) Consensus promoter identification in the human genome utilizing expressed gene markers and gene modeling. *Genome Research*, **12(3)**, 462-469.

[11] Lam, L. and Suen, C.Y. (1994) A theoretical-analysis of the application of majority voting to pattern-recognition. 12*th IAPR International Conference on Pattern Recognition, Jerusalem, Israel*, 418-420.

[12] Lam, L. and Suen, C.Y. (1997) Application of majority voting to pattern recognition: An analysis of its behavior and performance. *IEEE Transactions on Pattern Analysis and Machine Intelligence*, **27(5)**, 553-568.

[13] Stajniak, A., Szostakowski, J. and Skoneczny, S. (1997) Mixed neural-traditional classifier for character recognition. *SPIE-International Society for Optical Engineering*, **2949**, 102-110.

[14] Huang, Y.S. and Suen, C.Y. (1995) A method of combining multiple experts for the recognition of unconstrained handwritten numerals. *IEEE Transactions on Pattern Analysis and Machine Intelligence*, **17(1)**, 90-94.

[15] Lam, L., Huang, Y.S. and Suen, C.Y. (1997) Combination of multiple classifier decisions for optical character recognition. In: *Handbook of Character Recognition and Document Image Analysis*, Edited by Bunke, H. and Wang, P.S.P., World Scientific Publishing Company, New Jersey, 79-101.

[16] Rahman, A.F.R., Alam, H. and Fairhurst, M.C. (2002) Multiple Classifier Combination for Character Recognition: Revisiting the Majority Voting System and Its Variation. In: *Lecture Notes in Computer Science*, Springer Berlin/Heidelberg, **2423**, 319-328.

[17] Suen, C.Y., Nadal, C., Mai, T.A., Legault, R. and Lam, L. (1990) Recognition of totally unconstrained handwritten numerals based on the concept of multiple experts. In: *International Workshop Frontiers in Handwriting Recognition*, Montreal.

[18] Ho, T.K., Hull, J.J. and Srihari, S.N. (1992) Combination of Decisions by Multiple Classifiers. In: *Structured Document Image Analysis*, Edited by Baird, H.S., Bunke, H., Yamamoto, K., Springer Verlag New York, Inc., NewJersy, 188-202.

[19] Rahman, A.F.R. and Fairhurst, M.C. (1997) Exploiting second order information to design a novel multiple expert decision combination platform for pattern classification. *Electronics Letters*, **33(6)**, 476-477.

[20] Rohlfing, T., Russakoff, D.B. and Maurer, C.R. (2004) Performance-Based Classifier Combination in Atlas-Based Image Segmentation Using Expectation-Maximization Parameter Estimation. *IEEE Transactions on Medical Imaging*, **23(8)**, 983-994.

[21] Paik, J., Jung, S. and Lee, Y. (1993) Multiple combined recognition system for automatic processing of credit card slip applications. In: *The Second International Conference on Document Analysis and Recognition, IEEE Computer Society Press*, Washington, 520-523.

[22] Won, H.H., Kim, M.J., Kim, S. and Kim, J.W. (2008) EnsemPro: an ensemble approach to predicting transcription start sites in human genomic DNA sequences. *Genomics*, **91(3)**, 259-266.

[23] Peng, H., Long, F. and Ding, C. (2005) Feature selection based on mutual information: criteria of max-dependency, max-relevance, and min-redundancy. *IEEE Transactions on Pattern Analysis and Machine Intelligence*, **27(8)**, 1226-1238.

[24] Bucher, P., Périer, R.C., Praz, V. and Schmid, C. (2006) The eukaryotic promoter database user manual. *Nucleic Acid Research*, **34**, D82-85.

J. Biomedical Science and Engineering, 2010, 3, 727-734 **JBiSE**
doi:10.4236/jbise.2010.37097 Published Online July 2010 (http://www.SciRP.org/journal/jbise/).

Thermal analysis of different tips for various operating modes of phacoemulsification system

Radin Tahvildari, Hanieh Fattahi, Ahmad Amjadi

Laser and Medical Physics Laboratory, Department of Physics, Sharif University of Technology, Tehran, Iran.
Email: rtahvild@uwaterloo.ca; hanieh.fattahi@mpq.mpg.de; amjadi@sharif.ir

Received 16 April 2010; revised 15 May 2010; accepted 17 May 2010.

ABSTRACT

Cataract is an opacity that develops in the crystalline lens of the eye, due to alteration in some of its protein fibers, with the consequent impairment of visual acuity. The most effective and common treatment is to surgically remove the cloudy lens. In this process the crystalline lens are removed and the eye's refraction power is restored by inserting an artificial lens. Phacoemulsification refers to modern cataract surgery in which the eye's internal lens is emulsified with an ultrasonic hand piece, and aspirated from the eye. Aspirated fluids are replaced with irrigation of balanced salt solution, thus maintaining the anterior chamber, as well as cooling the hand piece. The patient can be released soon after the operation. The problem of this procedure in some cases is thermal damage. This research addresses the aforementioned problem through an important parameter, different operating modes of the system. The proposed in-vitro approach has been investigated in details.

Keywords: Cataract Surgery; Phacoemulsification; Thermal Damages; In Vitro Measurement; Thermocouples

1. INTRODUCTION

When the natural lens of eye becomes cloudy, usually because of the aging process, it keeps light rays from passing through or diffuses the light in such a way that vision becomes fuzzy or hazy. This cloudy lens is called a cataract. The object of cataract surgery is to remove this hazy lens and to replace it with a plastic prescription lens that is permanently implanted in the eye.

At present, the most widely used surgical technique is phacoemulsification, developed by Kelman (1967), in which ultrasonic emissions are utilized to fragment the crystalline lens inside the eye, the fragments then being drawn out through a very small incision – about 2.8-3 mm – at the zone where the cornea meets the sclera. This technique has several advantages such as faster surgical times, smaller incisions which make healing times quicker and increased surgeon control [2,3].

Three components constitute the heart of all phaco systems which are irrigation, aspiration and ultrasound [4].

The ultrasonic hand piece (**Figure 1**) incorporates a transducer for converting high-frequency, alternating current in to mechanical vibrations. By piezoelectric crystals electrical energy converts to mechanical energy and causes the hollow cylindrical tip attached to oscillate at frequency around 40 KHz to break up (emulsify) the cataract into tiny pieces [1,2].

The emulsified material is simultaneously suctioned from the eye by the tip. The front (anterior) section of the lens capsule is removed along with the fragments of the natural lens. The back (posterior) portion of the capsule is left in place to hold and maintain the correct position for the implanted intraocular lenses.

2. DISCUSSION

2.1. Lead-In

With an increase in the use of phacoemulsification concern about potential for thermal wound injuries during surgery has increased [9]. Phacoemulsification requires more attention to detail than any other ophthalmic surgical procedure. The success of each step of the procedure is critically dependent upon how well each previous

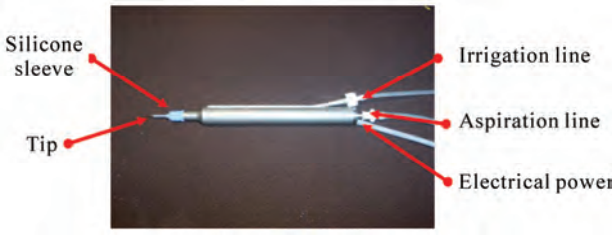

Figure 1. Phacoemusification hand piece.

step was performed. Errors early in the procedure will almost inevitably result in subsequent problems.

The small incision is what gives phaco most its advantages but, as with all steps in phacoemulsification, it must be fashioned very exactly [5].

The location, the size, the depth and configuration of the incision are all very critical factors in determining the final outcome in phaco.

In some cases burns can result in fusion of the cornea or the sclera, damage the corneal endothelium, wound gape and delayed wound healing.

It is important to note that the aim of this study is to compare and analyze the changes of temperature around the different tips for three operating modes of Sina Phacoemulsification System (**Figure 2**) which is one of the products of an Iranian medical engineering company (Aali-Payam Corporation) [9,10].

2.2. Instruments and Methodology

In this study, for the purpose of monitoring in vitro the changes of temperature values are based on the utilization of two different types of thermocouples;

1) Digital Thermocouple

2) Thin wires Thermocouple

In all of experimental tests the tip is in the chamber with dimension of 10 cm × 18 cm × 23 cm which is full of serum solution (Sodium Chloride 0.9%). The size of chamber is big enough so it acts as a thermal bath. Power of system is on its pre-set value, 50% and intensity of waves for this power are about 155 W/cm^2 [10,11].

2.2.1. Digital Thermocouple

Digital thermocouple has a probe and can measure temperatures near the phaco tip with sensitivity of 0.01℃. In measurement with digital thermocouple, each experimental test is repeated 5 times for every mode and the averages of temperature changes in a period of 60 seconds are plotted.

2.2.2. Thin Wires Thermocouple

Thin wires thermocouple which is made of two different metal wires (Ni-NiCr) with sealing wax on them for prevention of RF (radio frequency) waves [6]. With four thin wires thermocouple temperatures are measured in four different areas (**Figure 3**) near the tip indirectly by the changes of voltage with sensitivity of 1 μV and simultaneously are drawn by an X-Y recorder.

On the next stage temperature changes are measured by thin wires thermocouple for the same tip in a period of 60 seconds with the same initial conditions.

Because voltage changes are in the order of μV, then the numbers of peaks in a specific period of time are greater so in these graphs four points are important for us in comparison; starting point, maximum, minimum and ending.

Figure 2. Sina phacoemulsification system (Aali-Payam Co.).

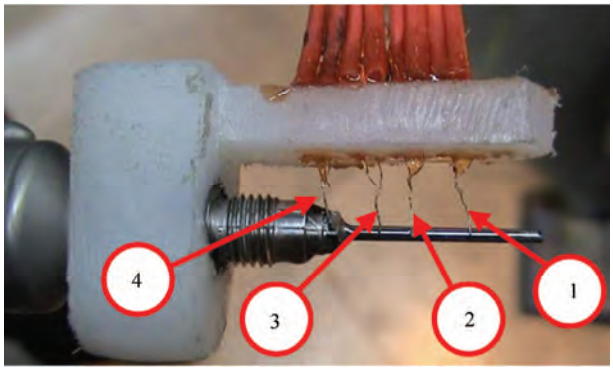

Figure 3. Four different thin wires thermocouples monitor the temperature changes of the tip.

According to the position of operator's foot on the pedal of system, four positions are defined [7].

Position 0: Foot is off the pedal, no action.

Position 1: Initial depression of foot pedal. Fluid flows from the bottle, no aspiration or emulsification.

Position 2: Pedal pushed to the detent. Aspiration now accompanies irrigation.

Position 3: Pedal pressed to the next detent. With phaco hand piece, emulsification now is added to irrigation and aspiration.

Three operating modes were analyzed;

1) Linear mode, in this mode the power of ultrasound waves are increased gradually from zero to the preset power of the system and it directly depends on how far down the pedal is pushed

2) Constant mode, in this mode the power of ultrasound emissions are equal to the preset power of system immediately in the stages in which waves were used

3) Pulse mode, in this mode the ultrasonic stream is not continuous but pulsed [8]

Phacoemulsifier tips come in a number of variations;

the three common ones are named for the angle of the cutting area. They are 0 degree, the 15 degree, the 30 degree and the 45 degree.

The 45 degree tip has the longest bevel and therefore the sharpest tip, so it cuts most easily. Because of the large bevel of the aspiration port it occludes less easily.

The 30 degree tip has smaller bevel. Therefore the port is smaller and occludes more easily so it is more efficient for the aspiration.

Some surgeons like to vary the tip depending on the density of the cataract: using a 45 degree tip for a hard cataract and a 30 degree tip for softer cataracts and they are the most popular so we have done all of the measurements and comparisons for these two tips.

3. ANALYSIS OF RESULTS

In this study, for the purpose of monitoring in vitro the temperature values around two tips with the angle of 30 and 45 degree, first the measurements are done by digital thermocouple for different operating modes of phaco system. On the next stage, same measurements are done but with thin wires thermocouples.

3.1. 30 Degree Tip – Digital Thermocouple

Shown in **Figure 4** and **Table 1** are the temperature values monitored by digital thermocouple during system is operating in linear and constant modes for the 30 Degree tip. In linear mode maximum temperature increase is 0.5 ℃ but in constant mode it is 0.47℃.

Shown in **Figure 5** and **Table 2**, in pulse mode, when the system is set to emit 10 pulses per second (pps), maximum temperature increase for linear – pulse mode around the tip is 0.2℃ but for constant – pulse mode this value is 0.23℃.

3.2. 30 Degree Tip – Thin Wires Thermocouples

In **Table 3**, the temperature values reached in linear and constant modes around the tip which are measured by thin wires thermocouples in four different areas around the 30 Degree tip is shown.

Figure 6 are the temperature changes that are plotted according to the voltage changes of each thermocouple versus time in linear mode.

The maximum temperature increase in this mode for thermocouples No.1 is 48, No.2 is 15, No.3 is 112 and No.4 is 69 μV.

Figure 7 are the temperature changes that are plotted according to the voltage changes of each thermocouple versus time in constant mode.

The maximum increase in this mode for thermocouples No.1 is 56, No.2 is 19, No.3 is 97 and No.4 is 83 μV.

In **Table 4**, the temperature values reached in linear – pulse and constant – pulse modes around the tip which are measured by thin wires thermocouples in four different areas around the tip is shown.

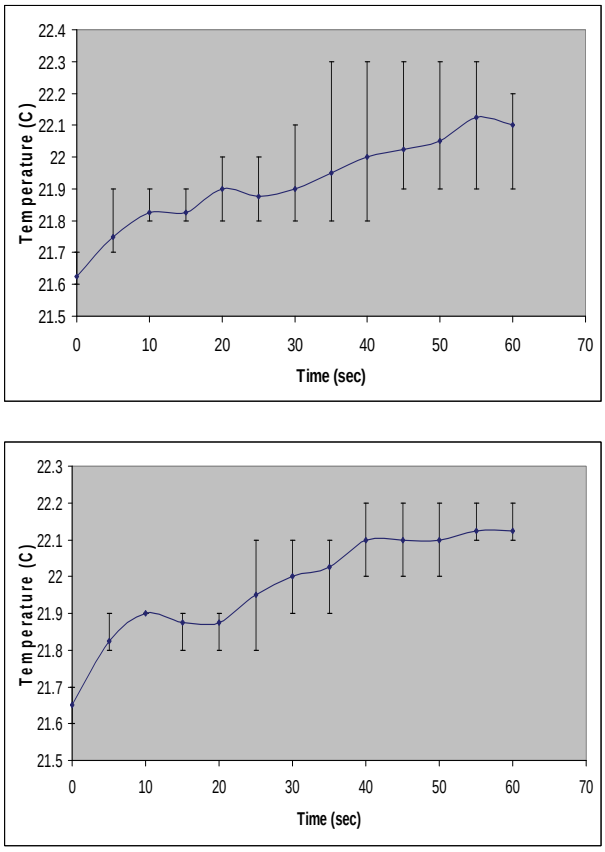

Figure 4. Linear mode – temperature values versus time [left]; constant mode – temperature values versus time [right].

Table 1. Temperature values for linear and constant modes measured by digital thermocouple.

	Average of Starting	Average of Maximums	Average of Minimums	Average of Endings
LINEAR MODE	21.62	22.12	21.87	22.1
CONSTANT MODE	21.65	22.12	21.87	22.12

Table 2. Temperature values for linear – pulse and constant – pulse modes measured by digital thermocouple.

	Average of Starting	Average of Maximums	Average of Minimums	Average of Endings
LINEAR PULSE MODE	22.05	22.25	22.1	22.27
CONSTANT PULSE MODE	21.62	21.85	21.72	21.82

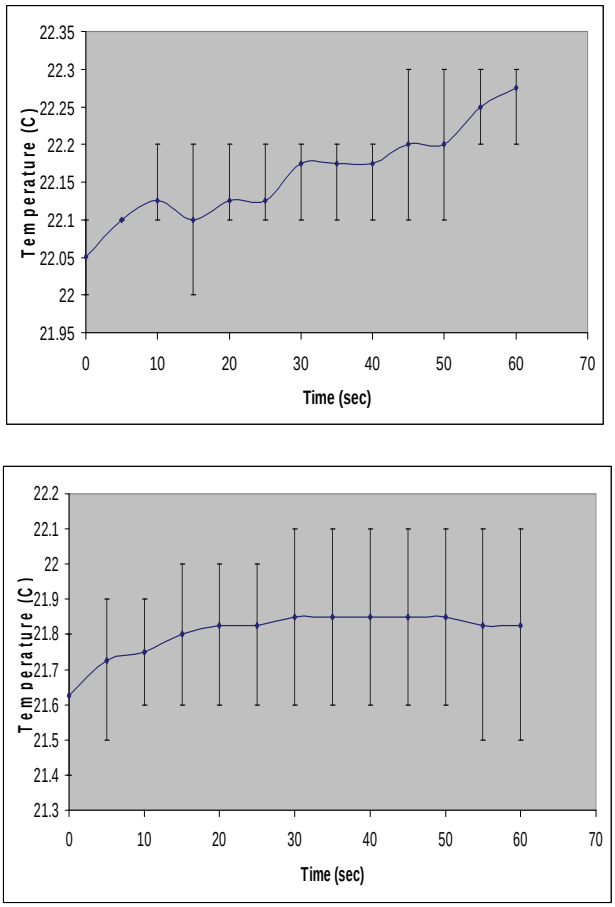

Figure 5. Linear-pulse mode (10 pps) – temperature values versus time [left]; constant-pulse mode (10 pps) – temperature values versus time [right].

Table 3. Temperature values for linear and constant modes measured by thin wire thermocouples.

		Starting	Maximum	Minimum	Ending
Linear mode	Thermo No.1	-10	38	8	22
	Thermo No.2	-3	12	-1	-2
	Thermo No.3	-10	102	35	80
	Thermo No.4	-4	65	41	50
Con-stant mode	Thermo No.1	-2	54	12	31
	Thermo No.2	-2	17	1	2
	Thermo No.3	3	100	59	89
	Thermo No.4	1	84	21	67

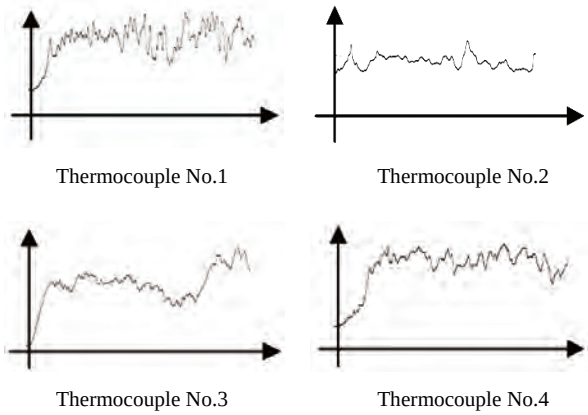

Figure 6. Linear mode – voltage changes (μV) versus time (sec.) for each thermocouple.

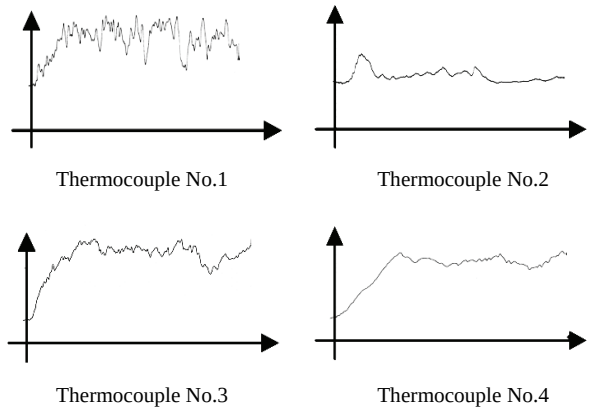

Figure 7. Constant mode – voltage changes (μV) versus time (sec.) for each thermocouple

Table 4. Temperature values for linear – pulse and constant – pulse modes measured by thin wire thermocouples.

		Starting	Maximum	Minimum	Ending
Linear Pulse mode	Thermo No.1	2	31	18	27
	Thermo No.2	-8	8	1	2
	Thermo No.3	-3	57	38	37
	Thermo No.4	-5	61	53	52
Constant Pulse mode	Thermo No.1	-11	21	8	10
	Thermo No.2	-2	17	9	11
	Thermo No.3	12	63	48	57
	Thermo No.4	6	90	78	9

Figure 8 are the temperature changes that are plotted according to the voltage changes of each thermocouple versus time in linear – pulse mode when the system is set to emit 10 pulses per second (10 pps). The maximum increase in this mode for thermocouples No.1 is 29, No.2 is 16, No.3 is 60 and No.4 is 66 μV.

Figure 9 are the temperature changes that are plotted according to the voltage changes of each thermocouple versus time in constant – pulse mode when again the system is set to emit 10 pulses per second (10 pps).

The maximum increase in this mode for thermocouples No.1 is 32, No.2 is 19, No.3 is 51 and No.4 is 84 μV.

3.3. 45 Degree Tip – Digital Thermocouple

Shown in **Figure 10** and **Table 5** are the temperature value monitored by digital thermocouple during the system is operating in linear and constant modes for the 45 Degree tip.

In linear mode maximum increase is 0.72℃ but in constant mode it is 0.67℃.

Shown in **Figure 11** and **Table 6**, in pulse mode, when the system is set to emit 10 pulses per second (10 pps), maximum increase for linear – pulse mode around the tip is 0.17℃ but for constant – pulse mode this value is 0.13℃.

3.4. 45 Degree Tip – Thin Wires Thermocouples

In **Table 7**, the temperature values reached in linear and constant modes around the tip which are measured by thin wires thermocouples in four different areas around the tip is shown.

Figure 12 are the temperature changes that are plotted according to the voltage changes of each thermocouple

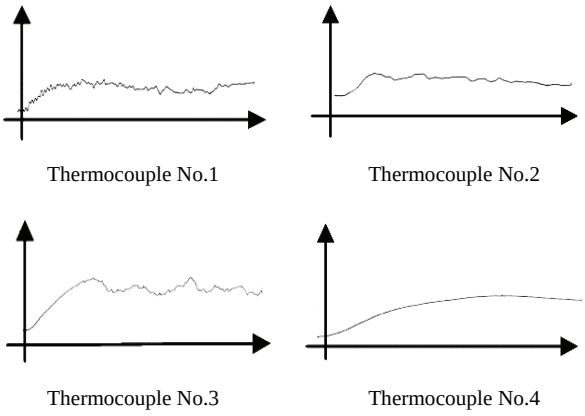

Figure 8. Linear – pulse mode (10 pps) – voltage changes (μV) versus time (sec.) for each thermocouple.

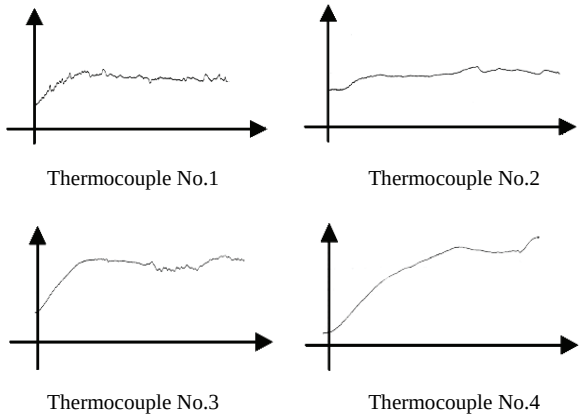

Figure 9. Constant – pulse mode (10 pps) – voltage changes (μV) versus time (sec.) for each thermocouple.

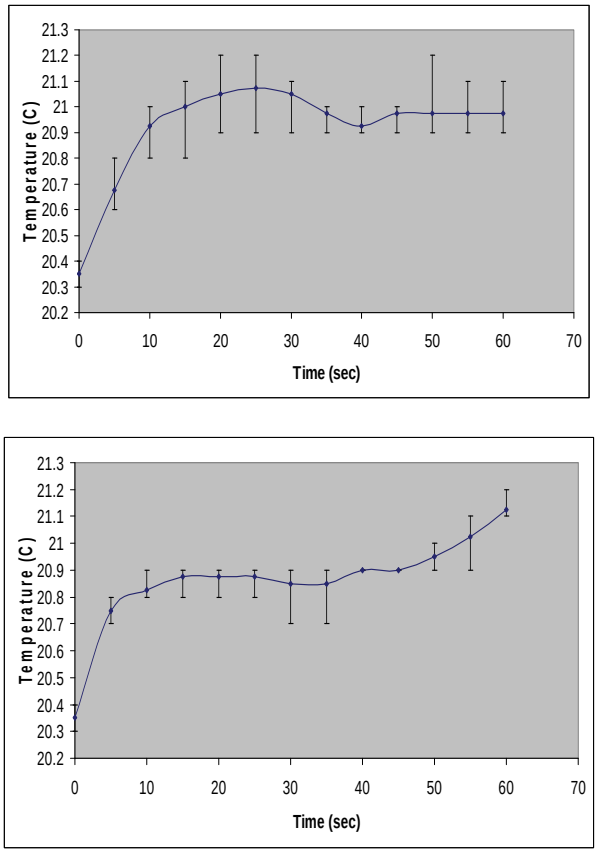

Figure 10. Linear mode – temperature values versus time [left]; constant mode – temperature values versus time [right].

Table 5. Temperature values for linear and constant modes measured by digital thermocouple.

	Average of Starting	Average of Maximums	Average of Minimums	Average of Endings
LINEAR MODE	20.35	21.07	20.92	20.97
CONSTANT MODE	20.35	21.02	20.85	21.12

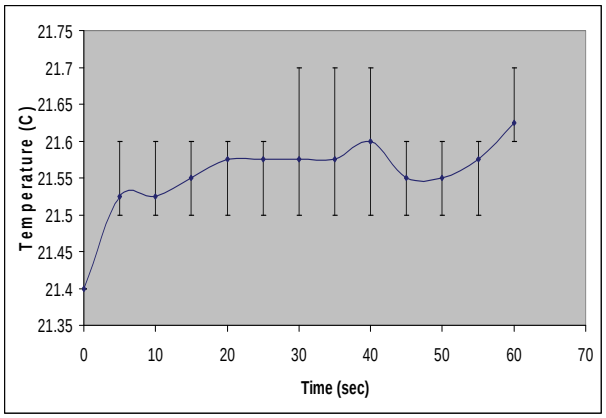

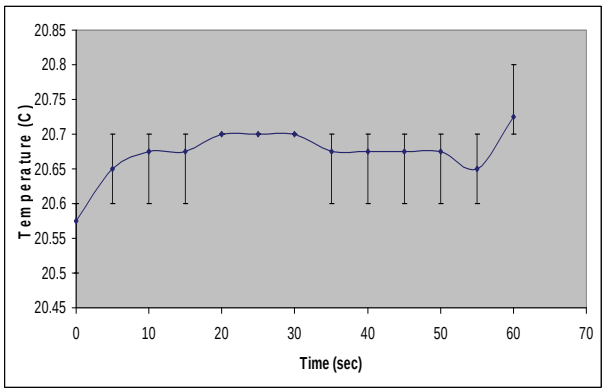

Figure 11. Linear -pulse mode (10 pps) – temperature values versus time [left]; constant -pulse mode (10pps) – temperature values versus time [right].

Table 6. Temperature values for linear – pulse and constant – pulse modes measured by digital thermocouple.

	Average of Starting	Average of Maximums	Average of Minimums	Average of Endings
LINEAR PULSE MODE	21.40	21.57	22.55	21.62
CONSTANT PULSE MODE	20.57	20.70	20.65	20.72

versus time in linear mode.

The maximum increase in this mode for thermocouples No.1 is 40, No.2 is 32, No.3 is 47 and No.4 is 13 μV.

Figure 13 are the temperature changes that are plotted according to the voltage changes of each thermocouple versus time in constant mode.

The maximum increase in this mode for thermocouples No.1 is 9, No.2 is 19, No.3 is 64 and No.4 is 67 μV.

In **Table 8**, the temperature values reached in linear – pulse and constant – pulse modes around the tip which are measured by thin wires thermocouples in four different areas around the tip is shown.

Table 7. Temperature values for linear and constant modes measured by thin wire thermocouples.

		Starting	Maximum	Minimum	Ending
LINEAR MODE	THERMO NO.1	0	40	-2	9
	THERMO NO.2	-9	23	7	18
	THERMO NO.3	-7	40	0	8
	THERMO NO.4	-7	6	0	2
CONSTANT MODE	THERMO NO.1	-5	4	-10	2
	THERMO NO.2	-8	11	-2	2
	THERMO NO.3	-14	50	10	15
	THERMO NO.4	-5	62	32	56

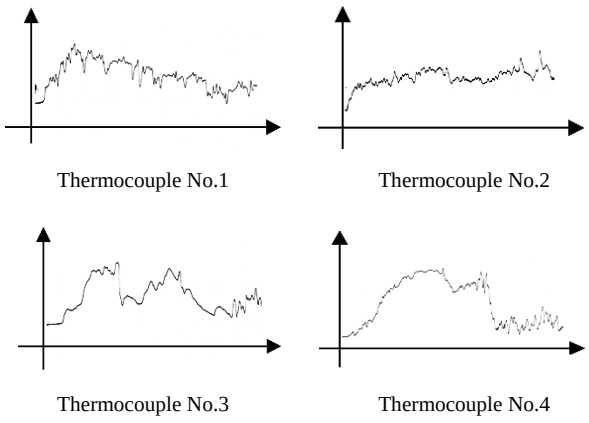

Figure 12. Linear mode – voltage changes (μV) versus time (sec.) for each thermocouple.

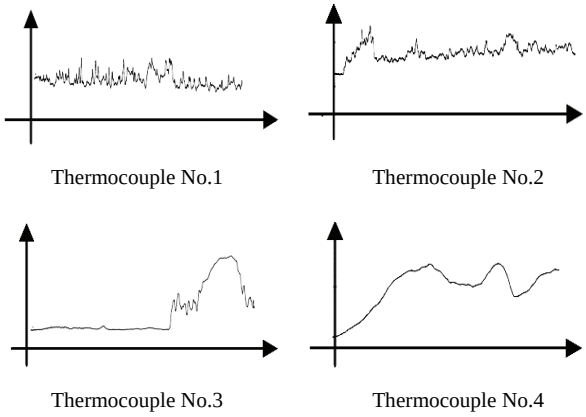

Figure 13. Constant mode – voltage changes (μV) versus time (sec.) for each thermocouple.

Table 8. Temperature values for linear – pulse and constant – pulse modes measured by thin wire thermocouples.

		Starting	Maximum	Minimum	Ending
Linear Pulse mode	Thermo No.1	0	12	-4	6
	Thermo No.2	0	26	16	23
	Thermo No.3	-2	12	-1	0
	Thermo No.4	4	58	33	54
Constant Pulse mode	Thermo No.1	-12	4	-8	2
	Thermo No.2	6	30	8	21
	Thermo No.3	-5	18	-7	-3
	Thermo No.4	9	40	16	33

Figure 14 are the temperature changes that are plotted according to the voltage changes of each thermocouple versus time in linear – pulse mode when the system is set to emit 10 pulses per second (10 pps). The maximum increase in this mode for thermocouples No.1 is 12, No.2 is 26, No.3 is 14 and No.4 is 54 μV.

Figure 15 are the temperature changes that are plotted according to the voltage changes of each thermocouple versus time in constant – pulse mode when the system is set to emit 10 pulses per second (10 pps).

The maximum increase in this mode for thermocouples No.1 is 16, No.2 is 24, No.3 is 23 and No.4 is 31 μV.

4. CONCLUSION

In this study thermocouples have been used as an instrument for measuring the temperature changes of different tips to monitor and compare three operating mode of phacoemulsification system.

All in vitro measurements are done with the same initial conditions. In evaluating the maximum temperature reach in each operating mode, it has been found that for both tips temperature changes in pulse mode (linear – pulse and constant – pulse) has fewer and lower peaks. The main reason is the periods of short time between each pulsed wave allow the tip to get cool between two successive emissions. Moreover, in these modes, the system produces a lower thermal increase with respect to the linear and constant modes.

It is strongly recommend that in cataract surgery with Sina phaco system only linear – pulse and constant – pulse modes should be used, so to reduce any possible surgical complications caused by the excessive release of heat.

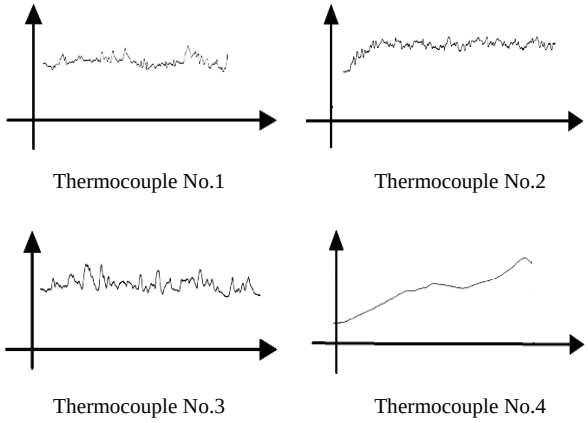

Figure 14. Linear – pulse mode (10 pps) – voltage changes (μV) versus time (sec.) for each thermocouple.

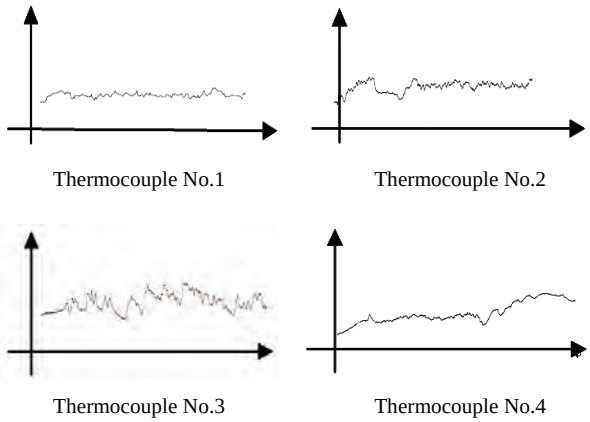

Figure 15. Constant – pulse mode (10 pps) – voltage changes (μV) versus Time (sec.) for each thermocouple.

At the end it should be mentioned that although all the experimental tests were performed in vitro and thermal increasing of tip during surgical operation is higher than these data, the results suggest this modern procedure can be performed at a safe temperature with the knowledgeable selection of surgeon-controlled parameters.

5. ACKNOWLEDGEMENTS

This research based on a collaboration research between Applied Physics Center at Sharif University of Technology and an Iranian medical engineering company (Aali-Payam Corporation).

We would like to thank Dr. M. Hashemi, Department of Ophthalmology at Iran University of Medical Sciences, for his guidance, helpful comments and support throughout this research.

Special thanks to all the members of Aali-Payam Co. for giving us the opportunity to do this research on Sina phacoemulsification system

which is one of their products. We also thank the anonymous paper reviewers for providing insightful comments.

REFERENCES

[1] Bond, L.J., Flake, M.D. and Tucker, B.J. (2003) Physics of phacoemulsification. *World Conference on Ultrasound*, Paris .

[2] Packer, M., Fishkind, W.J., Howard Fine, I. and Hoffman, R.S. (2005) The physics of phaco: A review. *Journal of Cataract & Refractive Surgery*, **31(2)**, 424-431.

[3] Corvi, A., Innocenti, B. and Mencucci, R., (2006) Thermography used for analysis and comparison of different cataract surgery procedures based on phacoemulsification. *Physiological Measurements*, **27(4)**, 371-384.

[4] Yow, L. and Basti, S. (1997) Physical and mechanical principles of phacoemulsification and their cilinical relevance. *Indian Journal of Ophthalmology*, **45(4)**, 241-249.

[5] Osher, R.H. and Injev, V.P. (2006) Thermal study of bare tips with various system parameters and incision. *Journal of Cataract & Refractive Surgery*, **32(5)**, 867-872.

[6] Jones, L.D. and Chin, A.F. (1991) Electronic instruments and measurements, Prentice-Hall, New Jersey, 300-303.

[7] Maloney, W.F., Grindle, L. and Fallbrook (1988) Textbook of phacoemulsification. Lasenda Publishers, California.

[8] Aali-Payam Co., (2006) Instruction manual of phaco system. *Sina Model*, Tehran, 23-24.

[9] Ernest, P., Rhem, M., McDermott, M. and Lavery, K. (2001) Phacoemulsification conditions resulting in thermal wound injury," *Journal of Cataract & Refractive Surgery*, **27(11)**, 1829-1839.

[10] Tahvildari, R., Fattahi, H. and Amjadi, A. (2008) An in-vitro Measurement of Temperature Changes in Phacoemulsification System during Different modes. *Proceedings of the* 2*nd International Conference on Bioinformatics and Biomedical Engineering*, Shanghai, 1569-1574.

[11] Tahvildari, R., Fattahi, H. and Amjadi, A. (2007) Thermal damage invesigation on Cataract surgery by Ultrasound waves. *Proceedings of the* 15*th Annual Physics Conference of Iran*, Yasuj, 433-436.

J. Biomedical Science and Engineering, 2010, 3, 735-741 **JBiSE**
doi:10.4236/jbise.2010.37098 Published Online July 2010 (http://www.SciRP.org/journal/jbise/).

Removal of hexavalent chromium by an aromatic alcohol

Ankita Basu, Rumpa Saha, Jayashree Mandal, Sumanta Ghosh, Bidyut Saha*

Bioremediation Lab, Department of Chemistry, the University of Burdwan, Golapbag, India;
Email: b_saha31@rediffmail.com

Received 17 May 2010; revised 21 May 2010; accepted 28 May 2010.

ABSTRACT

Cr(VI) is a widespread environmental contaminant and a known human carcinogen. Biosorption is a very common method to remove toxic Cr(VI) from industrial waste water. In biosorption Cr(VI) is reduced to less toxic Cr(III) and adsorbed in biosorbent as Cr(III). Effective biosorbents contain hydroxy groups; it may be aliphatic or aromatic. Kinetics of reduction of Cr(VI) by an aromatic alcohol, benzyl alcohol, (which is an important volatile component of flowers of some night blooming plants) in micellar media have been studied spectrophotometrically. Micellar media is a probe to establish the mechanistic paths of reduction of Cr(VI) to Cr(III). Effects of electrolytes are studied to support the proposed reaction mechanism. Suitable surfactant & suitable concentration of electrolyte enhance the biosorption property.

Keywords: Biosorption; Carcinogen; Kinetics; Chromium (VI); Benzyl Alcohol; Non Functional Surfactants; Salt Effect

1. INTRODUCTION

Chromate [Cr(VI)] compounds are widely used in industry. Large amounts of toxic Cr(VI) are annually reintroduced into the environment through the discharge of chromium-containing industrial waste [1-4]. In the last few decades, the amount of chromium in aquatic and terrestrial eco-systems has increased a consequence of different human activities. Chromium is the new entry, after lead, cadmium and mercury in the major toxic metal series. In the Hinkley (a small desert town in San Bernardino Country, USA) case hexavalent chromium was used by Pacific Gas and Electric Company (PG & E) in cooling systems to prevent pipes from rusting. The runoff of hexavalent chromium contaminated water on the PG & E property, seeped into the ground and contaminated local water supplies. PG & E was required to compensate the plaintiffs $ 333 million, clean up the hexavalent chromium contamination, and stop using hexavalent chromium in their operation this is the highest amount of compensation in metal toxicity history. Various methods used for removal of Cr (VI) ions include chemical reduction and precipitation, reverse osmosis, ion exchange and adsorption on activated carbon or similar material [5]. But all these methods suffer from severe constraints, such as incomplete metal removal, high reagent or energy requirements, generation of toxic sludge or other waste products that require safe disposal. Some of the treatment methods involve high operating and maintenance cost. The high cost of the chemical reagents and the problems of secondary pollution also make the above physico-chemical methods rather limited in application. There is, therefore, a need for some alternative technique, which is efficient and cost-effective. The process of heavy metal removal by biological mate- rials is known as biosorption and the biological materials used are called biosorbents. Various biosorbents like bacteria, fungi, yeasts, agricultural by products, industrial wastes, etc have been used for biosorption. In this regard, considerable attention has been focused in recent years upon the field of biosorption for the removal of heavy metal ions from aqueous solutions [6]. Recently it is established that for chromium (VI) biosorption, chromium (VI) is first reduced to chromium (III) and then it is adsorbed as chromium (III) in the biosorbent [7]. Understanding of mechanism of chromium (VI) reduction to chromium (III) by some alcohol is important in this context. In this respect benzyl alcohol is ideal one. Benzyl alcohol is a volatile component of flower of a night blooming plant *Gaura drummondii* [8] and strawberry leaves [9]. The present investigations have been carried out in micro-heterogeneous systems to substantiate the proposed reaction mechanism as we carried out for other systems [10-17]. Effects of electrolytes are studied to support the proposed reaction mechanism.

2. THEORETICAL

It is expected that the reduction of Cr(VI) by benzyl al-

cohol in aqueous surfactant media is proceed through normal oxidation mechanism by chromate ester. Benzyl alcohol is oxidized to benzaldehyde and Cr(VI) is reduced to Cr(IV). The over-all reaction can be written as:

$3\ PhCH_2OH + 2HCrO_4^- + 8H^+ \rightarrow 3\ PhCHO + 2Cr(III) + 8\ H_2O$.

3. EXPERIMENTAL

3.1. Table for Materials and Reagents

The materials and reagents are shown in **Table 1**.

3.2. Procedure and Kinetic Measurements

Under the kinetic conditions, solutions of the oxidant and mixtures containing the known quantities of the substrate(s) (*i.e*, benzyl alcohol) (under the conditions $[S]_T >> [Cr(VI)]_T$), acid and the other necessary chemi- cals were separately thermostated (±0.1℃). The reaction was initiated by mixing the requisite amounts of the oxidant with the reaction mixture. It is assumed that zero time was taken when half of the required volume of the oxidant solution had been added. The progress of the reaction was followed by monitoring the decay of oxidant [Cr(VI)] at 415 nm at different time intervals (2 minutes) with a UV-VIS spectrophotometer [UV-2450 (SHIMADZU)]. Quartz cuvettes of path length 1cm were used. The observed pseudo-first-order rate con- stants [$k_{obs}(s^{-1})$] were determined from the linear part of the plots of $\ln(A_{415})$ versus time(t). Reproducible results giving first-order plots (co-relation co-efficient, $R^2 \geq 0.998$) were obtained for each reaction run. A large ex- cess (≥ 15-fold) of reductant was used in all kinetic runs. No interference due to other species at 415 nm was verified. Under the experimental conditions, the possibility of decomposition of the surfactants by Cr(VI) was investigated and the rate of decomposition in this path was found to be kinetically negligible.

Table 1. Materials and reagents.

Materials	Brand
1. Benzyl alcohol	AR, Merck, India
2. $K_2Cr_2O_7$	AR, BDH, India
3. N-cetylpyridinium chloride (CPC)	AR, SRL, India
4. Sodium dodecylsulphate (SDS)	AR, SRL, India
5. TX-100	AR, SRL, India
6. NaCl	AR, Merck, India
7. NH_4Cl	AR, Ranbaxy, India

3.3. Product Analysis and Stoichiometry

Under the kinetic condition benzyl alcohol is oxidized to benzaldehyde and estimation of the reaction products was carried by gravimetrically as 2, 4-dinitrophenyl hydrazone [18]. In a typical experimental set, 10ml of 0.06 mol dm^{-3} Cr(VI) in 1.0 mol dm^{-3} H_2SO_4 was added to 40 ml of 0.2 mol dm^{-3} benzyl alcohol and the reaction was allowed to proceed to completion. Then the reaction mixture was added slowly with stirring to 60 ml of a saturated solution of 2,4-dinitrophenyl hydrazine in 2.0 mol dm^{-3} HCl. After storing for about 1hr in an ice-bath, the precipitate was collected weighed sintered glass crucible, washed with 2.0mol dm^{-3} HCl followed by water and dried to a constant weight at 100-105℃. The found ratio, $[Cr(VI)]_T/[\text{Carbonyl compound}]_T \approx 2/3$ (from 3 independent determinations) supports the fol- lowing Stoichiometry.

$3PhCH_2OH + 2HCrO_4^- + 8H^+ \rightarrow 3\ PhCHO + 2Cr(III) + 8\ H_2O$. (1)

4. RESULTS AND DISCUSSION

4.1. Dependence on $[Substrate]_T$ *i.e*, $[Benzyl\ Alcohol]_T$

From the plot of k_{obs} vs $[\text{benzyl alcohol}]_T$, it is established that the path shows a first order dependency on $[\text{substrate}]_T$ *i.e*, $[\text{benzyl alcohol}]_T$ *i.e*., with increasing substrate concentration the rate of the reaction increases in a straight line manner. (**Figure 1**).

$$\text{So, } k_{obs} = k_s[S]_T$$

The above first order dependence on $[S]_T$ also maintained in the presence of surfactant like CPC, SDS, TX-100.

4.2. Dependence on $[H^+]$

The acid dependence was followed in aqueous $HClO_4$ media at fixed Cr(VI) and $[S]_T$. From the experimental fit (**Figure 2**), the observation is

$$k_{obs} = k_H[H^+]^2$$

The above second order dependency is also maintained in the presence of surfactant (e.g, SDS).

5. EFFECT OF SURFACTANTS

5.1. Effect of SDS

Sodium dodecyl sulphate(SDS, a representative anionic surfactant) accelerate the reaction path. The plot of k_{obs} vs $[SDS]_T$ [**Figure 3**] shows a continuous increase up to the concentration of SDS.

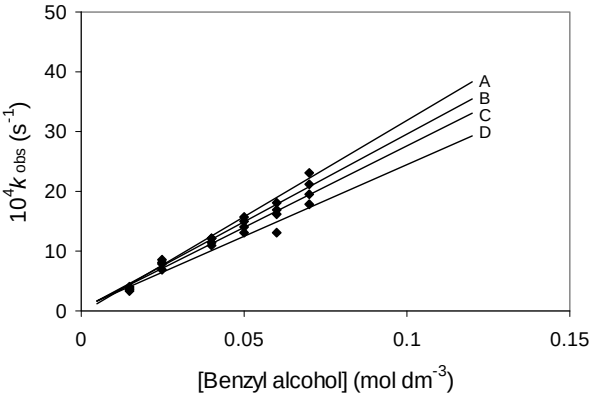

Figure 1. Dependence of k_{obs} on [benzyl alcohol] for the chromium (VI) oxidation of benzyl alcohol at 30℃. $[Cr(VI)]_T = 5 \times 10^{-4}$ mol dm^{-3}, $[H_2SO_4] = 0.25$ mol dm^{-3}. A($[SDS]_T = 2 \times 10^{-2}$ mol dm^{-3}, $[CPC]_T = 0$ mol dm^{-3}, $[TX\text{-}100]_T = 0$ mol dm^{-3}), B($[SDS]_T = 0$ mol dm^{-3}, $[CPC]_T = 0$ mol dm^{-3}, $[TX\text{-}100]_T = 2 \times 10^{-2}$ mol dm^{-3}), C ($[SDS]_T = 0$ mol dm^{-3}, $[CPC]_T = 0$ mol dm^{-3}, $[TX\text{-}100]_T = 0$ mol dm^{-3}), D($[SDS]_T = 0$ mol dm^{-3}, $[CPC] = 2 \times 10^{-3}$ mol dm^{-3}, $[TX\text{-}100]_T = 0$ mol dm^{-3}).

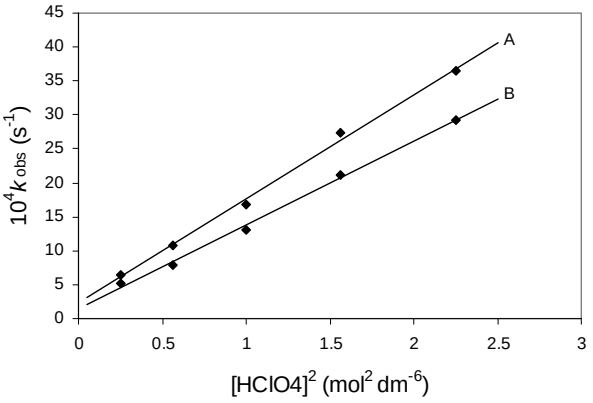

Figure 2. Dependence of k_{obs} on $[H^+]$ for the chromium(VI) oxidation of benzyl alcohol at 30℃ in aqueous medium. $[Cr(VI)]_T = 5 \times 10^{-4}$ mol dm^{-3}, $[\text{benzyl alcohol}]_T = 150 \times 10^{-4}$ mol dm^{-3}, $[H_2SO_4] = 0.25$ mol dm^{-3}. A($[SDS]_T = 2 \times 10^{-2}$), B($[SDS]_T = 0$).

5.2. Effect of CPC

Cetyl Pyridinium Chloride (CPC, a representative cationic surfactant is found to retard the reaction path. Plot of k_{obs} vs $[CPC]_T$ [**Figure 4**] shows a continuous decrease and finally it tends to level off at higher concentration of CPC. The observation is identical to that observed by Bunton and Cerichelli [19] in the oxidation of ferrocene by ferric salt salts in the presence of cationic surfactant cetyl trimethyl ammonium bromide (CTAB).

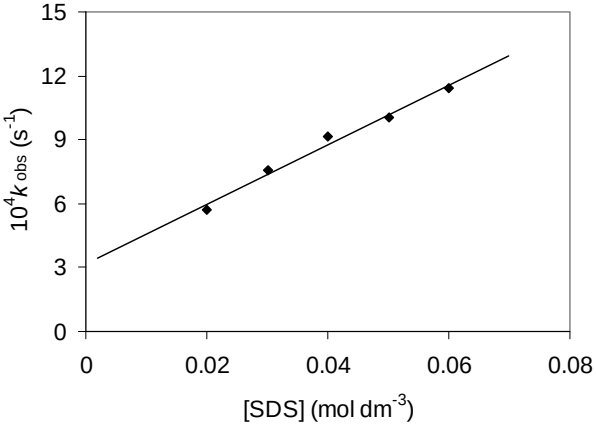

Figure 3. Dependence of k_{obs} on $[SDS]_T$ for the chromium (VI) oxidation of benzyl alcohol at 30℃. $[Cr(VI)]_T = 5 \times 10^{-4}$mol dm^{-3}, $[\text{benzyl alcohol}]_T = 150 \times 10^{-4}$ mol dm^{-3}, $[H_2SO_4] = 0.25$ mol dm^{-3}.

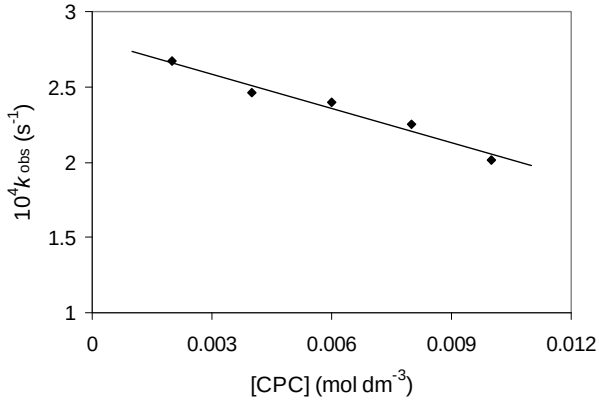

Figure 4. Dependence of k_{obs} on $[CPC]_T$ for the chromium(VI) oxidation of benzyl alcohol at 30℃. $[Cr(VI)]_T = 5 \times 10^{-4}$ mol dm^{-3}, $[\text{benzyl alcohol}]_T = 150 \times 10^{-4}$ mol dm^{-3}, $[H_2SO_4] = 0.25$ mol dm^{-3}.

5.3. Effect of TX-100

Triton X-100(TX-100, a representative neutral surfactant) accelerates the reaction path. But the acceleration rate in TX-100 is less than that of SDS. The plot of k_{obs} vs $[TX\text{-}100]_T$ [**Figure 5**], shows a continuous increase up to the concentration of TX-100.

5.4. Test for Acrylonitrile Polymerization

Under the experimental conditions, the existence of free radical was indicated by polymerization of acrylonitrile under a nitrogen atmosphere.

5.5. Mechanism and Interpretation

Scheme 1 leads to the flowing rate law:

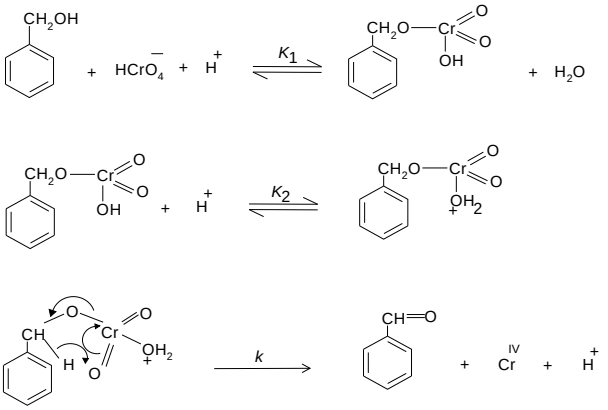

Scheme 1. Cr(Vl) reduction of Benzyl alcohol.

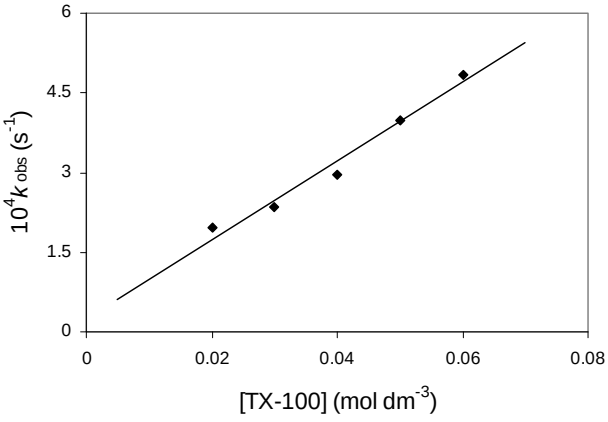

Figure 5. Dependence of k_{obs} on $[TX\text{-}100]_T$ for the chro- mium (VI) oxidation of benzyl alcohol at 30℃. $[Cr(VI)]_T$ = 5 × 10^{-4}mol dm^{-3}, $[benzyl\ alcohol]_T$ = 150 × 10^{-4}mol dm^{-3}, $[H_2SO_4]$ = 0.25 mol dm^{-3}.

$$k_{obs} = (2/3)\ kK_1K_2[S]_T[H^+]^2 \qquad (2)$$

The pseudo-first-order rate constants (k_{obs}) in the presence of various concentrations of different types of surfactants, SDS (Sodium dodecyl sulfate, a representative anionic surfactant), CPC (N-cetyl pyridinium chloride, a representative anionic surfactant) and TX-100 (Trian X-100, a neutral surfactant) are presented in **Figures 4-6**. The pseudo phase ion-exchange (PIE) [20] model is applied most widely in micellar catalysis. The basic assumption of the PIE is as follows:

1) Micelles act as a separate phase from water, all reactants are distributed quickly between water and micellar phase, and the reaction rate can be considered as the sum of that in two phases.

2) The reaction in the micellar pseudo phase occurs mainly at micelle surface.

3) The reactant ions and the inert ions compete at the charged micellar surface.

The data reveal that SDS and TX-100 accelerate the rate where as CPC decreases the rate. The rate acceleration is higher in the case of SDS than TX-100. This can be explained by **Schemes 2** and **3**.

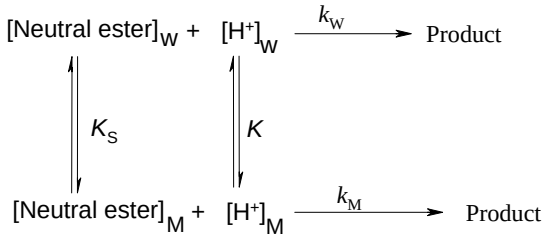

Scheme 2. Partitioning of the reactive species between the aqueous and micellar phases.

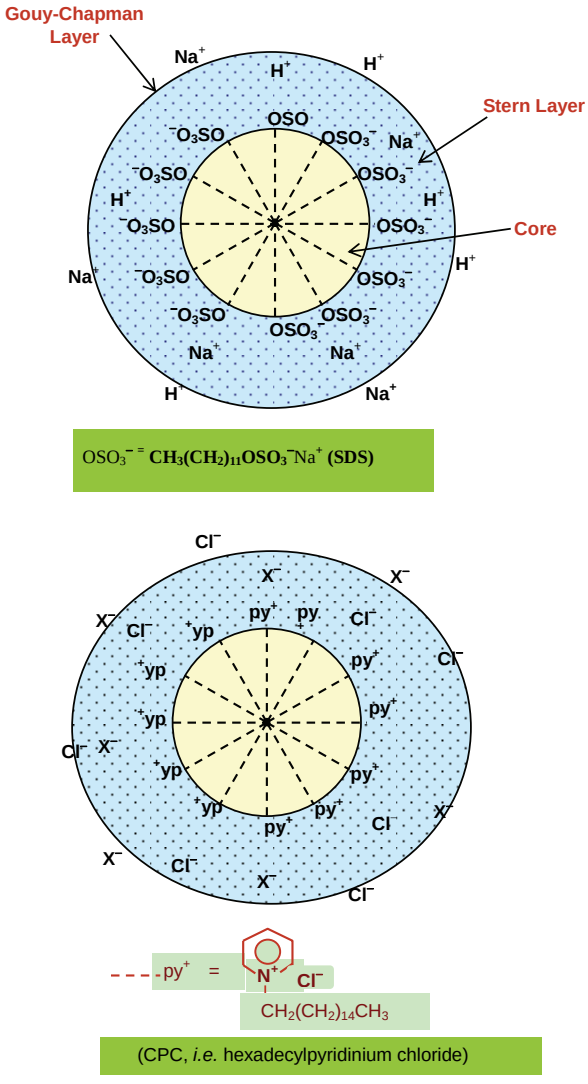

Scheme 3. Structural representation of anionic & cationic surfactants.

The formation of micelles by ionic surfactants is ascribed to a balance between hydrocarbon chain attraction and ionic repulsion. The net charge of micelles is less than the degree of micellar aggregates, indicating that a large fraction of counter ions remains associated with the micelle; these counter ions form the Stern layer at the micellar surface. For nonionic surfactants, however, the hydrocarbon chain attraction is opposed by the requirements of hydrophilic groups for hydration and space. Therefore, the micellar structure is determined by equilibrium between the repulsive forces among hydrophilic groups and the short-range attractive forces among hydrophobic groups. For bimolecular reactions inhibition arises from incorporation of one reactant into the micellar pseudo phase and exclusion of the other from it. Catalysis is apparently caused, for the most part, by concentration of the two reactants into a small volume in the micellar Stern layer [21].

The substrate is partitioned in the Stern layer of the micellar phase. SDS being an anionic surfactant, owing to the electrostatic attraction between the positively charged [H^+] species and negatively charged micellar head groups. [H^+] easily attaches to the Stern layer of the micelle. The reaction takes place in both the micellar and aqueous media. The observed rate acceleration is due to the favored reaction in the micellar phase, where both H^+ and the neutral ester are preferably accumulated. In the case of TX-100, H^+ also attaches to the Stern layer of the micelle, but the amount is less compared to SDS because TX-100 is a neutral surfactant, so no electrostatic attraction takes place. CPC is a cationic surfactant and consequently due to the electrostatic repulsion between the positively charged [H^+] species and positively charged micellar head group, [H^+] does not attaches to the Stern layer of micelle through the substrate. The reaction takes place only in aqueous media, which is depleted in the substrate concentration.

5.6. Effect of Added Electrolyte

Experimental evidence has shown that electrolyte inhibition of micellar catalysis is a general phenomenon [22-24] with one apparent exception [25]. The proposed study has taken into consideration for better under standing of reduction mechanism. Electrolyte inhibition is rationalized by assuming that a counter ion competes with an ionic reagent (e.g., OH^-, H_3O^+, and X^-) for a site on the ionic micelle [26]. When NH_4Cl is added the inhibition phenomena comes into play (**Figure 7**). But for the case of NaCl inhibition followed by enhancement takes place which is interesting (**Figure 6**). Enhancement of micellar catalysis by added salt is caused by their changing the shape or reducing the charge density

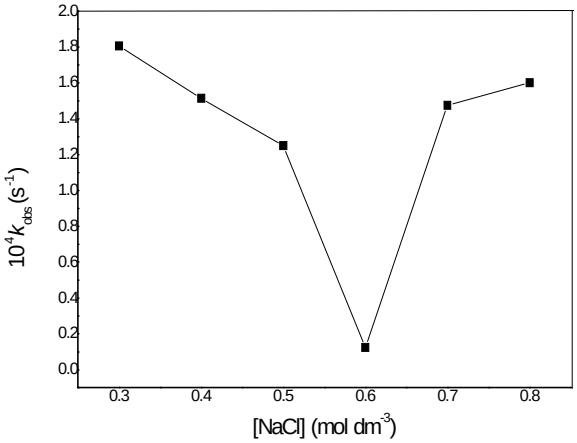

Figure 6. Dependence of k_{obs} on [NaCl] for the chromium(VI) oxidation of benzyl alcohol at 30^0C in SDS medium. $[Cr(VI)]_T = 5 \times 10^{-4}$mol dm^{-3}, $[benzyl\ alcohol]_T = 150 \times 10^{-4}$mol dm^{-3}, $[H_2SO_4] = 0.25$ mol dm^{-3}.

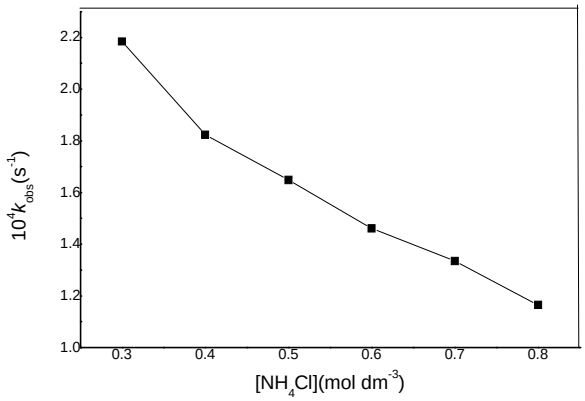

Figure 7. Dependence of k_{obs} on [NH_4Cl] for the chromium(VI) oxidation of benzyl alcohol at 30^0C in SDS medium. $[Cr(VI)]_T = 5 \times 10^{-4}$ mol dm^{-3}, $[benzyl\ alcohol]_T = 150 \times 10^{-4}$ mol dm^{-3}, $[H_2SO_4] = 0.25$ mol dm^{-3}.

of the micelle. Salts decrease the cmc (critical micelle concentration) and increase the aggregation no of ionic micelles [27-28] probably because increased screening by the counter ions decreases the effective charge density of the micelle.

6. CONCLUSIONS

Kinetics and mechanism of Cr(VI) reduction by benzyl alcohol in aqueous acid media have been studied under the conditions $[benzyl\ alcohol]_T >> [Cr(VI)]_T$. under the kinetic conditions, the monomeric species of Cr(VI) has been found kinetically active. Cr(VI)-substrate ester experiences a redox decomposition through $2e^-$ transfer at

Table 2. Presentation of rate constants values (k_{obs}) of benzyl alcohol oxidation in different surfactant medium.

$[benzyl\ alcohol]_T$ (mol dm^{-3})	$[SDS]_T$ (mol dm^{-3})	$10^4 k_{obs}(s^{-1})$	$[CPC]_T$ (mol dm^{-3})	$10^4 k_{obs}(s^{-1})$	$[TX\text{-}100]_T$ (mol dm-3)	$10^4 k_{obs}\ (s^{-1})$
1500×10^{-4}	0.02	5.68 ± 0.002	0.002(M)	2.668 ± 0.001	0.02	1.95 ± 0.003
1500×10^{-4}	0.03	7.54 ± 0.002	0.004(M)	2.46 ± 0.002	0.03	2.36 ± 0.002
1500×10^{-4}	0.04	9.14 ± 0.002	0.006(M)	2.395 ± 0.001	0.04	2.95 ± 0.001
1500×10^{-4}	0.05	10.04 ± 0.003	0.008(M)	2.25 ± 0.001	0.05	3.98 ± 0.003
1500×10^{-4}	0.06	11.39 ± 0.002	0.01(M)	2.013 ± 0.002	0.06	4.85 ± 0.003

the rate determining step. The reaction shows both 1st order dependency on $[benzyl\ alcohol]_T$ and $[Cr(VI)]_T$ and 2nd order dependency on $[H^+]$ ion. In the presence of some non-functional surfactants, the orders remain unchanged. CPC has been found to retard the rate while SDS and TX-100 shows the rate acceleration effect (**Table 2**). The effect of added electrolye gives different observations. Inhibition followed by enhancement is the effect of NaCl but for NH_4Cl inhibition is the only fate. So for waste water treatment with biosorbent, SDS or TX-100 and suitable concentration of NaCl may be used for quick result.

7. ACKNOWLEDGEMENTS

Financial support from UGC, New Delhi is thankfully acknowledged.

REFERENCES

[1] Nriagu, J.O. and Nieboer, E., Eds. (1988) Chromium in the natural and human environments. *Advances in Environmental Science and Technology*. John Willey and Sons, New York, **20**, 1-501.

[2] Sorahan, T., Burges, D.C., Hamilton, L. and Harrington, J.M. (1998) Lung cancer mortality in nickel/chromium plates. *Occupational and Environmental Medicine*, **55(4)**, 236-242.

[3] Mancuso, T.F. (1997) Chromium as an industrial carcinogen. *American Journal of* Industrial *Medicine*, **31(2)**, 129-139.

[4] Langardt, S. (1990) One hundred years of chromium and cancer: A review of epidemiological evidence and selected case reports. *American Journal of Industrial Medicine*, **17(2)**, 189-214.

[5] Ahluwalia, S.S. and Goyal, D. (2007) Microbial and plant derived biomass for removal of heavy metals from wastewater. *Bioresource Technology*, **98(12)**, 2243-2257.

[6] Volesky, B. and Holan, Z.R. (1995) Biosorption of heavy metals. *Biotechnology Progress*, **11(3)**, 235-250.

[7] Park, D., Yun, Y.S., Kim, J.Y. and Park, J.M. (2008) How to study Cr (VI) biosorption: Use of fermentation waste for detoxifying Cr (VI) in aqueous solution. *Chemical Engineering Journal*, **136**, 173-179.

[8] Shaver, T.N., Lingren, P.D. and Marshall, H.F. (1997) Nighttime variation in volatile content of flowers of the night blooming plant, *Gaum drummondii*. *Journal of Chemical Ecology*, **23(12)**, 2673-2682.

[9] Nkpwatt, D.A., Krimm, U., Coiner, H.A., Schreiber, L. and Schwab, W. (2006) Plant volatiles can minimize the growth suppression of epiphytic bacteria by the phytopathogenic fungus *Botrytis cinerea* in co-culture experiments. *Environmental and Experimental Botany*, **56(1)**, 108-119.

[10] Das, A.K., Roy, A., Saha, B., Mohanty, R.K. and Das, M. (2001) Micellar effect on the reaction of Chromium (VI) oxidation of D-fructose in the presence and absence of picolinic acid in aqeous media: A kinetic study. *Journal of Physical Organic Chemistry*, **14(3)**, 333-342.

[11] Bayen, R., Islam, M., Saha, B. and Das, A.K. (2005) Oxidation of D-glucose in the presence of 2,2'-bipyridine by Cr^{VI} in aqueous micellar media: a kinetic study. *Carbohydrate Research*, **340(13)**, 2163-2170.

[12] Islam, M., Saha, B. and Das, A.K. (2005) Kinetics and mechanism of 2,2'-bipyridyl and 1,10-phenanthroline-catalysed chromium(VI) oxidation of d-fructose in aqueous micellar media. *Journal of Molecular Catalysis A*: *Chemical*, **236(1-2)**, 260-266.

[13] Islam, M., Saha, B. and Das, A.K. (2006) Chromic acid oxidation of hexitols in the presence of 2,2'-bipyridyl catalyst in aqueos micellar media: a kinetic study. *International Journal of Chemical Kinetics*, **38(9)**, 531-539.

[14] Islam, M., Saha, B. and Das, A.K. (2007) Kinetics and mechanism of picolinic acid promoted chromic acid oxidation of maleic acid in aqueous micellar media. *Journal of Molecular Catalysis A*: *Chemical*, **266(1-2)**, 21-30.

[15] Saha, B., Sarkar, S. and Choudhury, K.M. (2008) Micellar effect of quinquivalent vanadium ion oxidation of D-glucose in aqueous acid media: a kinetic study. *International Journal of Chemical Kinetics*, **40(5)**, 282-286.

[16] Choudhury, K.M., Mandal, J. and Saha, B. (2009) Micellar catalysis of Chromium (VI) oxidation of ethane-1, 2-diol in presence and absence of 2,2'-bipyridine in aqueos acid media. *Journal of Coordination Chemistry*, **62(11)**, 1871-1878.

[17] Ghosh, S.K., Basu, A., Paul, K.K. and Saha, B. (2009) Micelle catalyzed oxidation of propan-2-ol to acetone by penta-valent vanadium in aqueous acid media. *Molecular Physics*, **107(7)**, 615-619.

[18] Vogel, A.I. (1958) Elementary practical organic chemistry, Part-III, quantitative organic analysis, ELBS and Longman Group Ltd., London, p. 739.

[19] Bunton, C.A. and Cerichelli, G. (1980) Micellar effects

upon electron transfer from ferrocenes. *International Journal of Chemical Kinetics*, **12(8)**, 519-533.

[20] Menger, F.M. and Portnoy, C.E. (1967) Chemistry of reactions proceeding inside molecular aggregates. *Journal of the American Chemical Society*, **89(18)**, 4698- 4703.

[21] Bunton, C.A. (1979) Reaction kinetics in aqueous surfactant solutions. *Catalysis Reviews - Science and Engineering*, **20(1)**, 1-56.

[22] Morawetz, H. (1969) Catalysis and inhibition in solutions of synthetic polymers and in micellar solutions. *Advances in Catalysis & Related Subjects*, **20**, 341-371.

[23] Cordes, E.M. and Dunlop, R.B. (1969) Kinetics of organic reactions in micellar systems. *Accounts of Chemical Research*, **2(11)**, 329-337.

[24] Fendler, E.J. and Fendler, J.H. (1971) Micellar catalysis in organic reactions: Kinetic and mechanistic implications. *Advances in Physical Organic chemistry*, **76**, 271-406.

[25] Bunton, C.A., Minch, M. and Sepulveda, L. (1971) Enhancement of micellar catalysis by added electrolyte. *Journal of Physical Chemistry*, **76(2)**, 2707-2709.

[26] Das, A.K. (2004) Micellar effect on the kinetics and mechanism of chromium (VI) oxidation of organic substrates. *Coordination Chemistry Review*, **248(1-2)**, 81-99.

[27] Mysels, K.J. and Princen, L.H. (1957) Light scattering by ideal colloidal electrolyte. *Journal of Colloid Science*, **12(6)**, 594-605.

[28] Shinoda, K. (1955) The critical micellar concentrations in aqueous solutions of potassium alkyl malonates. *Journal of Physical Chemistry*, **59(5)**, 432-435.

J. Biomedical Science and Engineering, 2010, 3, 742-749 **JBiSE**
doi:10.4236/jbise.2010.37099 Published Online July 2010 (http://www.SciRP.org/journal/jbise/).

Reconstruction of conductivity distribution of brain tissue from two components magnetic flux density

Wenlong Xu, Dandan Yan

College of Information Engineering, China JiLiang University, Hangzhou, China.
Email: dandanyan@cjlu.edu.cn

Received 13 April 2010; revised 25 May 2010; accepted 27 May 2010.

ABSTRACT

In this paper the recent Magnetic resonance electrical impedance imaging (MREIT) technique is used to image non-invasively the three-dimensional continuous conductivity distribution of the head tissues. With the feasibility of the human head being rotated twice in the magnetic resonance imaging (MRI) system, a continuous conductivity reconstruction MREIT algorithm based on two components of the measured magnetic flux density is introduced. The reconstructed conductivity image could be obtained through solving iteratively a non-linear matrix equation. According to the present algorithm of using two magnetic flux density components, numerical simulations were performed on a concentric three-sphere and realistic human head model (consisting of the scalp, skull and brain) with the uniform and non-uniform isotropic target conductivity distributions. Based on the algorithm, the reconstruction of scalp and brain conductivity ratios could be figured out even under the condition that only one current is injected into the brain. The present results show that the three-dimensional continuous conductivity reconstruction method with two magnetic flux density components for the realistic head could get better results than the method with only one magnetic flux density component. Given the skull conductivity ratio, the relative errors of scalp and brain conductivity values were reduced to less than 1% with the uniform conductivity distribution and less than 6.5% with the non-uniform distribution for different noise levels. Furthermore, the algorithm also shows fast convergence and improved robustness against noise.

Keywords: Magnetic Resonance Electrical Impedance Tomography; Magnetic Flux Density Measurement; Current Density; Conductivity Distribution

1. INTRODUCTION

Knowledge of the electrical conductivity distribution in the human body is of great importance in many biomedical applications. The information of the electrical properties of head tissues is used for electroencephalographic source location and functional mapping of brain activity and functions. And it has been proved that information about the vivo tissue conductivity values improves the solution accuracy of bioelectrical field problems [1].

A non-invasive Magnetic Resonance Electrical Impedance Tomography (MREIT) imaging modality has been developed to reconstruct high-resolution conductivity distribution images for the biological issues. In this new imaging modality, electrical impedance tomography (EIT) is combined with magnetic resonance-current density imaging (MR-CDI) techniques to solve the well-known ill-posedness of the image reconstruction problem in traditional EIT. Zhang [2] proposed an image reconstruction algorithm using internal current density and peripheral voltage measurement to reconstruct static conductivity images which initiated the development on the theory of MREIT.

In MREIT, currents are injected into the subject through pairs of surface electrodes. A Magnetic Resonance Imaging (MRI) scanner is used to measure the induced magnetic flux density inside the subject and the current density distribution can be calculated according to the Ampere's law. The conductivity distribution images can be reconstructed based on the relationship between the conductivity and the measured magnetic flux density combined with the current density [3].

MREIT reconstruction algorithms fall into two categories: those utilizing internal current density [4-7] and those making use of only one component of measured magnetic flux density [3,8-15]. Considering the rotation problem of the object in the MRI system, the latter has the advantages over the former without the object rotation dilemma. MREIT algorithms that are based on current density require knowledge of the magnetic flux

density vector B = (Bx, By, Bz). Due to the fact that only one component of the magnetic flux density which parallels to the direction of the main magnetic field of the MRI scanner can be measured once, the rotation of the object is required, which is impractical for MRI scanner.

Recently, several MREIT algorithms have been proposed which utilize only one component of magnetic flux density, such as the harmonic Bz algorithm [8,9], the gradient Bz decomposition algorithm [11], the algebraic reconstruction algorithm [12] and an anisotropic conductivity reconstruction algorithm [16]. For the head tissue conductivity, the relatively novel and concise RBF (Radial Basis Function) and RSM (Response Surface Methodology) MREIT algorithms were proposed to focus on the piece-wise homogeneous head tissue conductivity reconstruction [13,14]. However, the continuous conductivity estimation of the head tissue is more useful to obtain high resolution source localization and mapping results [17]. The MREIT algorithms recently applied on the head homogeneous and inhomogeneous conductivities reconstruction [18-20] show better results. Therefore, in this paper a MREIT approach is developed to realize the estimation of continuous conductivity distribution in the human head tissues based on the three-layer realistic FEM head model.

For the head tissues, the low skull conductivity is a dilemma for the conductivity reconstruction, since much of the current is shunted through the scalp and does not enter the brain compartment. Nevertheless, the reconstruction accuracy of MREIT is the same through the imaging space and the inner part of it will not blur, which will occur in traditional EIT. In this paper, with the feasibility of the human head being rotated twice in the MRI system, a modified continuous conductivity reconstruction MREIT algorithm which is based on two components magnetic flux density as [14] did is developed for the head tissues. With one more rotation, more information could be gained and used for the reconstruction. Even under the situation that there is only one current injection used in the simulation, better results also can be achieved. Herein, the realistic FEM head model is utilized, as the original hexahedral element meshing is unavailable in the finite element modeling. The tetrahedral element meshing is an optimum choice considering the computational efficiency. Computer simulations are performed on a three-sphere head model and the results show that the three-dimensional head model continuous conductivity reconstruction method with two magnetic flux density components could get better results than the method with only one magnetic flux density component used.

For the present approach, some assumptions should be given. First, generally speaking, it is assumed that the head geometry is known, since this data can be obtained from the MRI scanner. Second, the skull conductivity of the head tissues is fixed to the constant value to focus on the continuous conductivity distribution reconstruction of the scalp and the brain. And in the following sections, the proposed algorithm based on two components magnetic flux density is explained and an iterative conductivity update method is derived. First, the formulation and numerical solution of the forward problem and the inverse problem are presented in Section 2. Then, the performance of the proposed approach is assessed by a series of computer simulations using a three-layer uniform and non-uniform conductivity distribution realistic head models in Section 3. In Section 4, discussions and conclusion about present results are given.

2. METHODS

In this paper, reconstruction of conductivity image by MREIT begins with a numerically relationship between the conductivity combined with the measured magnetic flux density due to the injected currents. In the forward problem, we calculate the peripheral voltage values and the magnetic flux density for a known conductivity distribution. And the inverse problem is to reconstruct conductivity σ from the measured magnetic field distribution B = (By, Bz) and J as well as physical laws of electromagnetic.

In MREIT, MR magnitude images provide excellent structural information, and then different regions (the scalp, the skull and the brain) of the three-layer realistic head can be determined. Within each region, the conductivity values are considered continuous distribution instead of piece-wise. Such continuous conductivity of head model could be more practical for forward or inverse problem solutions and source reconstruction in functional brain imaging using magnetoencephalography (MEG) and electroencephalography (EEG).

2.1. Forward Problem

Forward problem is defined as the calculation of magnetic field generated by the internal current pattern for a given boundary injected current profile and known conductivity distribution. Forward problem formulation is used to supply simulation data to test the proposed reconstruction algorithm and it is also used in formulating the inverse problem. The relation between the conductivity and the electrical potential U(r) induced by the injected current is given by Poisson's equation together

with the Neumann boundary conditions as:

$$\nabla\cdot\left[\sigma(r)\nabla U(r)\right]=0,\qquad r\in\Omega$$
$$\sigma\frac{\partial U}{\partial n}=\begin{cases}J, \text{ on positive current electrode}\\ -J, \ n \text{ negative current electrode}\\ 0\ . \ \text{elsewhere}\end{cases}\tag{1}$$

where $\sigma(r)$ is the electrical conductivity and Ω is the imaging subject space. For complex conductivity distributions, analytical solution to the forward problem expressed in **Eq.1** does not exist. Therefore, a numerical method must be applied. Finite element method (FEM) is used to calculate the electrical potential and corresponding magnetic flux density distribution for a given conductivity distribution and boundary conditions.

After obtaining the electric potential distribution $U(r)$ from solving **Eq.1**, the electric field E and the interior current density distribution J are given as:

$$\begin{aligned}E&=-\nabla U\\ J&=\sigma E\end{aligned}\tag{2}$$

Then the magnetic flux density can be calculated using the Biot-Savat law:

$$B(r)=\frac{\mu_0}{4\pi}\int_\Omega J(r')\times\frac{r-r'}{|r-r'|^3}dv'\tag{3}$$

where $B(r)$ is the magnetic flux density at the measurement point, and $J(r')$ is the current density at the source point and μ_0 is the magnetic permeability of the free space. In order to avoid the singularity occurring when $r = r'$, $B(r)$ is treated as a node variable and $J(r')$ is used at the centre of each finite element in (3) (Lee *et al.* 2003). The comparison between analysis solution and numerical solution by FEM method is performed by Nuo Gao [13] to indicate the feasibility of solving the forward problem using the FEM.

2.2. Inverse Problem

The inverse problem is the reconstruction of $\sigma(r)$ using the measured magnetic flux density combined with the calculated current density. Since static conditions are assumed, the equation below can be gained [21]:

$$\nabla S\times J=-\nabla\times J\tag{4}$$

where S is defined as the natural logarithm of $\sigma(r)$. Based on the relation between current density and magnetic flux density, one can obtain:

$$\nabla S\times J=\frac{\nabla^2 B}{\mu_0}\tag{5}$$

The equation is rearranged by the matrix form:

$$\begin{bmatrix}0 & J_z & -J_y\\ -J_z & 0 & J_x\\ J_y & -J_x & 0\end{bmatrix}\begin{bmatrix}\frac{\partial S}{\partial x}\\ \frac{\partial S}{\partial y}\\ \frac{\partial S}{\partial z}\end{bmatrix}=-\begin{bmatrix}\frac{\partial J_z}{\partial y}-\frac{\partial J_y}{\partial z}\\ \frac{\partial J_x}{\partial z}-\frac{\partial J_z}{\partial x}\\ \frac{\partial J_y}{\partial x}-\frac{\partial J_x}{\partial y}\end{bmatrix}=\frac{1}{\mu_0}\begin{bmatrix}\nabla^2 B_x\\ \nabla^2 B_y\\ \nabla^2 B_z\end{bmatrix}\tag{6}$$

With the two components magnetic flux density being used, the last two rows of the matrix equation can give:

$$\begin{aligned}\frac{\partial S}{\partial z}J_x-\frac{\partial S}{\partial x}J_z&=\frac{\nabla^2 B_y}{\mu_0}\\ \frac{\partial S}{\partial x}J_y-\frac{\partial S}{\partial y}J_x&=\frac{\nabla^2 B_z}{\mu_0}\end{aligned}\tag{7}$$

An iterative algorithm is used to solve the above nonlinear partial differential equation. The two components B_z and B_y used promises the equation a unique solution which is theoretically the same as the situation that two currents injection are applied.

Discretization equation is obtained by replacing derivatives with finite difference equivalents:

$$\begin{aligned}\frac{S_{(i+1,j)}-S_{(i-1,j)}}{2\Delta z}J_{x(i,j)}-\frac{S_{(i,j+1)}-S_{(i,j-1)}}{2\Delta x}J_{z(i,j)}&=\left(\frac{\nabla^2 B_y}{\mu_0}\right)_{(i,j)}\\ \frac{S_{(i+1,j)}-S_{(i-1,j)}}{2\Delta x}J_{y(i,j)}-\frac{S_{(i,j+1)}-S_{(i,j-1)}}{2\Delta y}J_{x(i,j)}&=\left(\frac{\nabla^2 B_z}{\mu_0}\right)_{(i,j)}\end{aligned}\tag{8}$$

where Δx, Δy and Δz are the distances between adjacent pixels in the x, y and z directions, respectively. Operator ∇^2 is denoted by the simple three-point difference scheme as follows:

$$\begin{aligned}&\nabla^2 B(x_i,y_i,z_i)=\\ &\frac{B(x_{i+1},y_i,z_i)-2B(x_i,y_i,z_i)+B(x_{i-1},y_i,z_i)}{(\Delta x)^2}\\ &+\frac{B(x_i,y_{i+1},z_i)-2B(x_i,y_i,z_i)+B(x_i,y_{i-1},z_i)}{(\Delta y)^2}\\ &+\frac{B(x_i,y_i,z_{i+1})-2B(x_i,y_i,z_i)+B(x_i,y_i,z_{i-1})}{(\Delta z)^2}\end{aligned}\tag{9}$$

Then the equation is rearranged into the matrix form as:

$$PS = Q \Rightarrow \begin{bmatrix} P_y \\ P_z \end{bmatrix} S = \begin{bmatrix} Q_y \\ Q_z \end{bmatrix} \quad (10)$$

where P is the (2 KM × M) coefficient matrix, M is the element number of the FEM head model and K denotes the injected current number. S is the M × 1 vector which is the each quadratic tetrahedral element value and Q is a 2 KM × 1 vector. Herein $P_\ell = [p_{\ell 1}^T\ p_{\ell 2}^T\ \cdots p_{\ell K}^T]^T$ is the vector (KM × M) for internal current density distribution J = (J_x, J_y, J_z), and $Q_\ell = [q_{\ell 1}^T\ q_{\ell 2}^T \cdots q_{\ell K}^T]^T$ is the (KM × 1) vector for $\nabla^2 B_\ell / \mu_0$ where ℓ represents the x or y component, respectively. The matrix equation is being solved iteratively until the following stopping criterion is satisfied:

$$\left\| \sigma^{i+1} - \sigma^i \right\| < \varepsilon \quad (11)$$

where σ^{i+1} denotes the i + 1th iteration and σ^i the ith iteration, ε is a given tolerance and $\|\cdot\|$ is the Euclidian norm. How to select the ε will affect the accuracy of the conductivity reconstruction algorithm. The smaller the selected ε is, the higher the accuracy of the reconstruction and the more time the convergence would be.

Then the steps of the iterative reconstruction algorithm are as follows:

Step 1: According to the given target uniform and non-uniform conductivity distributions, the 'measured' two components magnetic flux density B_z^* and B_y^* for one and two currents injection are calculated using the FEM method.

Step 2: $\nabla^2 B_z^*$ and $\nabla^2 B_y^*$ are calculated with the three-point difference **Eq.9**, and the vectors Q_ℓ are obtained, ℓ = x or y.

Step 3: An initial conductivity distribution σ_m^{ini} is assumed for m = 1, 2, … , M. This initial conductivity distribution is randomly selected to be values $\sigma_m^{ini} \in (0, 15)$ for the first iteration.

Step 4: With $\sigma_m^{ini} \rightarrow \sigma_m^{i}$, the current density distributions J = (J_x, J_y, J_z) are calculated using FEM and coefficient matrix P_ℓ is obtained for ℓ = x or y.

Step 5: Rearrange P_ℓ and Q_ℓ as the **Eq.10** and solve the combined system equation, then the solution S is found and the conductivity distribution σ_m^{i+1} is achieved.

Step 6: Stop if the stopping criterion (11) is met. Othewise, set (i + 1)→i and go to *Step* 4 with σ_m^{ini} replaced by σ_m^{i+1}.

3. RESULTS

In order to test the performance of the reconstruction algorithm using two magnetic flux density components, numerical simulations were performed on a concentric three-layer realistic human head model (consisting of the scalp, skull and brain) to estimate the continuous conductivity values σ = (σ^{scalp}, σ^{brain}).

3.1. Preparation of Experiment Data

The three-layer realistic human head model has three compartments: scalp, skull and brain. Software ANSYS 10.0 was applied to the finite element modeling and meshing as well as the solving of the forward problem. A finite element meshing for the 3D three-layer realistic head model in **Figure 1** with 57041 quadratic tetrahedral elements and 78893 nodes is used. And the conductivity in each element is assumed to be different values.

In order to get the current density image, a bipolar rectangular current (5mA) is injected into the human head model through a pair of opposite electrodes along the equator of the realistic head model (seeing **Figure 2**). A MRI scanner is used to measure the component of the induced magnetic flux density parallel to the main magnetic field of the MRI system (along the z direction), denoted as B_z^*. Then the head model is rotated once, the other component of the induced magnetic flux density denoted as B_y^* (along the y direction) is measured.

The two components magnetic flux density is calculated with the given target human head conductivity distribution in the forward problem. To prove the noise tolerance of the algorithm, Gaussian White Noise (GWN) at different levels is added to the magnetic flux density to simulate the 'measured' noise-contaminated MR magnitude image B_z^* and B_y^*. The standard deviation of noise S_B in 'measured' magnetic flux density is introduced by [22]:

$$S_B = \frac{1}{2\gamma T_c SNR} \quad (12)$$

where $\gamma = 26.75 \times 10^7 radT^{-1}s^{-1}$ is the gyromagnetic ratio of hydrogen, T_c is the duration of injection current pulse and SNR is the signal-to-noise ratio of the MR magnitude image. The SNR of the GWN is set to be infinite, 80, 60, 40, 20 and 10 with T_c = 50ms, S_B is obtained to be $2.9356 \times 10^{-9}T$, $3.9142 \times 10^{-9}T$, $5.8713 \times 10^{-9}T$, $1.1742 \times 10^{-8}T$, and $1.5657 \times 10^{-8}T$, respectively.

Given the skull conductivity, the continuous conductivity of the scalp and the brain is reconstructed with the proposed algorithm based on the measured two components magnetic flux density when one or two currents are injected, respectively. Two types of numerical simulations were performed on the three-layer realistic head model: uniform and non-uniform isotropic target continuous conductivity distribution reconstructions. The parameters of the head model are listed in **Table 1**, where σ_m denotes the conductivity value of the mth element of the finite element realistic head model.

For uniform case, the conductivity distribution in each

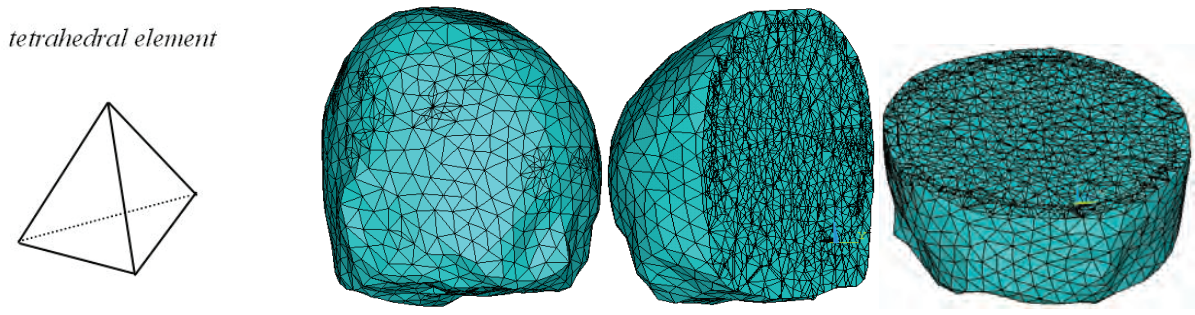

Figure 1. Three-layer realistic finite element head model: (a) a tetrahedral element is used to mesh the three-layer realistic head model (b) meshed model of the finite element realistic head model.

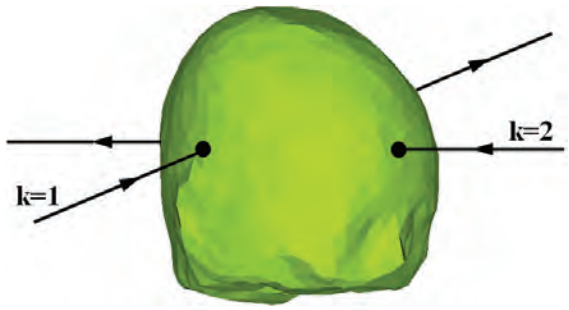

Figure 2. Current injection and electrodes locations of the realistic finite element head model.

Table 1. Uniform and non-uniform conductivity head model parameters.

	Uniform Conductivity (s/m)			Non-uniform Conductivity (s/m)		
σ_m^{target}	*Scalp*	*Skull*	*Brain*	*Scalp*	*Skull*	*Brain*
	1	1/15	1	(0.9,1.1)	1/15	(0.9,1.1)

element of the head FEM model is assumed to be identical in the scalp, skull and brain compartments, respectively. For non-uniform case, the conductivity distribution in each element is assumed to be different value in each compartment. In this study, the relative error (*RE*) between the estimated and the target conductivity distribution is used to quantitatively assess the performance of the MREIT reconstruction algorithm. The relative error is defined as follows:

$$RE(\sigma,\sigma^*)=\frac{\left\|\sigma^*-\sigma\right\|}{\left\|\sigma^*\right\|}\times 100\% \qquad (13)$$

where σ^* is the target conductivity distribution and σ is the estimation conductivity distribution.

3.2. Conductivity Image Reconstruction

The MREIT reconstruction algorithm based on two components magnetic flux density for the two different target conductivity distribution cases were tested with six noise levels, and some compared results are given below. With the tolerance ε = 0.01, it took seven iterations to reconstruct these continuous conductivity distributions. In each situation (uniform conductivity or non-uniform conductivity) with one current injection, simulation results are listed at **Table 2**. But with one current injection, meaningful reconstructions are not achieved even for noise-free simulations based on the only one component magnetic flux density algorithm. And given the two currents injection, the compared results between the algorithms based on two components and only one component magnetic flux density are given at **Table 2**.

For uniform simulation in **Table 2**, with different noise levels, all the *RE*s are less than 1% for one current injection and two currents injection simulations, which are reduced considerably compared with the algorithm based on only one magnetic flux density. It also suggests that the *RE* is insensitive to the added noise. The data also show that with the noise level of *SNR* = 10, one current injection results are more influenced than two injection ones. The case is same to the non-uniform simulation.

For non-uniform simulation, the *RE*s are less than 6.5% for one current injection and two currents injection simulations, which are not much less compared with the only one magnetic flux density algorithm. The reason is that the non-uniform distribution influences the performance of the algorithm. However, the non-uniform range of the real head conductivity distribution in one tissue changes not so severely, the feasibility of the algorithm on human head is confirmed.

The reconstruction conductivity images are shown in **Figure 3** and **Figure 4**, respectively. **Figures 3(a)** and **(b)** demonstrate the reconstruction conductivity images under the condition that without adding any noise, SNR = Infinite, SNR = 40 and SNR = 10 for uniform distribution. **Figure 4** is for the non-uniform case, respectively.

Table 2. Results of the conductivity reconstruction.

		RE (%)		SNR of the added GWN					
				Infinite	80	60	40	20	10
Uniform	K = 1	Brain	Based on B_y and B_z	0.0189	0.0243	0.0352	0.0510	0.0636	0.1848
		Scalp	Based on B_y and B_z	0.0394	0.0420	0.0528	0.1050	0.1665	0.4264
	K = 2	Brain	Based on B_y and B_z	0.0209	0.0251	0.0354	0.0468	0.0568	0.0830
		Scalp	Based on B_y and B_z	0.0484	0.0513	0.0586	0.0737	0.1227	0.1519
Non-niform	K = 1	Brain	Based on B_y and B_z	5.7802	5.7808	5.7811	5.7822	5.8315	6.0814
		Scalp	Based on B_y and B_z	5.7889	5.7894	5.7923	5.9451	6.1307	6.3492
	K = 2	Brain	Based on B_y and B_z	5.7806	5.7807	5.7808	5.7812	5.8274	5.9026
		Scalp	Based on B_y and B_z	5.7884	5.7890	5.7892	5.7898	5.9152	6.1483

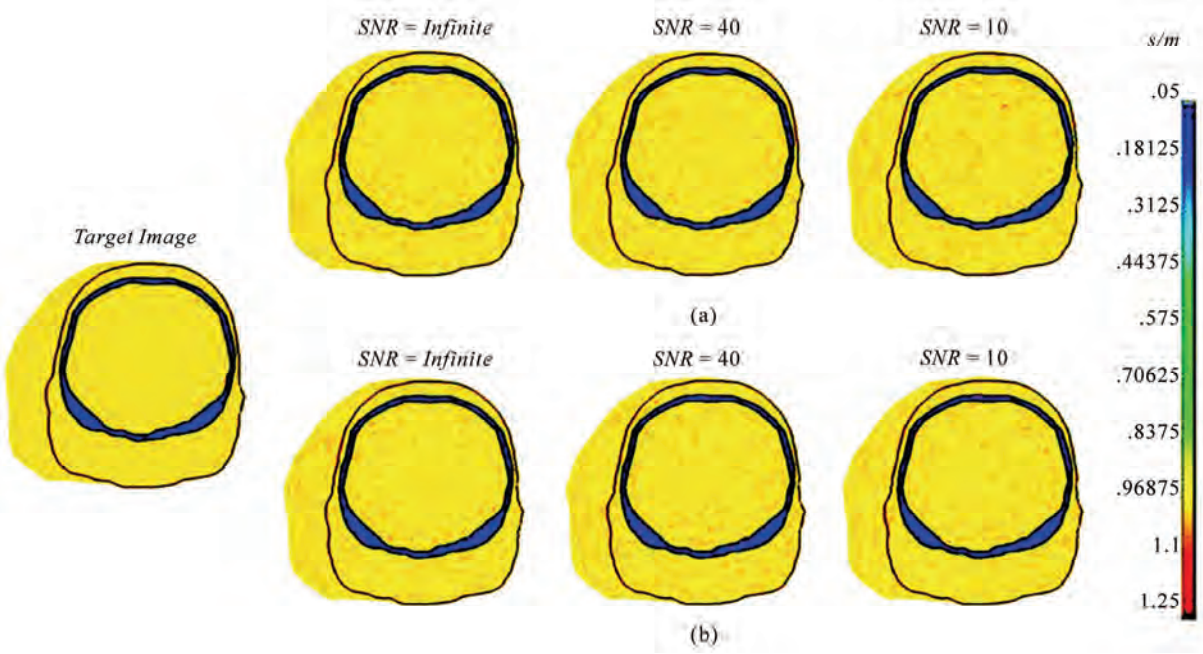

Figure 3. Uniform conductivity reconstruction images with different noise levels: (a) corresponding to one current injection, (b) corresponding to two currents injection. (a) current injection k = 1; (b) current injection k = 2.

4. DISCUSSION

In the present study, the continuous conductivity reconstruction MREIT algorithm for human head tissues utilizes measured two components magnetic flux density without using the impractical subject rotation procedure. The proposed approach is based on the algebraic reconstruction algorithm [12] and is extended to detect conductivity on object as human head model. The reconstructed image could be obtained through iteratively solving a non-linear matrix equation. Due to the two components magnetic flux density data available, the scalp and brain conductivity reconstruction which is important parameters for brain inverse problems could be figured out even with only one current injection into the brain.

The present study suggests that the full three dimensional conductivity reconstruction images over the entire subject instead of the image slice is obtained with the satisfied accuracy and spatial resolution. For uniform and non-uniform cases, the *RE*s between the target and the estimated conductivity distribution are less than 1% and 6.5% with different noise levels, respectively. The

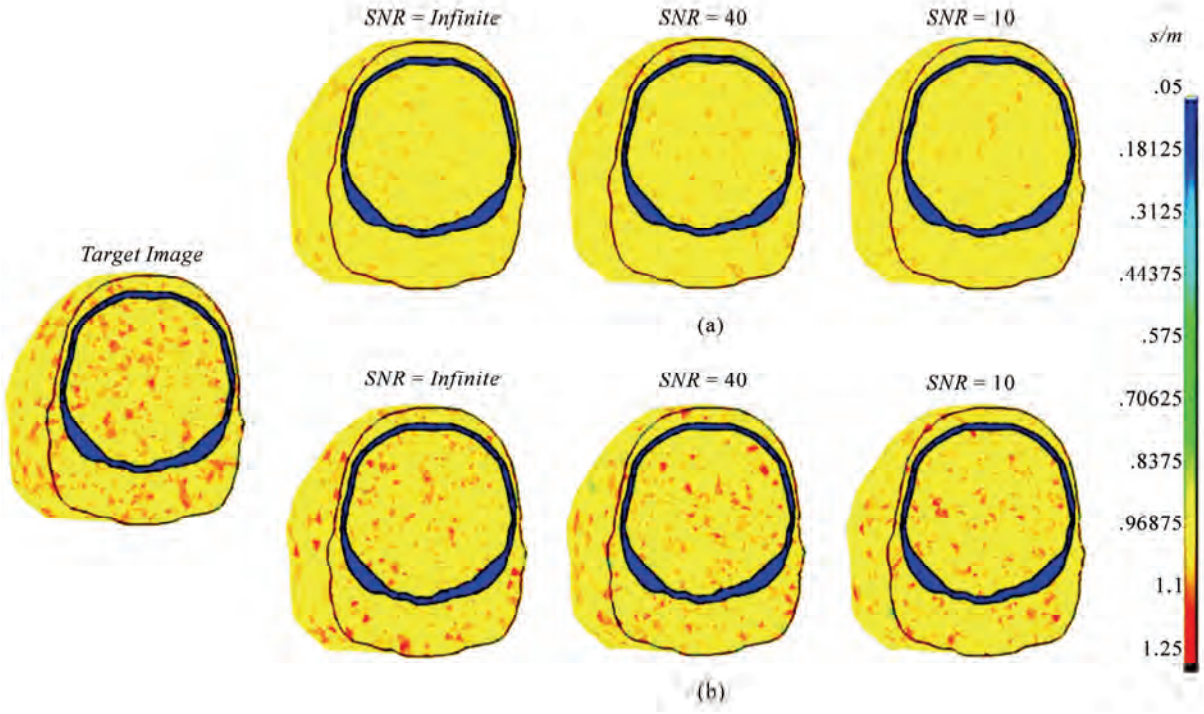

Figure 4. Non-uniform conductivity reconstruction images with different noise levels: (a) corresponding to one current injection, (b) corresponding to two currents injection. (a) current injection k = 1; (b) current injection k = 2.

present simulation results demonstrate the excellence performance of the algorithm for conductivity reconstruction of human head tissue.

In the procedure of the computation of $\nabla_2 B$, three-point difference method is utilized which will arise errors and vulnerable to measurement noise. So the means of finite difference modeling correction to the finite element modeling is a good choice to lessen the errors and improve the robustness against noise. A more sophisticated head model such as real geometry head model would be utilized to enhance the accuracy and resolution of reconstruction image at the cost of computation time. It is also found that increasing the number of injection currents does not obviously improve the solution of the reconstruction conductivity image when three or four currents are injected in the simulation.

In the present simulation, a current of 5 mA was used, which is thought to be the upper safe limit for human beings (IEC criterion). And for human head, it is a little higher. So it would be desirable to utilize a better MRI scanner, some denoising techniques and improved approaches.

In summary, we proposed MREIT approach based on two components measured magnetic flux density for noninvasive imaging of the three-dimensional continuous conductivity distribution of the head tissues. A series of computer simulations demonstrate the feasibility of the algorithm and fast convergence ability combined with improved robustness against noise. In our future studies, researches should focus on real geometry head model study and the experimental validation the algorithm on the human head phantom experiment, as well as ways to reduce the amount of the injection current down to less than 1 mA for human security consideration in clinical experiment and setting.

5. ACKNOWLEDGEMENTS

This research was possible thanks to the projects (No. Y1080215 and No. Y2090966) supported by the Zhejiang Provincial Natural Science Foundation of China.

REFERENCES

[1] Goncalves, S., de Munck, J.C., Heethaar, R.M., Lopes, da Silva, F.H. and van Dijk, B.W. (2000) The application of electrical impedance tomography to reduce systematic errors in the EEG inverse problem-a simulation study. *Physiological Measurement*, **21(3)**, 379-393.

[2] Zhang, N.P. (1992) Electrical impedance tomography based on current density imaging. MSc Thesis University of Toronto, Toronto.

[3] Birgül, Ö. and İder, Y.Z. (1996) Electrical impedance tomography using magnetic field generated by internal current distribution. *Proceedings of IEEE Engineering in Medicine and Biology*, 18*th Annual International Confe-*

rence, Amsterdam, 784-785.

[4] Birgül, Ö., Eyüboğlu, B.M. and İder, Y.Z. (2001) New technique for high resolution absolute conductivity imaging using magnetic resonance-electrical impedance tomography (MR-EIT). *Proceedings of SPIE International Symposium on Medical Imaging*, Florida, 880-888.

[5] Khang, H.S., Lee, B.I., Oh, S.H., Woo, E.J., Lee, S.Y., Cho, M.H., *et al.* (2002) J-substitution algorithm in magnetic resonance electrical impedance tomography (MREIT): phantom experiments for static resistivity images. *IEEE Transactions on Medical Imaging*, **21(21)**, 695-702.

[6] Kwon, O., Lee, J.Y. and Yoo, J.R. (2002) Equipotential line method for magnetic resonance electrical impedance tomography (MREIT). *Inverse Problems*, **18(2)**, 1089-1100.

[7] Özdemir, M.S., Eyüboğlu, B.M. and Özbek, O. (2004) Equipotential projection-based magnetic resonance electrical impedance tomography and experimental realization. *Physics in Medicine and Biology*, **49(21)**, 4765-4783.

[8] Seo, J.K., Yoon, J.R., Woo, E.J. and Kwon, O. (2003) Reconstruction of conductivity and current density imaging using only one component of magnetic field measurements. *IEEE Transactions on Biomedical Engineering*, **50(9)**, 1121-1124.

[9] Oh, S.H., Lee, B.I., Woo, E.J., Lee, S.Y., Cho, M.H., Kwon, O., *et al*. (2003) Conductivity and current density image reconstruction using harmonic Bz algorithm in magnetic resonance electrical impedance tomography. *Physics in Medicine and Biology*, **48(19)**, 3101-3116.

[10] Oh, S.H., Lee, B.I., Woo, E.J., Lee, S.Y., Kim, T.S., Kwon, O., *et al.* (2005) Electrical conductivity images of biological tissue phantom in MREIT. *Physiological Measurement*, **26(2)**, S279-S288.

[11] Park, C., Kwon, O., Woo, E.J. and Seo, J.K. (2004) Electrical conductivity imaging using gradient Bz decomposition algorithm in magnetic resonance electrical impedance tomography (MREIT). *IEEE Transactions on Medical Imaging*, **23(3)**, 388-394.

[12] İder, Y.Z. and Onart, S. (2004) Algebric reconstruction for 3D magnetic resonance-electrical impedance tomography (MREIT) using one component of magnetic flux density. *Physiological Measurement*, **25(1)**, 281-294.

[13] Gao, N., Zhu, S.A. and He, B. (2005) Estimation of electrical conductivity distribution within the human head from magnetic flux density measurement. *Physics in Medicine and Biology*, **50(11)**, 2675-2687.

[14] Gao, N., Zhu, S.A. and He, B. (2006) A new magnetic resonance electrical impedance tomography (MREIT) algorithm: The RSM-MREIT algorithm with applications to estimation of human head conductivity. *Phys Med Biol*, 3067-3083.

[15] Gao, N., He, B. (2008) Noninvasive Imaging of Bioimpedance Distribution by Means of Current Reconstruction Magnetic Resonance Electrical Impedance Tomography. *IEEE Trans Biomed Eng*, **55(5)**, 1530-1539.

[16] Seo, J. K., Pyo, H. C., Park, C., Kwon, O. and Woo, E. J. (2004) Image reconstruction of anisotropic conductivity tensor distribution in MREIT: computer simulation study. *Physics in Medicine and Biology*, **49(18)**, 4371-4382.

[17] Oostendorp, T.F., Delbeke, J. and Stegeman, D.F. (2000) The conductivity of the human skull: results of in vivo and in vitro measurements. *IEEE Transactions on Biomedical Engineering*, **47**, 1487-1492.

[18] Yan D.D., Zhang X.T., Zhu S.A. and He, B. (2006) A reconstruction algorithm for head 3D magnetic resonance electrical impedance tomography: Simulation study. *Acta Biophysica Sinica* (*in Chinese*), **22(6)**, 461-470.

[19] Yan D.D., Zhang X.T., Zhu S.A. and He B. (2007) A Two-stop MREIT algorithm for head tissue based on radial basic function neural network, *Space Medicine & Medical Engineering* (*in Chinese*), **20(2)**, 126-130.

[20] Yan D.D., Zhang X.T., Zhu S.A. and He B. (2008) Simulation study on two-step magnetic resonance electrical impedance tomography of brain anomaly tissues, *Journal of Zhejiang University* (*in Chinese*), **42(4)**, 661-666.

[21] İder, Y.Z., Onart, S. and Lionheart, W.R.B. (2003) Uniqueness and reconstruction in magnetic resonance electrical impedance tomography (MREIT). *Physiological Measurement*, **24(2)**, 591-604.

[22] Scott, G.C., Joy, M.L.G., Armstrong, R.L. and Henkelman, R.M. (1992) Sensitivity of magnetic-resonance current-density imaging. *Journal of Magnetic Resonance*, **97(2)**, 235-254.

Call for Papers

Journal of Biomedical Science and Engineering (JBiSE)

www.scirp.org/journal/jbise

JBiSE, an international journal, publishes research and review articles in all important aspects of biology, medicine, engineering, and their intersection. Both experimental and theoretical papers are acceptable provided they report important findings, novel insights, or useful techniques in these areas. All manuscripts must be prepared in English, and are subject to a rigorous and fair peer-review process. Accepted papers will immediately appear online followed by printed in hard copy.

Subject Coverage

- Bioelectrical and neural engineering
- Bioinformatics and Computational Biology
- Biomedical modeling
- Biomedical imaging, image processing and visualization
- Clinical engineering, wearable and real-time health monitoring systems
- Biomechanics and biotransport
- Software, tools and application in medical engineering
- Biomaterials
- Physiological signal processing
- Biomedical devices, sensors, artificial organs and nano technologies
- NMR/CT/ECG technologies and electromagnetic field simulation
- Structure-based drug design

Notes for Intending Authors

Submitted papers should not have been previously published nor be currently under consideration for publication elsewhere. Paper submission will be handled electronically through the website. All papers are refereed through a peer review process. For more details about the submissions, please access the website.

Website and E-Mail

www. scirp. org/journal/jbise

Email: jbise@scirp.org

Editor-in-Chief

Editorial Board

ISSN 1937-6871 (Print), 1937-688X (Online)

Journal of Biomedical Science and Engineering, 2010, 3, 645-749.
Published Online July 2010 in SciRes (http://www.scirp.org/journal/jbise).

TABLE OF CONTENTS

Volume 3 Number 7 July 2010

